INTERNATIONAL DOCTORAL
SCHOOL OF THE USC

Gonzalo
Díaz López

PhD Thesis

Sensitivity of NEXT-100 detector to neutrinoless double beta decay

Santiago de Compostela, 2022

Doctoral Programme in Nuclear and Particles Physics

TESE DE DOUTORAMENTO

SENSITIVITY OF NEXT-100 DETECTOR TO NEUTRINOLESS DOUBLE BETA DECAY

Gonzalo Díaz López

ESCOLA DE DOUTORAMENTO INTERNACIONAL DA UNIVERSIDADE DE SANTIAGO DE COMPOSTELA

PROGRAMA DE DOUTORAMENTO EN FÍSICA NUCLEAR E DE PARTÍCULAS

SANTIAGO DE COMPOSTELA

2022

DECLARACIÓN DO AUTOR/A DA TESE

D./Dna. **Gonzalo Díaz López**

Título da tese: **Sensitivity of NEXT-100 detector to neutrinoless double beta decay**

Presento a miña tese, seguindo o procedemento axeitado ao Regulamento, e declaro que:

1) A tese abarca os resultados da elaboración do meu traballo.
2) De ser o caso, na tese faise referencia ás colaboracións que tivo este traballo.
3) Confirmo que a tese non incorre en ningún tipo de plaxio doutros autores nin de traballos presentados por min para a obtención doutros títulos.
4) A tese é a versión definitiva presentada para a súa defensa e coincide a versión impresa coa presentada en formato electrónico

E comprométome a presentar o Compromiso Documental de Supervisión no caso de que o orixinal non estea na Escola.

En **Santiago de Compostela**, **16 de Decembro de 2022**.

Sinatura electrónica

AUTORIZACIÓN DO DIRECTOR/TITOR DA TESE

D./Dna. **José Ángel Hernando Morata**

En condición de: **Director/a**

Título da tese: **Sensitivity of NEXT-100 detector to neutrinoless double beta decay**

INFORMA:

Que a presente tese, correspóndese co traballo realizado por D/Dna Gonzalo Díaz López, baixo a miña dirección/titorización, e autorizo a súa presentación, considerando que reúne os requisitos esixidos no Regulamento de Estudos de Doutoramento da USC, e que como director/titor desta non incorre nas causas de abstención establecidas na Lei 40/2015.

En **Santiago de Compostela**, **16 de Decembro de 2022**

Sinatura electrónica

Preface

Neutrinos are special particles: they do not have electric charge, making them imperceptible to the electromagnetic interaction and they have a very small mass compared with the rest of fermions of less than 1 eV/c^2. Its massive nature was not clear until the discovery of neutrino oscillations at the end of the last century, and in fact the Standard Model of Particle Physics was built under the assumption that neutrinos were massless Dirac particles. Being neutrinos massive rises another unanswered question: is their fundamental nature Dirac or Majorana? Testing the Majorana nature involves the search for a lepton number not conserving process. The most sensitive process nowadays is the neutrinoless double beta decay.

In neutrinoless double beta decay $0\nu\beta\beta$ a nucleus decays emitting two electrons, with the lepton number violated by two units. Current limits show that the half-life of this process is higher than 10^{26} years. Any experimental proposal in this search must comply certain features: a good energy resolution, low background rate and large exposure. This thesis was carried out within the NEXT collaboration (*Neutrino Experiment with a Xenon TPC*), that proposes the measurement of the $0\nu\beta\beta$ decay of ^{136}Xe using a high pressure xenon electroluminiscence TPC.

In this thesis we explore the sensitivity of NEXT-100 detector, the hundred-kilogram escale detector of NEXT which is currently under construction at the *Laboratorio Subterráneo de Canfranc* (LSC) and is expected to be ready for data taking during the second semester of 2023. The thesis is organized in seven chapters. In Chapter 1 we give an academic introduction to Neutrino Physics in order to motivate its relevance within Particle Physics, with especial emphasis on neutrino masses. Chapter 2 describes the requirements and current experimental proposals in the search for neutrinoless double beta decay. Chapter 3 introduces the NEXT experiment, the detection concept and detector generations. The next four chapters constitute the main study of this thesis, consisiting in the simulation and estimation of NEXT-100 sensitivity. We start describing the simulation and data processing frameworks in Chapters 4 and 5. In Chapter 6 we describe the background model and the sensitivity analysis. Finally, Chapter 7 briefly summarizes and concludes this thesis.

December 16, 2022

Gonzalo Díaz López

USC
UNIVERSIDADE DE SANTIAGO DE COMPOSTELA

USC
UNIVERSIDADE
DE SANTIAGO
DE COMPOSTELA

Resumo

Nesta tese estúdiase a sensibilidade do detector NEXT-100 á desintegración dobre beta sen neutrinos. Existe un gran interese na busca desta desintegración xa que podería respostar preguntas fundamentais en física de neutrinos. O detector constitúe a terceira fase do experimento NEXT, colaboración na que se desenrolou esta tese.

A continuación inclúese un resumo de cada un dos capítulos nos que se divide a tese. Comézase introducindo o marco teórico e experimental nas seccións **Física de neutrinos**, **A busca da desintegración dobre beta sen neutrinos** e **O experimento NEXT**. Posteriormente descríbense a parte principal do análise da tese en **Simulación do detector**, **Procesamento de datos** e **Sensibilidade do detector NEXT-100**.

Física de neutrinos

Os neutrinos son particulas fermiónicas con dúas propiedades moi especiais: non teñen carga eléctrica e teñen unha masa moi pequena. O feito de que non teñan carga eléctrica fainas invisibles á interacción electromagnética, polo que a súa interación coa materia ordinaria só se produce mediante interacción feble o que as fai moi difíciles de detectar. Todavía non se coñece con exactitude a súa masa, pero sábese que é menor que 1 eV/c^2, unha masa moito máis pequena que a do resto de partículas masivas coñecidas. Hoxe en día sabemos que teñen masa grazas ás medidas realizadas polos experimentos de oscilacións de neutrinos.

Nos experimentos de oscilacións, os neutrinos son detectados a unha determinada distancia da fonte emisora. O que se observa é un cambio na composición dos neutrinos durante a súa viaxe, por exemplo parte dos neutrinos que foron producidos na fonte como muónicos son medidos tralo seu viaxe como electrónicos. Este cambio no sabor na medida dos neutrinos só pode explicarse coa existencia de neutrinos masivos, de tal forma que os neutrinos de sabor son en realidade unha composión de neutrinos masivos. O mínimo número de neutrinos masivos compatible coas observacións actuais de oscilacións é tres, con dúas posibles ordenacións de masas distintas, orde normal ou orde invertida. Sen embargo, os experimentos de oscilacións non son sensibles ao valor absoluto da masa dos neutrinos nin á súa descripción a nivel fundamental, que pode ser de Dirac ou de Majorana.

O feito de que os neutrinos teñan masa constituíu un descubrimento revolucionario na física de partículas a finais do século pasado. Ata ese momento, o Modelo Estándar (SM) da física de partículas, que é a teoría máis precisa en explicar as interacións entre as partículas, consideraba que os neutrinos non tiñan masa. Xa que os neutrinos son masivos e ademáis non teñen carga eléctrica, ábrese a posibilidade de que poidan ser

partículas de tipo Majorana. De ser así, o neutrino e o antineutrino serían partículas inditinguibles e poderíase explicar a súa pequena masa en comparación co resto dos fermións. Probar a natureza de Majorana dos neutrinos require a busca de procesos nos que non se conserve o número leptónico, ao contrario que se foran de Dirac. En particular, o proceso máis sensible nesta busca trátase da desintegración dobre beta sen neutrinos.

A desintegración dobre beta sen neutrinos é un proceso no que un núcleo desintégrase emitindo dous electróns

$$N(A,Z) \rightarrow N(A,Z+2)+2e^{-},$$

no que o número leptónico cambia en dúas unidades. De existir este proceso, significaría que os neutrinos son partículas de Majorana. A enerxía total dos electróns está ben definida pola diferenza de masas dos nucleos do proceso, cun valor ao que nos referiremos a continuación como o $Q_{\beta\beta}$. A día de hoxe todavía non existe evidencia da existencia deste proceso, que en base aos límites actuais é maior aos 10^{26} anos.

A busca da desintegración dobre beta sen neutrinos

A sensitividade dunha proposta experimental á medida de dobre beta depende de varios factores. En particular, pódese demostrar fácilmente que a sensitividade ven dada por

$$S(T^{0\nu}_{1/2}) \propto \epsilon_s \sqrt{\frac{t \cdot M}{b \cdot \Delta E}},$$

onde ϵ_s é a eficiencia de señal, t o tempo de operación do experimento, M a masa total do isótopo de interese, b a tasa de fondo na rexión de interese e ΔE a resolución enerxética. Non existe unha proposta experimental óptima á dobre beta, xa que os propios parámetros están correlacinados, senon que cada tecnoloxía trata de optimizar as súas propias fortalezas e minimizar as súas debilidades. En xeral, unha boa proposta debe de ter unha boa resolución enerxética, unha tasa de eventos de fondo baixa, unha boa eficiencia de identificación de sinal respecto aos eventos de fondo e a capacidade de escalado.

Unha boa resolución enerxética é chave xa que a enerxía total dos electróns emitidos na desintegración é fixa ($Q_{\beta\beta}$). Tipicamente a resposta do detector a unha deposición enerxética fixa é gaussina, polo que a enerxía medida fluctuará en maior ou menor medida do seu valor. Se a resolución enerxética é mala, a fluctuación no valor da enerxía medida é alto, polo que mais eventos de fondo con enerxías cercanas ao $Q_{\beta\beta}$ entraran nesa rexión de interese. En cambio cunha boa resolución enerxética a cantidade de eventos de fondo reduciráse, que é outra das características desexadas nun experimento de dobre beta. Tamén é posible mitigar o número de eventos de fondo medindo propiedades dos eventos a maiores da enerxía total. A maioría dos experimentos actuais teñen unha maneira de discriminar activamente entre eventos de sinal e fondo utilizando unha variable discriminante, como por exemplo o número de sinais distintas no detector por un evento: os eventos de fondo deixan máis sinais no detector que os eventos de sinal, que só deixan unha.

A capacidade de escalado refírese á adecuación da tecnoloxía a construír detectores máis grandes, con maiores masas do isótopo de interese e así aumentar a exposición.

USC DE SANTIAGO

Actualmente atopámonos na era de detectores na escala de cen kilogramos e comezando a era dos detectores de unha tonelada. Ademais, ainda que existen trinta e cinco posibles isótopos candidatos de desintegración dobre beta, actualmente só nove son utilizados. A condición máis restrictiva para escoller o isótopo tamén ten que ver co escalado do experimento, xa que é necesario que exista unha técnica de enriquecemento ou unha alta abundancia natural do isótopo en cuestión.

É posible clasificar os principais experimentos de dobre beta segundo a tecnoloxía utilizada: semiconductores, bolómetros, TPCs e centelleadores. Tanto semiconductores como bolómetros destacan pola súa excelente resolución enerxética, as TPCs destacan por unha boa resolución enerxética e capacidade de discriminación activa de eventos de sinal e fondo, e os centelleadores a súa capacidade de escalado. En particular, o experimento de unha tonelada que utiliza a tecnoloxía de centelleo KamLand-Zen é o que proporciona o límite máis restrictivo á vida media da dobre beta, de en torno aos 10^{26} anos. Outros experimentos destacados son: en semiconductores, GERDA, do que estase a construir a súa versión de unha tonelada LEGEND; en bolómetros, CUORE, do que tamén estase a construír a versión de unha tonelada CUPID; en TPCs, EXO e NEXT, o segundo será detallado a continuación.

O experimento NEXT

O experimento NEXT (*Neutrino Experiment with a Xenon TPC*) é unha colaboración internacional con destacada presencia de institucións españolas e estadounidenses. NEXT busca a desintegración dobre beta sen neutrinos no isótopo ^{136}Xe, utilizando unha tecnoloxía de cámara de proxección temporal (TPC) electroluminiscente con xenon gasoso a alta presión. Además da relativa simplicidade técnica ao non requerir un sistema de crioxénia, o feito de emplear xenon gasoso con respecto a líquido débese a dous factores fundamentais: a súa excelente resolución enerxética intrínsica ao redor de 0,3 % FWHM no $Q_{\beta\beta}$; a obtención de traxectorias extendidas no gas permitindo a súa reconstrucción. O uso de amplificación do sinal por medio de electroluminiscencia permite acadar resolucións enerxéticas moi cercanas ao valor intrínseco. A reconstrucción das traxectorias permite o acceso a unha variable discriminante fundamental entre eventos de sinal e de fondo: os electróns depositan a maior parte da súa enerxía ao final da traxectoria, o chamado pico de Bragg, polo que eventos de sinal con dous electróns terán dous picos de Brag, e os eventos de fondo só un ao estaren constituídos por traxectorias de un único electrón.

O proceso de detección en NEXT é o seguinte. Os electróns depositan a súa enerxía no xenon gasoso mediante a excitación e ionización dos seus átomos. A desexcitación dos átomos excitados produce luz de centelleo, que é medida no plano de enerxía do detector. O plano de enerxía está constituído por tubos fotomultiplicadores (PMTs) que miden a luz con boa resolución. A medida deste centelleo, ao ser instantáneo, proporciona unha sinal do comezo do evento. Por outra parte, os electróns de ionización son derivados á rexión de electroluminiscencia mediante a utilización dun campo eléctrico que evita a súa recombinación. Na rexión de electroluminiscencia, onde o campo eléctrico é moi intenso, os electróns de ionización emiten gran cantidade de luz. Esta luz é medida de novo no plano de enerxía, o que proporciona unha medida da enerxía total do evento. Ademais, a luz de electroluminiscencia é medida no plano de reconstrucción que consiste nunha matriz de fotomultiplicadores de silicio (SiPMs),

proporcionando a reconstrucción espacial da traxectoria do evento.

O experimento NEXT está constituido por varias fases, cada unha delas cunha maior masa total do isótopo de interese no detector, igual que sucede nos outros experimentos de dobre beta. O primeiro período (2009-2014) adicouse ao desenrolo da tecnoloxía e a demostración da boa resolución enerxética cos detectores NEXT-DBDM e NEXT-DEMO con ao redor dun kilo de xenon. No seguiente período (2016-2021) construíuse o detector NEXT-White con ao redor de catro kilos de xenon. NEXT-White demostrou a obtención de boa resolución enerxética $\sim 1\,\%$ FWHM no $Q_{\beta\beta}$ nun detector relativamente grande mediante técnicas de calibración, a discriminación de eventos de sinal e de fondo usando o pico de Bragg das trayectorias reconstruidas, a adecuación do modelo de fondo e finalmente a medida da vida media da desintegración dobre beta con neutrinos.

A seguinte fase do experimento consiste na construcción e operación de NEXT-100, detector de ~ 70 kg de xenon co obxectivo de buscar a dobre beta sen neutrinos. Para a redución do fondo de orixe cosmoxénico, NEXT-100 estáse a construir no *Laboratorio Subterráneo de Canfranc* (LSC) no Pirineo aragonés, onde tamén se operou con NEXT-White. NEXT-100 terminarase de construír e comezará a súa operación no segundo semestre de 2023, e a súa sensibilidade é estudiada nesta tese. A seguinte fase de NEXT consistirá na construcción dun detector na escala de unha tonelada, actualmente en proceso de R&D que estuda cambios de implementación da tecnoloxía como a inclusión dun prometedor sistema de captura de ións de $^{136}Ba^{2+}$, o producto da desintegración dobre beta do ^{136}Xe, que permitiría virtualmente a redución total dos eventos de fondo.

Simulación do detector

A correcta simulación do detector e os procesos físicos que ocorren nel é esencial nos experimentos de dobre beta. En particular, a construción do modelo de fondo e sinal baséase en simulacións que son empleadas para reportar en última instancia os resultados do experimento. Esta tese enfócase no estudo da sensitividade de NEXT-100, que estará completamente baseado na súa simulación e en coñecementos previos con NEXT-White.

A librería de software extensivamente empleado en física de partículas é GEANT4. Esta librería, escrita no linguaxe de programación *C++*, permite implementar en detalle a xeometría e materiais do detector, os procesos físicos de interese, a xeración dos eventos e accións de usuario. Nesta tese descríbese a implementación das distintas partes da xeometría e xeneración de eventos no detector NEXT-100 seguindo as pautas establecidas por GEANT4. A xeometría constrúese mediante a simplificación dos detallados debuxos de enxeñeiría. Para cada componente do detector, defínese un xerador de vértice para poder simular eventos dende as distintas rexións, que son empleados maioritariamente para simular a radiactividade dos materias de construcción.

No detectores de NEXT, por cada evento de enerxía ao redor de $Q_{\beta\beta}$, o número de fotóns emitidos na rexión de electroluminiscencia é moi grande, ao redor de cen millóns. Esto causa que as simulacións de GEANT4, que simula detalladamente a propagación de cada unha das partículas no detector, sexan moi lentas: un único evento na rexión de enerxía de interese levaría máis de unha hora de simulación. Esto

constitúe un gran impedimento nos estudos dos detectores de NEXT, que igual que noutros experimentos de dobre beta, requiren de simulacións de gran exposición con moita estatística.

Nesta tese desenrolase e valídase un algoritmo moi sinxelo que evita a lentitude das simulacións ópticas, pasando de tempos de simulación por evento maiores a unha hora a uns poucos segundos. Este algoritmo consiste en substituír a simulación dos fotóns por valores precalculados das probabilidades de detección dos sensores en función do punto de emisión. Defínense doús tipos de obxectos, as tablas de luz para os PMTs e a función de dispersión de punto dos SiPMs. Para cada PMT e posible posición de emisión dentro do volumen activo do detector, a tabla almacena os valores da probabilidade de detección. A tabla codifica así o efecto do ángulo sólido e as reflexións no tubo de luz entre o PMT e o punto de emisión. Por outra parte, para os SiPMs defínese a probabilidade de detección en función da distancia entre un SiPM e o punto de emisión. Ambos obxectos calcúlanse mediante simulacións ópticas intensivas previas en GEANT4. Debido á súa simplicidade, o algoritmo é implementado en *Python* e incluído na cadea de procesado de datos do experimento.

Procesado de datos

Nos detectores de NEXT mídense sinais electrónicas nos sensores, os PMTs e os SiPMs. Esas sinais deben ser procesadas por un conxunto de algoritmos para reconstruír as trazas dos eventos empleadas no análise de datos. No caso de simulacións, estas tamén proporcionan a resposta dos sensores polo que a cadea de reconstrucción é a mesma en ambos casos.

O procesado comeza coas funcións de onda dos sensores, que son obxectos co número de fotoelectróns medidos en cada sensor en bins temporais. Un algoritmo establece un corte sobre a suma das funcións de onda dos PMTs para buscar os dous tipos de sinais do detector, o sinal de centelleo (S1) e a de electroluminiscencia (S2). A sinal de S2 idéntificase nas funcións de onda dos SiPMs para a posterior reconstrucción da traxectoria. Posteriormente as sinais identificadas son correxidas en enerxía usando o método de calibración por mapas de krypton. Cada unha das sinais nos SiPMs é correxida empleando o valor xeométrico e de impurezas proporcionado polos mapas de krypton nesa posición. Desta forma obténse a traxectoria reconstruída do evento no volumen activo. Esta traxectoria está afectada polo fenómeno físico de difusión, polo que un algoritmo de tratamento de imaxes aplícase sobre a mesma para deconvolucionarla, proporcionando un obxecto espacialmente mellor definido e adecuado para a análise. Finalmente, a traxectoria pasa por un algoritmo que busca os seus extremos mediante unha técnica de pixelización volumétrica e maximización da lonxitude entre os cada par de píxeles. Coñecer os extremos permite calcular a enerxía do pico de Bragg, a variable discriminante entre sinal e fondo en NEXT.

A cadena de procesado de datos está implementada na linguaxe de programación *Python*, que proporciona flexibilidade e sinxeleza no desenrolo e comprensión das distintas compoñentes do software. Empléase o xestor de paquetes *conda*, que evita o solapamento entre dependencias das distintas librerías empleadas, principalmente de ámbito científico. Os algoritmos de procesado impleméntanse en bloques independentes chamados cidades, que permiten o procesado unitario de cada un deles.

USC UNIVERSIDADE DE SANTIAGO

A implementación do procesado de datos en NEXT resulta innovador no ámbito da física de partículas debido á adopción de ferramentas de uso xeral cunha amplia comunidade de contribuíntes que beneficia a eficiencia de integración continua.

Sensibilidade do detector NEXT-100

O estudo da sensibilidade de NEXT-100 consiste en estimar o valor da vida media á desintegración sobre beta sen neutrinos que podería reportar o experimento trala súa operación. O estudo involucra a simulación detallada dos eventos de sinal e de fondo no detector, así como o procesado empleando os mesmos algoritmos de reconstrucción utilizados na análise de datos, tratando de emular o que sucedería trala operación real do detector.

Na rexión de enerxía de interese ao redor do $Q_{\beta\beta}$ podemos atopar contribucións non despreciables de fondo de tipo radioxénico e cosmoxénico. Os fondos radioxénicos son aqueles provintes de impurezas nos materiais de construcción debido a trazas de elementos das cadenas de desintegración naturais do uranio e torio. En particular, hay dous elementos nas cadeas que poden xerar deposicións enerxéticas na rexión de interese: o ^{208}Tl e o ^{214}Bi. O $Q_{\beta\beta} \sim 2{,}5$ MeV atópase entre a pico de $\sim 2{,}6$ MeV e o límite compton $\sim 2{,}3$ MeV da desintegración do ^{208}Tl. A contribución provén de eventos de dobre compton. O ^{214}Bi ten un pico ao redor de $\sim 2{,}4$ MeV, moi cerca do $Q_{\beta\beta}$ co que solapa incluso para a boa resolución de NEXT. Por outra banda, a interacción dos muóns de orixe cosmoxénico cós materiais do detector xeran neutróns que producen contribucións de fondo tras activar outros materiais. En particular, na rexión de enerxía de interese distinguimos dous tipos de eventos: a desintegración γ instantánea de nucleos activados, esencialmente do cobre, e a desintegración β retardada do ^{137}Xe trala activación do ^{136}Xe.

Os eventos radioxénicos son simulados en base ás actividades dos distintos compoñentes do detector, que son medidas pola colaboración na súa campaña de cribado para asegurar a colocación de compoñentes altamente radiopuras. Por outra parte, os muóns cosmoxénicos son simulados en base ao fluxo total medido no LSC. Un total de $\sim 10^{10}$ eventos de fondo foron simulados, dos cales $\sim 3 \cdot 10^4$ depositan enerxía na rexión de interese en torno ao $Q_{\beta\beta}$ e son procesados para a súa posterior análise. Tamén se simulan quince mil eventos de sinal, e catro millons de eventos de krypton para o cálculo das correccións enerxéticas. Todas as simulacións e procesado foron realizadas no *Centro de Supercomputación de Galicia*.

Empleando a producción de sinais e fondo é posible estudar a sensibilidade do detector NEXT-100. Unha primeira aproximación conservadora ao estudo da sensibilidade consiste no límite de experimento de conteo, que asume que o sinal, desintegración dobre beta sen neutrinos neste caso, non existe na natureza. Neste límite, establécense un conxunto de seleccións sobre os datos simulados tratando de optimizar a discriminación entre os eventos de sinal e de fondo. Obtense que é posible obter unha tase de fondo menor a unha conta por ano na rexión enerxética de interese cunha eficiencia de sinal do 18 %, que se traduce nunha sensibilidade na vida media de $2{,}4 \cdot 10^{25}$ anos tras unha toma de datos de tres anos. Introdúcese tamén outra estimación da sensibilidade mediante o cálculo dos intervalos de confianza. Este proceso lévase a cabo mediante a emulación de experimentos nos que se estima a cantidade

de sinais presentes en función dun rango de vidas medias, axustando os experimentos ás variables discriminates. Obtense unha estimación da sensibilidade, tras tres anos de toma de datos, de $4{,}15 \cdot 10^{25}$ anos.

Como resultado principal da tese conclúese que o experimento NEXT está preparado para realizar unha busca da desintegración dobre beta sen neutrinos análoga a outras tecnoloxías con exposicións similares como EXO, CUORE e GERDA.

USC
UNIVERSIDADE
DE SANTIAGO
DE COMPOSTELA

USC
UNIVERSIDADE
DE SANTIAGO
DE COMPOSTELA

Acknowledgments

En primer lugar querría expresar mi agradecimiento a **José Ángel** por su dedicación, bondad y paciencia conmigo durante estos años. También a **Juanjo**, gracias por tu arropo y confianza. Thanks **Adam** for your insight, I have received from you one of the most important lessons in science: *devil is in the details*.

Gracias a los miembros de nuestro pequeño grupo de Santiago. **Josh**, por las inumerables cenas en el chino. **Marija**, por tu paciencia y ayuda técnica. **Gonzalo** y **Brais**, por introducirme en la colaboración. **Martín** y **Carlos**, por vuestra ayuda en tareas tediosas, con vuestra capacidad os auguro una gran contribución en el experimento.

Gracias a los 'valencianos'. **Paola**, **Justo**, **Javi**, **Helena**, sin vuestra ayuda esta tesis no hubiera sido posible. **Michel**, gracias por tus detalladas correciones. Ha sido un placer haber compartido esta experiencia y *collaborations* con vosotros **Alberto**, **Miryam**, **Ander**, **Neus**, **Pau**, **Carmen**, **Andrew**, **José María**...

Gracias a mis amigos de la USC. Desde primero de carrera he podido compartir este camino junto con vosotros **Alex**, **Gabi**, **Julián** y **Adrián**. Por esas discusiones de física para entender los *multipolos* y las interminables conversaciones de café.

Gracias a mis **padres** por enseñarme el valor del trabajo y la perseverancia. A mis **hermanos** por enseñarme a reírme de mi mismo. Sin el continuo apoyo y ayuda de mi **familia** no hubiera llegado hasta aquí.

En Santiago de Compostela, a 16 de Diciembre de 2022

USC
UNIVERSIDADE
DE SANTIAGO
DE COMPOSTELA

USC
UNIVERSIDADE
DE SANTIAGO
DE COMPOSTELA

Contents

Preface I

Resumo III

Acknowledgments XI

I Introduction and objectives 1

1. Neutrino Physics 3
1.1. Introduction . . . 3
1.2. Two component Dirac theory . . . 3
1.3. Neutrinos in the Standard Model . . . 6
1.4. Massive and mixed neutrinos . . . 10
1.4.1. Dirac neutrinos . . . 11
1.4.2. Majorana neutrinos . . . 13
1.4.3. Dirac and Majorana neutrinos . . . 16
1.5. Neutrino Oscillations . . . 18
1.5.1. A summary of oscillation experiments . . . 20
1.5.2. Mass orderings and global fits . . . 25
1.6. Direct searches of neutrino mass and nature . . . 26
1.6.1. Beta decay . . . 26
1.6.2. Neutrinoless double beta decay . . . 29

2. The search for neutrinoless double beta decay 33
2.1. Introduction . . . 33
2.2. Sensitivity of a double beta decay experiment . . . 35
2.2.1. Confidence intervals . . . 35
2.2.2. Sensitivity to the effective Majorana mass . . . 37
2.3. Design of a double beta decay experiment . . . 39
2.3.1. Choice of isotope . . . 39
2.3.2. Backgrounds . . . 40
2.3.3. Efficiency . . . 41
2.3.4. Exposure . . . 41
2.4. Experimental program . . . 42
2.4.1. Semiconductors . . . 42
2.4.2. Bolometers . . . 44
2.4.3. Time projection chambers . . . 45

USC UNIVERSIDADE DE SANTIAGO DE COMPOSTELA

2.4.4. Scintillators . . . 47
2.4.5. Tracking Calorimeters . . . 49

3. The NEXT experiment **51**
3.1. Introduction . . . 51
3.2. Gaseous xenon as detector medium . . . 51
3.2.1. Thermophysical properties . . . 51
3.2.2. Energy loss . . . 52
3.2.3. Electroluminiscence . . . 55
3.2.4. Energy resolution . . . 56
3.3. The SOFT detection concept . . . 59
3.4. NEXT detectors . . . 60
3.4.1. R&D detectors . . . 61
3.4.2. NEXT-White . . . 62
3.4.3. NEXT-100 . . . 72
3.5. Future plans . . . 74

II Methodology **75**

4. Detector Simulation **77**
4.1. Introduction . . . 77
4.2. NEXUS Overview . . . 77
4.3. DETSIM . . . 80
4.3.1. Introduction . . . 80
4.3.2. Light Tables . . . 80
4.3.3. Point Spread Function . . . 81
4.3.4. The algorithm . . . 84
4.3.5. Implementation details and performance . . . 89
4.3.6. Validation . . . 91
4.3.7. Conclusions . . . 93
4.4. NEXT-100 implementation in NEXUS . . . 97

5. Data processing in NEXT **105**
5.1. Introduction . . . 105
5.2. Processing pipeline . . . 105
5.3. Algorithms . . . 107
5.3.1. Simulation of sensor electronics . . . 107
5.3.2. Peak finding algorithm . . . 108
5.3.3. Energy corrections . . . 109
5.3.4. Lucy-Richardson deconvolution . . . 111
5.3.5. Longest path algorithm . . . 114
5.4. Software framework . . . 115

III Results and conclusions **117**

6. Sensitivity of NEXT-100 detector to $0\nu\beta\beta$ **119**
6.1. Introduction . . . 119
6.2. Background model . . . 119

USC UNIVERSIDADE DE SANTIAGO DE COMPOSTELA

6.2.1. Terrestrial backgrounds 120
6.2.2. Cosmogenic backgrounds 125
6.3. Simulation and data production 126
6.4. Sensitivity of NEXT-100 detector 128
6.4.1. Counting experiment 128
6.4.2. Confidence intervals 136

7. Summary and conclusions **141**

Bibliography **145**

A. NEXUS configuration files **155**

B. IC configuration files **157**

C. Permissions for the reproduction of figures **161**

USC UNIVERSIDADE DE SANTIAGO DE COMPOSTELA

USC
UNIVERSIDADE
DE SANTIAGO
DE COMPOSTELA

Part I

Introduction and objectives

USC
UNIVERSIDADE
DE SANTIAGO
DE COMPOSTELA

USC
UNIVERSIDADE
DE SANTIAGO
DE COMPOSTELA

CHAPTER 1

Neutrino Physics

1.1. Introduction

The existence of neutrinos was hypothesized in the famous letter by W. Pauli at the Tübingen conference in 1930 [1]. Originally it was proposed to explain the continuous energy spectra of β decay measured by Wooster and Ellis calorimetric experiment in 1927 [2]. He thought that neutrinos were neutral 1/2-spin particles living in the nucleus together with protons, being emitted with the electron in β decay. It was not until 36 years later, in 1956, that neutrinos were directly measured in the Cowan-Reines experiment [3].

For many years it was thought that neutrinos were massless, and the Stardard Model (SM) of particle physics is built under this assumption. However neutrino oscillation experiments have proven that massive neutrinos exist, constituting the first evidence that the SM is not the ultimate theory of nature after all. This was a major progress in particle physics and it opens many questions related to neutrinos, among others

- Are there only three neutrino families? Do sterile, non-interacting netrinos exist?
- What are the absolute values of neutrino masses? What is the neutrino mass ordering, normal or inverted?
- Are neutrinos Dirac or Majorana particles?
- Is CP violated in the lepton sector?
- What is the mechanism behind neutrinoless double beta decay?
- ...

This Chapter is intended motivate why do we have so many fundamental doubts about neutrinos and the conceptual framework in which they arise. Most of the material is based on the excellent references [4] and [1]. It is organized in 5 Sections. Sections 1.2 and 1.3 revisit how neutrinos are described in the SM, Section 1.4 discusses the different mass lagrangians, Section 1.5 introduces and reviews the status of neutrino oscillations and Section 1.6 describes the direct neutrino searches.

1.2. Two component Dirac theory

USC DE SANTIAGO

Fermion fields are described in the Stardard Model (§1.3) as chirality eigenstates. The reason behind such a non-trivial description resides in the discovery of parity violation by the C. S. Wu experiment in 1957 [5]. In this section we derive relevant results that will be used later in this Chapter.

Fermion fields are described as 4-component spinors $\psi(x)$ that satisfy *Dirac equation*

$$(i\gamma^\mu\partial_\mu - m)\psi(x) = 0, \tag{1.1}$$

where γ^μ ($\mu = 0,1,2,3$) are a set of 4×4 matrices satisfying

$$\{\gamma^\mu,\gamma^\nu\} = 2g^{\mu\nu} \quad \text{and} \quad \gamma^0\gamma^{\mu\dagger}\gamma^0 = \gamma^\mu. \tag{1.2}$$

Dirac equation (1.1) can be derived from the Dirac Lagrangian

$$\mathscr{L}^D(x) = \overline{\psi}(i\gamma^\mu\partial_\mu - m)\psi, \tag{1.3}$$

where the adjoint field $\overline{\psi}$ is defined as

$$\overline{\psi} \equiv \psi^\dagger\gamma^0. \tag{1.4}$$

Under a Lorentz transformation,

$$x^\mu \to \Lambda^\mu_\nu x^\nu, \quad \psi(x) \to S(\Lambda)\psi, \tag{1.5}$$

with

$$S(\Lambda)^{-1} = S(\Lambda)^\dagger \quad \text{and} \quad S(\Lambda)^{-1}\gamma^\mu S(\Lambda) = \Lambda^\mu_\nu\gamma^\nu, \tag{1.6}$$

we see that (1.3) is invariant, thus Dirac equation (1.1) is *relativistic covariant*.

By solving the Dirac equation it is found that two of the four spinor components correspond to *positive energy solutions*, and the other two to *negative energy solutions*. The existence of two-component like solutions with positive energy agrees with the Pauli bispinor extension of non-relativistic quantum mechanics of 1/2-spin particles. Nevertheless, the existence of mirrored non-negative solutions seemed questionable for some physicists like E. Majorana [6]. The interpretation of energy solutions corresponds to the existence of *antiparticles*, such that the same field $\psi(x)$ contains both particle and antiparticle creation operators. Therefore Dirac equation not only describes 1/2-spin particles in a relativistic setting, but also predicts the existence of antiparticles.

The two-component grouping inside the four-component spinor motivates whether we can split Dirac equation in two different equations. This idea was firstly proposed by Weyl [7] in 1929 and further developed by Landau, Lee and Yang [8] in 1957 to describe massles neutrinos. As we will see (§1.3) the two-component theory is not only relevant for massless fermions but it constitutes a building block of the Standard Model.

Let's define the *chirality* matrix as

$$\gamma^5 \equiv \gamma_5 \equiv i\gamma^0\gamma^1\gamma^2\gamma^3, \tag{1.7}$$

then, using (1.2),

$$\{\gamma_5,\gamma^\mu\} = 0, \quad (\gamma_5)^2 = \mathbf{1}, \quad {\gamma_5}^\dagger = \gamma_5. \tag{1.8}$$

USC UNIVERSIDADE DE SANTIAGO DE COMPOSTELA

Now we can define the chirality right-handed (R) and left-handed (L)[1] projectors as,

$$P_{R,L} = \frac{\mathbf{1}\pm\gamma_5}{2}. \tag{1.9}$$

[1]The nomenclature will be clear below.

Multiplying Dirac equation (1.1) by the projectors $P_{R,L}$

$$P_{R,L}(i\gamma^\mu\partial_\mu - m)\psi = (i\gamma^\mu\partial_\mu P_{L,R} - mP_{R,L})\psi = 0 \tag{1.10}$$

implies that we can split it in the so-called *Weyl equations*

$$i\gamma^\mu\partial_\mu\psi_R = m\psi_L, \tag{1.11}$$
$$i\gamma^\mu\partial_\mu\psi_L = m\psi_R, \tag{1.12}$$

where the right-handed and left-handed *chiral fields* are respectively given by

$$\psi_{R,L} \equiv P_{R,L}\psi. \tag{1.13}$$

From the properties of the chirality operator, we find that chiral fields are eigenfunctions of γ_5,

$$\gamma_5\psi_{R,L} = \pm\psi_{R,L}. \tag{1.14}$$

Therefore we have shown how Dirac equation (1.1) can be splited in the two coupled Weyl equations (1.11) and (1.12) such that

$$\psi = \psi_R + \psi_L. \tag{1.15}$$

In terms of the chiral fields, the Dirac Lagrangian (1.3) can be written as

$$\mathscr{L}^D = \overline{\psi_L}i\gamma^\mu\partial_\mu\psi_L + \overline{\psi_R}i\gamma^\mu\partial_\mu\psi_R - m(\overline{\psi}_R\psi_L + \overline{\psi_L}\psi_R). \tag{1.16}$$

As we will see in §1.3 the Stardard Model lagrangian is built based on this expression.

It is interesting to see that Weyl equations (1.11) and (1.12) decouple for massless fermions

$$i\gamma^\mu\partial_\mu\psi_{R,L} = 0. \tag{1.17}$$

which can be rewritten as,

$$\gamma^\mu P_\mu\psi_{R,L} = 0 \Rightarrow \gamma^0 P^0\psi_{R,L} = \vec{\boldsymbol{\gamma}}\cdot\vec{\boldsymbol{P}}\psi_{R,L} \xrightarrow{\frac{1}{2}\gamma^0\gamma_5\times} -\frac{1}{2}\gamma_5 P^0\psi_{R,L} = \frac{\gamma^0\vec{\boldsymbol{\gamma}}\gamma_5}{2}\cdot\vec{\boldsymbol{P}}\ \psi_{R,L}$$

where $P^\mu = i\partial^\mu \equiv (P^0, \vec{\boldsymbol{P}})$ is the momentum operator. Moreover, since the spin operator is given by $\vec{\boldsymbol{S}} = \frac{1}{2}\Sigma = \frac{\gamma^0\vec{\boldsymbol{\gamma}}\gamma_5}{2}$ [4], (1.17) for a massless fermion we obtain

$$\frac{\vec{\boldsymbol{S}}\cdot\vec{\boldsymbol{P}}}{1/2}\ \psi_{R,L} = -\gamma_5 P_0\psi_{R,L}. \tag{1.18}$$

Introducing now the positive energy (+) and negative energy (-) solutions of the Dirac equation (particles and antiparticles, respectively)

$$\psi^\pm_{R,L}(x) = \psi^\pm_{R,L}(p)e^{\mp ip_\mu x^\mu} = \psi^\pm_{R,L}(p)e^{\mp i(p^0x^0 - \vec{x}\cdot\vec{\boldsymbol{p}})}, \tag{1.19}$$

with $p^0 = |\vec{\boldsymbol{p}}|$ since we are assuming massless fermions, then $P^0\psi^\pm_{R,L} = \mp|\vec{\boldsymbol{p}}|\psi^\pm_{R,L}$ and (1.18) reads:

$$\frac{\vec{\boldsymbol{S}}\cdot\vec{\boldsymbol{P}}}{1/2|\vec{\boldsymbol{p}}|}\ \psi^\pm_{R,L} \equiv h\ \psi^\pm_{R,L} = \pm\gamma_5\psi^\pm_{R,L}, \tag{1.20}$$

USC UNIVERSIDADE

where we define the *helicity* h as the spin projection in the momentum direction. Recalling that chiral fields $\psi_{R,L}$ are chirality eigenfunctions (1.14), we find that for massless fermions they are also helicity eigenfunctions such that:

$$h\,\psi_R^{\pm} = \pm\psi_R^{\pm}, \tag{1.21}$$

$$h\,\psi_L^{\pm} = \mp\psi_L^{\pm}. \tag{1.22}$$

In conclusion, for massless fermions, ψ_R chiral fields describe positive helicity (right-handed) particles and negative helicity (left-handed) antiparticles, and ψ_L describe negative helicity particles and positive helicity antiparticles. In 1958, the Goldhaber, Grodzins and Sunyar experiment [9] found that neutrino helicity was negative, therefore they enter in the electroweak lagrangian as massless left-handed chiral fields ψ_L. Notice that at that time neutrinos were considered massless.

1.3. Neutrinos in the Standard Model

The Standard Model (SM) is the gauge theory that describes the strong, weak and electromagnetic interactions of the elementary particles. It is based on the local symmetry group $\mathrm{SU(3)_C \times SU(2)_L \times U(1)_Y}$ where C, L and Y denote color, left-handed chirality and weak hypercharge, respectively. The gauge group determines the number of vector gauge bosons to be twelve: eight from the eight $\mathrm{SU(3)_C}$ generators, which are the massless *gluons*; and four from the four $\mathrm{SU(2)_L \times U(1)_Y}$ generators, which are the massive bosons $W^{\pm}$ and Z^0 and the massless *photon*. Another boson exists in nature which is the massive *Higgs boson*. The *Higgs boson* confers mass to fermions and the $\mathrm{W^{\pm}}$ and Z^0 through the mechanism of spontaneous symmetry breaking of $\mathrm{SU(2)_L \times U(1)_Y \rightarrow U(1)_Q}$.

The fermions in the SM are divided in six massive and charged *quarks* (u, d, c, s, t, b) that constitute the hadrons and six *leptons*: three massive and charged (e, μ, τ) and three massless neutrinos $(\nu_e, \nu_\mu, \nu_\tau)$. Fermions are also divided in three families or generations with identical properties, but different masses (see Figure 1.1).

The SM depends on 19 external parameters whose values rely on experimental measurements: 6 quark masses, 3 angles and 1 CP phase from the quark mixing matrix (CKM matrix), 3 lepton masses (neutrinos are massles in the SM), 3 gauge coupling constants, 2 coupling constants from the Higgs sector and a small QCD parameter related with the *strong CP problem*. Due to its large number of parameters, the non-inclusion of gravitational interaction (either Dark Matter), the unexplained existence of three generations and neutrino oscillations, the SM is broadly thought to be a phenomenological low-energy effective theory derived from a more general one. Still, SM is in agreement with all experimental data to date except neutrino oscillations (§1.5).

The strong sector $\mathrm{SU(3)_C}$ of the SM is neither broken nor mixed into the electroweak sector $\mathrm{SU(2)_L \times U(1)_Y}$. Since neutrinos do not participate in strong interactions we will just consider the electroweak sector of the SM in what follows, which forms the unified theory of weak and electroweak interactions. The symmetry group generators of $\mathrm{SU(2)_L \times U(1)_Y}$ are related though the *Gell-Mann-Nishijima formula* which unifies weak and electromagnetic interactions,

$$\mathrm{Q} = I_3 + \frac{\mathrm{Y}}{2}, \tag{1.23}$$

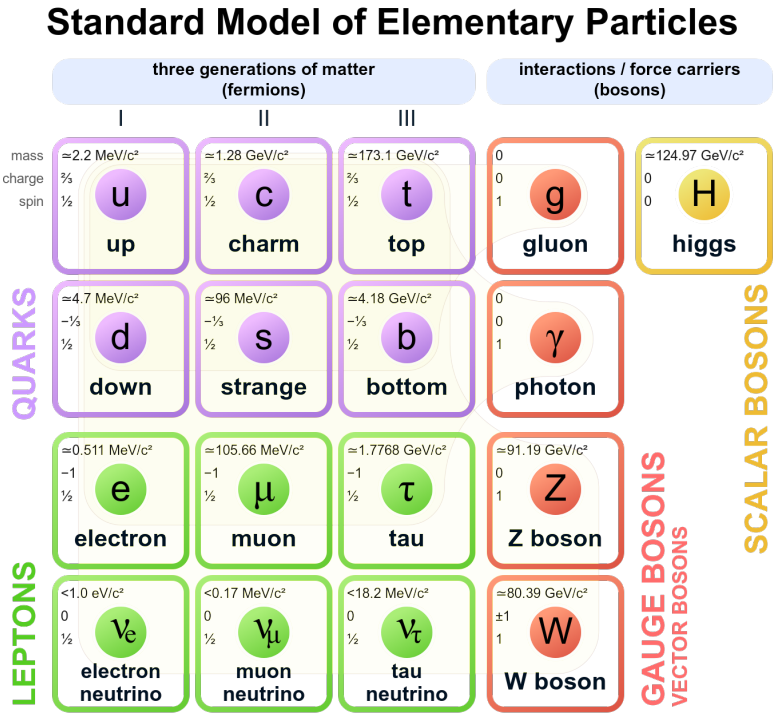


Figure 1.1: Particles in the Standard Model are divided in fermions and bosons. Fermions (leptons and quarks) are classified in three generation families (I, II, III). Neutrinos are considered massless in the SM. From [10].

where I_3 is the third component of $\mathrm{SU}(2)_L$ generators, Q is the charge operator, and Y is the $\mathrm{U}(1)_\mathrm{Y}$ generator. The $\mathrm{SU}(2)_L$ generators are given by $I_a = \sigma_a/2$ with $a = 1,2,3$ and σ_a the Pauli matrices. The electroweak lagrangian is invariant under the $\mathrm{SU}(2)_L \times \mathrm{U}(1)_\mathrm{Y}$ local gauge transformation matrix

$$U_{\mathrm{SU}(2)_L \times \mathrm{U}(1)_\mathrm{Y}}(\boldsymbol{\theta}(x), \eta(x)) = U_{\mathrm{SU}(2)_L}(\boldsymbol{\theta}(x)) U_{\mathrm{U}(1)_\mathrm{Y}}(\eta(x)) = e^{i\boldsymbol{\theta}(x)\cdot\boldsymbol{I} + i\eta(x)\mathrm{Y}} \tag{1.24}$$

The electroweak lagrangian is given by

$$\begin{aligned}
\mathscr{L}_{\mathrm{EW}} = {} & i \sum_{\alpha=e,\mu,\tau} \overline{L'_{\alpha L}}\, \not{D}\, L'_{\alpha L} + i \sum_{\alpha=1,2,3} \overline{Q'_{\alpha L}}\, \not{D}\, Q'_{\alpha L} \\
& + i \sum_{\alpha=e,\mu,\tau} \overline{l'_{\alpha R}}\, \not{D}\, l'_{\alpha R} + i \sum_{\alpha=d,s,b} \overline{q'^{D}_{\alpha R}}\, \not{D}\, q'^{D}_{\alpha R} + i \sum_{\alpha=uc,t} \overline{q'^{U}_{\alpha R}}\, \not{D}\, q'^{U}_{\alpha R} \\
& - \frac{1}{4} \boldsymbol{A}_{\mu\nu} \cdot \boldsymbol{A}^{\mu\nu} - \frac{1}{4} B_{\mu\nu} B^{\mu\nu} \\
& + (D_\mu \Phi)^\dagger (D^\mu \Phi) - \mu^2 \Phi^\dagger \Phi - \lambda (\Phi^\dagger \Phi)^2 \\
& - \sum_{\alpha,\beta=e,\mu,\tau} (Y'^{l}_{\alpha\beta}\, \overline{L'_{\alpha L}}\, \Phi\, l'_{\beta R} + Y'^{l*}_{\alpha\beta}\, \overline{l'_{\beta R}}\, \Phi^\dagger\, L'_{\alpha L}) \\
& - \sum_{\alpha=1,2,3} \sum_{\beta=d,s,b} (Y'^{D}_{\alpha\beta}\, \overline{Q'_{\alpha L}}\, \Phi\, q'^{D}_{\beta R} + Y'^{D*}_{\alpha\beta}\, \overline{q'^{D}_{\beta R}}\, \Phi^\dagger\, Q'_{\alpha L}) \\
& - \sum_{\alpha=1,2,3} \sum_{\beta=u,c,t} (Y'^{U}_{\alpha\beta}\, \overline{Q'_{\alpha L}}\, \tilde{\Phi}\, q'^{U}_{\beta R} + Y'^{U*}_{\alpha\beta}\, \overline{q'^{U}_{\beta R}}\, \tilde{\Phi}^\dagger\, Q'_{\alpha L}),
\end{aligned} \tag{1.25}$$

USC UNIVERSIDADE DE SANTIAGO DE COMPOSTELA

Table 1.1: Grouping of fields in the electroweak lagrangian (1.25) for the first fermion family. The quantum numbers of total isospin weak I, third component I_3, hypercharge Y and charge Q are the same for the second and third families. Higgs doublet is also included.

		I	I_3	Y	Q
lepton doublet	$L_{eL} \equiv \begin{pmatrix} \nu_{eL} \\ e_L \end{pmatrix}$	1/2	1/2 -1/2	-1	0 -1
lepton singlet	e_R	0	0	-2	-1
quark doublet	$Q_{1L} \equiv \begin{pmatrix} u_L \\ d_L \end{pmatrix}$	1/2	1/2 -1/2	1/3	2/3 -1/3
quark singlets	u_R d_R	0	0	4/3 -2/3	2/3 -1/3
Higgs doublet	$\Phi \equiv \begin{pmatrix} \Phi^+ \\ \Phi^0 \end{pmatrix}$	1/2	1/2 -1/2	1	1 0

where fermion and fields are defined in Table 1.1 and the covariant derivative is given by

$$D^\mu = \partial^\mu + ig\boldsymbol{A_\mu}\cdot\boldsymbol{I} + ig'B_\mu\frac{\mathrm{Y}}{2}, \tag{1.26}$$

with g and g' are the couplings constants of $\mathrm{SU}(2)_L$ and $\mathrm{U}(1)_\mathrm{Y}$. In the electroweak lagrangian (1.25), fermions are grouped as *weak isospin* doublets of left-handed fields. The right-handed field components of massive fermions are singlets under $\mathrm{SU}(2)_L$.

The first two lines in (1.25) represent the kinetic terms for fermions and their interaction with the gauge bosons. The third line is the kinetic term for the gauge bosons. The fourth line is the Higgs field lagrangian composed by its kinematic, interaction and potential terms. Finally the last three are the mass terms for fermions, composed by the Yukawa potential coupling of Higgs field and fermion fields. Notice that only left-handed neutrino fields $\nu_{\alpha L}$ appear in the SM, following the results described in §1.2.

Expanding the neutral and charged interaction currents in (1.25), we can deduce that the gauge vector boson fields $\boldsymbol{A_\mu}$ and B_μ are not the real fields of the particles we observe in nature. These particles are the $W^\pm$ and Z^0 bosons and the photon γ. The $W^\pm$ field is given by

$$W^\mu \equiv \frac{A_1^\mu - iA_2^\mu}{\sqrt{2}}, \tag{1.27}$$

and the photon A^μ and Z^0 fields

$$A^\mu = \sin\theta_\mathrm{W}A_3^\mu + \cos\theta_\mathrm{W}B^\mu, \tag{1.28}$$
$$Z^\mu = \cos\theta_\mathrm{W}A_3^\mu - \sin\theta_\mathrm{W}B^\mu, \tag{1.29}$$

where θ_W is known as the *Weinberg angle*. Since neutrinos are neutral, they do not participate in electromagnetic interactions. In order to cancel out the neutrino-photon

USC UNIVERSIDADE DE SANTIAGO DE COMPOSTELA

interaction in the electroweak lagrangian (1.25) and to recover the QED coupling constant e (elementary electric charge), we found the unification relations

$$g \sin\theta_W = g' \cos\theta_W = e. \tag{1.30}$$

The fermion mass terms in the electroweak lagrangian (1.25) are generated though the Yukawa interaction with the Higgs doublet. In order to explicitly see that these are mass terms for Dirac fields (recall (1.3) and (1.16)) we must plug in the Higgs doublet as

$$\Phi(x) = \frac{1}{\sqrt{2}} \begin{pmatrix} 0 \\ v + H(x) \end{pmatrix}, \tag{1.31}$$

which is the so-called *unitary gauge* in which the $H(x)$ field corresponds with the physical Higgs boson. The mass term for leptons reads

$$\mathscr{L}_{H,l} = -\left(\frac{v+H}{\sqrt{2}}\right) \sum_{\alpha,\beta=e,\mu,\tau} Y'^{l}_{\alpha\beta} \overline{l'_{\alpha L}} l'_{\beta R} + \text{H.c.} = -\left(\frac{v+H}{\sqrt{2}}\right) \overline{\boldsymbol{l}'_L} Y'^{l} \boldsymbol{l}'_R + \text{H.c.}. \tag{1.32}$$

where we employ the useful array notation,

$$\boldsymbol{l}'_{R,L} \equiv \begin{pmatrix} e'_{R,L} \\ \mu'_{R,L} \\ \tau'_{R,L} \end{pmatrix}, \quad \boldsymbol{l}' \equiv \boldsymbol{l}'_R + \boldsymbol{l}'_L, \quad \boldsymbol{\nu}'_{R,L} \equiv \begin{pmatrix} \nu'_{eR,L} \\ \nu'_{\mu R,L} \\ \nu'_{\tau R,L} \end{pmatrix}, \quad \boldsymbol{\nu}' \equiv \boldsymbol{\nu}'_R + \boldsymbol{\nu}'_L. \tag{1.33}$$

It can be shown that a general $N \times N$ matrix can be diagonalized by a biunitary transformation. Therefore the Yukawa coupling matrix Y'^{l} can be transformed such that

$$Y^l = V_L^{l\dagger} Y'^{l} V_R^l, \quad \text{with} \quad Y^l_{\alpha\beta} = y^l_\alpha \delta_{\alpha\beta} \quad (\alpha,\beta = e,\mu,\tau), \tag{1.34}$$

and if we define the massive lepton physical fields as

$$\boldsymbol{l}_L \equiv V_L^{l\dagger} \boldsymbol{l}'_L \equiv \begin{pmatrix} e_L \\ \mu_L \\ \tau_L \end{pmatrix}, \quad \boldsymbol{l}_R \equiv V_R^{l\dagger} \boldsymbol{l}'_R \equiv \begin{pmatrix} e_R \\ \mu_R \\ \tau_R \end{pmatrix}, \tag{1.35}$$

the Yukawa interaction lagrangian (1.32) becomes

$$\mathscr{L}_{H,l} = -\left(\frac{v+H}{\sqrt{2}}\right) \overline{\boldsymbol{l}_L} Y^l \boldsymbol{l}_R + \text{H.c.} = -\sum_{\alpha=e,\mu,\tau} \frac{y^l_\alpha v}{\sqrt{2}} \bar{l}_\alpha l_\alpha - \sum_{\alpha=e,\mu,\tau} \frac{y^l_\alpha}{\sqrt{2}} \bar{l}_\alpha l_\alpha H, \tag{1.36}$$

where we identify the lepton masses with $m^l_\alpha = y^l_\alpha v/\sqrt{2}$. The second term represents the interaction of massive leptons with the Higgs field.

We can now study the effect of the lepton field redefinition (1.35) in the lepton-boson interaction terms of the electroweak lagrangian (1.25). These terms for the $W^\pm$, Z^0 and photon γ, respectively, are given by

$$\mathscr{L}_L^{(\text{CC})} = -\frac{g}{\sqrt{2}} j^\mu_{W,L} W_\mu + \text{H.c.}, \qquad j^\mu_{W,L} = \overline{\boldsymbol{\nu}'_L} \gamma^\mu \boldsymbol{l}'_L, \tag{1.37}$$

$$\mathscr{L}_L^{(Z)} = -\frac{g}{2\cos\theta_W} j^\mu_{Z,L} Z_\mu, \qquad j^\mu_{Z,L} = \overline{\boldsymbol{\nu}'_L} \gamma^\mu \boldsymbol{\nu}'_L + (2s^2_W - 1) \overline{\boldsymbol{l}'_L} \gamma^\mu \boldsymbol{l}'_L + 2s^2_W \overline{\boldsymbol{l}'_R} \gamma^\mu \boldsymbol{l}'_R, \tag{1.38}$$

$$\mathscr{L}_L^{(\gamma)} = -e\, j^\mu_{\gamma,L} A_\mu, \qquad j^\mu_{\gamma,L} = \overline{\boldsymbol{l}'} \gamma^\mu \boldsymbol{l}' = \overline{\boldsymbol{l}'_R} \gamma^\mu \boldsymbol{l}'_R + \overline{\boldsymbol{l}'_L} \gamma^\mu \boldsymbol{l}'_L, \tag{1.39}$$

USC SANTIAGO DE COMPOSTELA

Table 1.2: Flavour lepton numbers for leptons and antileptons in the Standard Model.

	L_e	L_μ	L_τ		L_e	L_μ	L_τ
(e^-, ν_e)	+1	0	0	$(e^+, \overline{\nu}_e)$	-1	0	0
(μ^-, ν_μ)	0	+1	0	$(\mu^+, \overline{\nu}_\mu)$	0	-1	0
(τ^-, ν_τ)	0	0	+1	$(\tau^+, \overline{\nu}_\tau)$	0	0	-1

Since the V_L^l and V_R^l matrices in (1.34) are unitary, its effect will cancel out in the Z^0 and photon currents in (1.38) and (1.39), thus

$$\overline{\boldsymbol{l}'}_{R,L}\gamma^\mu \boldsymbol{l}'_{R,L} = \overline{\boldsymbol{l}}_R V_{R,L}^{l\dagger}\gamma^\mu V_{R,L}^l \boldsymbol{l}_{R,L} = \overline{\boldsymbol{l}}_{R,L}\gamma^\mu \boldsymbol{l}_{R,L} \tag{1.40}$$

and the expressions for the currents would be the same, with the change $\boldsymbol{l}'_{R,L} \to \boldsymbol{l}_{R,L}$. This effect is the so-called *GIM mechanism*. On the other hand, the charged current (1.37) would be

$$j^\mu_{W,L} = \overline{\boldsymbol{\nu}'}_L \gamma^\mu \boldsymbol{l}'_L = \overline{\boldsymbol{\nu}'}_L \gamma^\mu V_L^l \boldsymbol{l}_L = \overline{\boldsymbol{\nu}}_L \gamma^\mu \boldsymbol{l}_L, \tag{1.41}$$

where we have redefined the neutrino physical fields as

$$\boldsymbol{\nu}_L \equiv V_L^{l\dagger}\boldsymbol{\nu}'_L \equiv \begin{pmatrix} \nu_{eL} \\ \nu_{\mu L} \\ \nu_{\tau L} \end{pmatrix}. \tag{1.42}$$

Therefore the redefinition of neutrino fields ν'_L to ν_L avoids and extra factor in the interaction lagrangian. Note that this definition is possible since no neutrino mass term is present in the electroweak lagrangian (1.25). In the quark sector, the GIM mechanism holds in the Z^0 and electromagnetic interaction, but not in the $W^\pm$, inducing a relevant physical matrix known as the *Cabibbo-Kobayashi-Maskawa (CKM) matrix*.

Another relevant feature of the electroweak lagrangian (1.25) is its invariance under the global U(1) gauge transformation

$$\nu_{\alpha L} \to e^{i\phi_\alpha}\nu_{\alpha L}, \quad l_{\alpha L} \to e^{i\phi_\alpha} l_{\alpha L}, \quad l_{\alpha R} \to e^{i\phi_\alpha} l_{\alpha R}, \tag{1.43}$$

which implies the conservation of the three *flavour lepton numbers* L_α ($\alpha = e, \mu, \tau$) (See Table 1.2). As we will see in §1.4, flavour lepton number conservation is violated if neutrinos are massive.

1.4. Massive and mixed neutrinos

The discovery of neutrino oscillations (§1.5) have shown that neutrinos oscillate between flavours in their propagation through space (either in vacuum or matter). A neutrino produced at source as a flavour state α will be measured as flavour state β (equal or different than α) at some measurement distance L

$$\nu_\alpha \xrightarrow{L} \nu_\beta \quad (\alpha, \beta = e, \mu, \nu).$$

This phenomenon is explained by a model-independent mixing between flavour and mass neutrino states, linearly related through the mixing matrix U such that

$$\nu_\alpha = \sum_k U_{\alpha k}\, \nu_k \quad (\alpha = e,\mu,\tau). \tag{1.44}$$

The number of massive states ν_k is unconstrained, being three the minimal number of states compatible with current observations.

Neutrino massive nature can be described as a Dirac, Majorana, or Dirac-Majorana mass fields as we will see in this Section. Each of the descriptions has its own subtleties and physical consequences, which could shed light into neutrino fundamental nature.

1.4.1. Dirac neutrinos

Neutrinos masses can be included in the SM lagrangian (1.25) in the same footing as the other fermion fields, namely through the Yukawa coupling with the Higgs field. We will assume in what follows that we add the missing lepton right-handed $\nu_{\alpha R}$ fields, even though we could add another fields as long as they remain singlets under the SM symmetry group. The right-handed $\nu_{\alpha R}$ fields are called *sterile* since they do not participate in any SM interaction, to distinguish them from the interacting left-handed fields $\nu_{\alpha L}$ known as *active* fields. This modified theory is commonly known as the *minimally extended Standard Model*.

In order to get the upper field ($\nu_{\alpha L}$) in the lepton doublets $L_{\alpha L}$ (Table 1.1) the coupling is done through the Higgs transformed field $\tilde{\Phi}$ as in the up-like quark mass terms. The neutrino mass term would be

$$\mathscr{L}_{H,\nu} = -\sum_{\alpha,\beta=e,\mu,\tau} (Y'^{\nu}_{\alpha\beta}\, \overline{L'_{\alpha L}}\, \tilde{\Phi}\, \nu'_{\beta R} + Y'^{\nu *}_{\alpha\beta}\, \overline{\nu'_{\beta R}}\, \tilde{\Phi}^\dagger\, L'_{\alpha L}). \tag{1.45}$$

Using (1.31), $\tilde{\Phi}$ is given by

$$\tilde{\Phi}(x) = i\tau_2 \Phi^*(x) = \frac{1}{\sqrt{2}} \begin{pmatrix} v + H(x) \\ 0 \end{pmatrix}, \tag{1.46}$$

and (1.45) can be rewritten

$$\mathscr{L}_{H,\nu} = -\left(\frac{v+H}{\sqrt{2}}\right) \sum_{\alpha,\beta=e,\mu,\tau} Y'^{\nu}_{\alpha\beta}\, \overline{\nu'_{\alpha L}}\, \nu'_{\beta R} + \text{H.c.} = -\left(\frac{v+H}{\sqrt{2}}\right) \overline{\boldsymbol{\nu}'_L}\, Y'^{\nu}\, \boldsymbol{\nu}'_R + \text{H.c.}, \tag{1.47}$$

We can apply now the same diagonalization procedure as in (1.34) with the change $l \to \nu$ and $(\alpha,\beta = e,\mu,\tau) \to (k, j = 1,2,3)$, and define the neutrino massive fields

$$\boldsymbol{n}_L \equiv V_L^{\nu\dagger} \boldsymbol{\nu}'_L \equiv \begin{pmatrix} \nu_{1L} \\ \nu_{2L} \\ \nu_{3L} \end{pmatrix}, \quad \boldsymbol{n}_R \equiv V_R^{\nu\dagger} \boldsymbol{\nu}'_R \equiv \begin{pmatrix} \nu_{1R} \\ \nu_{2R} \\ \nu_{3R} \end{pmatrix}, \tag{1.48}$$

USC UNIVERSIDADE

thus (1.47) becomes

$$\mathscr{L}_{H,\nu} = -\left(\frac{v+H}{\sqrt{2}}\right) \overline{\boldsymbol{n}_L}\, Y^l\, \boldsymbol{n}_R + \text{H.c.} = -\sum_{k=1,2,3} \frac{y_k^\nu v}{\sqrt{2}} \overline{\nu}_k \nu_k - \sum_{k=1,2,3} \frac{y_k^\nu}{\sqrt{2}} \overline{\nu}_k \nu_k H, \tag{1.49}$$

where the neutrino masses are identtified as $m_k^\nu = y_k^\nu v/\sqrt{2}$.

The physical massive neutrino fields in the minimal extended SM are given by (1.48). We can ask now how these fields interact with the boson fields. For the Z_0 current in (1.38), the expression would be the same with the change $\boldsymbol{\nu}_L \to \boldsymbol{n}_L$, since the matrices in (1.48) are unitary. This is nothing more than the GIM mechanism at work again. Nevertheless, the expression for the charged current (1.37) reads

$$j^\mu_{W,L} = \overline{\boldsymbol{\nu}'}_L \gamma^\mu \boldsymbol{l}'_L = \overline{\boldsymbol{n}}_L V_L^{\nu\dagger} \gamma^\mu V_L^l \boldsymbol{l}_L = \overline{\boldsymbol{n}}_L U^\dagger \gamma^\mu \boldsymbol{l}_L, \quad \text{with} \quad U = V_L^{l\dagger}\, V_L^\nu. \tag{1.50}$$

From this expression we define the lepton fields

$$\boldsymbol{\nu}_L \equiv U \boldsymbol{n}_L \equiv \begin{pmatrix} \nu_{eL} \\ \nu_{\mu L} \\ \nu_{\tau L} \end{pmatrix}. \tag{1.51}$$

This relation between neutrino flavour states with neutrino massive fields is the so-called *neutrino mixing*. The lepton flavour fields have to be taken with caution now. They are only useful in the SM high energy limit when neutrino masses can be neglected, but in principle they are not physical fields as their mass in not defined. Note the difference with the massless neutrino case in §1.3, in which the neutrino flavour fields (1.42) are physical. The reason to define the flavour lepton fields in (1.51) is motivated by the fact that neutrinos are indirectly detected through the measurement of the charged lepton partner produced in their interaction with ordinary matter.

The *mixing matrix* U is a very relevant object in neutrino physics since it describes the neutrino oscillations between flavour states (§1.5). It is a $N \times N$ (with $N = 3$) complex unitary matrix, thus it is defined by N^2 real parameters. In general, its parameters can be divided into

$$\frac{N(N-1)}{2} = 3 \quad \text{mixing angles,} \tag{1.52}$$

$$\frac{N(N+1)}{2} = 6 \quad \text{phases.} \tag{1.53}$$

But not all of the phases are physical since they can be reabsorbed in the definition of the lepton and neutrino fields. To see this, notice that all terms except the charged current in the minimal extended SM lagrangian are invariant under

$$\nu_{kL} \to e^{i\phi_k} \nu_{kL}, \quad \nu_{kR} \to e^{i\phi_k} \nu_{kR}, \quad (k = 1,2,3), \tag{1.54}$$

$$l_{\alpha L} \to e^{i\phi_\alpha} l_{\alpha L}, \quad l_{\alpha R} \to e^{i\phi_\alpha} l_{\alpha R}, \quad (\alpha = e, \mu, \tau). \tag{1.55}$$

Including this transformation in (1.50) we obtain

$$j^\mu_{W,L} = \sum_{k=1,2,3} \sum_{\alpha=e,\mu,\tau} \overline{\nu}_{kL} e^{-i\phi_k} \gamma^\mu (U^\dagger)_{k\alpha} e^{i\phi_\alpha} l_{\alpha L}, \tag{1.56}$$

from which we can choose $2N-1$ transformation phases to reabsorb the $N(N+1)/2$ phases of U. Therefore U can be described by

$$\frac{N(N-1)}{2} = 3 \quad \text{mixing angles,} \tag{1.57}$$

$$\frac{N(N+1)}{2} - (2N-1) = \frac{(N-1)(N-2)}{2} = 1 \quad \text{physical phases.} \tag{1.58}$$

USC UNIVERSIDADE DE SANTIAGO DE COMPOSTELA

The mainstream parametrization is given by the so-called *Pontecorvo–Maki–Nakagawa–Sakata (PMNS) matrix*

$$U^D = \begin{pmatrix} c_{12}c_{13} & s_{12}c_{13} & s_{13}e^{-i\delta_{13}} \\ -s_{12}c_{23} - c_{12}s_{23}s_{13}e^{i\delta_{13}} & c_{12}c_{23} - s_{12}s_{23}s_{13}e^{i\delta_{13}} & s_{23}c_{13} \\ s_{12}s_{23} - c_{12}c_{23}s_{13}e^{i\delta_{13}} & -c_{12}s_{23} - s_{12}c_{23}s_{13}e^{i\delta_{13}} & c_{23}c_{13} \end{pmatrix}, \tag{1.59}$$

where $c_{ab} \equiv \cos\vartheta_{ab}$ and $s_{ab} \equiv \sin\vartheta_{ab}$. The three mixing angles ϑ_{ab} values may vary between $0 \leq \vartheta_{ab} \leq \pi/2$. The physical phase δ_{13} can take values in the range $0 \leq \delta_{13} \leq 2\pi$, and it is related with the CP-violation in the lepton sector: it can be shown that CP is conserved in the lepton sector if an only if the mixing matrix U is real ($U = U^*$), thus if δ_{13} is different from zero or π, CP is not a symmetry of the leptonic sector in the minimal extended SM.

In the minimal extended SM the lepton flavour number L_α is no longer conserved since the lagrangian is not invariant under (1.43) (plus the right-handed neutrino component transformation). Nevertheless, it is true for the transformation with global phase

$$\nu_{kL} \to e^{i\phi}\nu_{kL}, \quad \nu_{kR} \to e^{i\phi}\nu_{kR}, \quad (k = 1,2,3), \tag{1.60}$$

$$l_{\alpha L} \to e^{i\phi}l_{\alpha L}, \quad l_{\alpha R} \to e^{i\phi}l_{\alpha R}, \quad (\alpha = e,\mu,\tau), \tag{1.61}$$

implying the conservation of the total lepton number L. The total lepton number is $L = +1$ for negatively charged leptons and neutrinos (particles) and $L = -1$ for positively charged leptons and antineutrinos (antiparticles). Notice that neutrinos and antineutrinos are different particles in this theory, as they are in the SM, which would not be true if neutrinos were Majorana particles, as we will see in §1.4.2.

1.4.2. Majorana neutrinos

Neutral fermions can also be described as Majorana particles, [6]. The historical derivation of E. Majorana was an attempt of getting rid of the negative energy solutions from Dirac equation. In what follows we proceed with a modern derivation based on charge conjugation. First of all, we need to introduce the *charge conjugation* symmetry transformation such that if ψ describes a charged fermion field with charge q, then ψ^C describes the same field with charge $-q$, namely a particle-antiparticle transformation. Thus, by definition the equation of motion for the fermion and its charge conjugated field in an electromagnetic field would be

$$(i\partial\!\!\!/ - qA\!\!\!/ - m)\psi = 0 \qquad \text{(particle)}, \tag{1.62}$$

$$(i\partial\!\!\!/ + qA\!\!\!/ - m)\psi^C = 0 \qquad \text{(antiparticle)}. \tag{1.63}$$

We can easily verify that the transformation $\psi \to \psi^c$ would be given by

$$\psi^C = \xi_C \mathscr{C}\overline{\psi}^T, \tag{1.64}$$

where ξ_C is an arbitrary unobservable phase and $\mathscr{C}$ is the charge conjugation matrix that satisfies

$$\mathscr{C}\gamma^{\mu T}\mathscr{C}^{-1} = -\gamma^\mu, \quad \mathscr{C}^\dagger = \mathscr{C}^{-1} = -\mathscr{C}. \tag{1.65}$$

USC UNIVERSIDADE DE SANTIAGO DE COMPOSTELA

From (1.62) and (1.63) it is clear that ψ and ψ^C are different if $q \neq 0$. Nevertheless, when $q = 0$ the equations are the same and we could choose

$$\psi = \psi^C, \tag{1.66}$$

such that particle creation and annihilation operators are the same, namely

$$\text{particle} \equiv \text{antiparticle}. \tag{1.67}$$

Note that (1.66) is in fact an election, since a general solution of (1.62) with $q = 0$ is composed of positive and negative energy solutions $\psi = c_1\psi_{(+)} + c_2\psi_{(-)}$, that under charge conjugation $\psi^c = c_1^*{\psi_{(+)}}^C + c_2^*{\psi_{(-)}}^C$, which is a solution of (1.63) and the Majorana condition (1.66) would not be in general fulfilled.

The effect of the Majorana condition (1.66) in the chiral fields (1.13)) is very interesting, since using the properties of $\mathscr{C}$ (1.65) we have

$$P_R\psi^C = (\psi_L)^C, \tag{1.68}$$
$$P_L\psi^C = (\psi_R)^C \tag{1.69}$$

which converts the Majorana condition (1.66) in

$$\psi_R = (\psi_L)^C, \tag{1.70}$$
$$\psi_L = (\psi_R)^C. \tag{1.71}$$

Therefore in the Majorana description of fermions we do not have two independent fields $\psi_{R,L}$, but they are related through charge conjugation. Recalling that neutrinos in the SM are left-handed, we can choose the independent field to be [2] ν_L, then using (1.70),

$$\nu = \nu_L + (\nu_L)^C. \tag{1.72}$$

The equations of motion for Majorana fermions can be obtained by the Weyl equations (1.11) and (1.12). Using (1.70),

$$i\gamma^\mu\partial_\mu\nu_L = m(\nu_L)^C \tag{1.73}$$
$$i\gamma^\mu\partial_\mu(\nu_L)^C = m\,\nu_L, \tag{1.74}$$

that are in fact the same equation, since can be derived one from the other by charge conjugation. The Majorana lagrangian is given by [3]

$$\mathscr{L}^M = \overline{\nu}_L i\gamma^\mu\partial_\mu\nu_L - \frac{m}{2}\left(\overline{\nu_L^C}\,\nu_L + \overline{\nu_L}\,\nu_L^C\right), \tag{1.75}$$

in which we identify an identical kinematical term as for Dirac neutrinos in (1.16), but a rather different mass term. The mass term

$$\mathscr{L}^M_{mass} = \frac{1}{2}m\,\overline{\nu_L^C}\,\nu_L + \text{H.c.} = \frac{1}{2}m\,\nu_L^T\mathscr{C}\,\nu_L + \text{H.c.}. \tag{1.76}$$

[2] Note the notational change in order to be consistent with the neutrino field previously denoted as ν and a general fermion field as ψ.

[3] This derivation is not direct since it requires to assume the anticonmutation character of fermion fields, for further details see [4]

in Majorana neutrino theory is not invariant under the global U(1) gauge transformation

$$\nu_L \to e^{i\phi}\,\nu_L, \tag{1.77}$$

thus the associated charge, the lepton number, is not conserved. This motivates the active research interest in lepton number violating processes such as neutrinoless double beta decay (§1.6.2).

We can now study the mixing properties of Majorana neutrinos. The lagrangian term for three generation of neutrinos can be written

$$\mathscr{L}^M_{mass} = \frac{1}{2}\overline{\boldsymbol{\nu}^C}_L M^L \boldsymbol{\nu}_L + \text{H.c.} = \frac{1}{2}\boldsymbol{\nu}_L^T \mathscr{C}^\dagger M^L \boldsymbol{\nu}_L + \text{H.c.}, \tag{1.78}$$

where $\boldsymbol{\nu}_L$ are the three flavour neutrino fields given by (1.33) and M^L is a complex symmetric matrix (the symmetry of M^L can easily be seen by the second property in (1.65)). Following a similar diagonalization procedure as in §1.3 and §1.4.1, we can diagonalize the symetric M^L by

$$(V_L^\nu)^T M^L V_L^\nu = M, \quad \text{with} \quad M_{kj} = m_k \delta_{kj} \quad (k,j=1,2,3), \tag{1.79}$$

where V_L^ν is an unitary matrix and $m_k \geq 0$. Thus the three generation mass term in (1.78) can be written

$$\mathscr{L}^M_{mass} = -\frac{1}{2}\overline{\boldsymbol{n}^C_L} M \boldsymbol{n}_L + \text{H.c.} = -\frac{1}{2}\sum_{k=1}^{3} m_k \overline{\nu^C_{kL}}\,\nu_{kL} + \text{H.c.} \tag{1.80}$$

where the left-handed massive neutrino states are given by

$$\boldsymbol{n}_L \equiv V_L^{\nu\dagger}\boldsymbol{\nu}_L \equiv \begin{pmatrix} \nu_{1L} \\ \nu_{2L} \\ \nu_{3L} \end{pmatrix}. \tag{1.81}$$

As expected, the mass lagrangian for three generation neutrinos (1.80) is nothing more than the lagrangian (1.76) for each generation. The lepton number is not conserved since (1.80) is not invariant under

$$\nu_{kL} \to e^{i\phi}\,\nu_{kL} \quad (k=1,2,3). \tag{1.82}$$

This non-invariance has another important consequence, the mixing matrix in the case of neutrinos being Majorana contains two extra physical phases. To see this we can go back to the transformed charged current in (1.56) but removing the U(1) neutrino field transformation in (1.54),

$$j^\mu_{W,L} = \sum_{k=1,2,3}\sum_{\alpha=e,\mu,\tau} \overline{\nu}_{kL}\gamma^\mu (U^\dagger)_{k\alpha} e^{i\phi_\alpha} l_{\alpha L}, \tag{1.83}$$

USC DE SANTIAGO

therefore the number of fields we can redefine to absorb the phases is $N=3$. Then (1.58) for Majorana neutrinos become

$$\frac{N(N+1)}{2} - N = \frac{N(N-1)}{2} = 3 \quad \text{physical phases.} \tag{1.84}$$

The parametrization of the mixing matrix for Majorana neutrinos can be written from the PMNS matrix in (1.59)

$$U^M = U^D \operatorname{diag}\left(e^{i\lambda_1}, e^{i\lambda_2}, e^{i\lambda_3}\right), \quad \text{with} \quad \lambda_1 = 0, \tag{1.85}$$

where the choice $\lambda_1 = 0$ is a matter of convention.

Finally we can ask if it is possible to generate in the SM the mass term for Majorana neutrinos in (1.78). Unfortunately it is not possible to generate this term respecting the SM symmetries and being renormalizable. Recall that a lagrangian must have energy dimensions of four, $[E]^4$, that a fermion field has dimensions of $[E]^{3/2}$ and a boson field dimensions of energy $[E]^1$. In order for the theory to be renormalizable the field products must be of dimension smaller than four. To generate a renormalizable Majorana mass term using the SM fields it must contain the doublet L_L and its charge conjugate $L_L^C = C\overline{L_L}^T$, since left-handed neutrino fields enter in the SM as the upper field in this doublet. Then, the mass term should be of the form

$$\overline{L_L^C}\,\tilde{\Phi}\,L_L. \tag{1.86}$$

This term is fourth dimensional, but it is not compatible with the SM symmetry group $\mathrm{SU(2)_L \times U(1)_Y}$. Nevertheless, the fact that we can not include a Majorana mass term in the SM is not disturbing at all, since the SM is though to be the resultant low energy approximation of a more general theory, similarly as the non-renormalizable Fermi beta theory with respect to the electroweak theory. In this sense, we could expect a Majorana mass term that is compatible with the SM but non-renormalizable, namely a product of fields with dimension higher than four. The lowest dimensional term, with dimension $[E]^5$, happens to be

$$\mathscr{L}_5 = \frac{g}{\mathscr{M}}\left(L_L^T \tau_2 \Phi\right) C^\dagger \left(\Phi^T \tau_2 L_L\right) + \text{H. c.}, \tag{1.87}$$

where g is a dimensionless coupling constant and $\mathscr{M}$ is a constant with dimensions of $[E]$, in order for the lagrangian to be fourth dimensional.

As a final remark, note that in case neutrinos were massless, the only field entering in the SM lagrangian would be ν_L and then the phenomenological consequences between Dirac and Majorana neutrinos would be unobservable. There would be no lepton number violating processes or oscillations and we could not probe if neutrinos and antineutrinos are different (Dirac) or equal (Majorana) particles.

1.4.3. Dirac and Majorana neutrinos

In previous §1.4.1 and §1.4.2 we discussed the massive nature of neutrinos in the Dirac and Majorana cases, respectively. In the Dirac case, in order to account for neutrino mass we had to assume the existence of the non-interacting sterile fields ν_R. Then the mass term is generated through the Yukawa coupling with the Higgs field, but this mechanism appears somehow unnatural since neutrino masses are much smaller than the other fermions. In the Majorana case, since ν_L and ν_R are related through charge conjugation we just considered the active ν_L as part of the mass lagrangian. We can then try to create a general Dirac, left-handed Majorana and right-handed

Majorana for neutrinos such that

$$\mathscr{L}^{D+M}_{mass} = \mathscr{L}^{D}_{mass} + \mathscr{L}^{M,R}_{mass} + \mathscr{L}^{M,L}_{mass} = \\ -m_D \overline{\nu_R}\,\nu_L - \frac{1}{2} m_L \overline{\nu^C_L}\,\nu_L - \frac{1}{2} m_R \overline{\nu^C_R}\,\nu_R + \text{H.c.}, \tag{1.88}$$

where we assume for simplicity only one neutrino generation. We will shortly see why this case is interesting. First, we introduce the vector of fields

$$\boldsymbol{N}_L \equiv \begin{pmatrix} \nu_L \\ \nu^C_R \end{pmatrix}, \tag{1.89}$$

such that we can rewrite (1.88) as [4]

$$\mathscr{L}^{D+M}_{mass} = -\frac{1}{2}\overline{\boldsymbol{N}^C_L} M^{D+M} \boldsymbol{N}_L + \text{H.c}, \tag{1.90}$$

where M^{D+M} is the symmetric mass matrix

$$M^{D+M} = \begin{pmatrix} m_L & m_D \\ m_D & m_R \end{pmatrix}. \tag{1.91}$$

We can diagonalize this matrix through a unitary transformation U,

$$m = U^T M U = \text{diag}(m_1, m_2) \quad m_1, m_2 \geq 0. \tag{1.92}$$

Hence, the Dirac-Majorana mass term can be rewritten

$$\mathscr{L}^{D+M}_{mass} = -\frac{1}{2}\overline{\boldsymbol{n}^C_L} m \boldsymbol{n}_L + \text{H.c.} = -\frac{1}{2}\sum_{k=1,2} m_k \overline{\nu^C_{kL}}\,\nu_{kL} + \text{H.c}, \tag{1.93}$$

which is clearly the Majorana mass term of the massive Majorana fields defined by

$$n_L \equiv U \boldsymbol{N}_L \equiv \begin{pmatrix} \nu_{1L} \\ \nu_{2L} \end{pmatrix}. \tag{1.94}$$

We have arrived to an important result, a Dirac-Majorana mass term generates a Majorana mass term. We can deepen into this result by diagonalizing the mixing matrix U in (1.92) in order to find the relation between the Majorana neutrino mass fields $\nu_{1,2\ L}$ and the original mass parameters m_L, m_R and m_D. Assuming the mass parameters to be real, (which implies CP invariance in the lepton sector [4]) we obtain after a bit of algebra

$$m_2 = \frac{1}{2}\left[m_L + m_R + \sqrt{(m_L - m_R)^2 + 4m_D^2}\right] \tag{1.95}$$

$$m_1 = \frac{1}{2}\left[m_L + m_R - \sqrt{(m_L - m_R)^2 + 4m_D^2}\right] \qquad \text{if} \quad m_L m_R \geq m_D^2 \tag{1.96}$$

$$m_1 = \frac{1}{2}\left[\sqrt{(m_L - m_R)^2 + 4m_D^2} - (m_L + m_R)\right] \qquad \text{if} \quad m_L m_R < m_D^2 \tag{1.97}$$

[4] Note the use of the anticonmutation relation between fermion fields.

USC UNIVERSIDADE DE SANTIAGO DE COMPOSTELA

The most interesting case arises when $m_L = 0$ because it is not possible to generate the Majorana left-handed term $\mathscr{L}^{M,L}_{mass}$ in the SM respecting both the symmetry group and renormalizability (§1.4.2). But since the right-handed sterile neutrino field ν_R is a singlet under $SU(2)_L$, the $\mathscr{L}^{M,R}_{mass}$ term is allowed. The Dirac mass term could be generated through the standard Higgs mechanism as shown in §1.4.1. Assuming also that the Dirac mass is much smaller that the Majorana right-handed mass, $m_D \ll m_R$, the mass values for the Majorana massive neutrinos would be

$$m_2 \simeq m_R \tag{1.98}$$

$$m_1 \simeq \frac{m_D^2}{m_R}, \tag{1.99}$$

therefore a heavy ν_2 would be responsible for a lighter ν_1. This is the so-called *see-saw mechanism* that could naturally explain the smallness of neutrino masses compared with the other fermions. Since m_D is generated through the Higgs mechanism, its value would be proportional to the symmetry breaking scale, whose value is no larger than 10^2 GeV, the mass of the top quark. This fact is typically know as the protection of m_D by the SM symmetries. On the other hand, the mass term for m_R can be generated by new physics beyond the SM since ν_R is a singlet in this theory, and could belong to a non-trivial multiplet of the higher energy theory of which the SM is the lower energy limit. In this sense, m_R is protected by the symmetries of the high energy theory, which could be of the order of the grand-unification scale $10^{14} - 10^{16}$ GeV.

For clarity purposes, we presented above the simplest see-saw case with real parameters m_D, m_L, m_R in which CP is conserved, but it is possible to relax this assumption. Also, it was assumed that $m_L = 0$ since such term is incompatible with the SM symmetries, but we could think of this term as a lower energy limit of the higher energy theory. In general [11] we speak of *type I see-saw* when $|m_L| \gg m_D^2/m_R$ and *type II see-saw* when $|m_L| \ll m_D^2/m_R$. In both cases a high mass in one of the Majorana neutrino states induces a lower mass in its partner. The see-saw mechanism can also be generalized to a larger number of neutrino flavours.

1.5. Neutrino Oscillations

In §1.4 we introduced how neutrino massiveness can be accommodated in a theoretical framework. The consequence of neutrinos being massive is that the lepton neutrino states that we typically think off are not the real fundamental particles in nature. Neutrinos are identified by its lepton partner in a certain decay or reaction, for example in β^- decay $p \to n + e^- + \overline{\nu}_e$ we say that the product of the reaction is an electron antineutrino because we measure an electron. Since neutrinos are massive (as we will see in this Section) the real reaction in nature would be $p \to n + e^- + \overline{\nu}_k$ where $k = 1, 2, 3$, with different probabilities for the outgoing neutrino, but we can not directly identify which one of the $\overline{\nu}_k$ were produced in the decay because we measure the outgoing electron. Nevertheless, even though we can not directly measure the massive neutrino states we can study them in *neutrino oscillation experiments*.

USC UNIVERSIDADE DE SANTIAGO DE

Neutrino oscillation experiments have two components, the neutrino source where neutrinos are produced and the neutrino detector where they are detected. Neutrinos are produced in a flavour state α at source, and detected as a flavour state β. The

production being given by a generic decay process

$$S_I \to S_F + l_\alpha^+ + \nu_\alpha \quad \text{or} \quad S_I \to S_F + l_\alpha^- + \overline{\nu}_\alpha, \tag{1.100}$$

and the detection through

$$\nu_\beta + D_I \to D_F + l_\beta^- \quad \text{or} \quad \overline{\nu}_\beta + D_I \to D_F + l_\beta^+, \tag{1.101}$$

where $S_{I,F}$ and $D_{I,F}$ denote the initial and final states of the source and detection elements. Note that what is actually happening is that a fundamental massive neutrino is travelling between source and detector. Nevertheless since we can only identify flavour interactions, what it is measured is the number of events of type β produced by an α emiting source, $N_{\alpha\beta}$. If the production rate for flavour α at source is given by Γ_α and the detection cross section for flavour β at detection is σ_β, the number of events measured in the detector at distance L would be[5]

$$N_{\alpha\beta}(L) \propto \Gamma_\alpha \, P_{\nu_\alpha \to \nu_\beta}(L) \, \sigma_\beta, \tag{1.102}$$

where the proportionality constant would depend on the experiment's running time and detector and source compositions. The objective of an oscillation experiment is the measurement of the neutrino *oscillation probability* $P_{\nu_\alpha \to \nu_\beta}(L)$ in (1.102), since it depends on the mixing matrix and the square mass differences of neutrinos as we will see above.

Neutrino flavour states ν_α are in general linear combinations of the neutrino massive states[6]

$$\nu_\alpha = \sum_k U_{\alpha k} \, \nu_k. \tag{1.103}$$

The number of flavour neutrinos is compatible with three $\nu_{e,\mu,\tau}$, as measured from the invisible decay width of the Z^0 boson [12]. Nevertheless we do not know an upper limit on the number of massive states, which could be three or higher. In order for the mixing matrix U to maintain unitarity, the number of neutrino flavour states must be enlarged if more than three massive neutrinos exist. These hypothetical extra flavour neutrino states will be sterile, as they will not participate in weak interactions. The three flavour neutrino mixing matrix is given by the general form of (recall (1.59) and (1.85))

$$U = \begin{pmatrix} U_{e1} & U_{e2} & U_{e3} \\ U_{\mu 1} & U_{\mu 2} & U_{\mu 3} \\ U_{\tau 1} & U_{\tau 2} & U_{\tau 3} \end{pmatrix} = \begin{pmatrix} c_{12}c_{13} & s_{12}c_{13} & s_{13}e^{-i\delta_{13}} \\ -s_{12}c_{23} - c_{12}s_{23}s_{13}e^{i\delta_{13}} & c_{12}c_{23} - s_{12}s_{23}s_{13}e^{i\delta_{13}} & s_{23}c_{13} \\ s_{12}s_{23} - c_{12}c_{23}s_{13}e^{i\delta_{13}} & -c_{12}s_{23} - s_{12}c_{23}s_{13}e^{i\delta_{13}} & c_{23}c_{13} \end{pmatrix} \begin{pmatrix} 1 & 0 & 0 \\ 0 & e^{i\lambda_2} & 0 \\ 0 & 0 & e^{i\lambda_3} \end{pmatrix}, \tag{1.104}$$

where $c_{ab} \equiv \cos\vartheta_{ab}$ and $s_{ab} \equiv \sin\vartheta_{ab}$. The three mixing angles ϑ_{ab} values may vary between $0 \le \vartheta_{ab} \le \pi/2$. The phases δ_{13}, λ_2 and λ_3 are CP violation phases, the last two being only physically relevant in the case of Majorana neutrinos. If CP is conserved, the mixing matrix is real and all the phases would be zero or π.

[5] Note that we are implicitly assuming neutrino oscillations $\nu_\alpha \to \nu_\beta$, but the same holds for antineutrino oscillations $\overline{\nu}_\alpha \to \overline{\nu}_\beta$.

[6] For notational simplicity, we omit the left-handed L subscript in what follows.

USC UNIVERSIDADE DE SANTIAGO DE COMPOSTELA

Using (1.103) and (1.104) it is possible to compute the general approximate oscillation probability in vacuum [4],

$$P_{\nu_\alpha\to\nu_\beta} = \delta_{\alpha\beta} - 4\sum_{k>j}\mathrm{Re}\left[U^*_{\alpha k}U_{\beta k}U_{\alpha j}U^*_{\beta j}\right]\sin^2\left(\frac{\Delta m^2_{kj}L}{4E}\right) + 2\sum_{k>j}\mathrm{Im}\left[U^*_{\alpha k}U_{\beta k}U_{\alpha j}U^*_{\beta j}\right]\sin\left(\frac{\Delta m^2_{kj}L}{2E}\right), \tag{1.105}$$

where E is the energy of the produced neutrino states, and $\Delta m^2_{kj} \equiv m^2_k - m^2_j$. From this expression we find the following important features of oscillation neutrino experiments:

- They are sensible to the neutrino mass square differences $\Delta m^2_{kj} = m^2_k - m^2_j$, but not to the absolute neutrino mass values.
- They are sensible to the neutrino mixing matrix elements in (1.104). Nevertheless, the mixing matrix enters in the oscillation probability through a fourth product $U^*_{\alpha k}U_{\beta k}U_{\alpha j}U^*_{\beta j}$, hence the global Majorana phases are cancelled-out. Neutrino experiments are sensible to the mixing angles and the global Dirac CP phase δ_{13}, but they are not sensible to the Dirac or Majorana neutrino nature. This last statement also holds for neutrino oscillations in matter. Therefore, even if we measure δ_{13} to be zero or π, it does not necessarily mean that CP is conserved, since neutrinos could still be Majorana particles. Recall that CP violation is required to explain the matter anti-matter asymmetry of the Universe [13].

Assuming three neutrino families, we can summarize the following six independent physical parameters obtainable from neutrinos oscillation experiments

$$\text{3 mixing-angles}: \quad \vartheta_{12}, \vartheta_{13}, \vartheta_{23} \tag{1.106}$$

$$\text{1 CP phase}: \quad \delta_{13} \tag{1.107}$$

$$\text{2 mass square differences}: \quad \Delta m^2_{21}, \Delta m^2_{31} \tag{1.108}$$

From an experimental point of view the general three neutrino family oscillation probability (1.105) is redundant since neutrino experiments are unable to measure the three existing neutrino flavours and operate in a well defined energy and distance region. The probability can be reduced to the simplest scenario of two neutrino mixing with the disappearance and appearance oscillation probabilities are given by

$$P_{\nu_\alpha\to\nu_\beta} = \sin^2 2\vartheta \sin^2\left(\frac{\Delta m^2 L}{4E}\right) \quad (\alpha \neq \beta) \tag{1.109}$$

$$P_{\nu_\alpha\to\nu_\alpha} = 1 - P_{\nu_\alpha\to\nu_\beta}, \tag{1.110}$$

and the six parameters in the three family case has been reduced to just two: the *Cabbibo angle* ϑ and the mass square difference Δm^2. Nevertheless, the complete analysis of oscillation experiments is done through global fits to the full oscillation probability (1.105) using data from various experiments as we will see in §1.5.2.

USC UNIVERSIDADE DE SANTIAGO DE COMPOSTELA

1.5.1. A summary of oscillation experiments

First evidence of neutrino oscillations arises at 1970 in the measurement of solar neutrinos in the Homestake experiment [14]. The measurement technique was based

on the inverse β decay Cl-Ar

$$\nu_e + {}^{37}\mathrm{Cl} \rightarrow {}^{37}\mathrm{Ar} + e^-, \tag{1.111}$$

with a neutrino energy threshold of 0.814 MeV. The experiment counts the number of interactions through the collection of the radioactive ^{37}Ar, mainly due to solar ν_e. The induced cosmic muon ^{37}Ar background was greatly reduced by placing the experiment underground at Homestake Gold Mine, USA. The experiment ran for a total of 24 years, obtaining a solar neutrino rate three times slower than predicted by the *standard solar model*, SSM. This result is known as the *solar neutrino problem*, SNP. The lack of electron neutrino flux as compared with the SSM was further confirmed by Kamiokande, GALLEX/GNO, SAGE and Super-Kamiokande experiments. It was initially unclear if the SNP was due to a error in the SSM or to the existence of neutrino flavour transitions.

Neutrino oscillations were finally confirmed in a model-independent way in the Sudbury Neutrino Observatory (SNO) in 2001. The SNO experiment [15] detected solar neutrinos through the three reactions

$$\mathrm{CC}: \nu_e + d \rightarrow p + p + e^- \qquad E_\nu^{th} = 1.442 \text{ MeV} \tag{1.112}$$

$$\mathrm{NC}: \nu_\alpha + d \rightarrow p + n + \nu_\alpha \qquad E_\nu^{th} = 2.224 \text{ MeV} \tag{1.113}$$

$$\mathrm{ES}: \nu_\alpha + e^- \rightarrow \nu_\alpha + e^- \tag{1.114}$$

with $\alpha = e, \mu, \tau$, therefore being sensible not only to electron but to all lepton flavours. The final reported flux values (Figure 1.2) are compatible with a no null $\mu + \tau$ flux (in units of 10^6 cm^{-2}s^{-1}),

$$\phi_{CC} = \phi_{\nu_e} = (1.68 \pm 0.06^{+0.08}_{-0.09}) \tag{1.115}$$

$$\phi_{NC} = \phi_{\nu_e} + \phi_{\nu_\mu + \nu_\tau} = (4.94 \pm 0.21^{0.38}_{0.34}) \tag{1.116}$$

$$\phi_{ES} = \phi_{\nu_e} + 0.1553\ \phi_{\nu_\mu + \nu_\tau} = (2.35 \pm 0.22 \pm 0.15), \tag{1.117}$$

where ϕ_{ν_e} is the electron neutrino flux and $\phi_{\nu_\mu + \nu_\tau}$ is the sum of muon and tau flux. The $\mu + \tau$ fluxes from NC and ES are compatible and the NC total flux is compatible with the SSM electron flux.

Even though SNO results proved the model-independent existence of flavour transitions in neutrinos, SNO data is not enough to compute all of the six three family mixing parameters in (1.106), (1.107), (1.108). Solar neutrino oscillation data is analysed in the simplest two-neutrino oscillation scenario in which electron neutrino disappear as in (1.109). Since solar neutrino flux at source is unknown, obtaining evidence of neutrino oscillations in vacuum requires to compare the fluxes throughout the year, where the distance L between Earth and Sun is variable. The observed seasonal variation was compatible with the flux going with L^{-2} [16], thus a vacuum oscillation solution for the SNP was discarded.

The SNP was finally understood by the effect of flavour transitions in solar matter itself, by the so-called *MSW effect* [17]. Taking this effect into account, neutrino solar data can be described by the two neutrino oscillation model with the parameters [15]

$$\Delta m^2_{\mathrm{SOL}} = (6.5^{+4.4}_{-2.3}) \times 10^{-5}\ \mathrm{eV}^2, \quad \tan^2 \vartheta_{\mathrm{SOL}} = 0.45^{+0.09}_{-0.08}. \tag{1.118}$$

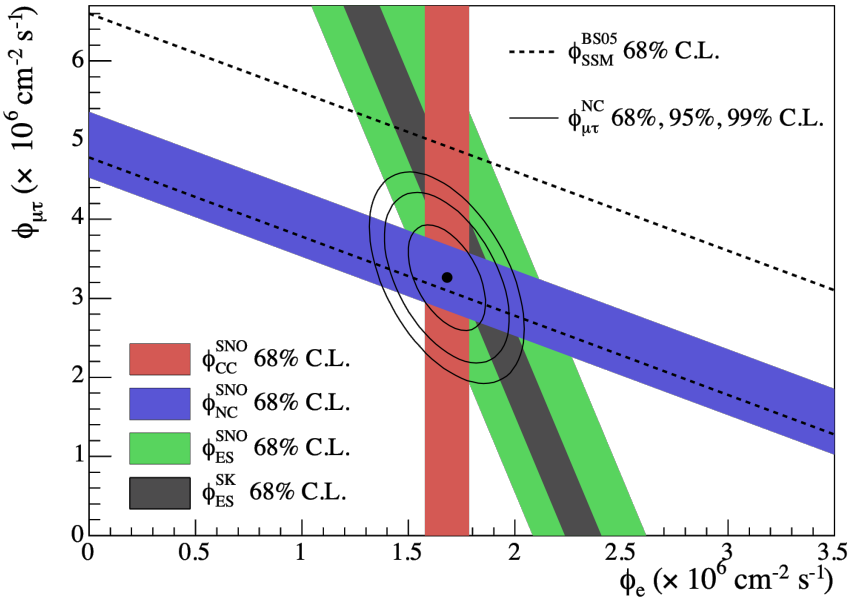


Figure 1.2: Flux of $\mu+\tau$ neutrinos versus flux of electron neutrinos for NC and ES reactions. The no null value of $\phi_{\mu\tau}$ indicates the existence of flavour transitions. From [15].

Solar neutrino matter effects in Earth are also seeing in the day-night flux asymmetry [18].

Another important source of natural neutrinos are the so-called *atmospheric neutrinos*. High energetic primary cosmic rays (mainly protons, but also heavier nuclei) interact with nuclei in the atmosphere producing hadrons. These hadrons and its decay products are known as the secondary cosmic rays. The energy spectrum of the secondary cosmic ray shower is peaked in the GeV range, expanding to higher energies following an approximate power law. Many secondary pions are produced, which decay via

$$\pi^+ \to \mu^+ + \nu_\mu, \quad \pi^- \to \mu^- + \overline{\nu}_\mu. \tag{1.119}$$

For energies of the order or less than GeV, muons decay before reaching the ground through

$$\mu^+ \to e^+ + \nu_e + \overline{\nu}_\mu, \quad \mu^- \to e^- + \overline{\nu}_e + \nu_\mu. \tag{1.120}$$

Atmospheric neutrino experiments can measure these neutrinos in energies ranging from 100 MeV to 100 GeV. Detector must be placed in underground laboratories in order to reduce the flux of the higher energy muons that do not decay in the atmosphere. Assuming energies less than GeV in which muons decay, the expected flux quotients between muon and electron neutrinos from the cascade reactions (1.119) and (1.120) would be

$$\frac{\phi_{\nu_\mu}^{\text{sub GeV}} + \phi_{\overline{\nu}_\mu}^{\text{sub GeV}}}{\phi_{\nu_e}^{\text{sub GeV}} + \phi_{\overline{\nu}_e}^{\text{sub GeV}}} \simeq 2, \tag{1.121}$$

The first evidence of a deviation from this quotient was obtained in Kamiokande experiment [19]. The solution toward neutrino oscillations was clearer with Super-Kamiokande measurement of the asymmetry between muon fluxes of upward and downward going neutrinos [20]. Upward going neutrinos cover more distance since they traverse the Earth and the neutrino muon flux is reduced, namely muon neutrinos

disappear when they propagate this extra distance. Super-Kamiokande results favour the $\nu_\mu \to \nu_\tau$ transition over the $\nu_\mu \leftrightarrows \nu_e$, obtaining the atmospheric mass square difference and mixing angle

$$\Delta m^2_{\text{ATM}} = 2.1 \times 10^{-3}\ \text{eV}^2, \quad \sin^2 \vartheta_{\text{ATM}} = 1.00. \tag{1.122}$$

Besides solar and atmospheric, two extra types of neutrino oscillations experiments exist nowadays:

- *Reactor experiments* measure electron antineutrinos coming from the β decays in nuclear reactors through the inverse neutron decay process $\overline{\nu}_e + p \to n + e^+$.
- *Accelerator experiments* in which a neutrino beam is created by protons hitting a target. The proton collisions create pions, kaons and muons that decay producing a neutrino beam. Several type of experiments exists depending on the production method: pion decay in flight (DIF), muon decay at rest (DAR) or beam dump.

Neutrino experiments can be classified by their sensitivity to Δm^2, which is defined using the phase in (1.110) such that

$$\frac{\Delta m^2 L}{4E} \sim \frac{\pi}{2}, \tag{1.123}$$

since for small values the probability would be zero and for large values only information on the mixing angle is obtainable. Approximate sensitivity values for different types of oscillation experiments are shown in Table 1.3. Depending on the source to target distance, reactor and accelerator experiments are also classified on *Short Baseline* (SBL) or *Long Baseline* (LBL).

Overall, the results of oscillation experiments can be summarized as [12]:

- Solar ν_e convert to ν_μ and/or ν_τ. The observed energy dependence of the effect is well described by massive neutrino conversion in solar matter according to the MSW effect.
- Atmospheric ν_μ ($\overline{\nu}_\mu$) convert to ν_τ ($\overline{\nu}_\tau$). The results show an energy and distance dependence perfectly described by mass induced oscillations.
- Accelerator ν_μ ($\overline{\nu}_\mu$) convert to ν_e ($\overline{\nu}_e$) over distances of $\sim$ 200 to 800 km. The energy spectrum of the results show a clear oscillatory behaviour in accordance with mass induced oscillations with wavelength in agreement with the effect observed in atmospheric experiments.
- Reactor $\overline{\nu}_e$ disappear with different probabilities for distances of $\sim$ 1.5 km and $\sim$ 200 km. The observed energy spectra show two different mass induced oscillation wavelengths: at short distances in agreement with the one observed in accelerator ν_μ disappearance, and a long distance compatible with the required parameters for MSW conversion in the Sun.

The minimum number of massive neutrinos to describe the results is three, therefore six neutrino oscillation parameters ought to be obtainable from oscillation experiments as described in §1.5.2. Nevertheless, it is worth mentioning that some experimental anomalous results exist that allows the existence of another neutrino mass scale in the order of ~ 1 eV^2. In this case a four neutrino model with a sterile neutrino ν_s would be required. In particular, accelerator SBL LSND [22] experiment found evidence of $\overline{\nu}_\mu \to \overline{\nu}_e$ transitions with $\Delta m^2 \sim 1$ eV^2. This effect was also searched

Table 1.3: Sensitivities of different types of oscillation experiments and their contribution to the oscillation parameters. The listed experiments are used in the global fits in [21].

Type of experiment	L (km)	E (GeV)	Δm^2 (eV^2)	Parameter sensitivity		Experiments used in global fit
				Dominant	Sub-dominant	
Solar	10^8	10^{-3}	10^{-11}	ϑ_{12}	$\Delta m^2_{21}, \vartheta_{13}$	Homestake, GALLEX/GNO, SAGE, Borexino, SK, SNO
Atmospheric	$10-10^4$	$0.1-10^2$	10^{-4}	$\Delta m^2_{31}, \vartheta_{23}$	$\vartheta_{13}, \delta_{13}$	SK, IceCube
Reactor SBL	$0.1-1$	10^{-3}	$10^{-2}-10^{-3}$	$\Delta m^2_{31}, \vartheta_{13}$		Daya Bay, RENO
Reactor LBL	$10-10^2$	10^{-3}	$10^{-4}-10^{-5}$	Δm^2_{21}	$\vartheta_{12}, \vartheta_{13}$	KamLAND
Acelerator SBL	0.1	$1-10$	0.1			
Acelerator LBL	10^2-10^4	$10-10^2$	$10^{-2}-10^{-3}$	$\Delta m^2_{31}, \vartheta_{23}, \delta_{13}$	ϑ_{13}	NOνA, T2K, MINOS, K2K

USC UNIVERSIDADE DE SANTIAGO DE COMPOSTELA

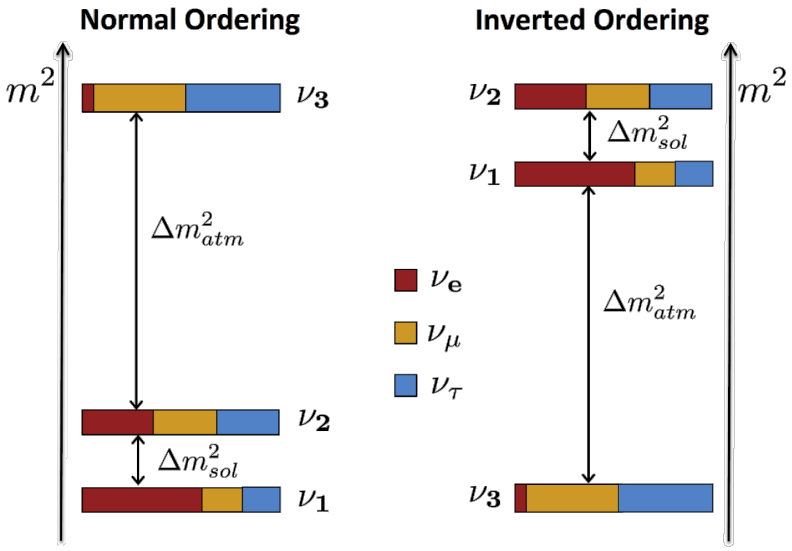


Figure 1.3: Two different mass orderings for neutrino masses in the three neutrino mixing scenario compatible with current observations. Absolute value of the masses is still unknown. From [28].

in MiniBooNE [23] acelerator SBL experiment, founding an excess of neutrino and antineutrino events in the low energy region of the spectra that would be compatible with LSND result. This effect will be further studied by MicroBooNE and ICARUS at Fermilab [24].

The purposes of the next generation oscillation experiments will be the precision measurement of oscillation parameters, with special enphasis on the CP violation phase, and the determination of the mass ordering through atmopheric day-night matter effects. Three large experiments are under construction: the long baseline accelerator experiments HyperKamiokande [25] and DUNE [26], and short baseline reactor experiment JUNO [27].

1.5.2. Mass orderings and global fits

Neutrino oscillation experimental data was historically analysed in the simpler two neutrino mixing scenario. This analysis provided the two values of the mass square differences for solar (1.118) and atmospheric neutrinos (1.122). Since $\Delta m^2_{\text{SOL}} << \Delta m^2_{\text{ATM}}$ it is possible to accomodate both results in a three neutrino mixing scenario, conventionally defining $\Delta m^2_{\text{SOL}} \equiv \Delta m^2_{21}$ and $\Delta m^2_{\text{ATM}} \equiv |\Delta m^2_{31}|$. Since none of the absolute mass values (m_1, m_2, m_3) is known, it is possible to distinguish between two different mass orderings depending on the sign of Δm^2_{31}

- Normal ordering (NO): $m_1 < m_2 < m_3$,
- Inverted ordering (IO): $m_3 < m_1 < m_2$,

squematically in Figure 1.3. Neutrino masses can also be classified in three hierarchies depending on the value of the still unknown lightest mass: normal hierarchy ($m_1 \ll m_2 \ll m_3$), inverted hierarchy ($m_3 \ll m_1 \lesssim m_2$) and quasi degenerate hierarchy ($m_1 \simeq m_2 \simeq m_3$).

The six oscillation parameters are obtained in the three mixing model by joining the results of the different type of oscillation experiments and performing a global

Table 1.4: Results of the global oscillation fits [21] to the three neutrino mixing model.

Parameter	Normal Ordering		Inverted ordering	
	best fit $\pm 1\sigma$	3σ range	best fit $\pm 1\sigma$	3σ range
Δm^2_{21} $[10^{-5}\text{eV}^2]$	$7.50^{+0.22}_{-0.20}$	6.94–8.14	$7.50^{+0.22}_{-0.20}$	6.94–8.14
$\lvert\Delta m^2_{31}\rvert$ $[10^{-3}\text{eV}^2]$	$2.55^{+0.02}_{-0.3}$	2.47–2.63	$2.45^{+0.02}_{-0.3}$	2.37–2.53
$\sin^2\vartheta_{12}$	3.18 ± 0.16	2.71–3.69	3.18 ± 0.16	2.71–3.69
$\sin^2\vartheta_{13}$	$2.200^{+0.069}_{-0.062}$	2.000–2.405	$2.225^{+0.064}_{-0.070}$	2.018–2.424
$\sin^2\vartheta_{23}$	5.74 ± 0.14	4.34–6.10	$5.78^{+0.10}_{-0.17}$	4.33–6.08
δ_{13}/π	$1.08^{+0.13}_{-0.12}$	0.71–1.99	$1.58^{+0.15}_{-0.16}$	1.11–1.96

multi-parametric fit. Each type of experiment contributes differently to the oscillation parameters (see Table 1.3). Roughly, data is fitted by minimizing a χ^2 such that

$$\chi^2 = \sum_i \frac{(N_i^{\text{meas}} - N_i^{\text{exp}})^2}{\sigma_i^2}, \tag{1.124}$$

where N_i^{meas} and N_i^{exp} are the number of measured and expected events in the energy bin i, respectively. The number of expected events would depend on the oscillation parameters through the corresponding $\nu_\alpha \to \nu_\beta$ transition in (1.105) or its matter effect equivalent. The most recent global fits are performed using the experiments in Table 1.3, obtaining the oscillation parameters shown in Table 1.4 and a prefered normal ordering over inverted. The results for normal ordering are compatible with CP conservation as $\delta_{13} \sim \pi$ within errors.

1.6. Direct searches of neutrino mass and nature

Neutrino oscillation experiments have provided the most relevant source of information in neutrino physics so far. The phenomenological parameters we can extract from neutrino oscillation experiments is restricted to the measurement of the mass square differences and mixing angles. Nevertheless they are not sensible to the absolute scale of neutrino masses neither the Dirac or Majorana nature. Setting lower limits in the heavier neutrino mass is the objective of direct mass searches and neutrinoless double beta decay experiments as we will see below. Also neutrinoless double beta decay is a lepton number violation process and therefore a candidate for testing the Majorana nature of neutrinos.

1.6.1. Beta decay

Neutrino mass measurements have been historically attempted by studying the electron energy spectrum of β decay, but no significant deviations have been found from the massless neutrino hypothesis and just lower bounds exist. Nonetheless, the study of β decay stands as the most promising and sensitive method for obtaining a model independent (in the sense of number of massive states) neutrino mass measurement

by pure kinematical constraints. The differential beta decay rate [4] is given by

$$\frac{\mathrm{d}\Gamma}{\mathrm{d}E_e} = \frac{G_F^2 m_e^5}{2\pi^3} \cos^2\theta_C |\mathscr{M}|^2 F(Z,E_e) E_e p_e E_\nu p_\nu, \tag{1.125}$$

where G_F is the Fermi constant, m_e is the electron mass, θ_C is the Cabbibo angle, $\mathscr{M}$ is the nuclear matrix element (which is energy independent in the case of allowed decays), $F(Z,E_e)$ is the Fermi function which describes the interaction of the outgoing electron with the final nucleus and $E_{e,\nu}, p_{e,\nu}$ are the energy and momentum of the outgoing electron and neutrino, respectively. Since the final nucleus is much heavier than the outgoing electron and neutrino, by conservation of energy we have

$$E_\nu = Q_\beta - T, \quad \text{with} \quad Q_\beta \equiv M_i - M_f - m_e \tag{1.126}$$

where T is the electron kinetic energy ($E_e = T + m_e$) and $M_{i,f}$ are the masses of the initial and final nucleus. Beta spectrum can be analyzed through the differential decay rate in (1.125) by defining the *Kurie function*

$$K(T) \equiv \sqrt{\frac{\mathrm{d}\Gamma/\mathrm{d}E_e}{\frac{G_F^2 m_e^5}{2\pi^3}\cos^2\theta_C |\mathscr{M}|^2 F(Z,E_e) E_e p_e}} = \left[(Q_\beta - T)\sqrt{(Q_\beta - T)^2 - m_{\nu_e}^2}\right]^{1/2} \tag{1.127}$$

where we used the kinematic relation (1.126) and the fact that $p_\nu = \sqrt{E_\nu^2 - m_{\nu_e}^2}$, where the electron neutrino mass is denoted by m_{ν_e}. If $m_{\nu_e} = 0$ the Kurie function would be linear in T. The deviation from linearity at the end point of the spectrum would produce a difference that gives a direct measurement of m_ν from $T_{max} = Q_\beta - m_\nu$, as show in Figure 1.4. The number of events in this region $T \sim Q_\beta$ is very small, thus a low value of Q_β is prefered. Notice that the definition of the Kurie function gets rid of the Fermi function, but it must be known in order to get neutrino mass estimates from experiments, which measure energy and decay rates.

The most used reaction in experiments is the tritium super-allowed beta decay

$$^3\mathrm{H} \rightarrow {}^3\mathrm{He} + e^- + \overline{\nu}_e, \quad Q_\beta = 18.574 \text{ KeV}, \tag{1.128}$$

since it has a low Q_β and a manageable short half life of ~ 12.3 years. This reaction has allowed KATRIN experiment [29] to set the lowest known upper limit on electron neutrino mass up to date

$$m_{\nu_e} < 0.8 \text{ eV} \quad \text{at } 90\% \text{ C.L}, \tag{1.129}$$

improving by a factor of two the previously ~ 2 eV limit set by its predecessor the Mainz and Troitzk experiment. Nevertheless, KATRIN is designed to reach a sensitivity of ~ 0.2 eV and new results are expected in near future.

KATRIN apparatus [30] is ≈ 70 m long and it is composed of several parts as shown in Figure 1.6. Molecular tritium in injected (b) in a windowless gaseous tritium source (WGTS) where it decays with an activity of $\sim 10^{11}$ Bq. The rear section (a) is used to monitor the activity. The tritium is removed from the beam at the pumping section (c) and the electrons pass to the pre-spectrometer (d). The pre-spectrometer works as a filter to reduce the flux of electrons by many orders of magnitude selecting a desired range of energies. Finally the electrons enter in the main spectrometer (e) of 10 m

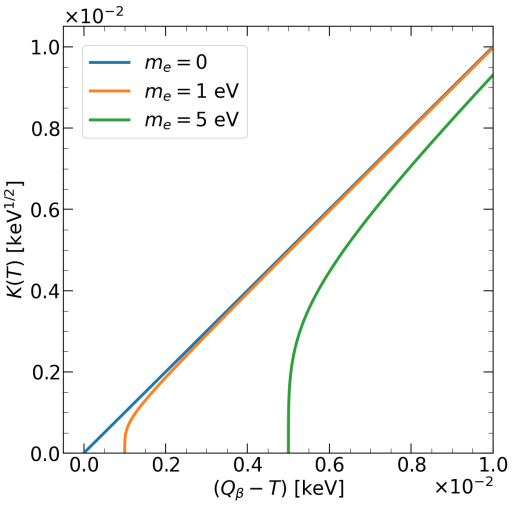


Figure 1.4: Kurie function near the spectra end-point showing the deviation for different neutrino masses.

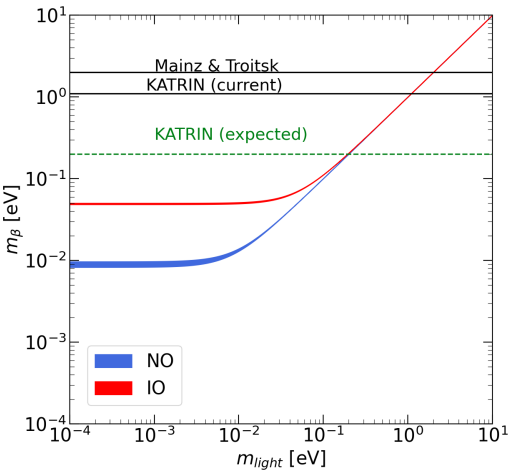


Figure 1.5: Effective electron neutrino mass as a function of the lightest neutrino for normal (NO) and inverted (IO) ordering.

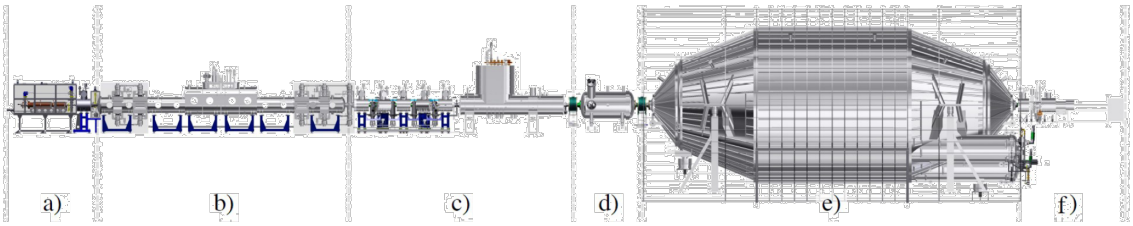


Figure 1.6: KATRIN experimental setup: a) rear section for monitoring, b) WGTS where tritium is injected, c) pumping section for tritium removal, d) pre-spectrometer for filtering, e) main spectrometer for energy splitting, f) focal section where electrons are counted. From [30].

diameter and 24 m long and are counted at the focal section (f) by a monolithic silicon detector array. Besides KATRIN, another tritium based experiment is Project 8 [31] that proposes an energy measurement based on the cyclotron radiation emitted by electrons in a magnetic field.

An alternative decay to tritium is been explored at ECHo [32] and HOLMES [33] experiments that use the electron capture of ^{163}Ho into ^{163}Dy with a very low Q-value of $Q_\beta = 2.8$ KeV. This is a β^+ decay, then it gives direct mass information on electron neutrino instead of antineutrino mass as in tritium β^- decay.

Above we have considered the lepton neutrino state in beta decay as a real particle, but flavour neutrino states are a linear superposition of mass states (§1.5). Considering the mixing matrix between flavour and massive states in the three neutrino scenario, the Kurie function in (1.127) becomes [34]

$$K(T) = \left[(Q_\beta - T) \sum_{k=1}^{3} |U_{ek}|^2 \sqrt{(Q_\beta - T)^2 - m_k^2} \right]^{1/2} . \tag{1.130}$$

USC UNIVERSIDADE DE SANTIAGO

Notice that the mixing matrix elements enter as module square, therefore CP phases are indistinguishable. If an experiment's resolution is not good enough to reach the neutrino small mass values, then $m_k \ll Q_\beta - T$ and the Kurie function can be approxi-

mated by

$$K(T) \simeq \left[(Q_\beta - T)\sqrt{(Q_\beta - T)^2 - m_\beta^2}\right]^{1/2}, \tag{1.131}$$

where the *effective electron neutrino mass* is defined by

$$m_\beta \equiv \left[\sum_{k=1}^{3} |U_{ek}|^2 m_k^2\right]^{1/2}. \tag{1.132}$$

Therefore the reported value in (1.129) should be better written as $m_\beta < 0.8$ eV. Figure 1.5 shows the value of m_β as a function of the lightest neutrino mass for both neutrino mass ordering. If any experiment finds evidence of non-zero neutrino masses, an analysis based on the approximate (1.131) would no longer be valid and (1.130) must be used, which could also resolve between normal or inverted ordering schemes.

In the discussion above just beta decay has been considered as a method for direct neutrino measurements. Another neutrino mass upper limits have been obtained through the kinematics of pion and tau decays, but the limits are orders of magnitude [12] higher than the ∼1 eV obtained from beta decay.

1.6.2. Neutrinoless double beta decay

1.6.2.1. Lepton number violating processes

Beta decay can provide a direct measurement of the neutrino mass. However the Kurie function (1.130) is not sensible to the mixing phases and therefore can not distinguish between Dirac or Majorana neutrino nature.

In order to devise an experiment to determine the neutrino nature, we should go back to the charged current interaction lagrangian in (1.37), with the lepton neutrino being substituted by the massive neutrino states in (1.50). This interaction term represent the neutrino production and absorption vertices together with a lepton. We could think of the following experiment: a pion π^+ decays into a neutrino ν_i through $\pi^+ \to \mu^+ + \nu_i$ and then interacts with a nucleus N. Recall from Section 1.4 that total lepton number is conserved if neutrinos are Dirac, but it is not in the Majorana case. The possible outcomes of the experiment would be

$$\begin{aligned} \text{if Dirac:} \quad & \nu_i + N \to \mu^+ + X, \\ \text{if Majorana:} \quad & \nu_i + N \to \mu^+ + X \quad \text{or} \quad \nu_i + N \to \mu^- + X, \end{aligned}$$

where X is the output nucleus. Observing the μ^- would be an evidence of the Majorana neutrino nature. The problem is that the μ^- outcome is strongly suppressed with respect to the μ^+. The suppression factor [1] being of the order of $\sim (m_i/E)^2$ with m_i the neutrino mass and E the energy of the incoming neutrino. Since typical neutrino interaction energies with matter are $E \gtrsim 1$ MeV and $m_i \sim 1$ eV, the suppression becomes $\lesssim 10^{-12}$, a sensitivity out of the scope with current technology. On the other hand, we could try to find a process in which the neutrino ν_i is not physically emitted but virtually exchanged instead. Such a case could be the *neutrinoless double beta decay*.

USC DE SANTIAGO DE COMPOSTELA

1.6.2.2. Double beta decay modes

Double beta decay ($2\nu\beta\beta$) is a rare process in which two neutrons or protons in a nucleus $N(A,Z)$ decay simultaneously

$$2\nu\beta^-\beta^-: \quad N(A,Z) \to N(A,Z+2)+2e^-+2\overline{\nu}_e \tag{1.133}$$
$$2\nu\beta^+\beta^+: \quad N(A,Z) \to N(A,Z-2)+2e^++2\nu_e \tag{1.134}$$

It was proposed for the first time in 1935 by M. Goeppert-Mayer [35]. The first direct observation [36] was done in 1987 using a time projection chamber, with an estimated half life of $T^{2\nu}_{1/2} \sim 10^{20}$ years for ^{82}Se $\to^{82}$ Kr transition. Notice that the $N(A,Z) \to N(A,Z-2)$ transition could also occur through the electron capture processes

$$2\nu\text{EC}\beta^+: \quad N(A,Z)+e^- \to N(A,Z-2)+e^++2\nu_e \tag{1.135}$$
$$2\nu 2\text{EC}: \quad N(A,Z)+2e^- \to N(A,Z-2)+2\nu_e \tag{1.136}$$

Neutrinoless double beta decay ($0\nu\beta\beta$) is a similar process in which no neutrinos are emitted

$$0\nu\beta^-\beta^-: \quad N(A,Z) \to N(A,Z+2)+2e^- \tag{1.137}$$
$$0\nu\beta^+\beta^+: \quad N(A,Z) \to N(A,Z-2)+2e^+. \tag{1.138}$$

This is forbidden in the SM since it violates lepton number by two units $|\Delta L| = 2$. It was originally proposed by Wendell H. Furry [37] in 1939 in order to test Majorana theory of neutrinos. As we will see below, the existence of $0\nu\beta\beta$ inevitable requires neutrinos to be Majorana. The same applies to the neutrinoless electron capture processes $0\nu\text{EC}\beta^+$ and $0\nu 2\text{EC}$. Nowadays no evidence of the zero neutrino mode has been found. A detailed discussion on $0\nu\beta\beta$ experimental status is given in Chapter 2.

The kinematics of $2\nu\beta\beta$ and $0\nu\beta\beta$ are different (see Figure 1.7). The former is a four body decay, then the total kinetic energy of the electrons will be continuously distributed between zero and the reaction's Q-value. On the other hand, in the neutrinoless mode, the Q-value corresponds to the total kinetic energy of the electrons. Neglecting the nuclear recoil of the daughter nucleus and the small neutrino mass, the Q-value is given by

$$Q_{\beta\beta} = M(A,Z) - M(A,Z\pm 2) - 2m_e, \tag{1.139}$$

where $M(A,Z)$ is the mass of the decaying nucleus with massive and atomic numbers A and Z, respectively. For $\beta\beta$ to occur, the Q-value must be positive. Nevertheless the process will not be effectively observable if the nucleus can also β decay, because $\beta\beta$ half-lives are orders of magnitude higher. In order for the single β mode be suppressed, the process must be energetically forbidden or highly unlikely due to a large spin transition. This is only satisfied by 35 isotopes in nature [39] but not all of them are adequate to $\beta\beta$ searches due to experimental constraints.

USC UNIVERSIDADE DE SANTIAGO DE COMPOSTELA

1.6.2.3. The black box theorem

The tree level diagram for $2\nu\beta\beta$ is shown in Figure 1.8. The $0\nu\beta\beta$ process is obtained if we could join the lepton vertices by virtualizing the outgoing antineutrinos as in Figure 1.9. This is forbidden in the SM since the lepton vertex would absorb a neutrino

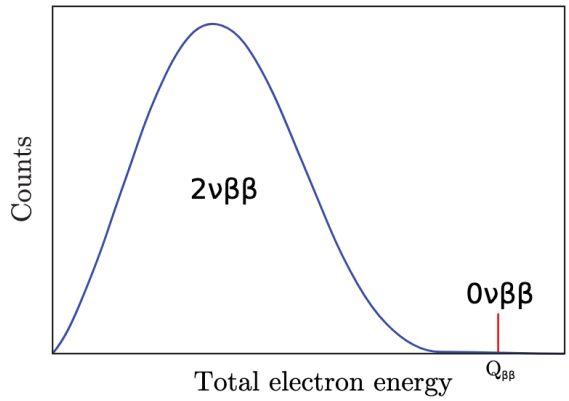


Figure 1.7: Schematic spectra for the sum of the kinetic energies of the electrons in double beta decay for the two-neutrino mode $2\nu\beta\beta$, zero-neutrino mode $0\nu\beta\beta$. From [38].

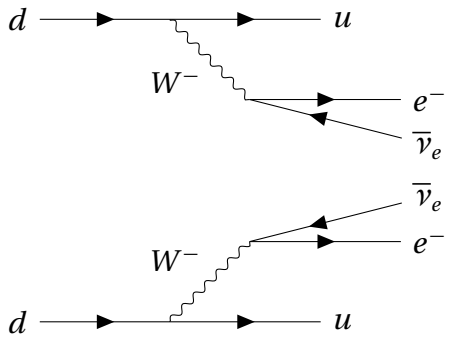


Figure 1.8: Tree level diagram for $2\nu\beta\beta$.

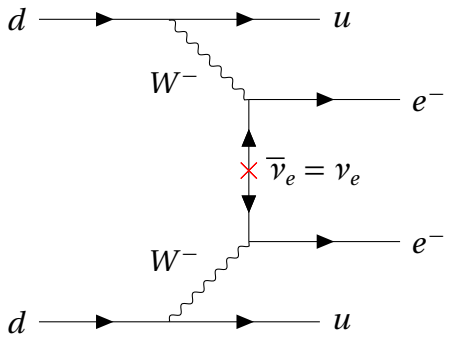


Figure 1.9: Tree level diagram for $0\nu\beta\beta$.

instead of an antineutrino, a condition that would be satisfied only if neutrinos were massive Majorana particles. Thus neutrinos being Majorana is a sufficient condition for $0\nu\beta\beta$ to exist. However, this argument alone does not imply that discovering $0\nu\beta\beta$ means that neutrinos are Majorana, since other beyond SM mechanisms could exist [40].

Fortunatelly, the *black box theorem* [41] demonstrates that $0\nu\beta\beta$ and Majorana neutrinos is a two way correspondence

$$0\nu\beta\beta \Longleftrightarrow \text{Majorana neutrinos},$$

namely the existence of $0\nu\beta\beta$ implies that neutrinos are Majorana, and viceversa. Whatever new physics is behind $0\nu\beta\beta$, neutrinos being Majorana is assured. The proof is based on the $\overline{\nu}_e \to \nu_e$ transition, depicted in Figure 1.10 in which the vertices in the tree level diagram of Figure 1.9 are rearranged. This transition generates the neutrino Majorana mass through radiative corrections at some order in perturbation theory. For this mass to be null, the diagram contribution has to be cancelled out in all possible BSM diagrams and for all orders. This is unlike because it would require a fine-tuning of the oscillation parameters at all orders, unless some global symmetry forbids the electron neutrino Majorana mass term in (1.75). However the existence of this symmetry is incompatible with the existence of $0\nu\beta\beta$ [42].

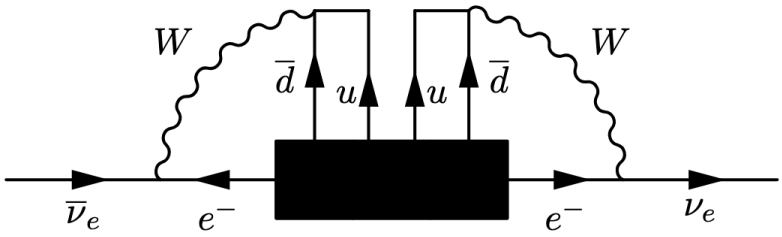


Figure 1.10: Contribution of the black-box operator to Majorana neutrino mass. From [43].

1.6.2.4. The standard mechanism

As it happened in the analysis of oscillation data (§1.5) and beta decay (§1.6.1), a model must also be chosen to analyze double beta decay. Since no incontestable evidence of $0\nu\beta\beta$ has been found so far, the most natural model is the three-neutrino Majorana scenario introduced in §1.4.2. In this model, the tree diagram for $0\nu\beta\beta$ is the same as in Figure 1.9 with the electron neutrino vertex substituted by a massive neutrino state ν_i. The half-life for a decaying nucleus N is given by [44], [39]

$$[T^{0\nu}_{1/2}(N)]^{-1} = G^N_{0\nu}|M^N_{0\nu}|^2\left(\frac{m_{\beta\beta}}{m_e}\right)^2 \tag{1.140}$$

where $G^N_{0\nu}$ is the *phase space factor* (PSF), $M^N_{0\nu}$ is the *nuclear matrix element* (NME) and $m_{\beta\beta}$ is the *effective Majorana mass*. The PSF depends on the Q-value and the atomic number Z of the decaying nucleus and can be computed analytically [45]. On the other hand the NME can greatly differ between nuclear models [46]. Both parameters must be known accurately in order to extract the value of $m_{\beta\beta}$ in (1.140) if $0\nu\beta\beta$ is ever measure. This last factor contains the most fundamental neutrino parameters

$$m_{\beta\beta} \equiv \left|\sum_{k=0}^{3} U^2_{ek} m_k\right|, \tag{1.141}$$

where U_{ek} are the components of the Majorana mixing-matrix and m_k the neutrino masses. The explicit expansion of $m_{\beta\beta}$ as a function of the mixing matrix parameters in (1.104) is given by

$$m_{\beta\beta} = |c^2_{12}c^2_{13}m_1 + s^2_{12}c^2_{13}e^{i2\lambda_2}m_2 + s^2_{13}e^{i2(\lambda_3-\delta_{13})}m_3|, \tag{1.142}$$

Notice the similarity of the effective Majorana mass $m_{\beta\beta}$ with the already introduced effective electron neutrino mass m_β in (1.132). The later was used to estimate the sensitivity of the different experiments on neutrino mass. For neutrinoless double beta decay experiments, the estimator is $m_{\beta\beta}$ since it does not depend on the concrete nuclear decay under study.

USC UNIVERSIDADE DE SANTIAGO DE COMPOSTELA

CHAPTER 2

The search for neutrinoless double beta decay

2.1. Introduction

The observation of neutrinoless double beta decay ($0\nu\beta\beta$) is a major experimental challenge due to the large half-life of the process. Current upper limits report values higher than $\sim 10^{26}$ years, which is several orders of magnitude above the two neutrino mode decay that range between $\sim 10^{18}$ and $\sim 10^{21}$ years. The twelve known $2\nu\beta\beta$ half-lifes are shown in Table 2.1 and the upper limit for its neutrinoless counterpart.

We can distinguish three types of $\beta\beta$ experiments [39]: *geochemical*, *radiochemical* and *direct*. The geochemical experiments consist in the measurement of the decay's daughter in a sample from the Earth's crust. The advantage of such an experiment is the high exposure time ($\sim 10^9$ years) of the sample, but the number of initial parent nuclei must be precisely estimated to discard mechanisms different than double beta. The radiochemical experiments are similar with the sample being prepared by the experimenters, thus the initial number of nuclei are known in this case. Both, radiochemical and geochemical can not distinguish between the zero and two neutrino decay modes since can not measure the energy of the outgoing electrons. In this Chapter we will focuss on direct experiments, which can identify between decaying modes by measuring the electron's energy.

The number of decaying events in a radioactive sample follow the well known exponential decay. For $0\nu\beta\beta$ the half-life is much larger than the exposure time $T^{0\nu}_{1/2} \gg t$, thus the expected number of $0\nu\beta\beta$ events measured in a given sample would be

$$N = \log 2 \, \epsilon \, \frac{N_A}{W} \, \frac{M \; t}{T^{0\nu}_{1/2}} \tag{2.1}$$

where N_A is the Avogadro number, W is the molar mass of the isotope, ϵ is the detection efficiency, M is the total mass of the isotope sample and t is the exposure time. We could use (2.1) to compute the half-life if we were certain on the number of decaying events N. Such a case will happen if we could clearly identify the $0\nu\beta\beta$ energy peak around the $Q_{\beta\beta}$ with extremely good energy resolution and a background rate much lower than the number of signal events, which is not the case nowadays and experiments can only report upper limits to the half-life (see Table 2.1).

This Chapter is organized as follows. In Section 2.2 we discuss how to estimate the sensitivity of $0\nu\beta\beta$ experiment. Based on this result, we analyze the desired features of

Table 2.1: Neutrinoless double beta isotope candidates. Isotopic compositions are taken from [47], $0\nu\beta\beta$ half-life upper limits (at 90% CL) and sensitivities from referenced experiments and $2\nu\beta\beta$ half-lifes from [48] or referenced experiments. (*) symbol in $2\nu\beta\beta$ half-lifes indicates composite measurement of the two modes, either from geochemical or direct experiments.

	Isotopic abundance	Process	Transition	$Q_{\beta\beta}$ (keV)	$T^{2\nu}_{1/2}$ ($\times 10^{19}$ y)	$T^{0\nu}_{1/2}$ ($\times 10^{22}$ y)	$m_{\beta\beta}$ (meV)	$\beta\beta$ Experiment
^{48}Ca	0.187	$2\beta^-$	$0^+ \to 0^+$	4267.00	4.39 ± 0.58	> 5.8	$< (3.5-22) \cdot 10^3$	ELEGANT-VI [49]
^{76}Ge	7.8	$2\beta^-$	$0^+ \to 0^+$	2039.06	192.6 ± 9.4	> 18000	$< 79-180$	GERDA [50]
^{82}Se	8.8	$2\beta^-$	$0^+ \to 0^+$	2996.40	9.39 ± 0.75	> 25	$< (1.2-3.0) \cdot 10^3$	NEMO-3 [51]
^{96}Zr	2.8	$2\beta^-$	$0^+ \to 0^+$	3349.00	2.35 ± 0.30	> 0.92	$< (7.2-19.5) \cdot 10^3$	NEMO-3 [52]
^{100}Mo	9.7	$2\beta^-$	$0^+ \to 0^+$	3034.37	0.693 ± 0.004	> 110	$< 330-620$	NEMO-3 [53]
			$0^+ \to 0^+_1$	2339.30	57.0 ± 13.2	-	-	-
			$0^+ \to 0^+_1$	2339.30	61.2 ± 2.0 *	-	-	-
^{116}Cd	7.5	$2\beta^-$	$0^+ \to 0^+$	2813.44	2.74 ± 0.22	> 10	$< (1.4-2.5) \cdot 10^3$	NEMO-3 [54]
^{128}Te	31.7	$2\beta^-$	$0^+ \to 0^+$	866.50	$(3.49 \pm 1.99) \times 10^5$ *	> 11	-	-
^{130}Te	34.1	$2\beta^-$	$0^+ \to 0^+$	2527.51	77.1 ± 1.1	> 3200	$< 75-350$	CUORE [55], [56]
^{136}Xe	8.9	$2\beta^-$	$0^+ \to 0^+$	2457.99	234 ± 13	> 10700	$< 61-165$	KamLAND-Zen [57]
^{130}Ba	0.11	2EC	$0^+ \to 0^+$	2620.10	140 ± 80 *	-	-	-
^{150}Nd	5.6	$2\beta^-$	$0^+ \to 0^+$	3371.38	0.934 ± 0.084	> 2	$< (1.6-5.3) \cdot 10^3$	NEMO-3 [58]
			$0^+ \to 0^+_1$	2696.00	13.3 ± 4.0 *	-	-	-
^{238}U	99.3	$2\beta^-$	$0^+ \to 0^+$	1144.20	200 ± 60 *	-	-	-

USC UNIVERSIDADE DE SANTIAGO DE COMPOSTELA

an experiment in Section 2.3. Finally, Section 2.4 includes a description of the different experiments and techniques in $0\nu\beta\beta$ searches.

2.2. Sensitivity of a double beta decay experiment

2.2.1. Confidence intervals

Netrinoless double beta decays experiments report limits on the half-life as no evidence for signal has been obtained up to date. Here we introduce how to compute the *frequentists confidence intervals* for experiments expecting a very low number of signal events.

Assume that we design an experiment to measure $0\nu\beta\beta$ signals, denoted by n. It is well know that this random variable is poisson distributed with parameter μ,

$$n \sim \text{Pois}(n;\mu) = \frac{\mu^n}{n!} e^{-\mu}. \tag{2.2}$$

In an experiment we want to estimate the mean number of decays μ. For high decay rates we might have several measurements of n and we cold perform a *maximum likelihood fit* to estimate μ. But this is not the case in $0\nu\beta\beta$ which requires very large exposure times, thus we can just perform a single measurement n_{obs}. The question now is how to report a value of μ and how certain we are about this estimation. The answer was provided by J. Neyman [59] in 1937. For the observed number of decays n_{obs} we would report a *confidence interval* for the parameter μ, together with the *confidence level* of this interval to be true.

The confidence interval CI of n_{obs} with a confidence level CL is defined such that if we repeated the experiment many times, the fraction CL of confidence intervals of these hypothetical experiments will contain the true value of μ.

The classical construction of confidence intervals goes as follows. For each μ we compute the values n_1 and n_2 such that $\text{Pois}(n_1 \leq n \leq n_2;\mu) = \text{CL}$, or equivalently

$$\text{Pois}(n \leq n_1;\mu) = \sum_{n=0}^{n_1} \text{Pois}(n;\mu) \gtrsim \alpha \tag{2.3}$$

$$\text{Pois}(n \geq n_2;\mu) = \sum_{n=n_2}^{\infty} \text{Pois}(n;\mu) \gtrsim \beta \tag{2.4}$$

where α and β are chosen such that $\text{CL} = (1-\alpha-\beta)$. The inequality here comes from the fact that we are using a discrete random variable and by convention we assume conservative limits. For a continuous variable the $\gtrsim$ sign is substituted by an equality. The set of $\left[n_1(\mu), n_2(\mu)\right]$ values constitute what is known as a *confidence belt*. An example of confidence belts is shown in Figure 2.1.

The $n_1(\mu)$ and $n_2(\mu)$ constitute two curves in the plane n-μ. By definition, the confidence interval for a measurement n_{obs} is given by the intersection of the line $n = n_{obs}$ with the confidence belt curves. Therefore the true value of μ from which n_{obs} was sampled will be contained in the fraction CL of confidence intervals. A CI with lower and upper limit is called a central CI. Similarly we could define a lower and upper CI in which just a single confidence limit is given. For example $T^{0\nu}_{1/2}$ are reported as lower limits, since an upper limit would imply the existence of $0\nu\beta\beta$.

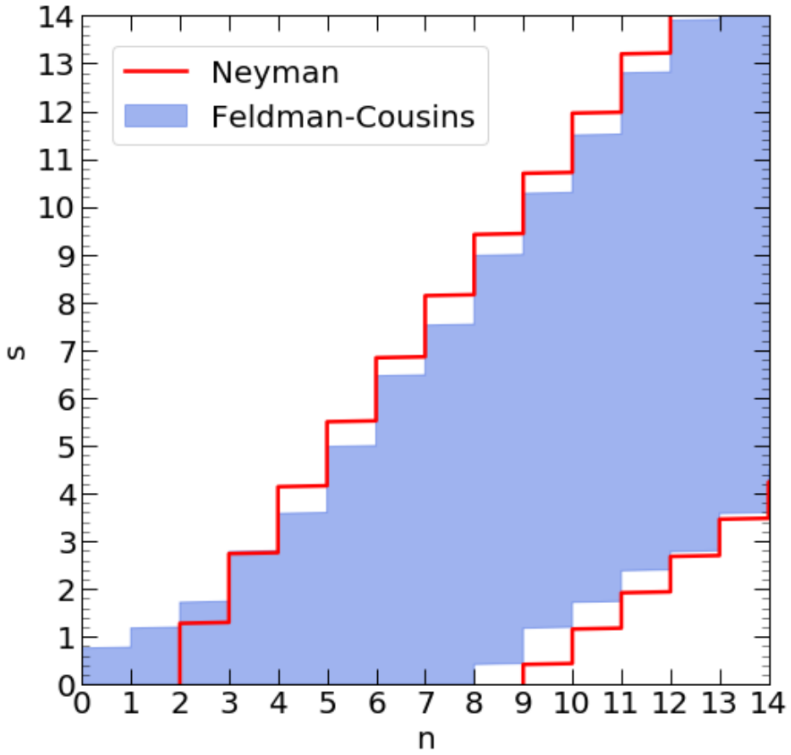


Figure 2.1: Confidence belts (at 90% CL with $\alpha = \beta = 5\%$) for poisson distributed number of decays (2.5) with $b = 5.0$. Both construction methods Neyman (classical) and Feldman-Cousins are shown.

Until now we have considered the unrealistic scenario of negligible background. Unfortunately this is not the case in $0\nu\beta\beta$ experiments. The measured value n_{obs} is composed by signal and background events. We will assume in what follows that we can characterize all the backgrounds in the region of interest of the signal (ie around $Q_{\beta\beta}$) with great accuracy, with a mean number of background events b. The mean value in (2.2) will be given by $\mu = s + b$

$$n \sim \text{Pois}(n; s+b) = \frac{(s+b)^n}{n!} e^{-(s+b)}. \tag{2.5}$$

The classical confidence intervals for s are shown in Figure 2.1 assuming $b = 5.0$. Notice that if an experiment measures an unlikely $n_{obs} = 0$ or $n_{obs} = 1$, neither confidence interval or upper limit is obtained. In order to avoid empty sets for confidence intervals, a modified method for the construction of confidence belts was devised by G. J. Feldman and R. D. Cousins [60]. This method is based on an ordering principle. The confidence belt for μ is obtained by adding values of n in decreasing order of the value of the ordering parameter

$$R = \frac{\text{Poiss}(n;\mu)}{\text{Poiss}(n;\mu_{\text{best}})}, \tag{2.6}$$

where μ_{best} is the value of μ that maximizes the likelihood $\text{Poiss}(n;\mu)$. Figure 2.1 shows how this construction avoids the undefined limits. This method also solves the so-called *flip-flopping* policy in reporting confidence intervals, that consist on the following. Suppose that instead a poisson random variable we built the CI for a continuous gaussian variable x with mean μ. This variable is well defined for all real

x values. For $x \gtrsim 0$ the lower confidence limit would be negative. But if the physical variable μ is by definition positive it would not make sense to report such a negative lower limit. We could report and upper limit if $x_{obs} \gtrsim 0$ and a central CI otherwise. In such a case we would be using a different reporting convention depending on the value measured itself. We could fix beforehand the convention of reporting an upper limit for values of $x \gtrsim 0$ and a central CI otherwise, but the confidence belts would be ill-defined.

Confidence intervals are useful to report the result of an experiment in which $n_{obs} \sim b$. What if $n_{obs} \gg b$? In such a case we may have found a new signal. Instead of a CI, we must report the *significance* of the discovery [61]. This is reported in number of standard deviations from the null hypothesis $s = 0$. Typically we would claim a discovery if the signal is above $\sim 5\sigma$ significance.

2.2.2. Sensitivity to the effective Majorana mass

Suppose we design an experiment searching for a new signal. Even before the experiment has been carried out, we would like to report a value that shows its discovery potential. If we were convinced that the signal exists (for example from previous indirect searches) and that our experiment will measure $n_{obs} \gg b$ we could report what is know as the *expected significance* [61]. It is defined as the average significance over the null hypothesis $s = 0$ that we will achieve assuming the signal exists with mean value s. For a large number of signals (poisson becomes gaussian) this is given by the quotient $s/\sqrt{b}$.

In $0\nu\beta\beta$ the situation is different since we expect to find $n_{obs} \sim b$. The discovery potential is measured by the physical limits we could reach. For example we can report the achievable lower limit in $T^{0\nu}_{1/2}$ under an unlikely measurement $n_{obs} \lesssim b$. However the half-life depends on the isotope and a more adequate parameter to compare all $0\nu\beta\beta$ experiments would be the effective Majorana mass $m_{\beta\beta}$. In what follows we denote $s_{up}(n; b, \mathrm{CL})$ the value of the upper limit for a measured value $n \equiv n_{obs}$ and known background b at confidence level CL. Also, we will use the definition of *sensitivity* as given in [62].

In the hypothetical background free experiment $b = 0$, we define the sensitivity as the upper limit we would obtain if $n_{obs} = 0$. This upper limit is obtained through the confidence belt construction in (2.5) with $b = 0$. For example for 90% CL, $s_{up}(0; 0, 0.9) \simeq 2.3$.

In the realistic experiment with known background b, we define the sensitivity as the mean value of the upper limit we would obtain if no true signal exists $s = 0$,

$$\overline{N}_{\mathrm{CL}}(b) = \sum_{n=0}^{\infty} \mathrm{Pois}(n; b)\, s_{up}(n; b, \mathrm{CL}) \tag{2.7}$$

Figure 2.2 shows the sensitivity as a function of background. At large background, the curves can be approximated by

$$\overline{N}_{\mathrm{CL}}(b) \simeq k_{\mathrm{CL}} \sqrt{b}. \tag{2.8}$$

The sensitivity definitions given above can be translated to an upper limit for the

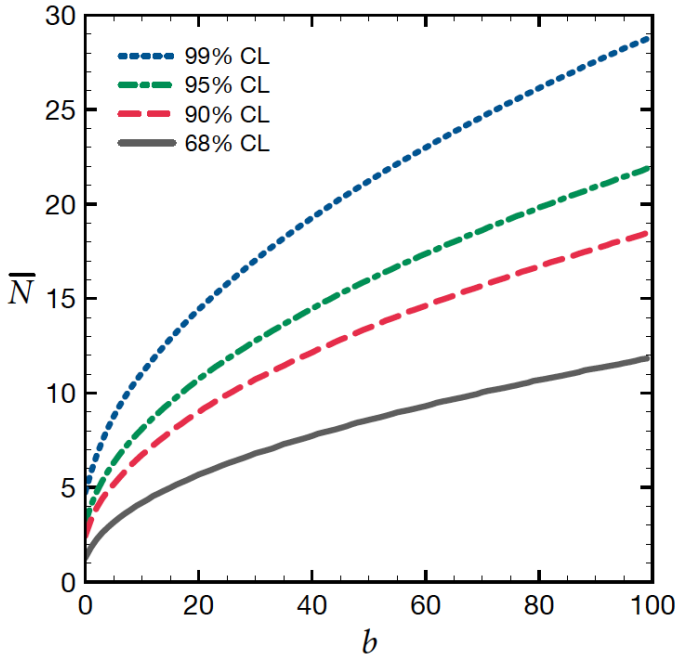


Figure 2.2: Sensitivity curves as a function of background b for different confidence levels CL. From [63].

effective Majorana mass $m_{\beta\beta}$. From (2.1) and (1.140) we obtain

$$m_{\beta\beta} = K\sqrt{\frac{N}{\epsilon\, M\, t}}, \quad \text{with} \quad K = m_e\left[\log 2\,\frac{N_A}{W}\,G^N_{0\nu}|M^N_{0\nu}|^2\right]^{-1/2} \tag{2.9}$$

Accordingly, the sensitivity to $m_{\beta\beta}$ is given by

$$\text{null background: } S(m_{\beta\beta}) = K\sqrt{\frac{s_{up}(0;0,\text{CL})}{\epsilon\, M\, t}} \tag{2.10}$$

$$\text{large background: } S(m_{\beta\beta}) = K\sqrt{\frac{k_{\text{CL}}\sqrt{b}}{\epsilon\, M\, t}} \tag{2.11}$$

The mean value of background b is relative, in the sense that it depends on the running time t of the experiment and the energy resolution ΔE at $Q_{\beta\beta}$. We can conventionally define the background rate per unit mass and energy c such that

$$b = c \cdot M \cdot t \cdot \Delta E. \tag{2.12}$$

Therefore the sensitivity for an experiment with background (2.11) for a large enough exposure time reads

$$S(m_{\beta\beta}) = K\sqrt{k_{\text{CL}}}\sqrt{\frac{1}{\epsilon}}\left(\frac{c\,\Delta E}{M\, t}\right)^{1/4} \tag{2.13}$$

Note that in general our experimental sensitivity will improve for larger exposures $M \cdot t$. However the trend changes between having an hypothetical background free $\sim (M\, t)^{-1/2}$ and a realistic experiment with background $\sim (M\, t)^{-1/4}$. The design of a $0\nu\beta\beta$ experiment must carefully optimize the parameters in (2.13), as we will see in Section 2.3.

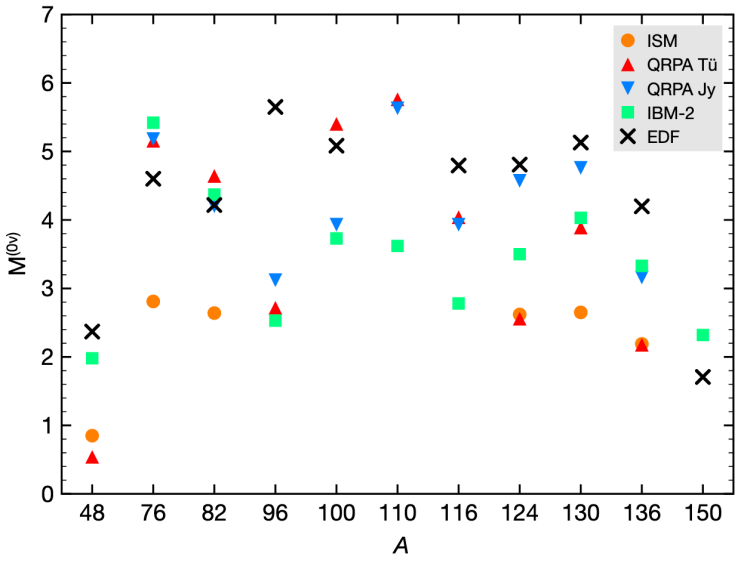


Figure 2.3: Nuclear matrix element for $0\nu\beta\beta$ decay candidates as a function of mass number A from several nuclear models. From [63].

2.3. Design of a double beta decay experiment

Unless we could effectively remove the background rate, in principle it does not exist an optimal $0\nu\beta\beta$ experiment. The sensitivity of a realistic experiment is given by (2.13), in which several factors are involved. As we will see below, these factors are not independent and they ultimately rely on the choice of the experimental technique.

2.3.1. Choice of isotope

There are thirty-five possible $\beta\beta$ emitters in nature, of which twelve have known two neutrino mode half-lifes, listed in Table 2.1. Nine of them are or have being used in $0\nu\beta\beta$ experiments. There are some relevant features to consider for the choice of isotope in $0\nu\beta\beta$ experimental design. Recall that the half-life in (1.140) is composed by three factors. Two of them depend on the isotope, the phase space factor $G^N_{0\nu}$ and the nuclear matrix element $M^N_{0\nu}$. The PSF varies with $\propto Q^5_{\beta\beta}$ [45]. On the other hand, even though NME depend on the particular nuclear model used on the computation (see Figure 2.3), their value does not change much between different isotopes. For isotopes above $A = 48$ (^{48}Ca), the maximum variation could be ~ 2. This is large for precise computations on the parameter of interest $m_{\beta\beta}$, but does not dominate over the PSF dependence on the $Q_{\beta\beta}$. For a factor ~ 2 change in the $Q_{\beta\beta}$, the rate would be $\sim 2^5$ larger. In fact isotopes used in $0\nu\beta\beta$ experiments have $Q_{\beta\beta} \gtrsim 2$ MeV, which is roughly a factor of 2 larger from other existing $\beta\beta$ candidates.

The suppression of the intrinsic background from the two-neutrino mode also depends on $Q_{\beta\beta}$ through [64]

$$\frac{s}{b} \propto \left(\frac{Q_{\beta\beta}}{\Delta E}\right)^6 \frac{T^{2\nu}_{1/2}}{T^{0\nu}_{1/2}}. \tag{2.14}$$

USC UNIVERSIDADE DE SANTIAGO DE COMPOSTELA

Therefore large $Q_{\beta\beta}$ is preferred. Of course this suppression will ultimately depend also on the energy resolution at *region of interest* (ROI) and the half-life of the two-neutrino

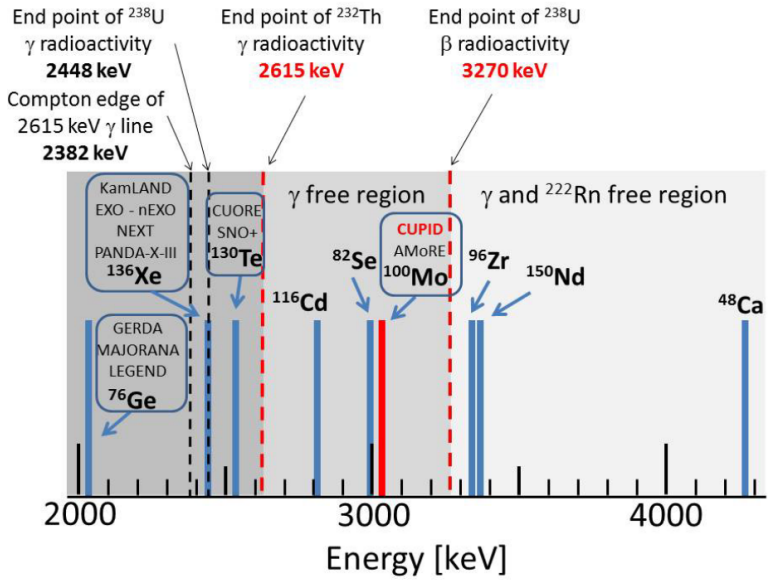


Figure 2.4: Positions of $Q_{\beta\beta}$ values and background contamination for double beta candidates. From [65], courtesy of the CUPID Collaboration.

mode. Worse energy resolution will include 2ν events from the tail of the continuous spectra in the $Q_{\beta\beta}$ peak. Higher $T^{2\nu}_{1/2}$ are preferably, but this intrinsic contamination will also depend on the particular shape of the spectra near $Q_{\beta\beta}$. Nevertheless the main sources of background will come from primordial isotope chains. To avoid them, the $Q_{\beta\beta}$ must be larger than $\sim$3.3 MeV (see Subsection 2.3.2). This is only satisfied by ^{48}Ca and ^{96}Zr (see Table 2.1), but unfortunately they can not be easily enriched (see Subsection 2.3.4).

2.3.2. Backgrounds

The main challenge of $0\nu\beta\beta$ experiments is background contamination. Reducing and characterizing the backgrounds is a must. The main background contribution comes from the natural decay series of ^{238}U and ^{232}Th, present in detector materials and laboratory surroundings. Even though their half-lifes are comparable to the age of the universe, they are very short in comparison with the $\beta\beta$ half-lifes. The beta decays of the chain products ^{214}Bi and ^{208}Tl are specially relevant due to their high Q-value (3.27 MeV and 4.99 MeV, respectively) and their prompt internal conversion after the β emission which can mimic two electron $\beta\beta$ signals. Background energy spectrum depends on the particular detector arrangement, but in general it consists of an exponential drop until the 2614 keV gamma line of ^{208}Tl from the ^{232}Th chain. Most $Q_{\beta\beta}$ values lie close to this peak (see Figure 2.4). Traces of U and Th are also present in the laboratory walls, whose gamma radiation can reach the active volume. Also ^{222}Rn and ^{220}Rn emanating from the walls can diffuse through detector components, with their subsequent progeny. These external backgrounds are commonly reduced through a two or three layer shielding. An external shielding with high atomic number like lead or iron absorbs the gamma radiation. The next layer is usually copper, used by its intrinsic radiopurity, that shields against the lead layer. Lastly a low atomic number layer protects against neutrons. Contributions from Rn can be greatly reduced by flushing the detector surroundings with clean air.

Besides terrestial backgrounds we have cosmogenic radiation. Detectors are placed in underground laboratories to reduce the flux of cosmic muons. Muons can interact in the detector medium and produce a signal. In tracking detectors those are easily identified by the linear tracks crossing the detector. Also a surrounding veto system can be used to identify them by coincident signals. Muon interaction in laboratory walls also produce neutrons and electromagnetic cascades. Gammas and neutrons produced in the rocks can be absorbed by an external shielding. Neutrons are specially problematic since they can activate detector materials or the detection medium itself. Solar neutrinos might also be relevant in future kilo-tonne scale scintillation detectors, since they can produce electrons in the MeV scale through neutrino-electron scattering.

2.3.3. Efficiency

The signal detection efficiency is determined by the particular experimental technique and detector geometry. It is a relevant relevant factor in experiments with background since from (2.13), halving the efficiency would require four times the exposure. Higher efficiencies are obtained in calorimetric experiments, reaching values around 90%. In principle detectors using the $\beta\beta$ isotope as detector medium are also more efficient because of the higher geometrical acceptance.

Tracking experiments identify the signal candidates using a two-electron cut based on some topological discrimination observable. For example in EXO-200 two-electron candidates are selected by requiring that the event is not splitted in multiple energy depositions. This observable, namely the number separated of depositions per event, is discontinuous. However the variable could also be continuous as in NEXT (see Chapter 3). The signal efficiency and background rate will depend on the value of this discrimination observable. If we relax the value of the discriminator, we will be accepting more events of both types, signal and background. On the other hand, a tighter cut would reduce the background but also the signal candidates. Then we can ask which is the optimal value of the discriminator. From (2.11), the highest sensitivity is achieved when the ratio $\epsilon/\sqrt{b}$ is maximum.

2.3.4. Exposure

The exposure is defined as the product of the total isotopic mass M and the running time t. The sensitivity scales with $(M \cdot t)^{-1/4}$ for an experiment with background. As we will see, most of the experimental techniques are designed to allow scaling. Larger detector volumes might worsen the background, which in part can be mitigated with a tighter fiducialization. The next generation of experiments would require ~ 1000 kg of isotope mass which is challenging for some isotopes. Achieving higher masses not only relies on the technique suitability to scaling, but the particular choice of isotope. Depending on the availability and the enrichment process some isotopes could be harder to deploy. Except Ca the $\beta\beta$ elements are very rare, but ^{48}Ca isotopical abundance is low and difficult to enrich. The most advanced and cheaper enrichment technique is the well known gas centrifugation, which can only be used [66] if a stable hexafluoride compound exists for the element in question (e.g, SeF_6). The gas compound is fed into an high speed spinning vessel which makes heavier compound to move closer to the walls. Heating the lower edge also establishes a temperature

Table 2.2: Summary of the results and parameters of the main $0\nu\beta\beta$ searches. Values are taken from references in text. It is worth noting that both signal efficiencies and exposures are reported with respect to the fiducial selection. Final KamLAND-Zen background rate is not explicitly reported in reference.

Experiment	Isotope	Exposure (kg·yr)	ΔE (%)	ϵ_s (%)	Background (keV·kg·yr)$^{-1}$	$m_{\beta\beta}$ (meV)
GERDA [50]	^{76}Ge	127.2	0.15	90	$5.2\cdot10^{-4}$	79-180
CUORE [55]	^{130}Te	103.6	0.3	90	$1.38\cdot10^{-2}$	75-350
KamLAND-Zen [57]	^{136}Xe	970	10	100	-	36-156
EXO-200 [72]	^{136}Xe	234.1	2.7	96	$1.8\cdot10^{-3}$	93-286

gradient that push heavier compounds to the bottom. This method can be used to enrich the $\beta\beta$ isotopes: ^{100}Mo, ^{82}Se, ^{116}Cd, ^{130}Te and ^{124}Sn. Of course, ^{136}Xe being a noble gas do not form a hexafluoride compound but can also be enriched with this technology. In all cases, above 90% enrichment is achievable. For ^{48}Ca, ^{150}Nd and ^{96}Zr affordable enrichment techniques are still under investigation.

2.4. Experimental program

Double beta decay searches started in the 50s [67]. The first experiments were geochemical, radiochemical and counting experiments with half-life sentitivities around $10^{12}-10^{15}$ years [39], where no distinction between 0ν and 2ν modes could be made. The interest in $0\nu\beta\beta$ declined after the discovery of parity violation in weak interactions and the confirmation of the so-thought fixed neutrino helicity. However the development of GUTs allowed the possibility that lepton number is conserved at lower energies attracted again the attention in neutrinoless double beta decay. Finally with the discovery of neutrino oscillations (Section 1.5), $0\nu\beta\beta$ search interest upraised due to the massive nature of neutrinos.

The first modern $0\nu\beta\beta$ experiments were Heidelberg-Moscow (HM) [68] and IGEX [69], both using high purity ^{76}Ge semiconductor detectors (HPGe). Particularly controversial is the case of HM experiment that operated during the period of 1990-2003 with 11 kg of ^{76}Ge at *Laboratori Nazionali del Gran Sasso* (LNGS), Italy. After several reanalysis they claimed a $\sim 6\sigma$ significance for $0\nu\beta\beta$ [70]. Their measurement of $T^{0\nu}_{1/2} \sim 2.23\cdot10^{25}$ years could not be confirmed by subsequent experiments. The current limit to ^{76}Ge by GERDA [50] is more stringent (Table 2.1) and also KamLAND-Zen reported a 97.5% CL rejection for the claimed half-life in the light Majorana neutrino exchange model [71]. In what follows we review the current experimental techniques used in $0\nu\beta\beta$ searches and some future proposals.

USC UNIVERSIDADE DE SANTIAGO DE COMPOSTELA

2.4.1. Semiconductors

This technology constitutes the first approach to $0\nu\beta\beta$ searches. The high purity ^{76}Ge-enriched (HPGe) detectors rely on the semiconductor working principle of hole-



Figure 2.5: Representation of GERDA experimental setup and platform. From [74].

pair creation. They are well known and commercially available detectors since are commonly used in γ-spectroscopy. They are very clean detectors as impurities are removed in the fabrication process, and can also be enriched in ^{76}Ge, making them suitable to be used in the isotope-as-detector-medium configuration. The key feature of HPGe detectors is their excellent energy resolution around $\sim 0.1\%$ FWHM. Experiments using this technology were GERDA [50] and MAJORANA DEMONSTRATOR [73]. Actually both collaborations merged to form LEGEND, which is under construction. The more stringent bound on $T^{0\nu}_{1/2}$ was provided by GERDA, that we briefly discuss below.

GERDA and LEGEND

GERDA (*Germanium Detector Array*) ran between Dec 2015 to Nov 2019 in *Laboratori Nazionali del Gran Sasso* (LNGS), Italy, where the muon flux is reduced 6 orders of magnitude. It consists of an array of HPGe detectors inside a 64 m^3 vessel filed with liquid Ar (LAr) acting as a cryostat (Figure 2.5). The inner vessel is inside a purified water tank of 590 m^3 covered with PMTs that used as muon veto. Both water and LAr also shield against natural radioactivity and muon induced neutrons from cave walls. A total of 41 HPGe detectors were used with an enrichment of $\sim 87\%$ in ^{76}Ge, leading to a total mass of 44.2 kg in the last running phase. The detectors are assembled in seven strings and placed inside a nylon cylinder to avoid ^{42}K beta background coming from ^{24}Ar long-lived isotope, which lies above ^{76}Ge $Q_{\beta\beta}$. GERDA achieved an excellent resolution of $\Delta E \sim 0.15\%$ FWHM at $Q_{\beta\beta}$, a signal efficiency of $\epsilon \sim 0.9$, a background rate of $c \sim 5.2 \cdot 10^{-4}$ counts/(keV$\cdot$kg$\cdot$yr) and a total exposure of 127.2 years (see Figure 2.6). Background is rejected via pulse shape discrimination for multi-site and surface events. No evidence for $0\nu\beta\beta$ was obtained, achieving the upper limit of $T^{0\nu}_{1/2} > 1.8 \cdot 10^{26}$ years at 90% CL. This translates in the $m_{\beta\beta} < 79-180$ meV lower limit, assuming light Majorana neutrino exchange.

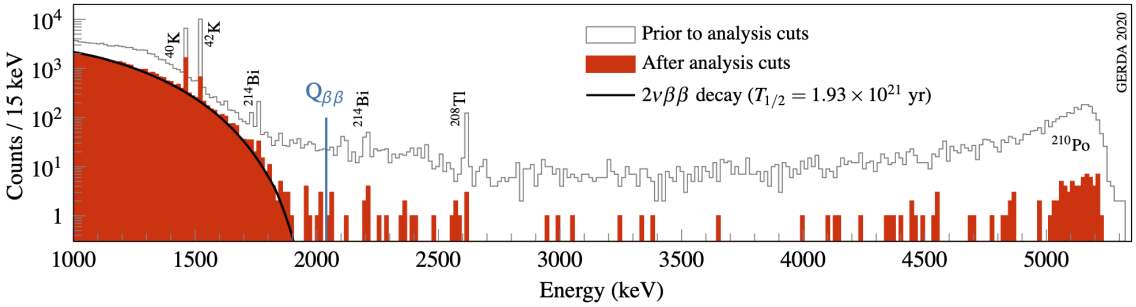


Figure 2.6: GERDA final energy spectra clearly showing the 2ν mode and the excellent background reduction in the ROI around $Q_{\beta\beta}$ after a 127.2 kg·year exposure. From [50].

GERDA infrastructure has already been dismounted to be replaced by its next generation experiment LEGEND-200 [75]. This is a joined collaboration between GERDA and MAJORANA, that will combine its strengths, namely the background shielding and veto system of GERDA and material ultra-purity of MAJORANA DEMONSTRATOR. It is the first phase of the so-planned ^{76}Ge tonne scale experiment LEGEND, with a claimed half-life discovery potential in the 10^{28} years, corresponding to a $m_{\beta\beta}$ in $15-50$ meV, fully covering the inverted ordering region.

2.4.2. Bolometers

Bolometers are calorimeters working at very low temperatures $\sim 10-20$ mK. Similarly as semiconductor experiments, the detector material crystallization process confer them a very low radioactivity from impurities. They can be produced with several $\beta\beta$ isotopes [76]: $^{130}TeO_2$, $^{116}CdWO_4$, $Li_2^{100}MoO_4$, $Ca^{100}MoO_4$, $Zn^{100}MoO_4$, $Pb^{100}MoO_4$ and $Zn^{82}Sn$. An energy deposition of $\sim$ 1 MeV rises the detector temperature by ~ 0.1 mK, which is registered by ultra sensitive thermometers. The thermometers can use several technologies, being the most common the neutron transmutation doped Ge or Si (NTD). However, in the future other technologies could be used like transition edge sensors (TED) and kinetic inductance detectors (KID). Bolometers achieve excellent energy resolutions $\sim 0.15-0.4\%$ FWHM. The main inconvenient of bolometers compared to semiconductor experiments is the technical challenge of reaching ultra-low temperatures. Double beta experiments of this type are CUORE [55], that will be upgraded to CUPID [65], and AMoRE [77].

CUORE and CUPID

CUORE (*Cryogenic Underground Observatory for Rare Events*), the upgraded version of CUORICINO, is a tonne-scale detector located in LNGS that search $0\nu\beta\beta$ in ^{130}Te. It consists (Figure 2.7) of an array of 988 TeO_2 crystals working at cryogenic temperature ~ 10 mK. The crystals are cubes of $5\times5\times5$ cm^3 of 750 g mass and are arranged in 19 towers instrumented with NTD thermometers. It uses unenriched ^{130}Te taking advantage of its relatively high isotopic abundance, which is the highest among $0\nu\beta\beta$ candidates (Table 2.1), achieving a total isotopic mass of $M \simeq 230$ kg. The cryostat shields the detector from natural gamma radioactivity and is cooled by a ^{3}He/^{4}He dilution refrigerator. Events with unphysical or noisy waveforms are rejected through pulse shape analysis. The total efficiency is of $\epsilon \simeq 0.87$ and the resolution $\Delta E \simeq 0.3\%$

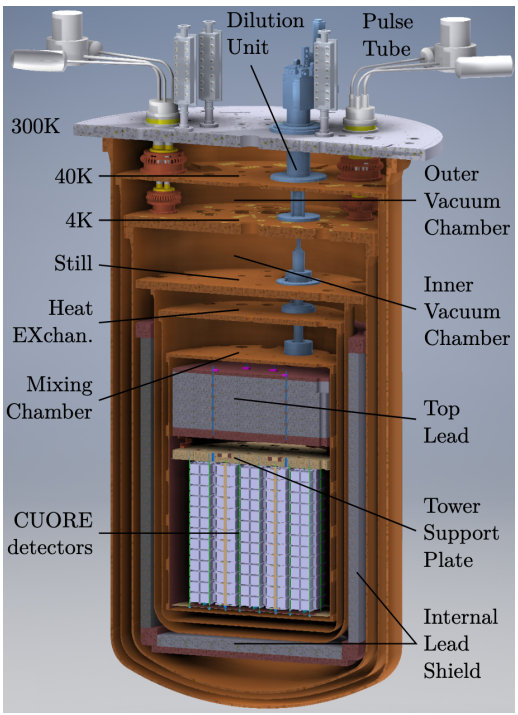


Figure 2.7: Representation of CUORE cryostat and detectors. From [65], courtesy of the CUPID Collaboration.

FWHM at $Q_{\beta\beta}$. The last reported result [55] shows a background rate of $c \simeq 1.38 \cdot 10^{-2}$ counts/(keV$\cdot$kg$\cdot$yr), achieving the upper limit of $T^{0\nu}_{1/2} > 3.2 \cdot 10^{25}$ years at 90% CL, corresponding to a $m_{\beta\beta} < 75-350$ meV assuming light Majorana neutrino exchange. CUORE measures the total energy of the interactions but it does not have a method for particle identification, thus background events, mainly coming from degraded alphas, can not be removed in the analysis.

CUPID (*CUORE Upgrade with Particle IDentification*) will reuse the cryogenic infrastructure of CUORE in LNGS. It will consist of an array of 1534 Li_2Mo0_4 crystals with ^{100}Mo enrichment higher than 95%. Each crystal weights 308 g, accounting for a total isotopic mass of 253 kg. Particle ID will be possible through the measurement of the Cherenkov and scintillation light of alpha backgrounds. This light will be measured with a thin Ge wafer layer acting as an absorber and facing the crystal detector. Both detectors will be instrumented with a NDT thermometer, nevertheless the possibility of using a TED or KID is under discussion due to the better signal to noise ratio. Using this new technique of active background discrimination, its rate is expected to be reduced two orders of magnitude $c \sim 10^{-4}$counts/(keV$\cdot$kg$\cdot$y) in the ^{100}Mo ROI. Expected efficiency and energy resolution is similar to CUORE, allowing the exploration of the inverted ordering region up to $m_{\beta\beta} < 10$ meV.

2.4.3. Time projection chambers

TPC (*Time Projection Chamber*) measures both scintillation and ionization signals. This allows a 3D-reconstruction of the event, whose topological or positional variables can be used to perform active background rejection. Also the scintillation-to-ionization ratio can be used as alpha discriminator. From now, just single-phase xenon

TPCs are being used in $0\nu\beta\beta$ searches. Since ^{136}Xe is gas at room temperature, high enrichment can be achieved at moderate costs. In general both gas or liquid phase detectors are well suited to scaling since they use an isotope-as-detector-medium configuration. Liquid-phase TPCs require a cryogenic system, and the higher density makes topological discrimination unfeasible due to larger scattering. On the other hand, gas-phase TPCs allows a full topological reconstruction and no cryogenic system is needed, but lower density requires greater detector volumes. Energy resolution is also better in gas-phase TPCs with $\Delta E \sim 0.7\%$ FWHM compared to $\Delta E \sim 1.2\%$ FWHM in liquid-phase. Liquid-phase xenon TPC has been used in EXO-200 [78] and its future successor nEXO [79], that will be briefly described below. Gaseous xenon TPCs are used in NEXT, whose description is left to Chapter 3, and PANDAX-III [80]. A planned dual-phase $0\nu\beta\beta$ experiment is DARWIN [81], in which liquid-phase is used as detector medium and a gas-phase to produce scintillation light from drifted ionization electrons.

EXO-200 and nEXO

EXO-200 (*Enriched Xenon Observatory*) detector was placed at the underground *Waste Isolation Pilot Plant* (WIPP), USA. It consisted of a cylindrical TPC with two grounded anodes at the extremes and one cathode at the center of the chamber filled with liquid xenon enriched at 80.6% in ^{136}Xe. The mass of LXe in the active volume is 110 kg of the total 200 kg available. Each drifting region has a length of $\sim$ 20 cm and radius $\sim$ 18 cm. The scintillation signal is read by two arrays of large area avalanche photodiodes (LAAPDs) at the extremes of the chamber. In front of them, two sets of crossed wireplanes read the charge of the ionization electrons. The wires are crossed in order to provide the transverse $x-y$ position of the event, that together with the scintillation signal provides a full three dimensional reconstruction. Besides the underground facility overburden, the detector (Figure 2.8) is surrounded with a passive shielding of $\sim$ 50 cm of HFE-700 cryofluid, $\sim$ 5.4 cm of copper and $\sim$ 25 cm of lead in all directions. Also an active muon veto allows the prompt identification of $>94\%$ of muons passing thought the detector. Events are reconstructed as single-site (SS) and multiple-site (MS) depending if they left a single or multiple energy depositions. Most of $0\nu\beta\beta$ candidates are SS and most of backgrounds are MS, allowing active background discrimination. Backgrounds from detector walls are effectively removed though fiducialization. The entire dataset results [72], with a total exposure of $M\cdot t \simeq 234.1$ kg$\cdot$yr, reports a signal efficiency of $\epsilon \simeq 97\%$ an energy resolution of $\Delta E \simeq 2.7\%$ FWHM at $Q_{\beta\beta}$ and background rate $c \simeq 1.8\cdot 10^{-3}$counts/(keV$\cdot$kg$\cdot$yr). The reported half-life at 90% CL is $T^{0\nu}_{1/2} > 3.5\cdot 10^{25}$ years, corresponding to a $m_{\beta\beta} < 93-286$ meV. The Phase II spectrum is shown in Figure 2.9.

nEXO is the successor of EXO-200. It is a planned five-ton single-phase LXe TPC with 90% enrichment in ^{136}Xe placed at SNOLAB. The overall design follows that of EXO-200 with the change to a single drift region. After 10 years of data taking, they expect a sensitivity of $T^{0\nu}_{1/2} \sim 9.2\cdot 10^{27}$ years, corresponding to a $m_{\beta\beta} \sim 5.7-17.7$ meV, allowing the full exploration of the inverted ordering region.

USC UNIVERSIDADE DE SANTIAGO DE COMPOSTELA

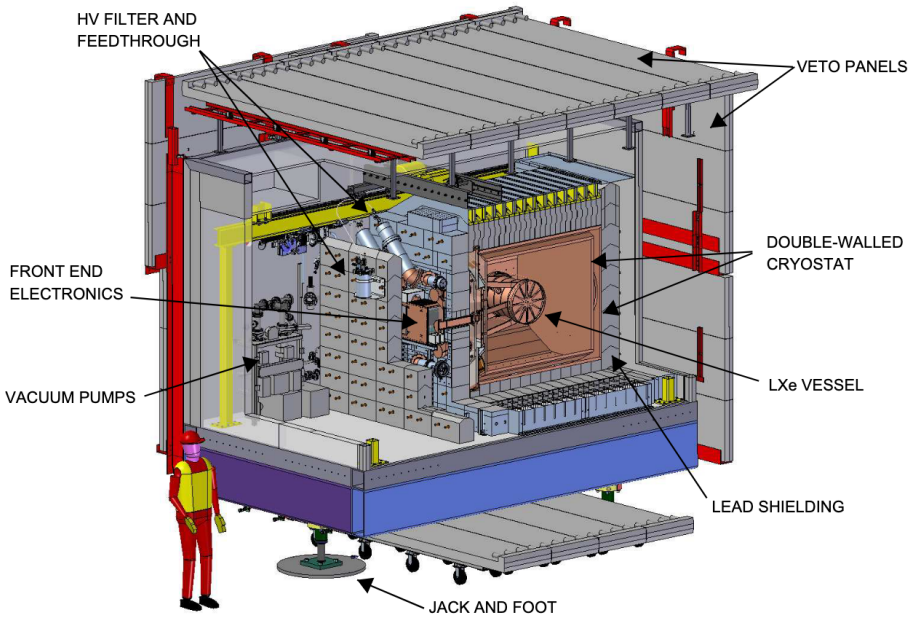


Figure 2.8: Representation of EXO-200 setup and shielding. From [78].

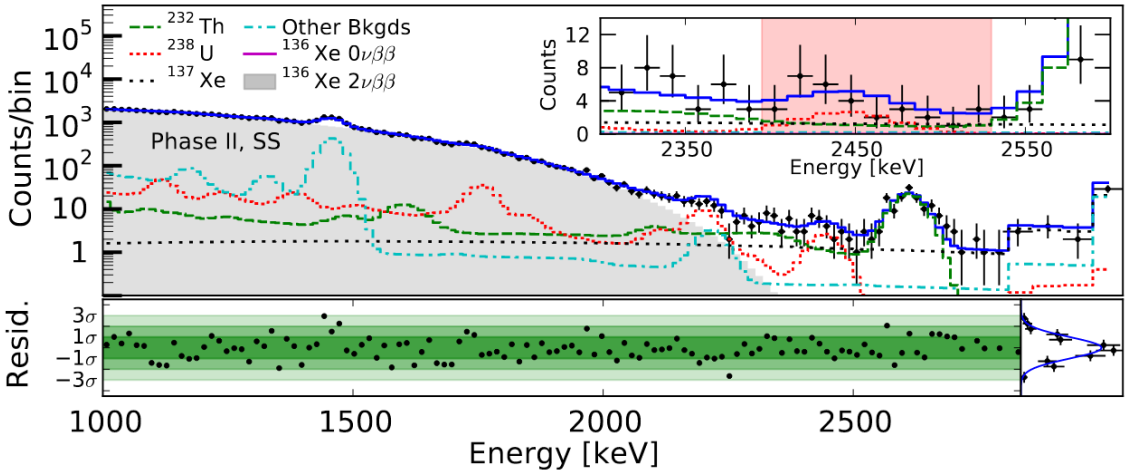


Figure 2.9: EXO-200 Phase II energy spectra with the different background contributions. From [72].

2.4.4. Scintillators

Scintillators are materials that emit de-excitation light in response to traversing radiation. This light is typically measured in photomultiplier tubes (PMTs), thus a wavelenght shifting medium is needed to convert the emitted light to the PMTs characteristic detection range. We can distinguish between organic liquid and inorganic solid scintillator experiments. The main advantage of liquid scintillator experiments is their scalability, in fact they use the infrastructures already provided by neutrino oscillation experiments. The experiments that use liquid scintillator as detector medium are KamLAND-Zen [57], SNO+ [82] and ZICOS [83]. Solar neutrinos scattering with atomic electrons constitute a relevant background in these large volume experiments. They could be vetoed through the directional correlation of Cherenkov light with Sun position for scattered electrons, and its higher intensity compared to scintillation light [84]. This would allow huge detector volumes as the 50 kilo-tonne THEIA detector [85].

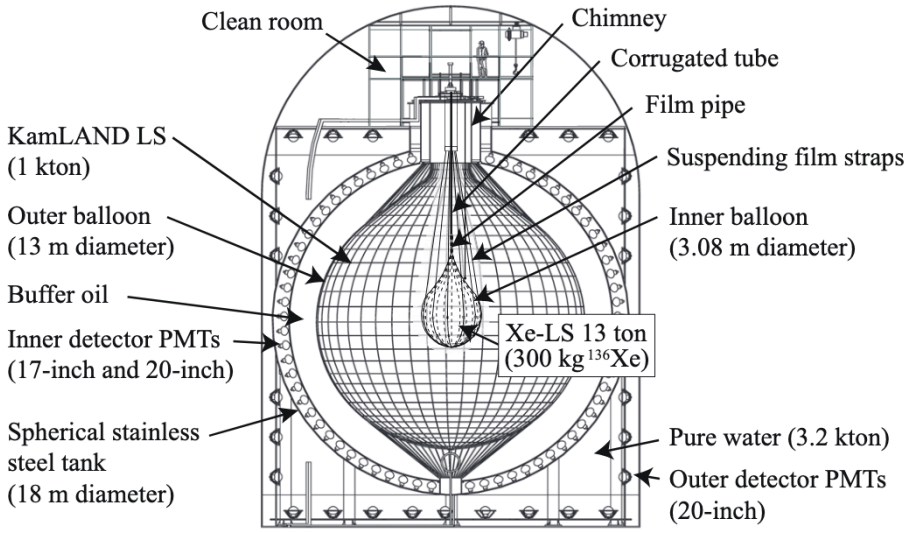


Figure 2.10: Representation of KamLAND-Zen detector. From [87].

Inorganic solid scintillators are used in ELEGANT-VI [49] and CANDLES-III [86]. Both use CaF_2 crystals in order to measure ^{48}Ca double beta decay. The advantage of this isotope is that its $Q_{\beta\beta}$ is well above the 2.6 MeV ^{208}Tl photo-peak greatly reducing the background in comparison of commonly used isotopes. However producing large quantities of ^{48}Ca is challenging due to its low relative abundance (Table 2.1).

KamLAND-Zen

KamLAND-Zen (*Kamioka Liquid scintillator Antineutrino Detector, Zero neutrino*) is a $0\nu\beta\beta$ experiment that uses the infrastructure of KamLAND neutrino oscillation experiment in Kamioka Observatory, Japan. It consists of two detectors as shown in Figure 2.10, the inner and outer detector. The cylindrical outer detector is filled with 3.2 kilo-tonnes of water acting as muon veto. The inner detector consists of an 18 m diameter spherical stainless steel vessel instrumented with 1325 PMTs and filled with no scintillating buffer oil. This vessel contains a 3.8 m diameter spherical inner ballon (IB) filled with 13 tons of Xe-loaded liquid scintillator (LS-Xe). The IB is constructed from a transparent nylon film of 25 μm thickness and placed at the center of the 13 m spherical outer ballon (OB) which is filled with an organic liquid scintillator (LS) acting as active background shield and wavelenght shifter. The LS-Xe consist of 2.91% of xenon enriched at 90% in ^{136}Xe, providing a total isotope mass of 745 kg. The scintillation light is collected by the PMTs in the inner detector. Using the time difference in signal the position of the event can be reconstructed.

The experiment ran in two phases. A first multi-phase between October 2011 to October 2015 and an upgraded phase with a higher isotopic mass between February 2019 to May 2021 (Figure 2.11). The total exposure was 970 kg·yr, achieving an energy resolution of $\sigma_E/E \simeq 4.3\%$ at $Q_{\beta\beta}$. It provided the best limit to the neutrinoless double beta decay up to date of $T^{0\nu}_{1/2} > 2.3 \cdot 10^{26}$ years at 90% CL corresponding to an effective Majorana mass of $m_{\beta\beta} < 36-156$ meV, constituting the first exploration of the inverted ordering region.

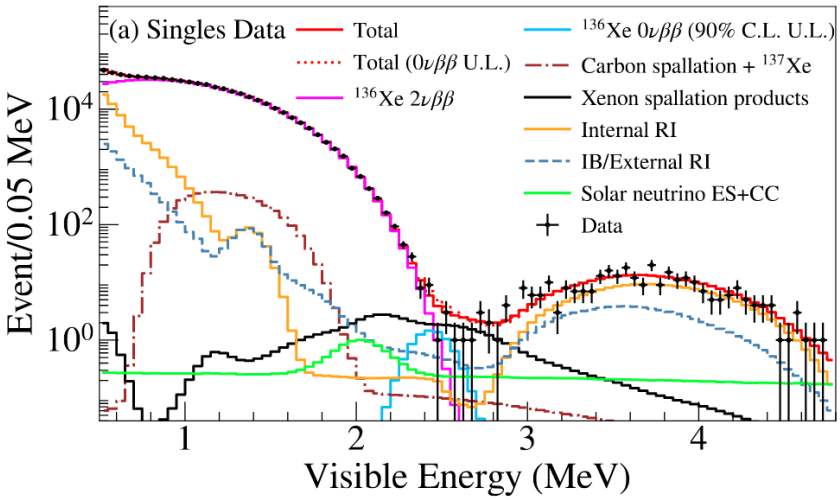


Figure 2.11: Energy spectra of the KamLAND-Zen experiment after 970 kg·yr exposure. From [57].

2.4.5. Tracking Calorimeters

The approach of this technology is highly focused on topological reconstruction. The source is a thin foil of material surrounded in both sides by two detection layers. The first layer is a low pressure gas tracking chamber which reconstructs the trajectory of the β particles. The external part is a calorimetric layer that measures the energy. The source foil can be substituted which allows the study of different $\beta\beta$ isotopes. The topological reconstruction allows active reduction of background with very high efficiency. However scaling is greatly disfavoured, requiring the construction of more or larger detection modules. This technology was used in NEMO-3 ([52], [54], [53], [58], [51]) experiment and planned for its successor SuperNEMO [88].

NEMO-3 and SuperNEMO

NEMO-III has stablished many of the double beta half-lifes known (Table 2.1). It was a cilindrical tracking calorimeter that ran during 2003 to 2011 in Laboratoire Souterrain de Modane (LSM), France. It consisted of a total of 20 sectors housing several $\beta\beta$ isotopes: ^{100}Mo (6.91 kg), ^{82}Se (0.93 kg), ^{130}Te (0.45 kg), ^{116}Cd (0.4 kg), ^{150}Nd (36.5 g), ^{96}Zr (9.4 g) and ^{48}Ca (7 g). The events are reconstructed by two 50 cm deep and 270 cm long wire tracking chambers surrounded the source foil. The chambers are filled with helium with ethanol quencher at 4% and Ar at 1% acting as geiger cells, with a transverse and longitudinal resolutions of 0.5 mm and 8 mm, respectively. Tracking chambers are surrounded by the calorimetric walls, which consists of polystyrene scintillator blocks coupled to low background PMTs that measure the total energy of the crossing particles. The energy resolution lies between $\sigma_E/E = (5.8-7.2)\%/\sqrt{E[\text{MeV}]}$ depending on the optical module and the time resolution is of 250 ps. The detector itself was surrounded by a soleneid generating a 25 G magnetic field which allows the rejection of 95 % of positrons at 1 MeV. The reported results for $\beta\beta$ decays are summarized in Table 2.1, with $m_{\beta\beta}$ upper limits well above the limits imposed by other experiments.

SuperNEMO is the next phase of the project with an expected sensitivity of 20^{26} years after 5 years of data taking with 100 kg of ^{82}Se.

USC
UNIVERSIDADE
DE SANTIAGO
DE COMPOSTELA

CHAPTER 3

The NEXT experiment

3.1. Introduction

NEXT (*Neutrino Experiment with a Xenon TPC*) [89] is an international collaboration searching neutrinoless double beta decay in ^{136}Xe. The main groups of the collaboration are from institutions in Spain and EEUU. It uses high pressure electroluminiscence xenon gas TPC technology featuring a good energy resolution and tracking that allows an active background discrimination.

The collaboration started the construction of NEXT-100 detector at the *Canfranc Underground Laboratory* (LSC) in 2021, and data taking is expected to start during 2023. NEXT-100 is the hundred-kilogram detector of the collaboration after NEXT-DBDM, NEXT-DEMO and NEXT-White. The main objective of this thesis is the study and estimation of the sensitivity of NEXT-100 to $0\nu\beta\beta$ (Chapter 6).

This Chapter is organized as follows. In Section 3.2 we describe features and benefits of xenon gas as detection medium, following Section 3.3 with the detection concept proposed by NEXT. Finally, Section 3.4 describes the NEXT detectors and its main results.

3.2. Gaseous xenon as detector medium

The study of noble gases as radiation detection medium has started in the 40s with the discovery of the electron conductivity induced by radiation in liquid argon [90]. The interest raised due to their suitability to detect high energy radiation with good energy resolution: high stopping power, small Fano factor and the relatively low energy required to excite and ionize gaseous atoms. Also their availability and easiness to purify make them good candidates to scalable detectors. In what follows we will focus on xenon, which is a particularly interesting detector medium due to the presence of $0\nu\beta\beta$ ^{136}Xe candidate among their isotopes (See Table 3.1).

3.2.1. Thermophysical properties

USC UNIVERSIDADE

Xenon ($Z = 54$) is a polarizable noble gas, thus a dipole moment is induced between nearby atoms, causing an attractive Van der Waals force which can empirically be

Table 3.1: Relative isotopic abundances of xenon. From [47].

Mass number	124	126	128	129	130	131	132	134	136
Abundance (%)	0.0095	0.009	1.9	26.4	4.1	21.2	26.9	10.4	8.9

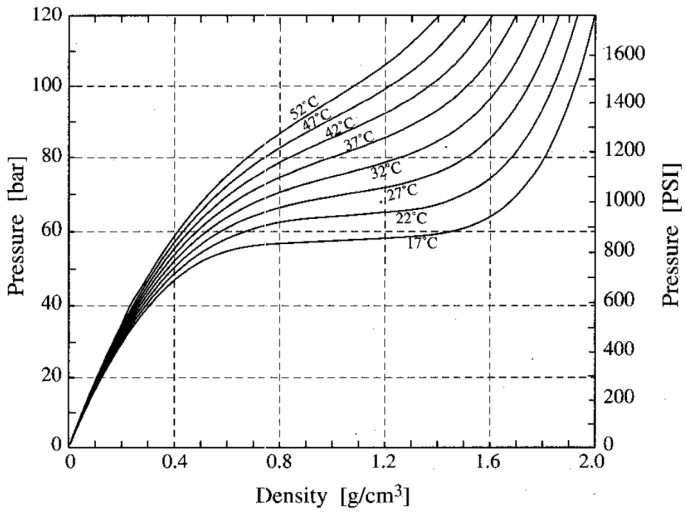


Figure 3.1: Isotherms for xenon gas. From [92] ©1998 IEEE.

described by the Lennard-Jones potential [91]

$$U(r) = k_B 4\epsilon \left[\left(\frac{\sigma}{r} \right)^{12} - \left(\frac{\sigma}{r} \right)^{6} \right] \tag{3.1}$$

where r represents the inter-molecular distance. For xenon, the parameters are $\epsilon = 221$ K and $\sigma = 4.055$ Å, obtained from the second coefficient in the virial expansion. In general a fluid at relative low densities can be described by the virial expansion

$$\frac{p}{\rho k_B T} = 1 + B(T)\rho + C(T)\rho^2 + \ldots \tag{3.2}$$

which accounts for gas deviations from ideal behaviour. Isotherms for xenon gas are shown in Figure 3.1. In what follows we will be interested in the pressure regime of $p \sim 8-20$ bar in which deviations from ideal gas law are still negligible.

3.2.2. Energy loss

Radiation is measured by the signal induced on a detector medium. In what follows we are interested in the signal induced by charged and γ radiation in gaseous xenon in the ideal regimen $\rho \sim 0.1\ g/cm^3$. In the discussion above we assume radiation energies below a few MeV, the energy scale of neutrinoless double beta decay experiments.

Photons can deposit their energy in a detection medium via *photoelectric effect*, *Compton scattering* and *pair production*. Photoelectric interaction produce an electron with the energy of the impinging gamma (neglecting the small work function). Compton scattering shares the initial energy between the output electron and photon which can again subsequently interact in the medium or escape and remain undetected. If the ejected electron from photoelectric or Compton interactions comes from a tightly bound inner shell, the xenon atom is left in an excited state which will decay

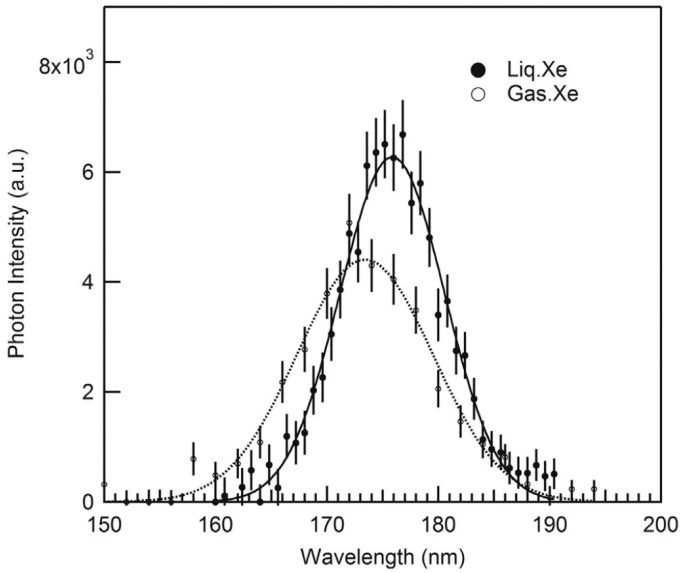


Figure 3.2: Scintillation light wavelength spectra of gaseous and liquid xenon. From [93].

through a characteristic x-ray. For xenon we distinguish two characteristic x-rays with energies around 30 keV (K-shell) and 5 keV (L-shell). Those rays may subsequently interact via photoelectric or Compton scattering. Lastly, if photon energy is above two times the electron mass ($2m_e = 1.022$ MeV), pair production $\gamma \rightarrow e^- e^+$ is allowed and energy is shared between both particles. The positron will recombine with an electron from a xenon atom after lossing its initial energy producing two annihilation photons of $m_e = 0.511$ MeV. Both, one or none of this gammas may subsequently interact in detection medium.

Charged particles deposit their energy in xenon via *scintillation* and *ionization*. For reasons that will become clear later, we denote the scintillation signal as S1 and the ionization signal as S2. Typical charged particles are electrons from β decays or produced by a gamma interaction, but could also be α particles and cosmic muons. They leave a track in gaseous xenon by transfering their initial energy to the xenon atoms. Depending on the interaction channel they produce S1 or S2 signals.

Scintillation (S1) is produced when the charged particle excites a xenon atom. The light is not the product of the direct de-excitation of the atom, but it involves the formation of an excited dimer [93]

$$\begin{aligned} \text{Excitation:} \quad & q + \text{Xe} \rightarrow \text{Xe}^* + q, \\ \text{Dimerization:} \quad & \text{Xe}^* + 2\text{Xe} \rightarrow \text{Xe} + \text{Xe}_2^* \\ \text{De-excitation:} \quad & \text{Xe}_2^* \rightarrow 2\text{Xe} + h\nu\,(\text{VUV}) \end{aligned}$$

where q represents the charge particle and $h\nu$ the emitted VUV (vacuum ultra-violet) photon. For xenon gas at pressures greater that 0.4 bar, the triple xenon collision in the dimer formation occurs in a time scale of picoseconds after the excitation [94]. The wavelength spectra for scintillation photons is shown in Figure 3.2, peaking at ~ 175 nm. Another scintillation channel by which scintillation light can be produced is *recombination*. This process involves ionization an dimer formation. First a charged particle ionizes xenon to produce ions and ionization electrons. The ion becomes a charged dimer that can be annihilated by an ionization electron, producing a dimer

excited state that also decays,

$$\begin{aligned}
\text{Ionization:} &\quad q + \mathrm{Xe} \rightarrow \mathrm{Xe}^{+} + e^{-} + q \\
\text{Dimerization:} &\quad \mathrm{Xe}^{+} + 2\mathrm{Xe} \rightarrow \mathrm{Xe} + \mathrm{Xe}_2^{+} \\
\text{Recombination:} &\quad \mathrm{Xe}_2^{+} + e^{-} \rightarrow \mathrm{Xe} + \mathrm{Xe}^{**} \\
\text{Dimerization:} &\quad \mathrm{Xe}^{**} + 2\mathrm{Xe} \rightarrow \mathrm{Xe} + \mathrm{Xe}_2^{**} \\
\text{De-excitation:} &\quad \mathrm{Xe}_2^{**} + \mathrm{Xe} \rightarrow 2\mathrm{Xe} + \mathrm{Xe}^{*} \\
\text{Dimerization:} &\quad \mathrm{Xe}^{*} + 2\mathrm{Xe} \rightarrow \mathrm{Xe} + \mathrm{Xe}_2^{*} \\
\text{De-excitation:} &\quad \mathrm{Xe}_2^{*} \rightarrow 2\mathrm{Xe} + h\nu\,(\mathrm{VUV}).
\end{aligned}$$

Scintillation is characterized by the mean energy required to produce a scintillation photon, denoted W_{sc}. This quantity is commonly reported as if no external field is present in the gas region to neglect recombination. Nevertheless, current measurements of this quantity are inconsistent and may vary between $W_{sc} = 30-120$ eV, [95]. The differences are still not understood and partially attributed to different gas density and drift field conditions. Note that the definition of W_{sc} differs from the characteristic first excitation level of xenon of 8.3 eV, since deposited energy is distributed between scintillation and ionization.

Ionization (S2) is the process by which charged particles pull bound atomic electrons. Charged particles left an ionization track whose length would depend on xenon density an initial particle energy. The ionization track is composed by the inonization electrons e^{-} and Xe^{+} ion pairs. Recombination is avoided through an electric field. Due to a much larger mass, the Xe ion drift velocity is much slower than ionization electrons. Collection of ionization electrons provides a macroscopic signal proportional to the total energy of the ionizing charged particle. Ionization is characterized by the mean energy required to produce an ion pair, W_i. This value has been accurately measured to be around $W_i = 22$ eV [96], and is constant in the pressure range of interest of $p \sim 20$ bar at room temperature, where recombination effects are negligible due to the low densities. At larger densities $\rho \gtrsim 0.3\ g/\mathrm{cm}^3$ the value varies with both density and electric fields. Note the definition of W_i differs from that of ionization potential, I. The latter is the energy needed to extract an electron from the less energetic energy level ($I = 12.13$ eV in xenon), but W_i accounts for all the possible interaction processes of energy deposition of an ionizing particle in the medium under certain working conditions.

Explicitly we can write the total energy of the ionizing charged particle E to be shared among ionized N_i and excited N_{ex} atoms such

$$E = N_i \overline{E}_i + N_i \overline{\mathscr{E}} + N_{ex} \overline{E}_{ex} \tag{3.3}$$

where $\overline{E}_i$ is the mean energy spent in ionization and $\overline{E}_{ex}$ the mean energy spent in excitation. The energy spent in elastic scattering at energies below the ionization potential is represented by $\overline{\mathscr{E}}$, which is ultimately dissipated as heat. By definition, the ionization yield would be given by

$$W_i \equiv \frac{E}{N_i} = \overline{E}_i + \overline{\mathscr{E}} + \frac{N_{ex}}{N_i}\overline{E}_{ex}. \tag{3.4}$$

USC UNIVERSIDADE DE SANTIAGO DE COMPOSTELA

Equivalently the scintillation yield $W_{sc} \equiv E/N_{sc}$, where N_{sc} is the number of scintillation photons which is given by $N_{sc} = rN_i + N_{ex}$ with r the recombination fraction which would depend on the medium conditions, namely the density and drift field.

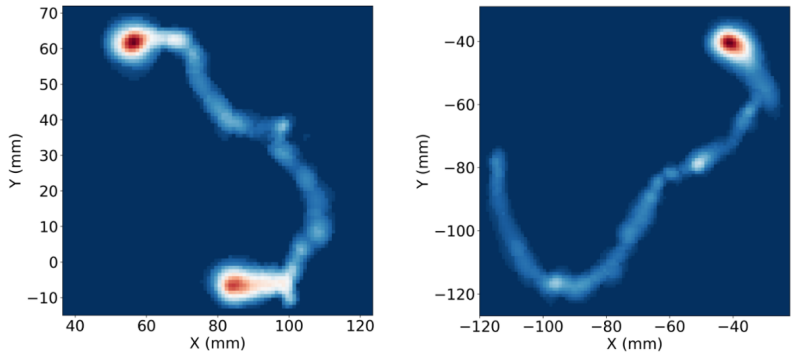


Figure 3.3: Double beta (left) and background (right) candidates in the 2 MeV energy region from NEXT-White data. We can identify the two Bragg peaks of the signal event (left), and only one in the background (right). From [97].

A very relevant feature of the energy transfer is its distribution throughout the electron trajectory as it slows down. This energy loss is commonly refered as the stopping power

$$S = -\frac{1}{\rho}\frac{\mathrm{d}E}{\mathrm{d}x} \tag{3.5}$$

where dE/dx is the energy loss by the travelling particle in a medium of density ρ. For our energies of interest below few MeV electrons the stopping power greatly increases at lower energies when electrons become no-relativistic, meaning that electrons loss a relatively large amount of energy at the end of the trajectory. This feature is the so-called Bragg peak, refered in NEXT as *blob*, which allows for double electron and single electron discrimination as shown in Figure 3.3.

3.2.3. Electroluminiscence

The process of *electroluminiscence* [98] occurs when electron produced through ionization acquire enough energy to excite but not ionize the gaseous Xe, namely for energies between the excitation energy of 8.3 eV and ionization potential of 12.13 eV. As we will see (§3.4) this mechanism is used in NEXT experiment to convert the ionization signal to a proportional optical measurable signal. Electroluminiscence signal is realized by the use of a strong electric field region to which ionized electrons arrive. Once electrons enter in the so-called EL region they acquire and loss energy several times during their travel to the anode, providing an uniform distributed depositions during their drift. The excited xenon atoms decay via the scintillation mechanism (Subsection 3.2.2). The number of total photons emitted by an ionization electron is given by the so-called EL gain, G_{EL}, or electroluminiscence yield. For example, for Xe at 8 bar the EL gain is given by

$$G_{EL} = 170 \cdot (E/p[\mathrm{kVcm^{-1}bar^{-1}}] - 0.75) \cdot p[\mathrm{bar}] \cdot d_{EL}[\mathrm{cm^{-1}}]. \tag{3.6}$$

It is important to note that the EL gain slope (here 170 $\mathrm{kVcm^{-2}}$ for 8 bar) on the reduced drift field E/p grows with the pressure p [98], a property still not understood. The mechanism of electroluminiscence is suited to detectors aiming excellent energy resolutions (Subsection 3.2.4), since it avoids the larger fluctuations of charge amplification in avalanche based detectors. The variance in the number of produced EL

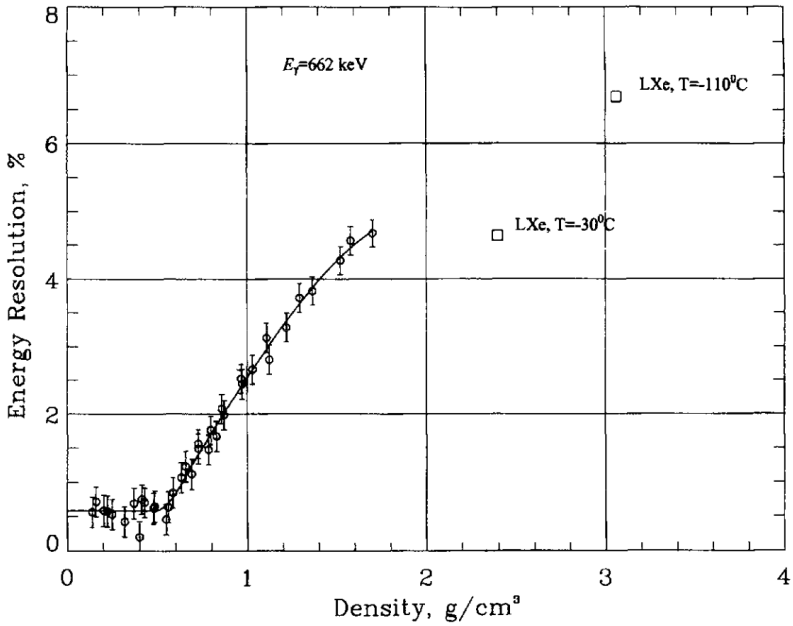


Figure 3.4: Intrinsic energy resolution in xenon as a function of density. The energy resolution is about ∼ 0.6% FWHM in the low density region, and greatly degrades for higher densities. From [100].

photons $N_{ph} = G_{EL} \cdot N_i$ is described by the *conde-policarpo factor* [99], J_{CP}

$$\sigma^2_{EL} = J_{CP} \cdot N_{ph}, \tag{3.7}$$

with values depending on the EL electric field and gas pressure. For the common working conditions of NEXT detectors this value is lower than unity.

3.2.4. Energy resolution

Energy resolution is a key factor to determine the suitability of your detector to a specific application involving some energy range of interest. It is ultimately determined by the processes involved in the detection, including the physical processes of scintillation and ionization, the amplification and the charge readout, the light and charge collection efficiency or the geometrical effects. In gaseous xenon in the ideal regimen the energy is measured from the deposited charge in the ionization since nearly 100% of collection efficiency can be achieved, whereas for scintillation light is of a few percent. A very relevant feature of xenon is its intrinsic energy resolution dependence with density, as shown in Figure 3.4. The resolution is very good ∼ 0.6% FWHM at low densities for $E = 662$ keV, but greatly degrades above $\rho \sim 0.55$ g/cm^3. This sharp behaviour is suggested to be related to a new deposition channel between δ-electron and xenon atom cluster collision. In any case, we are interested in the low density region where the resolution saturates. In this region the measured charge comes from the creation of electron-ion pairs through ionization collisions. The number N of such pairs is normally distributed with a variance given

$$\sigma^2_N = F \cdot N \tag{3.8}$$

where F is the *fano-factor*. For $F = 1$ we recover the Poisson statistics, but this value is commonly lower, for xenon under ideal regime conditions $F = 0.15$ [101].

USC UNIVERSIDADE DE SANTIAGO DE COMPOSTELA

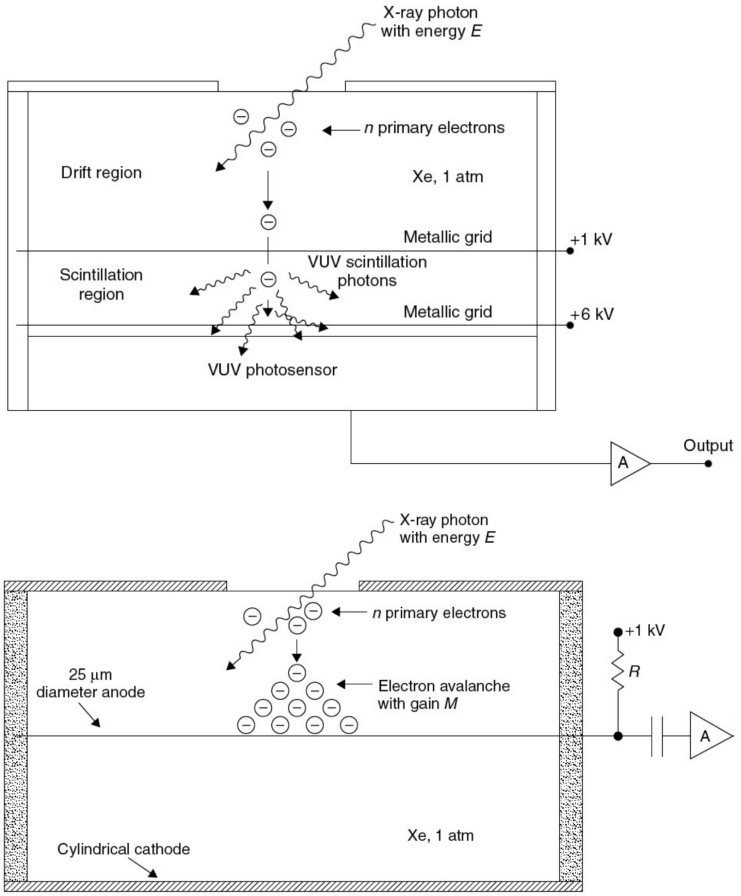


Figure 3.5: Different charge collection a approaches, a GPSC (top) and GPAC (bottom). From [102].

The energy resolution will ultimately rely on the charge collection method. We can distinguish between a *gas proportional scintillation counter* (GPSC) based on electroluminiscence amplification or a *gas proportional avalanche counter* (GPAC) based on avalanche amplification (see Figure 3.5). As we will see below, better energy resolutions can be achieved with the use of a GPSC. This is in fact the technology used in NEXT detectors (Section 3.3).

A detection process is composed by consecutive steps, each containing an input signal x_i and an output signal x_{i+1} with a probability distribution $G(x_{i+1}, x_i)$. Then the energy resolution after the $i+1$ process would be given by [103]

$$\left(\frac{\sigma_{i+1}}{\overline{x}_{i+1}}\right)^2 = \left(\frac{\sigma_{i+1}(\overline{x}_i)}{\overline{x}_{i+1}(\overline{x}_i)}\right)^2 + \left(\frac{\sigma_i}{\overline{x}_i}\right)^2. \tag{3.9}$$

We can study the energy resolution of a GPSC. The detection process consists of four steps $i = 0, 1, 2, 3$: production of ionization, electroluminiscence charge amplification, collection efficiency and sensor gain conversion.

• Production of ionization $i = 0$: this is the process by which an high energetic electron produces a number of ionization electrons $x_0 \equiv N_i$. If the total deposited energy, the mean number of electrons produced is given by (3.4) and their fluctuation

by (3.8). Then we can write:

$$\left(\frac{\sigma_0}{\overline{x}_0}\right)^2 \equiv \left(\frac{\sigma_{N_i}}{N_i}\right)^2 = \frac{F}{N_i} \tag{3.10}$$

• Electroluminiscence amplification $i=1$: assuming that all N_i electrons arrive at the EL region (ie neglecting attachment and recombination), the number of emitted photons is given by $N_{ph} = G_{EL} \cdot N_i$ and the fluctuation by (3.7), thus

$$\left(\frac{\sigma_1(\overline{x_0})}{\overline{x}_1(\overline{x}_0)}\right)^2 \equiv \left(\frac{\sigma_{EL}}{N_{ph}}\right)^2 = \frac{J_{CP}}{N_{ph}} = \frac{J_{CP}}{G_{EL}N_i} \tag{3.11}$$

• Collection efficiency ($i=2$): it is determined by the wavelength shifting process (xenon scintillation UV light must be converted to the sensor's detection range), the relative positions between the event position and sensor, and the sensor sensibility. We can simply model the collection efficiency by a binomial distribution of with probability ϵ, thus the collected photons will be given by $N'_{ph} = \epsilon \cdot N_{ph}$ with variance $\sigma^2_{N'_{ph}} = (1-\epsilon)N'_{ph}$. Then we obtain

$$\left(\frac{\sigma_2(\overline{x_1})}{\overline{x}_2(\overline{x}_1)}\right)^2 \equiv \left(\frac{\sigma_{N'_{ph}}}{N'_{ph}}\right)^2 = \frac{(1-\epsilon)}{N'_{ph}} = \frac{(1-\epsilon)}{\epsilon G_{EL}N_i} \tag{3.12}$$

• Sensor gain conversion ($i=3$): a single photon arriving a photo-multiplier (PMT) produces a charge response given by a number of photo-electrons (pes), the so-called SPE response. It is a characteristic response of the PMT, and we can assume that it is normally distributed with mean q and variance σ_q. For a number of arriving photons N'_{ph}, the total signal would be $Q = q \cdot N'_{ph}$ and variance $\sigma^2_Q = \sigma^2_q \cdot N'_{ph}$, thus

$$\left(\frac{\sigma_3(\overline{x_2})}{\overline{x}_3(\overline{x}_2)}\right)^2 \equiv \left(\frac{\sigma_Q}{Q}\right)^2 = \frac{1}{N'_{ph}} \cdot \left(\frac{\sigma_q}{q}\right)^2 = \frac{1}{\epsilon G_{EL}N_i} \cdot \left(\frac{\sigma_q}{q}\right)^2 \tag{3.13}$$

Finally we can plug in the previous equations in the general expression (3.9) to obtain the energy resolution of an electruminiscent GPSC to be

$$\frac{\sigma_E}{E} \equiv \frac{\sigma_3}{\overline{x}_3} = \sqrt{\frac{F}{N_i} + \frac{1}{N_i} \cdot \left(\frac{J_{CP}-1}{G_{EL}} + \frac{(\sigma_q/q)^2+1}{\epsilon G_{EL}}\right)} = \sqrt{\frac{F+G}{N_i}}. \tag{3.14}$$

The factor

$$G = \frac{J_{CP}-1}{G_{EL}} + \frac{(\sigma_q/q)^2+1}{\epsilon G_{EL}} \tag{3.15}$$

represents the fluctuation of energy resolution due the detection process. An intrinsic energy resolution is achieved when $G << F = 0.15$.

The first term in (3.15) is small, since $J_{CP} < 1$ for working conditions of interest in NEXT [99]. Typical values for modern PMTs lie in $(\sigma_q/q)^2 \sim 0.5$. Then the intrinsic energy resolution condition is fulfilled if $\epsilon G_{EL} >> 10$, ie that the number of detected photons per ionization electron to be considerably higher than 10. In such a limit the collection of ionization electrons is perfect and the resolution is only limited by

the physics of ion-pair creation in xenon. For the ^{136}Xe $Q_{\beta\beta} = 2458$ keV we obtain an intrinsic energy resolution for a high pressure xenon GPSC of

$$R|_{Q_{\beta\beta}} \equiv 2\sqrt{2\ln 2}\frac{\sigma_E}{E}\bigg|_{Q_{\beta\beta}} = 0.27\ \%, \tag{3.16}$$

a limit which could be achievable with a high enough electroluminiscence amplification factor.

In the case of an avalanche detector, the measured signal is proportional to the number of ionization electrons, namely $N_A = A \cdot N_i$ with variance $\sigma^2_{N_A} = \sigma^2_A \cdot N_i$ where σ_A is the variance of the factor A. Then the resolution factor in (3.15) would be given by $G = (\sigma_A/A)^2$. Values of G for avalanche detectors vary between 0.4-0.7 for amplification factors $> 10^2$ [104], significantly above the fano-factor F=0.15. Notice that in this simple analysis we have neglected the ionization electron's attachment by impurities and the multiplication of charge if the ionization electron adquires enough energy to ionize xenon atoms while drifting. A complete discussion including these effects can be found in [103].

3.3. The SOFT detection concept

As we have seen in previous Section 3.2, xenon can provide good energy resolution and active topological discrimination between signal and background. Both are essential features for a neutrinoless double beta decay experiment, together with the fact that ^{136}Xe being a $0\nu\beta\beta$ candidate makes it possible to built a *source as detection medium* experiment. The only missing piece of the design is the particular detection arrangement and technology. Since tracking is needed in order to reconstruct the electron paths, the natural choice would be a high pressure xenon *time projection chamber* (TPC). TPCs were invented by D. R. Nygren in the 70s [105], and nowadays are used in a large number of experiments in nuclear and high energy physics [106], as well as in rare-search experiments. The working principle of a TPC is simple. A high energetic charged particle losses its energy by ionizing the detection medium atoms, leaving an ionization track of ions and electrons. Through the application of an electric field, the released ionization electrons drift towards the anode and the positive ions toward the cathode. Since electrons are much lighter, their drift velocity is also much shorter. The electrons are collected in a planar instrumented surface, which allows the transverse reconstruction of the initial ionization track. For example a *multi wire proportional chamber* (MWPC) was initially used as charge collection plane. The longitudinal position can also be reconstructed through signal time differences. In the case of collision experiments the collision point is known thus longitudinal position is the difference between initial and final signal times, but in rare-searches experiments a trigger signal is needed, provided by scintillation.

The NEXT experiment TPC design is based on the *separated optimized function for tracking* (SOFT) concept [107]. The idea is achieving both good energy resolution and tracking capabilities with the combination of two asymmetrically instrumented sensor planes. As shown in Figure 3.6, the ionization electrons left by the high energetic particle are avoided to recombine by applying an electric field. They drift to the anode in which another high electric field region (red dotted) works as electroluminiscence amplification, the so-called EL region. The EL light is collected at both, the

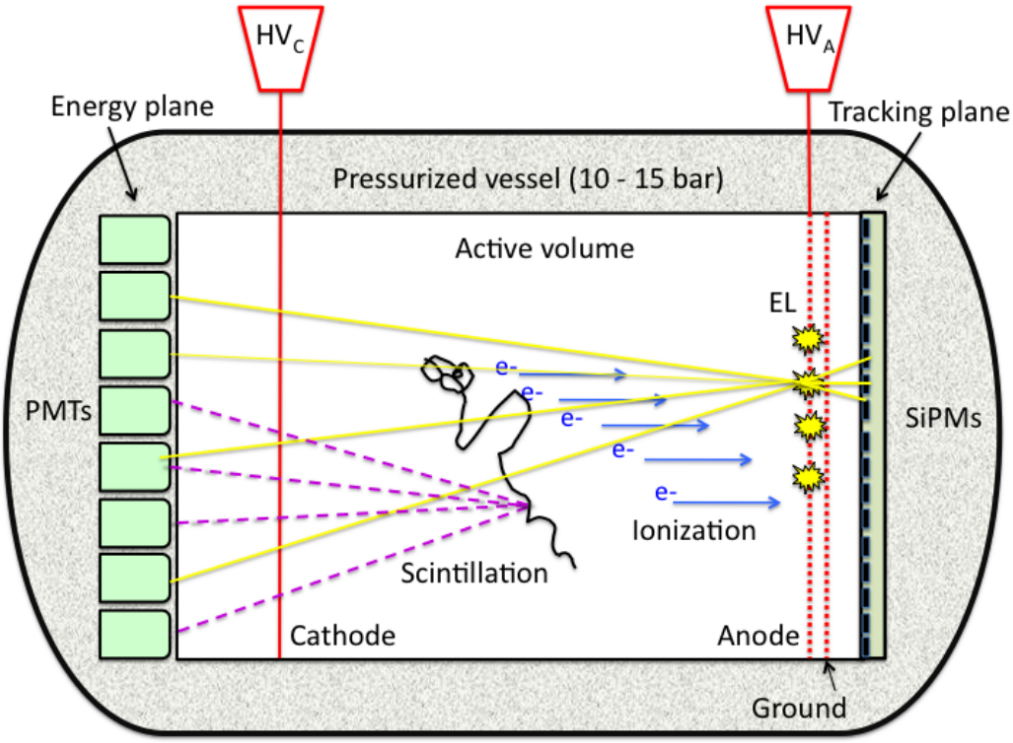


Figure 3.6: Schematic description of the SOFT concept. Scintillation (S1) signal is collected in the energy plane providing start of the event signal. Ionization electrons drift to the EL amplification region. The EL light (S2) is collected in both the energy and tracking planes. From [108].

tracking plane (TP) and the *energy plane* (EP). The tracking plane is instrumented by a dense array of small area and low gain *silicon photo-multipliers* (SIPMs) that allow the transverse reconstruction of the light emission point in the EL. In front of it, behind the cathode, the energy plane is instrumented with large area and high gain PMTs allowing an efficient light collection and providing a precise energy measurement. The collected EL photons constitute the so-called S2 signal. On the other hand, the prompt primary scintillation light, the so-called S1, is collected by the energy plane providing the start of the event reference time. The time difference between S1 and S2 signals allow the longitudinal reconstruction of the event.

3.4. NEXT detectors

The NEXT program is divided in several phases. The first period (2009-2014) was dedicated to R&D with the construction and operation of NEXT-DBDM and NEXT-DEMO detectors. Their objective was the demonstration of the SOFT detection concept and the prove of good energy resolution, also gaining technical experience to larger detectors. The second phase consisted in the construction and operation of a larger detector, NEXT-White (NEW), which operated during the period of (2016-2021) in *Laboratorio Subterráneo de Canfranc* (LSC). Its objective was to demonstrate the scalability of the detection concept while maintaining good energy resolution and the measurement of the $\beta\beta$ two-neutrino mode. The current phase consists in the construction of the NEXT-100 detector aimed to the search of neutrinoless double beta decay.

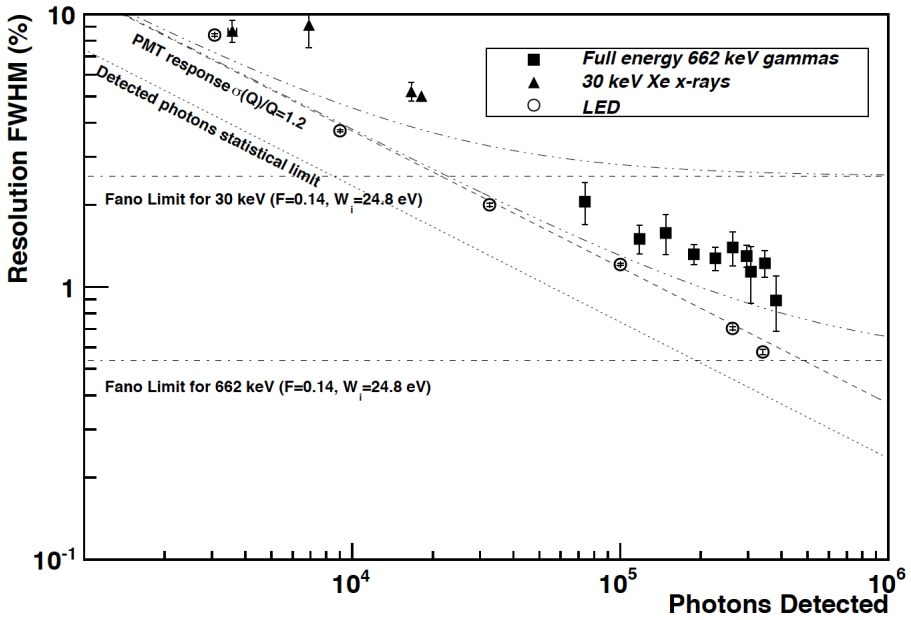


Figure 3.7: NEXT-DBDM near intrinsic energy resolution results. From [103].

3.4.1. R&D detectors

NEXT-DBDM

NEXT-DBDM (*double beta, dark matter*) (for further details see references [103], [109]) prototype was constructed and operated in *Lawrence Berkeley National Laboratory* (LBNL), USA. The detector was inside a 10 L stainless steel pressure vessel supporting a maximum of 17 atm pressure. The detector itself was composed by a hexagonal field cage (12.4 cm apothem) divided in buffer, drift (8 cm) and EL (5 mm) regions by three wire meshes made of crossed wires separated by 0.5 mm. The field cage was made of 18 PTFE (teflon) rectangular panels with copper strips connected by resistors that grade the field between the wire meshes. The energy plane was composed by 19 Hamamatsu R7378A PMTs forming a regular hexagon. The tracking plane was composed by an 8x8 array of Hamamatsu S10362-11-025P SIPMs.

The major achievement of NEXT-DBDM was the first proof of near intrinsic energy resolution in a high pressure xenon TPC with EL amplification (see Figure 3.7). Working at 10 bar, a drift field of 530 V/cm and EL field of 26.4 kV/cm ($G_{EL} = 1250$), it obtained an energy resolution of ~ 1 % at FWHM for 662 keV gammas from ^{137}Cs decay and ~ 5 % at FWHM for 30 keV xenon x-rays. This extrapolates to ~ 0.5 % at FWHM at $Q_{\beta\beta}$. Besides, NEXT-DBDM also started to study the tracking capabilities of the TPC with SIPMs sensors.

NEXT-DEMO

NEXT-DEMO (*demonstrator*) was initially built [110], [111] to prove the good energy resolution, but also the topological discrimination capabilities needed in NEXT-100. Even thought this was the main motivation of NEXT-DEMO construction, it represents only the first phase of the detector since has been used up to date as a multi-purpose test-bench. NEXT-DEMO is operated in a semi-clean room at *Instituto de Física Corpuscular* (IFIC) and it used a reduced version of almost all the major subsystems used

in NEXT-White and NEXT-100, namely the TPC, energy plane, tracking plane, pressure vessel, electronics, gas system and monitoring system. It is a reduced version TPC, but larger than NEXT-DDBM, with around 9 cm active radius, 30 cm drift length, 10 cm buffer and 5 mm EL. The tracking plane is instrumented with four 8x8 SiPM arrays accounting a total of 256 SiPMs. After Run-9, the SiPMs were changed from SensL C series model MicroFC-10035-SMT-GP to the larger area Hamamatsu S13372-1350TE, which would be implemented in NEXT-100. The energy plane was instrumented with 19 Hamamatsu R7378A PMTs during the first phase, but changed to 3 Hamamatsu R11410-10 PMTs afterwards.

The first running phase finished with the construction of NEXT-White in 2016 . During the next period, several detector configurations and run types were performed with different purposes: diffusion studies with Xe-He mixtures and studies for NEXT-100 on energy resolution and topological discrimination. Nowadays NEXT-DEMO continues its activity investigating possible NEXT-100 hardware updates and R&D for the future tonne scale NEXT-HD detector.

3.4.2. NEXT-White

NEXT-White[1] (NEW) was the second phase of the NEXT program. With an active length of length of 507 mm and 416 mm of diameter, it was a 1:2 scaled version of NEXT-100 (in both transverse and longitudinal dimensions). The detector hosted $\sim$ 4 kg of xenon which becomes $\sim$ 3.3 kg after fiducialization. NEXT-White detector operated during the period of October 2016-August 2021 in Laboratorio Subterráneo de Canfranc (LSC). NEW accomplished its main objectives of

- demonstrate the scaling capabilities of HPXe TPC to larger volumes,
- demonstrate the calibration procedure to achieve both a near intrinsic energy resolution and topological discrimination,
- understanding of background contributions based on simulated models,
- measurement of the two neutrino mode half-life.

A thorough description of NEW detector can be found for example in [108] and [112]. In what follows we summarize the main detector components and subsystems. Among the detector components we outline the TPC itself and the energy and tracking planes. The detector subsystems are classified in gas system, pressure vessel and inner copper shielding, lead castle, electronics and monitoring system.

TPC

Similarly as in NEXT-DBDM and NEXT-DEMO, NEW TPC is composed by: the field cage, the light tube, the cathode grid, the gate mesh, the anode plate and the high voltage feedthroughts (HVFTs). They divide the detector in three functional regions: the buffer region (129.5 mm) from the PMT windows in the energy plane to the cathode; the drift region (507 mm) from the cathode to the gate mesh; and the electroluminiscence region (6 mm) from the gate mesh to the anode.

The field cage is a cylindrical shell made of a high density polyethylene (HDPE) of 21 mm thickness. Radiopure copper rings (see Figure 3.8) are inserted in the inner part of the HDPE with the goal of achieving electric field uniformity and are connected

[1] Named in memory of Prof. James White.

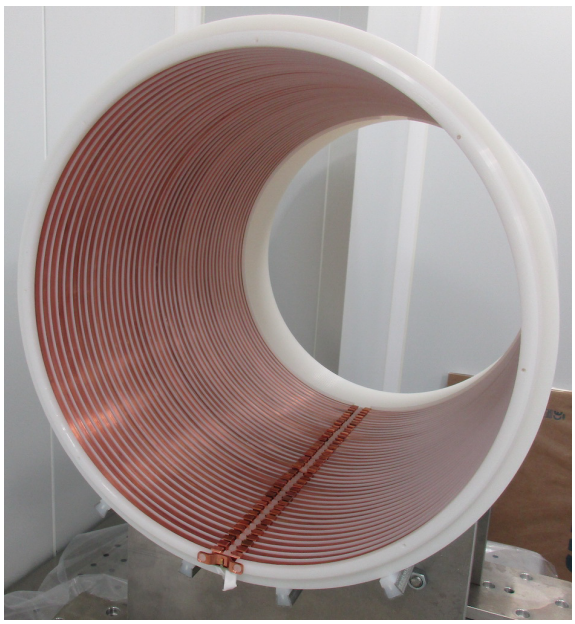


Figure 3.8: Field cage and internal copper rings.

between them by radiopure 1 GΩ resistors. Inside the field cage (see Figure 3.9), the light tube consists of a PTFE (teflon) cylinder of 416 mm diameter and 10 mm thickness. The light tube is coated with tetraphenyl butadiene (TPB), a wavelength shifting agent of scintillation VUV light to visible blue (400-450 nm). The use of TPB in NEXT is motivated by two main reasons: PMTs itself can not resist the high gas pressures, therefore they are located behind a sapphire window which absorbs VUV light; the light tube reflectivity in the blue is considerably higher than in VUV. Moreover, SIPMs quantum efficiency in the VUV is low. The light tube provides a total 98% light reflectivity, a crucial feature to maximize light collection. TPB is degraded in liquid xenon but no evidence was found in gaseous Xe after almost five years of NEXT-White data taking. In order to optimize light collection in the energy plane, the cathode is designed to maximize optical transparency. It is composed by series of 0.15 mm diameter steel wires at 10 mm pitch, offering a 98.5% optical transparency. On the other hand, the gate is made from a grid of woven steel wires of 40 μm diameter separated by 500 μm, constituting a total 90% of open area allowing a 100% electron transparency under normal operation conditions. This gate configuration is chosen in order to allow a better electric field definition while maintaining electron transparency, since EL region is one of the most sensible parts of the detector due to its high electric field. Also electric field must be uniform to avoid a degradation in the light yield which would worsen the energy resolution.

The anode is a 15 nm thickness layer of indium tin-oxide (ITO) surface coated over a fused silica plate of 522 mm diameter and 3 mm thickness. The ITO is grounded via with a 1 mm thickness indium wire that surrounds the perimeter of the coating. A thin layer TPB is deposited over the ITO. The total transparency of ITO layer to blue is of 93%. The anode plate is mounted in the tracking plane to assure both are parallel. NEW electrodes are shown in Figure 3.10

USC UNIVERSIDADE DE SANTIAGO DE

The high voltage feedthroughts (HVFTs) must hold at least the design voltages of -41 kV in the cathode and -16.2 kV in the gate. This is a though technical task due to the bad insulator behaviour of noble gasses. They are designed to avoid gas surface discharges

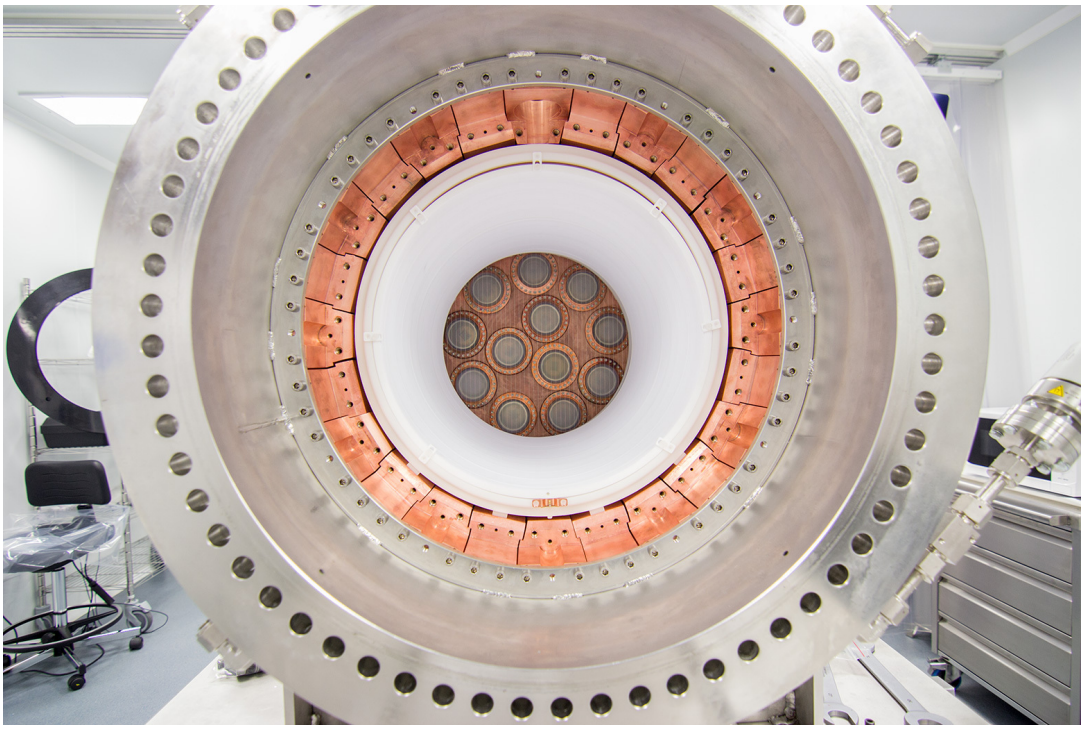


Figure 3.9: View of NEW TPC field cage, light tube, cathode and inner copper shielding inside the pressure vessel as seen from the tracking plane. At the front end, the energy plane.

to allow an stable operation of the detector. Since the commercial HVFTs are typically made from non-radiopure materials, the HVFTs of NEXT had been custom designed. Two different HVFTs were designed for the cathode and the gate (see Figure 3.11). Both were made of HDPE and cryo-fitted in an radiopure stainless steel piece. The rate of cathode surface sparks is very small, less than one each 6 months. On the other hand, the gate HVFT is a simple straight metal rod, with dielectric just in the HVFT chamber entry point. Final working voltages are decided based upon maintaining good energy resolution and a negligible rate of sparks in the EL region, which could ultimately be damaged.

Energy plane

NEXT-White energy plane is composed by 12 Hamamatsu R11410-10 PMTs embeded in a radiopure copper structure (see Figure 3.12). The PMT model is chosen by their low radiactivity levels and good performance. The PMTs reside in the 120 mm thick copper plate, that acts as external radiation shielding and support. The PMT photocathodes are protected against the high pressure of the xenon by sapphire windows in the copper plate (see Figure 3.12). The sapphire windows are coated with a thin (<100 nm) layer of poly-ethylenedioxythiophene (PEDOT) in order to ground the windows and nullify the electric field in the PMT front surroundings. The PEDOT transparency is of the order of 95% for blue light. The PEDOT is covered by a thin layer of TPB. The PMTs are optically coupled to the windows using NyoGel OCK-451 and held in place with a HDPE brace and spring. Backside caps in the copper plate create an independent residing volume that allows the PMTs to work in vacuum or at low pressure. They were mostly operated in a N_2 atmosphere at 1 bar. The PMTs are circularly distributed

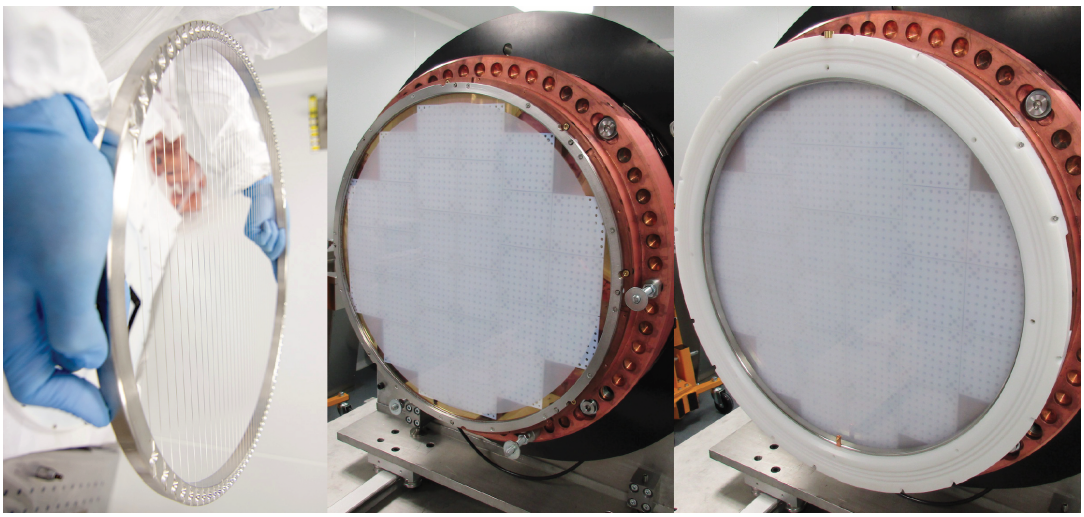


Figure 3.10: NEW electrodes. From left to right: cathode grid, anode plate and gate. The anode plate is mounted on top of the tracking plane and the gate grid over it, constituting the EL region.



Figure 3.11: NEW HVFTs for cathode (left) and gate (right).

providing a 31% coverage area.

Tracking plane

NEXT-White tracking plane (see Figure 3.13) is composed by a sparse array of SIPMs mounted on top of a 120 mm thickness copper plane. The copper plate serves as supporting structure and external shielding, similarly as in the energy plane. The sensors are distributed between 28 low-radiactivity kapton boards (DICE boards) with 8×8 each, constituting a total 1792 SIPMs. The SIPMs are SensL C series model MicroFC-10035-SMT-GP with 35 μm cell size and 576 cells per sensor. The distance between SIPMs is 10 mm. The distance between the tracking plane and the end of anode plate is 2 mm. Besides the SIPMs, each DICE board contains a sensor to monitor the gas temperature and a blue LED to calibrate the PMTs in the front energy plane. To improve the reflectivity of the tracking plane, the DICE boards are covered by PTFE (teflon) masks. The mask tickness is 5 mm, with 7 mm diameter holes for SIPMs.

USC UNIVERSIDADE DE SANTIAGO DE COMPOSTELA

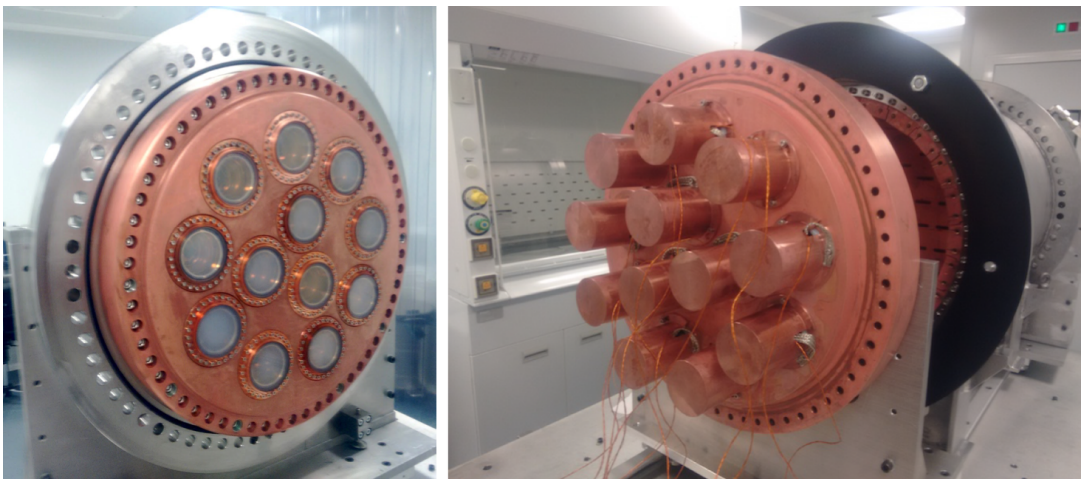


Figure 3.12: Energy plane frontside (left) and backside (right).

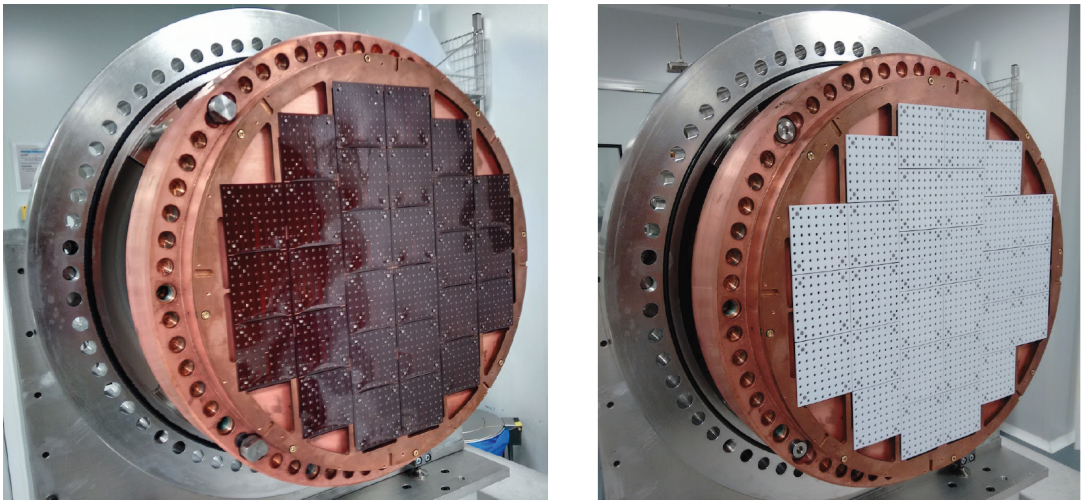


Figure 3.13: Front side of the tracking plane showing the kapton dice boards (left) and the teflon covering (right).

Inner shielding and pressure vessel

The detector field cage is surrounded by 6 cm thick radiopure copper bars (see 3.9) that together with the energy and tracking plates constitute the detector shielding against external radiations from laboratory walls, the external vessel or electronic components. The inner copper shielding (ICS) fully covers the detector except in the two holes that serve as calibration ports for the placement of radioactive sources.

The detector and copper shielding is enclosed in a radiopure stainless steel pressure vessel (see Figure 3.14) of 950 mm length, 640 mm diameter and 12 mm thickness, which can withstand pressures up to 20 bar.

Electronics and DAQ

In order to simplify the detector mechanics and safety, the PMT photocathodes are grounded [113]. The other alternative would require the isolation of each PMT from ground to set the high voltage between PMT anode and cathode. Even though this implementation is simpler, it requires the PMT AC coupling with a high-voltage capacitor. The circuit behaves at first order as a high pass filter (HPF). Therefore, since the

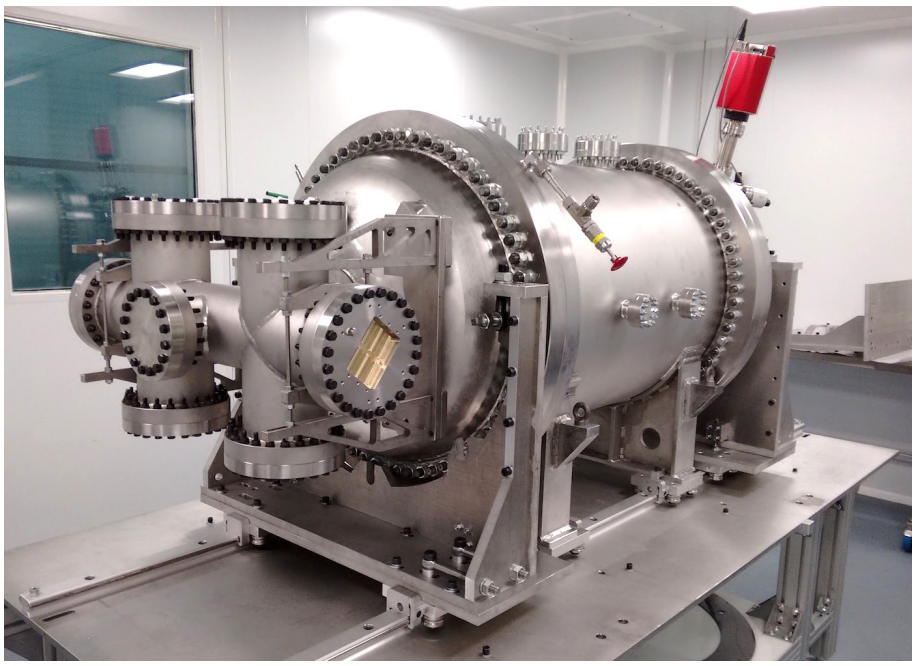


Figure 3.14: Pressure vessel during assembly in the LSC clean tent.

energy is proportional to the area of the input signal, the output of the HPF must be deconvoluted to recover the original input. This is implemented through a baseline restoration algorithm (BLR) that applies the inverse function of the circuit.

The tracking front end electronics [114] consist of a differential input transimpedance amplifier followed by an integrator. After a 1 μs charge accumulation time, a 12-bit 1 MHz ADC sample the integrated value. A FPGA controlled switch discharges the capacitor in 20 ns to start a new integration period.

A thorough discussion of NEXT DAQ and trigger system can be found in [115]. They were a co-developed effort of NEXT Collaboration with RD51 Collaboration at CERN and IFINHH Bucharest in 2011. The objective was to design a scalable readout system for small and medium scale experiment. The DAQ system consist of three parts: the energy plane, the tracking plane and the trigger. PMT signals are digitized at 40 MHz rate meanwhile SIPMs are digitized at 1 MHz. The system is recording data continuously in a circular buffer until a trigger is found. Trigger configuration parameters are modifiable. The trigger implements a two level system, such that events can be filtered into two triggers: *trigger 1* used for low energy events (mainly used for ^{83m}Kr and x-rays) and *trigger 2* for higher energies.

Gas system

The gas system maintains a continuous gas flow and cleaning. The cleaning keeps the gas impurities at a low level in order to minimize electron attachment. This is done through two types of getters: the so-colled cold getter which removes O_2, CO, H_2, H_2O, volatile acids and bases, organic compounds and refractory compounds; and the hot getter which reduces the impurity levels of O_2, CO, H_2, H_2O, N_2, CH_4 to the order of parts per billion (ppb) or below.

Moreover the gas system also manages the pressurization and depressurization of the detector and assures the system's working conditions. A leakage would be fatal

due to the high price of enriched xenon. Therefore it is also responsible for the gas evacuation and recovery if needed. During NEXT-White operation, the NEXT-100 vessel acted as recovery tank. The whole system is automated by a Compact RIO, a FPGA based programmable logic controller. The Compact RIO is connected to the different monitoring devices of the gas system such as gauges, valves, the compressor, chiller, etc... and acts accordingly. It also outputs this information to the monitoring system.

Lead castle and platform

NEXT-White is placed in Laboratorio Subterráneo de Canfranc (LSC) in Hall A. Detector and components are mounted on a seismic structure to mitigate possible ground vibrations inside an emergency pool (see Figure 3.15). The detector is surrounded by a 20 cm thick lead castle (see Figure 3.16) which serves as external gamma shielding. A pipe system from the radon abatement machine of the LSC flushes pure air inside the castle, making the radon background contribution negligible.

Monitoring system

NEXT detectors (both DEMO, NEW and NEXT-100) are monitored though a *slow control system* (SCS) that provides information on the current running status and sends alarms or warnings to shifters. Issues that can fire alarms during detector operation are sparks (not very common), sensor disconnections or overcurrents, gas pressure out of the safety limits, etc... Some alarms are automatically managed by the system, but other require direct input from the shifter. The NEXT slow control is divided in five interconnected modules:

- Gas system: provides information on the gas flow, such as gauge pressures or compressor state. It communicates with Compact RIO and allows a manual activation of an emergency stop.
- High voltage: monitors the cathode and gate voltages and currents. Allows the manual setting of voltages and fires alarms in case of spark. In such a case, shifter intervention is required and data taking must be stopped until recovery of normal conditions.
- Power supplies: monitors the energy and tracking plane front-end electronics and SiPM dice board power supplies. It allows switching on and off the electronics if needed.
- PMT high voltages: controls PMT's bias voltages and currents and the vacuum pump connected to the energy plane.
- Sensors: monitors the temperatures of electronic system and allow some DAQ devices switching on and off. In case of over temperatures an alarm is raised and the corresponding electronics must be turn off.

3.4.2.1. Summary of main results

After the demonstration of an excellent energy resolution and topological discrimination during the R&D phase, NEXT-White was constructed to verify the results in a larger detector, and also to measure the two neutrino mode of ^{136}Xe double beta decay. NEXT-White operated with ^{136}Xe-depleted xenon (3% isotopic abundance) from October 2016 to January 2019 (Run I–IV), and with ^{136}Xe-enriched xenon (91%



Figure 3.15: NEXT platform inside Hall A in LSC. Reproduced with permission from J. Larrea.



Figure 3.16: NEXT-White detector inside the open lead castle in LSC. Reproduced with permission from J. Larrea.

USC UNIVERSIDADE DE SANTIAGO DE COMPOSTELA

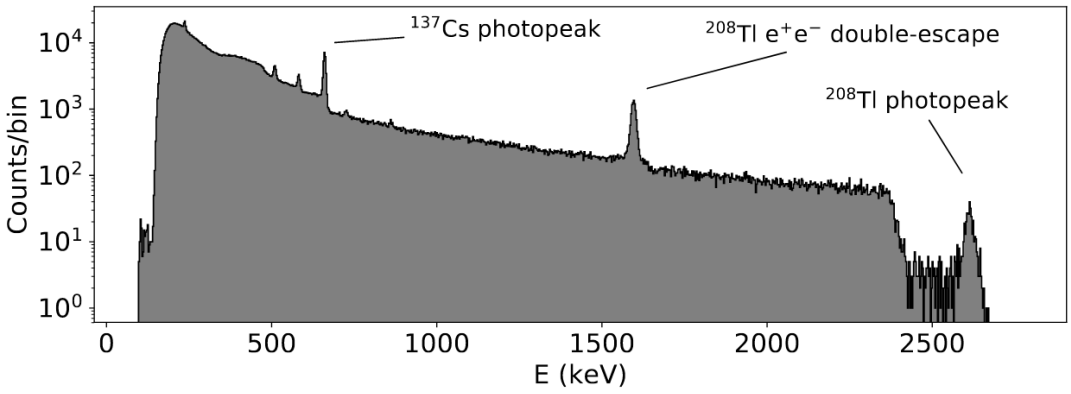


Figure 3.17: Full energy spectrum of a high energy calibration run with ^{137}Cs and ^{228}Th sources. The spectrum is corrected by geometrical, lifetime and axial effects. The main peaks of study are indicated. The large dip at $\sim$ 150 keV correspond with a *trigger 2* selection. From [116].

isotopic abundance) from February 2019 to June 2021 (Run V-VI). We summarize below the main results of energy resolution [116], topological discrimination [117], [97], background model [118] and the measurement of the two neutrino mode half-life [119].

Both energy resolution and topology were studied using high energy calibration runs. Two high energy radioactive sources are placed in the detector ports, ^{137}Cs providing a 661.6 keV gamma and ^{228}Th whose decay to ^{208}Tl provides a gamma of 2614.5 keV. The full spectrum is shown in Figure 3.17. The spectrum is obtained after geometrical and lifetime corrections, a procedure based in ^{83m}Kr decays (§5.3.3.1). Besides, an extra correction for an unexpected and undesired effect is added. This is the so-called *z-effect* or *axial-effect* which consist on a biasing in the event energy as a function of its length along the detector longitudinal dimension, as is shown in Figure 3.18. The origin of this effect is unknown and nowadays is the most limiting factor to achieve a near intrinsic energy resolution. The effect is also present in NEXT-DEMO. Once this z-effect is corrected, a resolution of $\sim$ 0.9% FWHM at $Q_{\beta\beta}$ is achieved [116]. Understanding the origin of the effect is a must in order to evaluate the real experimental potential of the NEXT proposal.

The topological discrimination in NEXT is studied using the ^{208}Tl double escape peak (see Figure 3.17). It provides a natural source of signal-like (two electrons) and background-like (one electron) events. The double escape comes from the pair production e^+e^- of the 2615 keV gamma, the recombination of the e^+ with an electron in xenon produces two photons of total energy $2m_e = 1022$ keV. If the two gammas remain undetected, the total energy registered in the detector would be 1593 keV. Since this peak is below the Compton edge of the 2615 keV photopeak, the energy region around the double escape provides a sample of both two electron and one electron events. The topological discrimination can be evaluated by estimating the number of signal-like and background-like events as a function of the energy of the less energetic blob, the discriminant variable. Therefore we can compute the signal efficiency and background rejection, two important parameters in a non-background free $0\nu\beta\beta$ experiment (§2.3). The results obtained for NEXT-White are shown in Figure 3.19. Even though the results show discrimination capabilities, they can be greatly improved by deconvoluting the effect of electron diffusion. This is achieved [97] through the

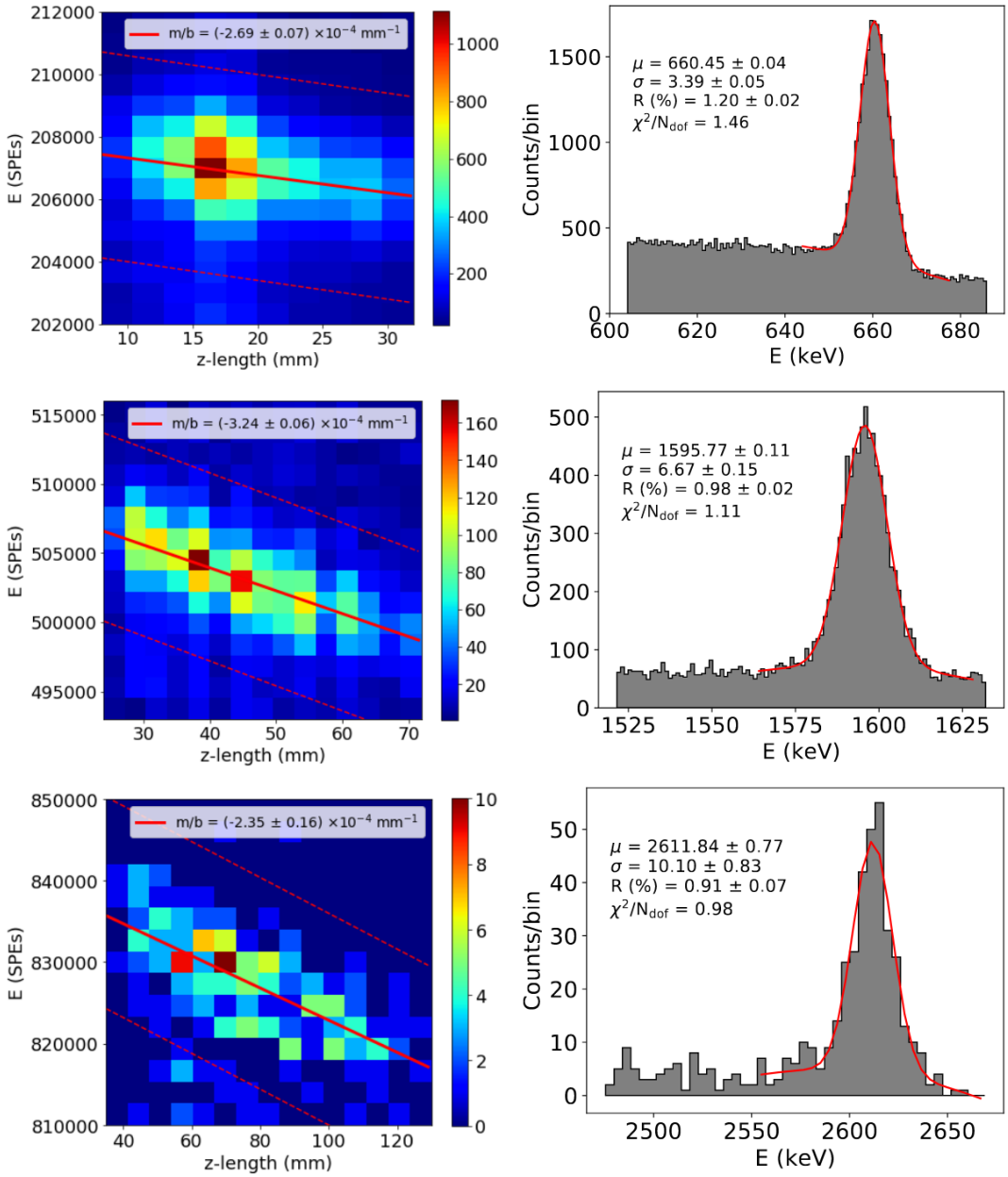


Figure 3.18: Left plots show the linear dependence of photopeak energies with track longitudinal length. The energies are corrected by geometry and lefetime using ^{83m}Kr maps. Right plots show the photopeak also corrected by this linear effect. The photopeaks correspond to the 662 keV, 1593 keV and 2615 keV in Figure 3.17. From [116].

USC UNIVERSIDADE DE SANTIAGO DE COMPOSTELA

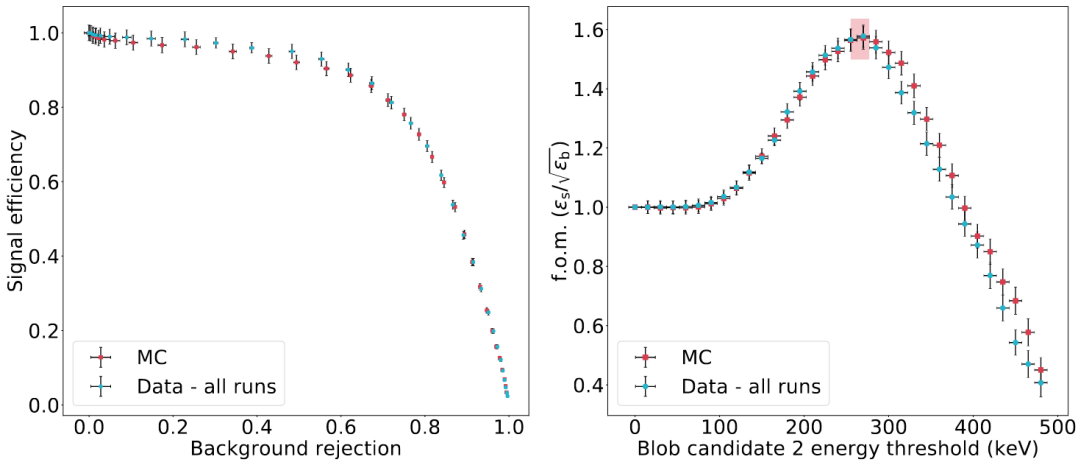


Figure 3.19: Left plot shows the signal efficiency ϵ_s as a function of background rejection ϵ_b in the ^{208}Tl double escape peak for data and MC. Right plot show the figure of merit $\epsilon_s/\sqrt{\epsilon_b}$ as a function of the less energetic blob. The results are obtained through the so-called classical analysis were electron diffusion is not deconvoluted. From [117].

Richardson-Lucy deconvolution algorithm (§5.3.4), providing an improvement of factor two in the figure of merit versus the classical analysis (Figure 3.19).

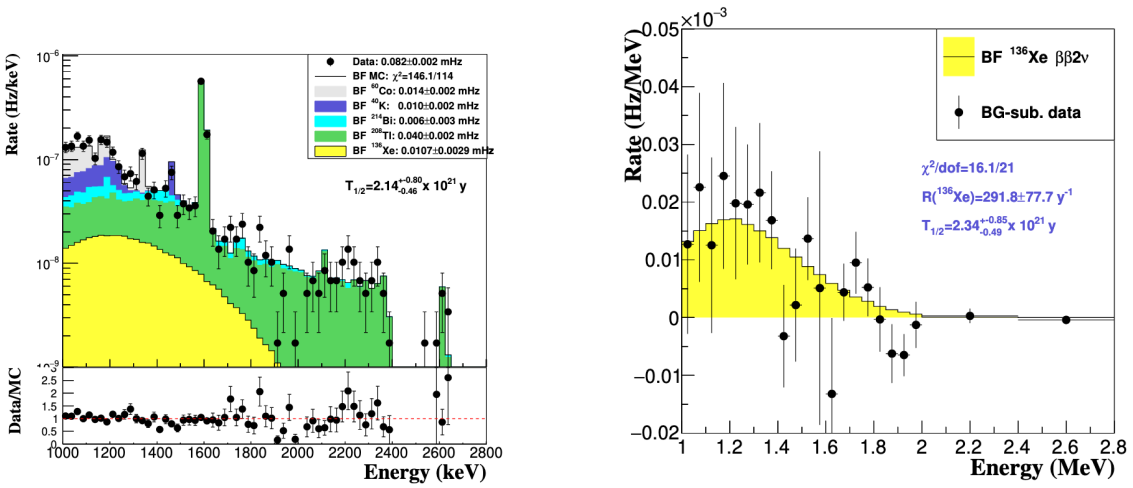
NEXT-White background model is developed based on radioactivity measurements performed before detector construction. Using the activity of the multiple detector components, the background model was validated by comparing the simulations with data under similar detector conditions and exposure [118]. Measurements previous to the implementation of the radon abatement system in LSC also probe that the contribution from airborne ^{222}Rn in the background budget is negligible.

The most impressive achievement of NEXT-White was the measurement of the two neutrino mode half-life [119]. Two independent methods were used: a background model dependent fit and a subtraction fit to the $2\nu\beta\beta$ spectrum. The former is based on the background model with the assumed contributions from the different backgrounds (Figure 3.20a). On the other hand, the later subtracts the spectra of the data taking periods Run-V (enriched) and Run-VI (depleted) to estimate the half-life in a background model independent way (Figure 3.20b). Both measurements are compatible with EXO-200 and KamLand-Zen measurements using around one and two orders of magnitude more xenon, respectively.

3.4.3. NEXT-100

NEXT-100 detector is under construction (Figure **??**) at LSC since the end of 2021. It is a double sized version of NEXT-White with the same elements and subsystems already described (§3.4.2), thus in what follows we will only highly the relevant differences.

The active volume has a drift length of 1180 mm, 984 mm diameter and 10 mm of EL region. It is designed to host around 80 kg of ^{136}Xe-enriched xenon operating at 13 bar pressure. The PMT's model is the same as in NEXT-White, with an increase in the number of PMTs from 12 to 60. On the other hand, the 3584 SiPMs mounted are Hamamatsu model S13372-1350TE, whose larger area provides a higher light collection than the smaller SensL SiPMs of NEXT-White.



(a) **(b)**

Figure 3.20: Measurements of the two neutrino mode half-life in NEXT-White. Left plot (a) shows background model dependent fit with the contributions of each isotope in the total energy spectrum for Run-V (enriched) after blob energy selection. Right (b) plot shows the subtracted energy spectrum of Run-V (enriched) and Run-VI (depleted) and the best fit to the $2\nu\beta\beta$ rate. From [119].

The anode is no longer composed by an ITO surface placed over a silica plate, but instead a photo-etched grid mesh is used for both anode, cathode and gate. Recall that ITO is coated with TPB in NEXT-White, therefore the NEXT-100 implementation needs to include the TPB somewhere in between the anode and the SiPMs. The coating is placed at the SiPM's windows. SiPMs are buried in 6 mm teflon masks with rectangular holes acting as light collimators, and their inner walls are also coated with TPB to enhance the WLS probability. The distance between adjacent SiPMs is increased from 10 mm in NEXT-White to 15.55 mm in NEXT-100, since maintaining the same pitch would require a significant investment in electronics.

The distance between the anode and the tracking plane was raised from 5 mm in NEXT-White to 16.1 mm. This was a major concern during preliminary detector simulations which predicted a wide photon spread at the tracking plane, significantly degrading the spatial resolution. The effect was also studied in several NEXT-DEMO configurations in order to probe topological discrimination at this larger distance. It was concluded that obtaining a good topological discrimination in NEXT-100 will require the use of a dedicated algorithm to deconvolve the photon spread in the tracking plane (§5.3.4).

From the shielding side, the lead castle is the same as for NEXT-White with the external painting removed, which happened to be highly radioactive. The inner copper shielding width is doubled from 6 mm to 12 mm, providing extra gamma attenuation.

The main objective of NEXT-100 is the search of $0\nu\beta\beta$ in xenon. Data taking is expected to start during 2023, employing the same calibration method based on ^{83m}Kr decays as in NEXT-White (5.3.3.1). This thesis studies the sensitivity of NEXT-100 to $0\nu\beta\beta$.

USC DE SANTIAGO DE COMPOSTELA



Figure 3.21: NEXT-100 vessel mounted on the pedestal inside the external lead copper shielding. The red castle paint was removes due to its large radiactivity.

3.5. Future plans

Current results of neutrinoless double beta decay experiments show that exposures in the tonne scale will be needed in order to start exploring the normal hierarchy region (Chapter 2). NEXT-100 detector is an intermediate step towards a future tonne scale high pressure xenon TPC with a similar technology, NEXT-HD (*High Definition*). Even though detector scaling is a must in $0\nu\beta\beta$ searches due to the large half-life of the process, NEXT is also developing a new line of research which could lead to a virtually background free experiment.

Current technology focuses on the measurement of event energy and a discrimination variable to reject background events. NEXT's variable is the Bragg peak at the end of the track, but electrons might follow curly trajectories in the gas making the identification of the end points challenging. Also since in $0\nu\beta\beta$ the energy is shared among the two electrons, it might be that one of the electrons carries most part of the energy, thus the Bragg peak of one of the electrons is not enough to allow discrimination. Even with an efective detection technology and reconstruction algorithms, this effects might lead to a significant reduction of the signal acceptance.

Nevertheless, we could exploit the fact that ^{136}Xe decays into a doubly ionized $^{136}Ba^{2+}$ atom in double beta decay. Identifying the $^{136}Ba^{2+}$ atom after the decay would constitute a virtually 100% efficiency discrimination variable since barium won't be produced in background events. Measuring the $^{136}Ba^{2+}$ is possible through single-molecule fluorescence imaging as proved by NEXT collaborators [120], using the original idea of D. Nygren [121]. The method relies on the design of a molecule with the ability to capture the $^{136}Ba^{2+}$ ion and change its fluorescence properties.

Part II

Methodology

USC
UNIVERSIDADE
DE SANTIAGO
DE COMPOSTELA

USC
UNIVERSIDADE
DE SANTIAGO
DE COMPOSTELA

CHAPTER 4
Detector Simulation

4.1. Introduction

Detector response simulation is a crucial task in understanding detector performance and guiding detector design. The NEXT collaboration has used simulations for multiple purposes: estimations on detector sensitivity to $0\nu\beta\beta$, contributions to background rates from different isotopes and detector components, signal to background efficiencies at the ROI, evaluation of the reconstruction procedure, optimized designs for future detectors, etc. Nevertheless simulations are CPU-time-consuming since they keep track of all the particles and interactions, especially for an optical detector in which hundreds of thousands of photons are produced. This causes the scaling of simulation time with event energy. For example, a 41.5 keV ^{83m}Kr event simulation takes ∼2 min whereas an event at $Q_{\beta\beta} \sim 2.5$ MeV requires >1 hour for the NEXT-100 detector with the standard NEXT simulation toolkit. This fact makes high exposure studies unfeasible, in which large samples of events are needed. This Chapter presents a simple algorithm to replace the time-consuming part of the simulation process. The algorithm is based on a parametric version of the geometry of the NEW detector in [122]. The version presented here is no longer constrained to a fixed detector geometry and allows the simulation of any of the NEXT detectors.

This Chapter is organized as follows. In Section 4.2, we introduce the NEXT simulation toolkit. In Section 4.3 we show a method to overcome the CPU-time-consuming process of optical TPC simulation, and compare it with the standard simulation mode. Finally, Section 4.4 describes the software implementation of NEXT-100 detector.

4.2. NEXUS Overview

NEXUS [63], *NEXt Utility for Simulation*, is the computer program that implements the simulation of NEXT detectors. It is based on GEANT4 [123], a standard simulation library in Particle Physics. GEANT4 is a *C++* toolkit for simulating the passage of particles through matter using Monte-Carlo methods. GEANT4 manages all aspects of the simulation process of the detector, which include (Figure 4.1):

- *Detector geometry*: describes the components and materials that make up the detector.
- *Physics lists*: collection of the physical processes and particles considered in the simulation.

USC UNIVERSIDADE DE SANTIAGO DE COMPOSTELA

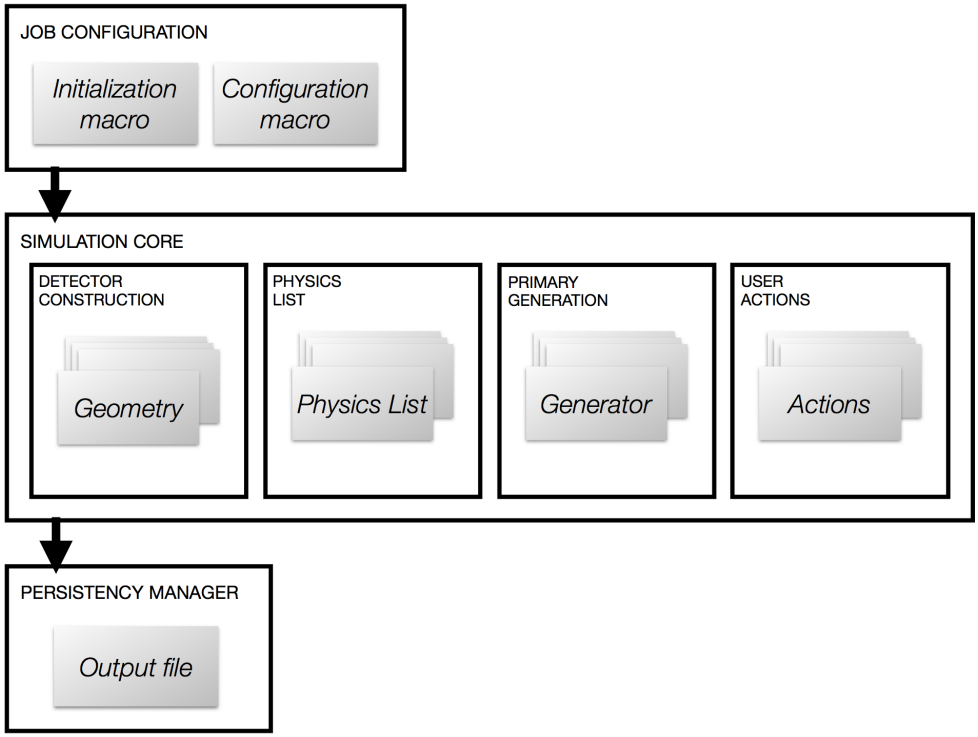


Figure 4.1: Diagrammatic structure of a GEANT4 simulation program. From [63].

- *Event generation*: description of the event that will be simulated; the particle type (ie a photon, an electron-positron pair, a radioactive element, etc.) and their initial conditions such as position in the detector and three-momentum.
- *User actions*: control the simulation process and allow the user to be informed about the current state of the simulation, the particles and interactions taking place.

NEXUS particularizes these components for NEXT detectors (Chapter 3): NEXT-White, DEMO, NEXT-100, and also the virtual NEXT-FLEX detector created for geometry-dependent studies for future proposals or upgrades. Detector geometries are implemented in great detail, with their corresponding shapes, sizes and materials. The elements are created in a *matryoshka* structure, such that external elements contain inner elements inside. For example, detector's light tube is contained inside the vessel. Also the optical properties of detector materials are defined, for example the light sensors (PMTs and SiPMs) implement the quantum efficiency provided by the manufacturer. The starting position and momentum of a simulated event are set via *vertex generators*. Vertex generators are needed not only to simulate the events occurring inside the xenon active volume like krypton or $\beta\beta$ events, but also the different backgrounds coming from detector components.

We can defferenciate two simulation modes implemented in NEXUS: the full-simulation and the fast-simulation. In what follows, *primary particles* are defined as the particles of the simulated event. The rest of the particles produced in the simulation would be considered as *secondary particles*. For example, $0\nu\beta\beta$ primary particles are e^+e^-. Ionization electrons, scintillation photons, and EL photons are secondary particles. The simulation modes are described below.

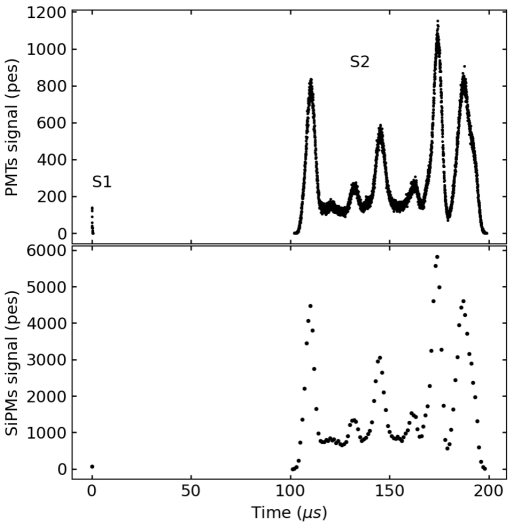


Figure 4.2: Zero-suppressed waveforms obtained in the full-simulation mode of NEXUS, representing the signal collected in the light sensors.

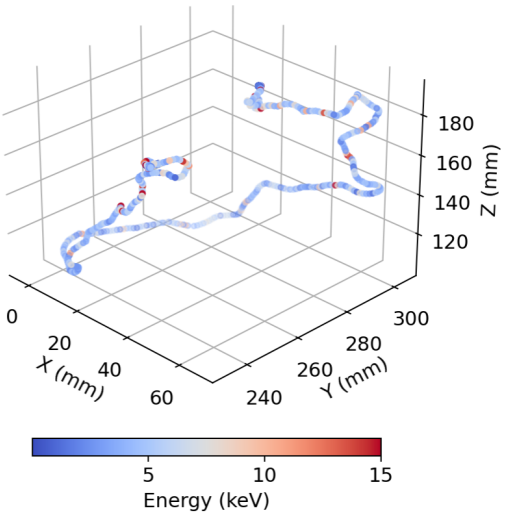


Figure 4.3: Ionization track produced in the fast-simulation mode of NEXUS. The color-bar represents the energy of the hits.

Full-Simulation: In this mode the propagation of all particles (primary and secondary) is carried out until they reach the sensors. Particles are considered as individual entities with a unique ID-number, making it possible to trace their interactions throughout the detector. Therefore the overall simulation would be composed by the simulation of each individual particle. This is a CPU-time-consuming task, growing with the number of particles involved, which scales with the energy of the simulated event. Since each of the emitted photons is also simulated, the final result of the simulation will be a number of photons arriving at the photo-sensors. The output of the simulation is given as zero-suppressed time histograms with the photo-electrons generated in each sensor (Figure 4.2). This simulation mode is both CPU-time-consuming and memory demanding, with a time-scale on the order of 2 min to simulate a 41.5 keV ^{83m}Kr event and >1 hour for a $Q_{\beta\beta} \sim 2.5$ MeV event. The advantage of this simulation mode is its extreme detail and that its outcome is the actual signal measured at the light sensors.

Fast-Simulation: In this mode the simulation is stopped after the creation of the ionization electrons and scintillation photons. The ionization electrons and scintillation photons are produced by the direct propagation of primary particles, or by secondary particles emitted by the primaries, like delta electrons or bremsstrahlung that subsequently interact. Once they are created, the simulation stops, and neither drift nor light propagation is simulated. The ionization electrons and scintillation photons created are collected in voxels of a certain volume (usually around 1x1x1 mm^3 voxels). Each voxel represents an energy deposition, a so-called *hit*, and is characterized by a 3D position $\boldsymbol{r} = (x, y, z)$, the energy E required to produce them, and the delay time t from the start of the event (Figure 4.3). The collection of hits for a given even is saved, defining a *track* in the detector's active volume. The fast-simulation is very fast compared with the full-simulation mode, on the μs scale. However, since the simulation is stopped we do not know the signal that would be measured at the sensors.

4.3. DETSIM

4.3.1. Introduction

As described above, the full-simulation and fast-simulation modes provide different results. The goal of DETSIM (*DETector SIMulation*) algorithm is to provide a fast and reliable method to simulate the detector response from fast-simulation tracks and to overcome the lengthy full-simulation process.

The algorithm must implement the simulation steps that convert tracks into signal measured at the photo-sensors. These steps can be classified into *physical processes* or *geometrical effects*. Three physical processes ought to be simulated: *diffusion* of ionization electrons, *photo-emission* at the EL-region and primary *scintillation*. The geometrical effects arise from the signal dependence on the light emission position, which are a convolution of a solid-angle effect and reflections throughout the light tube. Obviously both physical and geometrical effects are accounted for in the full-simulation mode, since particles are individually propagated until they reach the photo-sensors, at the expense of a much slower simulation. Therefore the algorithm's reliability can be estimated by direct comparison between full-simulated and fast-simulated events, the later being produced by the output of DETSIM over fast-simulated tracks.

The most important part of the algorithm lies in the definition of two objects, the *Light Tables* for the PMTs at the energy plane and the *Point Spread Function* for SiPMs at the tracking plane which will be introduced below.

4.3.2. Light Tables

By definition, the *Light Table* (LT) of a PMT in the energy plane (EP) is the quotient between the number of photo-electrons (pes) produced at the PMT by a number of uniformly emitted photons at some point inside the detector ($\boldsymbol{X}$),

$$\mathrm{LT}(\boldsymbol{X}|\mathrm{PMT}) = \frac{\text{produced pes at PMT}}{\text{emitted photons at } \boldsymbol{X}} \quad \text{(pes/photons)} \tag{4.1}$$

This definition is motivated by the need to overcome the time-consuming task of photon propagation from the emission point to its detection at the PMTs. Given a fast-simulation track-hit in the active or buffer region we can compute the number of scintillation photons produced by its energy deposition. Then the S1 signal generated by this hit at any PMT can be easily computed using the LT value at this particular emission point. The same applies for S2 signal using the electroluminiscence photons produced by ionization electrons at the EL-region.

Two types of LTs can be defined since S1 and S2 photons are emitted in different regions of the detector. The S1 scintillation is emitted throughout the active volume, thus a 3D dependence (x, y, z) is required. However S2 LTs are restricted to the EL-region, which is located far from the EP and its width is negligible compared to the active volume, thus we assume only transverse dependence (x, y). Photo detection at PMTs is approximately constant throughout the EL width (see Figure 4.10 in [122]).

Therefore,

$$\text{S1 Light Table} \equiv \text{LT}_{S1}(x, y, z|\text{PMT}) \tag{4.2}$$

$$\text{S2 Light Table} \equiv \text{LT}_{S2}(x, y, z = \text{EL-center}|\text{PMT}) \tag{4.3}$$

The production of the Light Tables is carried out in the full-simulation mode of NEXUS as shown in Figure 4.4 for a single emission point. For a grid of points inside the chamber, a large number of photons (~50 million) is simulated and the LT is computed using the measured signal at each PMT. The number of photons emitted is chosen to induce a statistically relevant signal at the photo-sensors, and the number of points to cover the whole detector volume. The photons are simulated using a scintillation generator in NEXUS following the energy spectrum of xenon (Figure 3.2) and in uniformly distributed directions.

The LT definition can be roughly interpreted as the probability of a photon emitted at $\boldsymbol{X}$ to be measured at certain PMT. Nonetheless there are two subtleties that are worth pointing out. First, the computation of the LT is explicitly done through the photo-electrons, or signal, produced at the sensors. The emitted photons belong to the UV-region, but PMTs are mostly sensitive to visible. The UV to visible conversion is done in the TPB which coats the detector walls. Also the PMTs photoelectron-collection-efficiency (PDE) is simulated, which is wavelength dependent and smaller than unity. Second, the number of photons emitted in the production must be large enough to generate a significant signal in the PMTs and avoid statistical fluctuations. Uniform emission also assures consistency with the expected behaviour of the photons.

An interesting property of the S2 LTs is that they are almost identical to the krypton map's $\overline{E}_0$ introduced in §5.3.3.1, being related by,

$$\overline{E}_0(\boldsymbol{X}) \equiv N_{ph}^{Kr} \times \sum_{\text{PMT}} \text{LT}(\boldsymbol{X}|\text{PMT}), \tag{4.4}$$

where the sum is done over the PMTs used to compute the krypton map (commonly all the PMTs) and N_{ph}^{Kr} is the mean number of photons generated by a krypton in the EL, given by

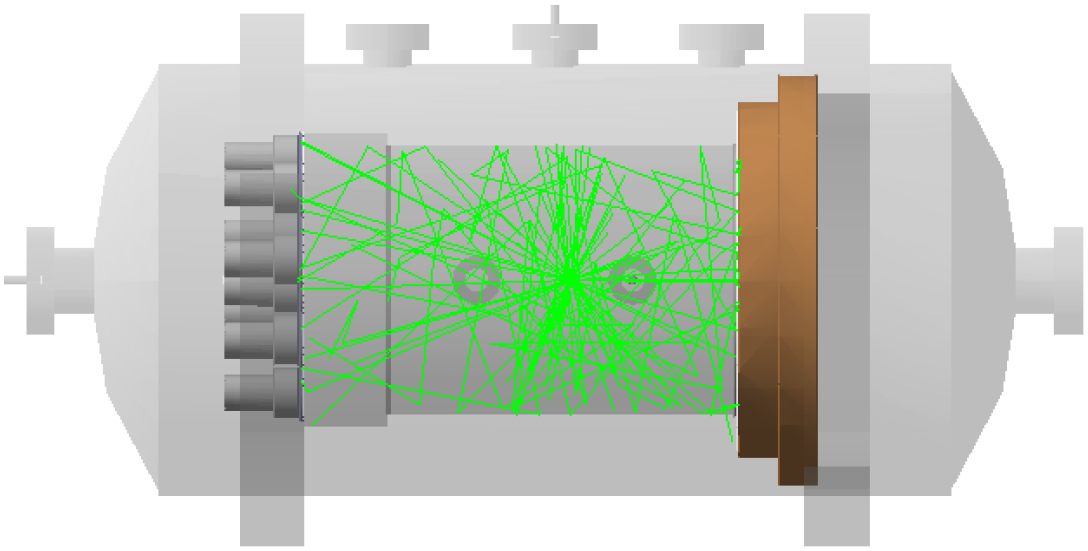
$$N_{ph}^{Kr} = G_{EL} \times \frac{E_{Kr}}{w_i} \tag{4.5}$$

where G_{EL} is the EL gain (§3.2.3) and w_i is the inverse of the ionization yield.

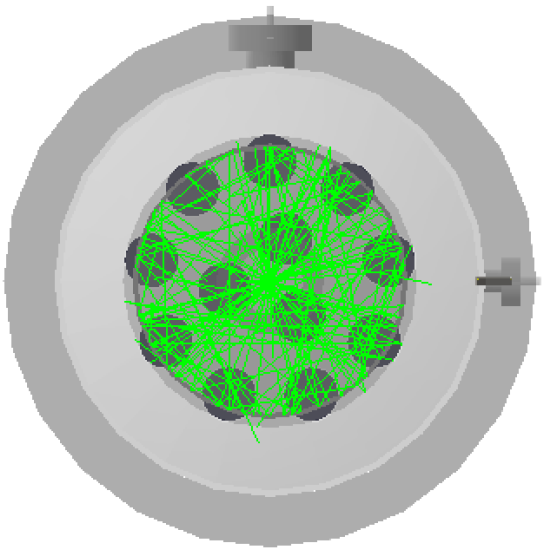
In conclusion, the Light Tables are objects that codify the detector geometry, surface reflectance and wavelength shifting process. This allows one to compute the signal produced in the EP by a photo-emission at some point from the LT values, substituting the entire burden of fully simulating all the individual photons emitted. Figure 4.5 shows an example of PMT Light Tables for the NEXT-100 detector.

4.3.3. Point Spread Function

The number of SiPMs is two orders of magnitude larger than the number of PMTs in NEXT detectors. The SiPMs are placed in the tracking plane (TP), which is much closer to the S2 light emission region (EL-region) than the PMTs placed in the other extreme of the chamber. SiPMs are effectively not sensitive to S1 light due to their



(a) Longitudinal view.



(b) Transverse view from the TP.

Figure 4.4: Full simulation of 60 photons in the longitudinal center of the chamber in the NEXT-White detector at 25 cm from the EL gate ($x = 0, y = 0, z = 25$ cm). The induced signal of the photons in the PMTs is collected to compute the LT value for this emission point. Some detector components are omitted for better visualization.

USC UNIVERSIDADE DE SANTIAGO DE COMPOSTELA

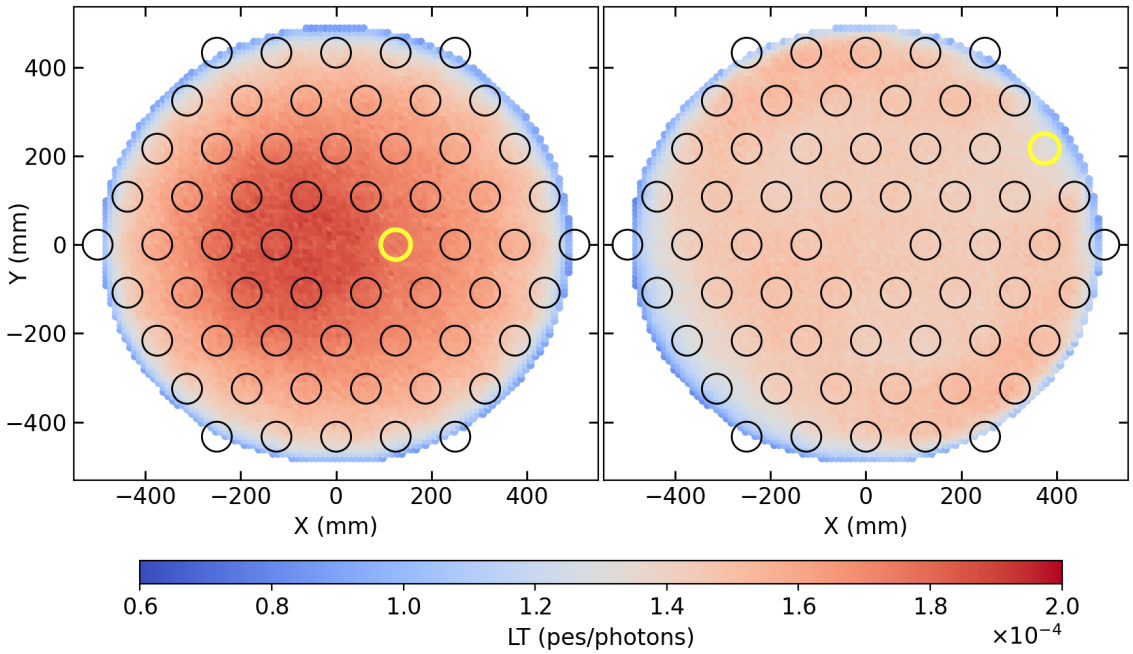


Figure 4.5: S2 light tables for two PMTs (yellow) in NEXT-100 energy plane. Empty circles represent PMT positions. LT values get smaller at high radius due to the degradation of the photon collection efficiency.

smaller active area and collection efficiency. These properties make the definition of the equivalent Light Table for SiPMs different than that of PMTs.

For a uniform emission of photons at point $\boldsymbol{X}$ in the EL at longitudinal distance z from the TP, the *Point Spread Function* (PSF) is the quotient between the number of photo-electrons (pes) produced at a SiPM at transverse distance d and the number of emitted photons

$$\text{PSF}(d|z) = \frac{\text{produced pes at SiPM at } d}{\text{emitted photons at } \boldsymbol{X}} \quad \text{(pes/photons)} \tag{4.6}$$

Similar to LTs, this definition is motivated in order to easily compute the signal produced at SiPMs by the EL-light emitted by ionization electrons. Note the nomenclature for PSF is the same as in the deconvolution procedure in §5.3.4 even though they are different objects. The PSF used in deconvolution is computed as the quotient of the signal measured at some distance and the total signal measured, and it is created using krypton events. Nevertheless we will use the same nomenclature in what follows and explicit reference to which PSF object will be given when needed.

The PSF production is similar to that of the LTs: scintillation photons are emitted from different points in the EL-region to compute the signal produced at the SiPMs. Nevertheless, we are no longer interested in which concrete SiPM has measured some signal, but its distance to the emission point. Since SiPMs have discrete positions in the chamber, more than one emission point is needed to get a fine binned PSF. For example in NEXT-White, the SiPMs closer to the center of the chamber are placed ($x = \pm 5$ mm, $y = \pm 5$ mm) and if we emit photons from a single point, let's say $x, y = 0, 0$ we will only have signals measured above $d = 5$ mm and we could not cover distances below. Then our PSF bin width should be 5 mm to avoid empty values in the PSF function. In order to fine bin the PSF, not only in transverse but also in longitudinal

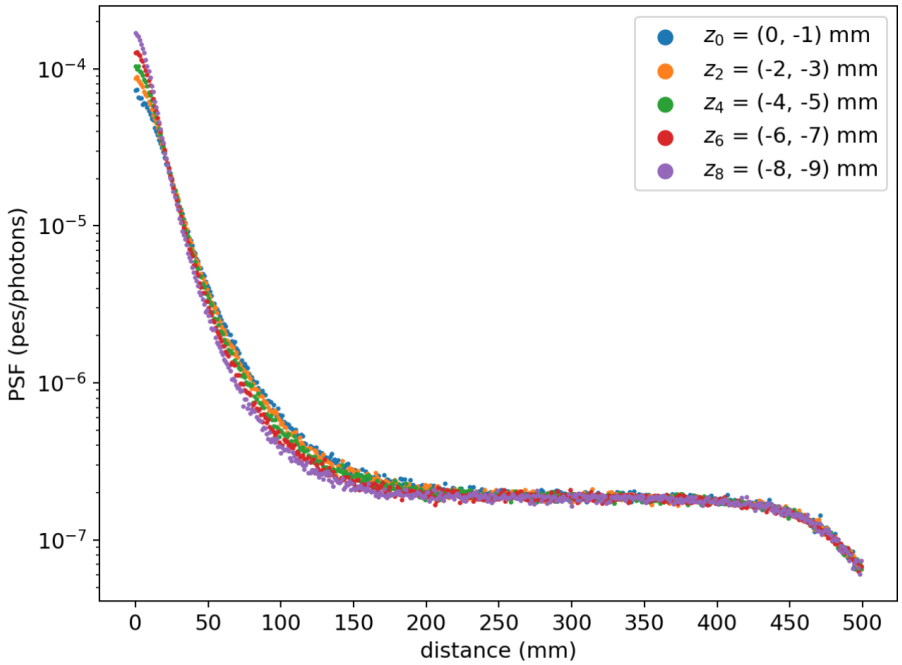


Figure 4.6: PSF for the NEXT-100 detector for several EL partitions. By convention, the EL gate is placed at $z = 0$ with $z < 0$ for the EL-region. The EL-region width is 10 mm, thus $z_p \in [-10, 0]$ mm.

distances, the emission points are uniformly simulated inside a cylinder of small radius centered at $x, y = 0, 0$ and covering the z extent of the EL-region. This is accomplished with a dedicated NEXUS vertex generator. The reason for centering the cylinder at $x, y = 0, 0$ is to avoid the border effects at the edges of the chamber. As in the LTs production, the total number of photons simulated should be high enough to minimize statistical fluctuations in the SiPM signal.

The z values of the PSF will also be discrete and pre-determined in its production. In what follows (§4.3.4) we will denote the PSF z dependence with the integer index $p = 0, 1, 2, ...n_z$, where n_z is the total number of EL z partitions. Also, z_p will represent the distance between the EL gate and the p partition. Figure 4.6 shows the PSF as a function of z_p for the NEXT-100 detector.

4.3.4. The algorithm

The objective of the DETSIM algorithm is to have a reliable simulation procedure that overcomes the slow process of tracking all the individual particles and interactions in the full-simulation mode.

The algorithm's conceptual flow is shown Figure 4.7. The flow is sequential from top to bottom, starting from the fast-simulated track and returning the full detector response. We can identify two branches for the simulation of each type of signal, S1 and S2. Also, the algorithm's components are grouped in five different blocks that implement a certain functionality inside the flow: *hits filtering*, *electron simulation*, *photon simulation*, *signal simulation* and *waveform creation*. The description of the algorithm is presented below and the input parameters are summarized in Table 4.1.

The starting point of the algorithm is the fast-simulated *track*, which is a collec-

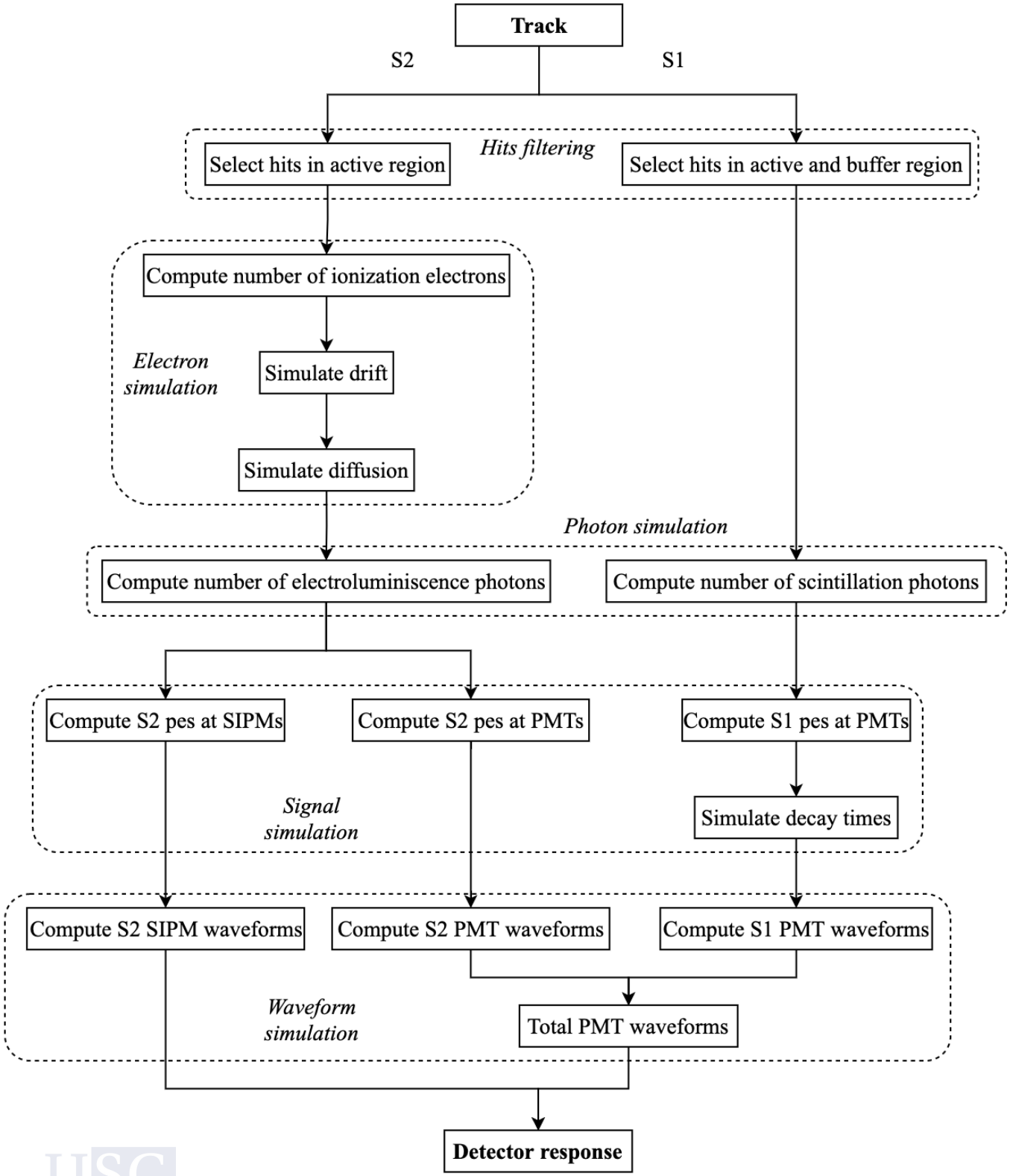


Figure 4.7: DETSIM flow diagram.

USC UNIVERSIDADE DE SANTIAGO DE COMPOSTELA

Table 4.1: List of DETSIM parameters used at each stage of the algorithm.

	Parameter
Electron simulation	inverse ionization yield w_{io}
	fano-factor F
	drift velocity v_d
	lifetime τ
	diffusion D_L, D_T
Photon simulation	inverse scintillation yield w_{sc}
	EL gain G_{EL}
	conde-policarpo factor J_{CP}
Signal simulation	EL drift velocity v_d^{EL}
	S1 Light Tables
	S2 Light Tables
	point spread function (PSF)
Waveform creation	pre-trigger time
	buffer length
	PMT waveforms bin width
	SiPM waveforms bin width

tion of *hits*. Recall that each hit is a five-dimensional vector of position, energy and production time (x, y, z, E, t) of the simulated event (Figure 4.3).

Hits filtering. Hit position determines in which region of the detector the energy deposition occurs. Energy depositions, ie ionization electrons, can only be created in the gaseous part of the detector which is composed by the *active*, *buffer* and EL regions. The ionization electrons drift towards the EL only if they are produced in the active region, therefore only hits at this region are selected in the S2 simulation. On the other hand, scintillation photons can be emitted and produce signal from anywhere inside the gas, thus the S1 simulation keeps all the hits in the active and buffer regions. Hits in the EL-region are removed to avoid duplication of S1 and S2 LTs and implementation complications. This is a good approximation since the S1 of tracks with hits in the EL-region is overlapped with the subsequent S2, and the event would be reconstructed anyway as an no-S1 event.

Electron simulation. This step starts by computing the ionization electrons produced in each hit, which is the value of the hit energy divided by the inverse ionization yield w_{io}. Defining $n = E/w_{io}$, the number of ionization electrons in a hit n'_{ie} is simulated

USC UNIVERSIDADE DE SANTIAGO DE COMPOSTELA

following the distribution

$$n'_{ie} \sim \begin{cases} \text{Pois}(n) & \text{if } nF < 1 \\ \text{Gauss}(\mu = n, \sigma = \sqrt{nF}) & \text{if } nF \geq 1 \end{cases}, \tag{4.7}$$

motivated by the definition of the fano-factor F. Next the electrons are drifted toward the EL region. During the drifting some of the electrons are absorbed due to impurity attachment, a process described by an exponential with characteristic lifetime τ. Or equivalently, the time it takes the drifting electrons to be absorbed t_{abs} is given by

$$t_{abs} \sim \text{Exp}(\lambda = \tau^{-1}). \tag{4.8}$$

Then the number of electrons that survive n_{ie} can be computed by

$$n_{ie} = \sum_{i=1}^{n'_{ie}} \begin{cases} 1 & \text{if } t^i_{abs} < t_{drift} \\ 0 & \text{if } t^i_{abs} \geq t_{drift} \end{cases}, \tag{4.9}$$

where $t_{drift} = z/v_d$ is the time it takes to the ionization electrons produced at z to reach the gate with drift velocity in the active volume v_d. The last electron physical process to simulate is the diffusion, characterized by the longitudinal and transverse diffusion coefficients D_L and D_T respectively. The position of each electron arriving at the gate is diffused following

$$X_{diff} \sim \text{Gauss}(x,\ D_T\sqrt{z}), \tag{4.10}$$
$$Y_{diff} \sim \text{Gauss}(y,\ D_T\sqrt{z}), \tag{4.11}$$
$$Z_{diff} \sim \text{Gauss}(z,\ D_L\sqrt{z}). \tag{4.12}$$

where x, y, z are the initial position of the electrons, ie the hit position in which they are created.

Photon simulation. The S1 photons are generated from the initial hits through the inverse scintillation yield w_{sc}

$$n_{S1} \sim \text{Pois}(E/w_{sc}) \tag{4.13}$$

The S2 photons are computed using the number of ionization electrons arriving at the EL n_{ie},

$$n_{S2} \sim \text{Gauss}\left(n_{ie}G_{EL}, \sqrt{n_{ie}G_{EL}J_{CP}}\right), \tag{4.14}$$

where G_{EL} is the EL gain (number of photons emitted by a single electron) and J_{CP} is the conde-policarpo factor (§3.2.3).

Signal simulation. In this stage we compute the photon-electrons (pes) measured in each sensor and their arrival times. The treatment is different for S1 and S2 signals and also for PMTs and SiPMs.

S1. In the photon simulation block, we computed the number of scintillation photons produced by each hit. By the definition of the S1 LT, the number of photo-electrons generated by the scintillation photons at x, y, z is given by

$$S_{S1}(\text{PMT}) \sim \text{Pois}(n_{S1} \times \text{LT}_{S1}(x, y, z|\text{PMT})). \tag{4.15}$$

The next step is to simulate the arrival time of the photons to the sensors, which is given by

$$t_{arrival} = t + t_{decay} + t_{travel} \tag{4.16}$$

where t is the hit production time, t_{decay} the scintillation decay time and t_{travel} is the time it takes the photons to go from the hit position to the particular PMT. The travel time is neglected in DETSIM since its simulation would require a complete photon propagation. The photon travel time is in fact negligible compared to the drift time of the ionization electrons that produce the S2, thus we can safely omit it (recall that S1 is used to compute the drift time of the event, namely its longitudinal position). The decay time is simulated for xenon using its fast and slow scintillation components [95] given by

$$t_{decay} \sim 0.1\ \exp(-t/\tau_f) + 0.9\ \exp(-t/\tau_s) \tag{4.17}$$

where $\tau_f = 4.5$ ns and $\tau_s = 100$ ns are the fast and slow scintillation decay times, respectively. For each measured photo-electron, a $t_{arrival}$ is computed. The total S1 signal would be given by the time histogram of the arrival times for the generated photo-electrons. The S1 signal at the SiPMs is not simulated.

S2. The computation of the number of photo-electrons in the PMTs is similar to that of the S1,

$$S_{S2}(\text{PMT}) \sim \text{Pois}(n_{S2} \times \text{LT}_{S2}(x, y|\text{PMT})), \tag{4.18}$$

but the arrival times are treated differently. The arrival time will be given by the sum of the production time, the drift time and the EL emission time,

$$t_{arrival} = t + t_{drift} + t_{EL}. \tag{4.19}$$

The drift time is given by $t_{drift} = z/v_d$. The t_{EL} is the emission time at the EL gap. Assuming that photons are emitted uniformly throughout the EL gap,

$$t_{EL} \sim \text{Uniform}(0, T_{EL}) \quad \text{with} \quad T_{EL} = \frac{w_{EL}}{v_d^{EL}}, \tag{4.20}$$

where w_{EL} is the width and v_d^{EL} the drift velocity in the EL. Notice that we are implicitly neglecting the travel time from the emission point to the sensor, which is much lower that the drift and EL times.

The signal in the SiPMs is computed with the PSF function. Recall that the PSF is z dependent, covering the EL width in several partitions. For an ionization electron arriving at the EL at position x, y and emitting n_{S2} total photons, the signal produced at the SiPM at distance d would be

$$S_{S2}(\text{SiPM}, z_p) \sim \text{Pois}\big(n_{S2}/n_z \times \text{PSF}(d|z_p)\big), \tag{4.21}$$

where n_z is the total number of EL partitions. Notice that this is the signal produced by photons emitted at partition z_p, which are assumed to be uniformly emitted throughout the EL width. The arrival times would also depend on the partition

$$t_{arrival\ p} = t + t_{drift} + t_{drift\ p} + t_{EL\ p} \tag{4.22}$$

where $t_{drift\ p} = |z_p|/v_d^{EL}$ and

$$t_{EL\ p} \sim \text{Uniform}\big(0, \Delta T_p\big) \quad \text{with} \quad \Delta T_p = \frac{w_p}{v_d^{EL}}, \tag{4.23}$$

USC UNIVERSIDADE DE SANTIAGO

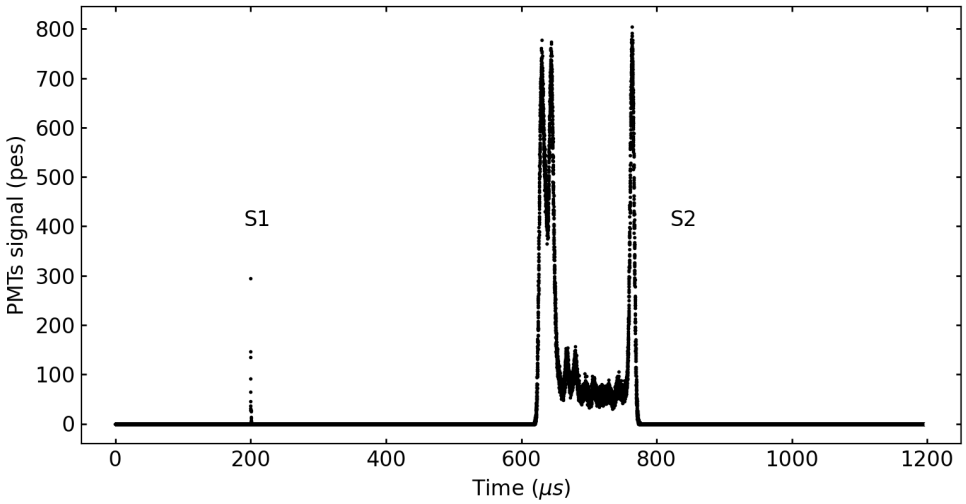


Figure 4.8: Summed PMT waveforms for a $0\nu\beta\beta$ event after a DETSIM simulation. The buffer length of the waveform is 1200 μs and the pre-trigger time (S1 placement) is 200 μs. The waveform is not zero-suppressed.

where w_p is the partition width. Again, in both PMTs and SiPMs the arrival time is computed for each measured photo-electron.

Waveforms creation. By definition, a waveform is a time histogram of the arrival times. Therefore this step consists of histograming the photo-electron's arrival times for each sensor. The PMT and SiPM waveforms are assumed to have the same *buffer-length* but different *bin width*. By convention the waveform times go from 0 to buffer-length, and in order to mimic the DAQ triggering system we add an extra *pre-trigger buffer time* that fixes the start of the signals inside the buffer. An example is shown in Figure 4.8. Notice that DETSIM waveforms are non zero-suppressed as they are in the full-simulation output in Figure 4.2.

There is no explicit reference to the concrete detector being simulated in the algorithm. All geometry considerations are codified in the LTs and the PSFs. Of course, in order to obtain consistent simulations the LTs and PSFs used must belong to the same detector.

4.3.5. Implementation details and performance

Determining the best implementation for the DETSIM algorithm was not a trivial task. In order for the algorithm to be publicly accessible by all the potential users it should be constrained to the rules of the collaboration software framework for data production, IC (Chapter 5). This software is mostly written in *Python*, which presents disadvantages in the DETSIM implementation for reasons that will be clear below.

In order to compute the number of photo-electrons at the light sensors, the algorithm must loop over the photo-emission points, namely the direct scintillation emissions from the track for the S1 signal and ionization electron emissions at the EL for the S2 signal. This is a two-level loop for the signal at the EP: a loop over PMTs and over emission points; and a three level loop for TP: a loop over SiPMs, emission points and EL partitions. As long as the number of iterations is relatively small, *Python* performance is similar to a lower level language like *C*. This is the case for S1 signal

Table 4.2: Simulation time for single ^{83m}Kr and $0\nu\beta\beta$ events in the full and fast simulation modes. The times are mere estimations as they can vary between the CPU employed and detector conditions of the simulation.

Event type	Energy (keV)	full-simulation + BUFFY [1]	fast-simulation + DETSIM
^{83m}Kr	41.5	1-2 mins	$\sim$2 s
$0\nu\beta\beta$	2458	1-2 hours	$\sim$20 s

simulation, since at $Q_{\beta\beta}$ the number of hits is $\sim$ 600 and PMTs $\sim$ 60 for NEXT-100. Nevertheless the number of ionization electrons at $Q_{\beta\beta}$ is $\sim 10^5$, thus the number of S2 iterations for PMTs is $\sim 10^3$ times higher than for S1. The number of SiPMs is around 60 times higher than the PMTs and the EL is also partitioned, raising the number of iterations by two orders of magnitude. In this scenario the number of S2 iterations becomes unmanageable in *Python*. This problem was solved using *Cython* [124], a third party tool which allows one to easily write *C* extensions to *Python*. In this way the functions used to compute the photo-electrons arriving at each sensor are written in *C* and called when needed, allowing the algorithm to be implemented within the IC software framework.

Another implementation detail that improves the simulation time is how we deal with the generation of arrival times for the measured photons in the S2. Instead of generating an independent arrival time for all the photons, we use the fact that the EL emission is uniform. In this way, we first create a waveform object that histograms the arrival time of ionization electrons at the EL gate ($t + t_{drift}$) weighted by the number of measured photons at that time. Afterwards, the effect of uniform EL emission is generated over the waveform by uniformly distributing the photoelectrons in each time bin in their next time bins within T_{EL}. The same approach is used for the SiPM response, taking into account the partition time ΔT_p. This approach is not used for S1 due to the much lower number of photons detected.

Recall the output type of each NEXUS mode of simulation: full-simulation provides a zero-suppressed waveform (Figure 4.2) and fast-simulation provides a set of track-hits (Figure 4.3). After the fast-simulation, DETSIM computes the signal waveforms for each light sensor. These waveforms are not zero-suppressed (4.8), unlike full-simulation output. Then, in order to compare computation times between fast and full modes we also need to *bufferize* the full-simulation waveforms. The bufferization takes zero-suppressed waveforms and creates the full-simulation not zero-suppressed waveforms, setting the buffer length and the pre-trigger buffer time. We can define the *full* mode of simulation by the combination of NEXUS full-simulation and bufferization, and the *fast* simulation mode by the combination of NEXUS fast-simulation plus DETSIM. However, the computation time of bufferization is negligible compared to the full-simulation time in the full mode; and the computation time of fast-simulation is negligible in the fast mode. Table 4.2 shows the computation times for commonly simulated events ^{83m}Kr and $0\nu\beta\beta$.

As stated at the start of this chapter, DETSIM is based on a previous work done in [122]. The main drawback of the old implementation is that it is only valid for the NEXT-White detector. Instead of using the LTs and PSFs to compute the arrival photons

directly from a database of precomputed values, it uses a parametrized model of these tables. The new DETSIM avoids the burden of creating the parametric model of light collection, since LT and PSF computed values are saved and easily accessible by using a *hdf5* file format [125]. Also, the old implementation was entirely written in *C++* and not included in the IC framework.

4.3.6. Validation

DETSIM substitutes photon propagation by PMT light tables and the SiPM point spread function. As described in §4.3.5 the computation time is improved around a factor of 300 with respect to the full-simulation for events at $Q_{\beta\beta}$. This makes large exposure studies feasible since large datasets can be generated on a relative small time scale, which would be impossible for full simulated events. This section is dedicated to compare the results of full and fast simulations.

To validate DETSIM, we perform full and fast simulations of around 10 thousand ^{83m}Kr and 3 thousand $0\nu\beta\beta$ events in the NEXT-100 detector. The gas conditions are the same in both simulation modes: 10 bar pressure, 14 kV/cm EL field and 1.2 and 0.3 mm/sqrt(cm) transverse and longitudinal diffusion, respectively. Both full and fast simulation datasets are processed with the standard NEXT reconstruction procedure (Chapter 5) until the creation of DSTs. The DSTs are data tables with information of several variables of interest for each event, such as total S2 PMT energy. Neither geometrical nor lifetime corrections are performed in this processing in order to compare raw quantities.

A minimal set of selections on signal variables is performed in the data processing, with the same parameters used for full and fast simulation datasets. The efficiency achieved by the minimal set of cuts is 99.9%, thus virtually all simulated events are reconstructed by the software chain. Another minimal required selection which allows to reconstruct the event drift position is the selection of events with a unique S1, discarding events with overlapped S1 and S2 signals. The results are shown below for the two types of events.

^{83m}Kr

Distributions for S1 variables for fast and full simulation modes are shown in Figure 4.9. Due to their large variability we do not compare the S1 variables for each event, but the whole distributions. The S1 energy, which depends on the S1 LT, is well reproduced in the fast simulation. On the other hand, the height and width do not match. The reason comes from one of the assumptions described above: DETSIM neglects the travel time in (4.16) because photon propagation is neglected. This travel time depends on the particular trajectory of each photon. This mismatch is not problematic since S1s are properly found, but it is worth noticing for data-MC comparisons.

The comparisons in the S2 variables are shown in Figure 4.10. We show the distribution of the ratios between the full and fast simulation variables for each event. Notice the good match in S2 energy, width, height and maximum SiPM charge. The last represents the time integrated maximum charge seen by a SiPM. On the other hand, the total charge of the event is slightly biased. This bias is understood in Figure 4.10f. At higher radius, the full simulated events have more charge due to the non-

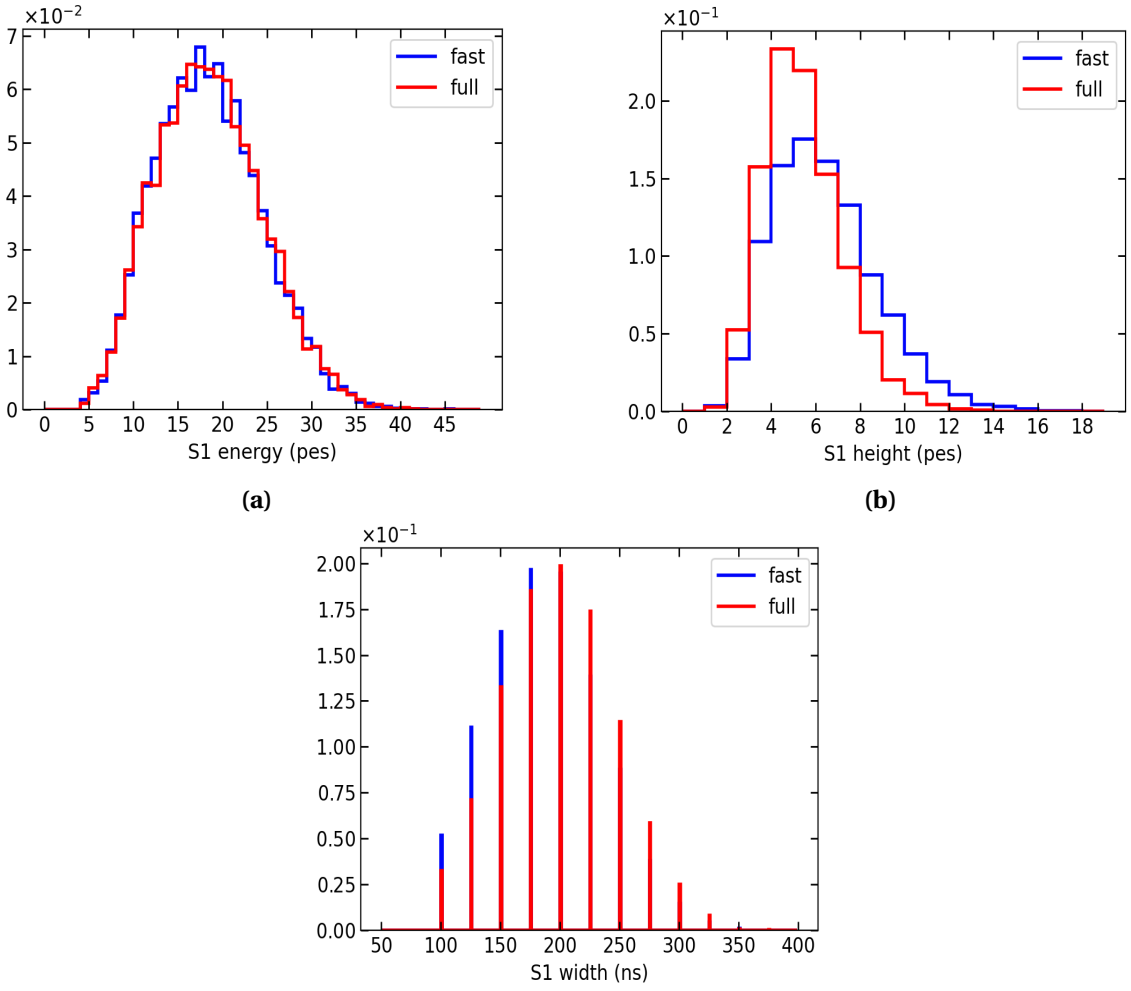


Figure 4.9: S1 energy, height and width distributions for fast and full modes of simulation of ^{83m}Kr events. The difference in height and width arises from the lack of simulation of travel time in DETSIM.

USC UNIVERSIDADE DE SANTIAGO DE COMPOSTELA

radial dependence of the PSF in DETSIM. Recalling §4.3.3, the PSF is computed from the center of the chamber, but at high radius the PSF changes due to the different reflection patern.

$0\nu\beta\beta$

The plots for the S1 and S2 are shown in Figure 4.11 and 4.12, respectively. Notice the difference arising in the S1 height and width, as it occurs in the ^{83m}Kr simulation. Also the S2 charge difference is correlated with the radial position due to the radial PSF dependence not being implemented in DETSIM. The $0\nu\beta\beta$ are extended events and this causes the radial bias to be larger than in ^{83m}Kr events.

Notice also the slight tail at the S2 energy ratio (Figure 4.12a) from events with hits near the borders. It is identified as a lower resolution of the LT for that region, in wich the change of light collection varies faster. A finer LT would be needed, at the expense of a larger computational effort as more points are simulated.

4.3.7. Conclusions

We found several limitations of DETSIM that prevent the exact reproduction of the full-simulation. Nevertheless the limitations are not relevant considering the purpose for which DETSIM will be used. Recall that DETSIM is intended as a fast replacement of the full-simulation in order to allow for large exposure background studies. Even though DETSIM variables match reasonably well, there are some mismatches that would be relevant in pure data-MC comparisons. Also the data reconstruction is barely affected by those differences. Slight charge disagreement is not important from the point of view of its use in NEXT detectors, the TP signals are relevant for tracking and its exact absolute levels are not important, but the relative contribution to each hit. Also, the cause of the disagreement was identified and understood as a different light pattern due to border effects which are not reproduced in DETSIM.

Finally, the tails in the S2 PMT energy will vanish after map corrections and the same energy resolutions are obtained for both full and fast simulation modes. It is worth noting that the simulations performed in this section correspond to an old version of NEXT-100 detector different from the final design, which is described in the next section.

USC UNIVERSIDADE DE SANTIAGO DE COMPOSTELA

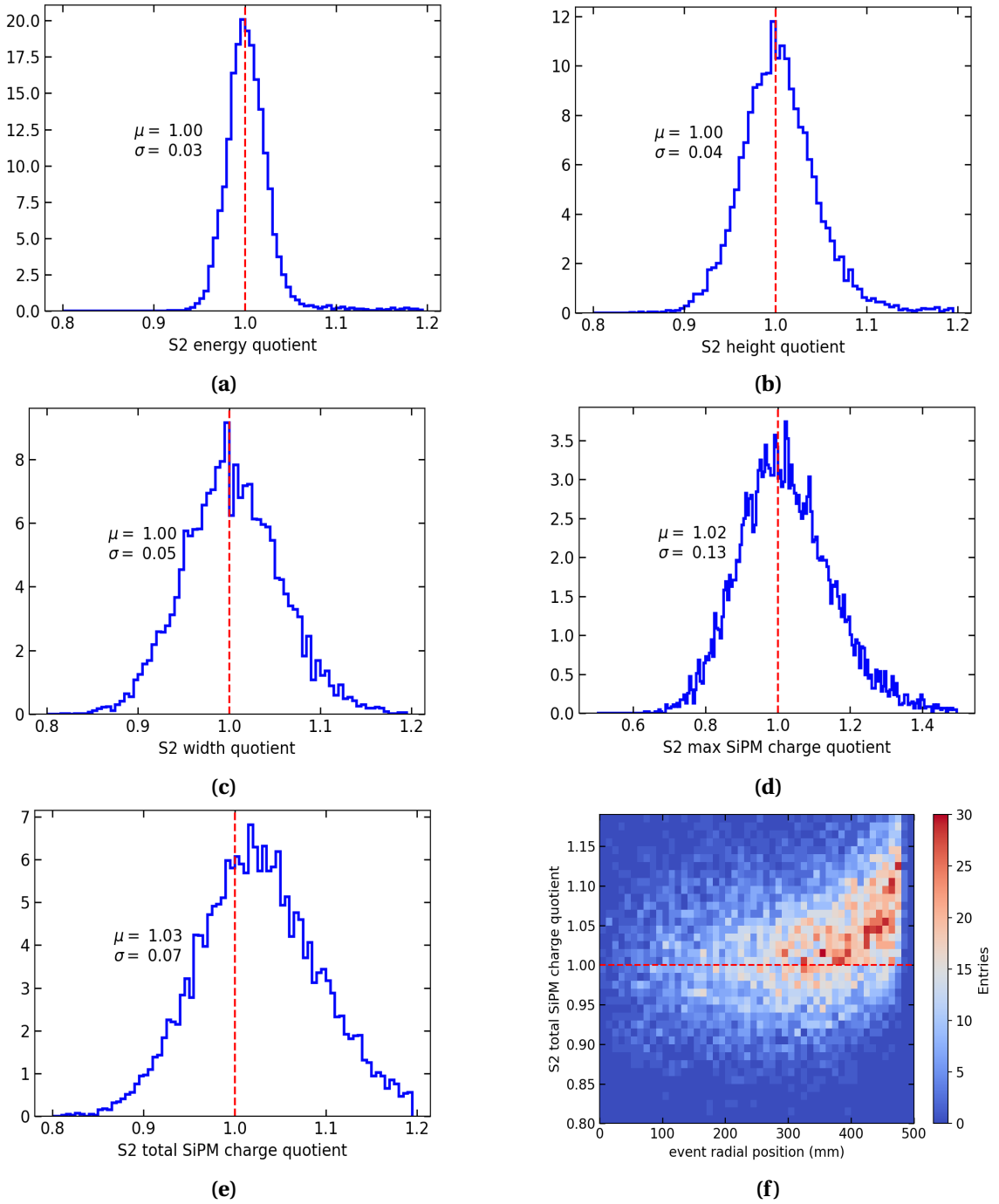


Figure 4.10: Full and fast simulation quotient between S2 variables for ^{83m}Kr events. Red dotted line is plotted at unit quotient for visualization purposes only. Bottom right plot shows the 2D correlation between the total S2 charge at TP and event radial position.

USC UNIVERSIDADE DE SANTIAGO DE COMPOSTELA

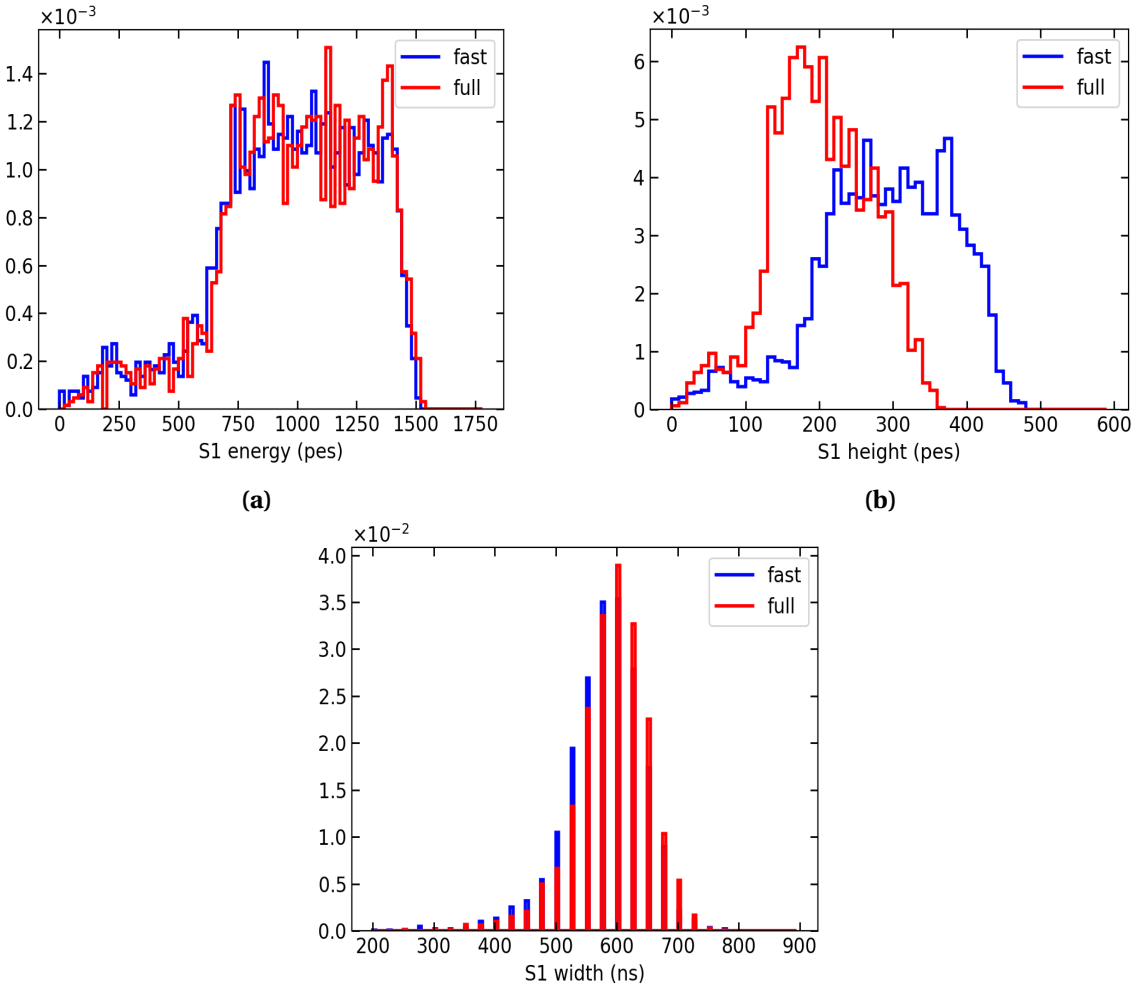


Figure 4.11: S1 energy, height and width distributions for fast and full modes of simulation of $0\nu\beta\beta$ events. The difference in height and width arises from the lack of simulation of travel time in DETSIM.

USC UNIVERSIDADE DE SANTIAGO DE COMPOSTELA

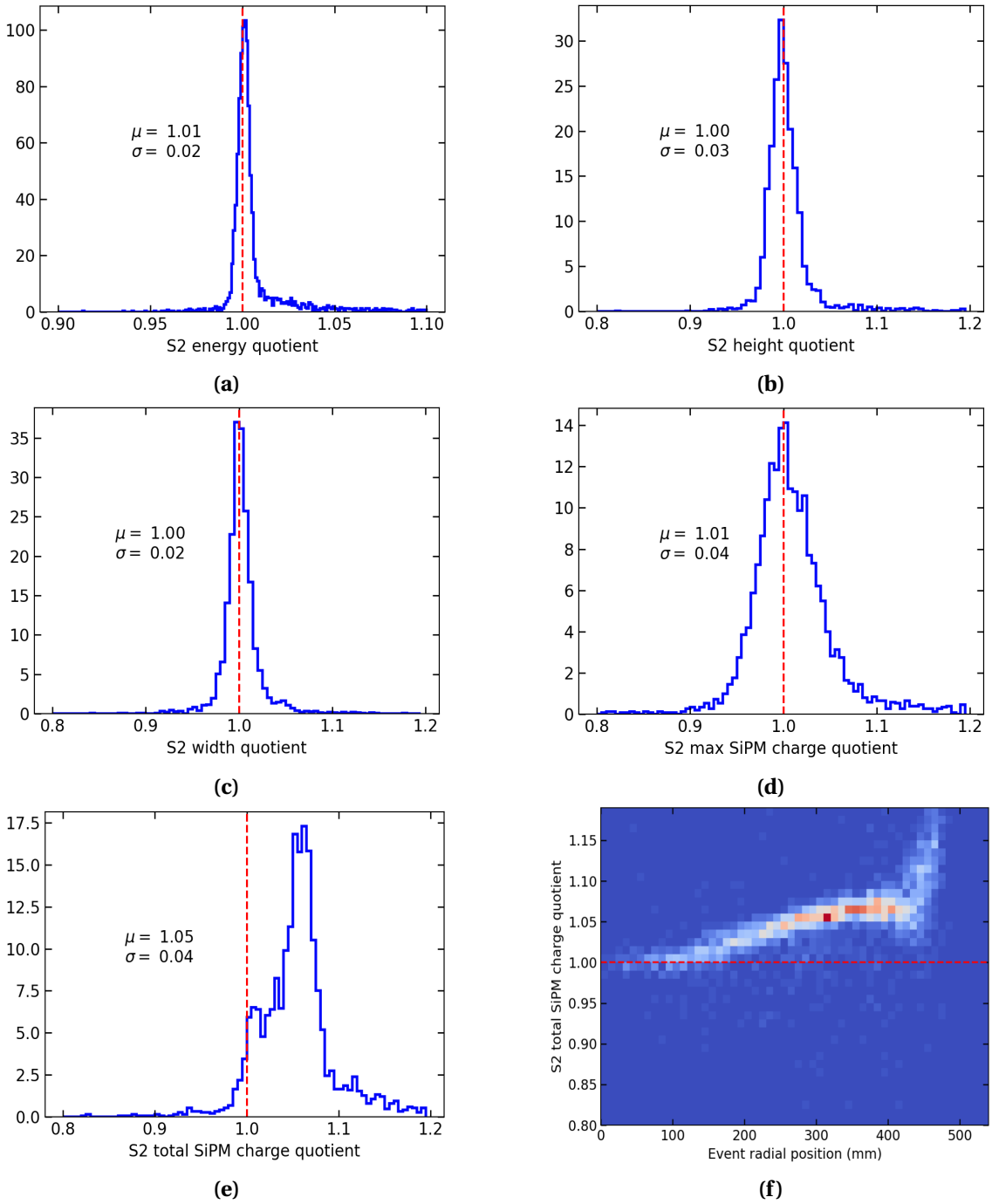


Figure 4.12: Full and fast simulation quotient between S2 variables for $0\nu\beta\beta$ events. Red dotted line is plotted at unit quotient for visualization purposes only. Bottom right plot shows the 2D correlation between the total S2 charge at TP and event radial position.

USC UNIVERSIDADE DE SANTIAGO DE COMPOSTELA

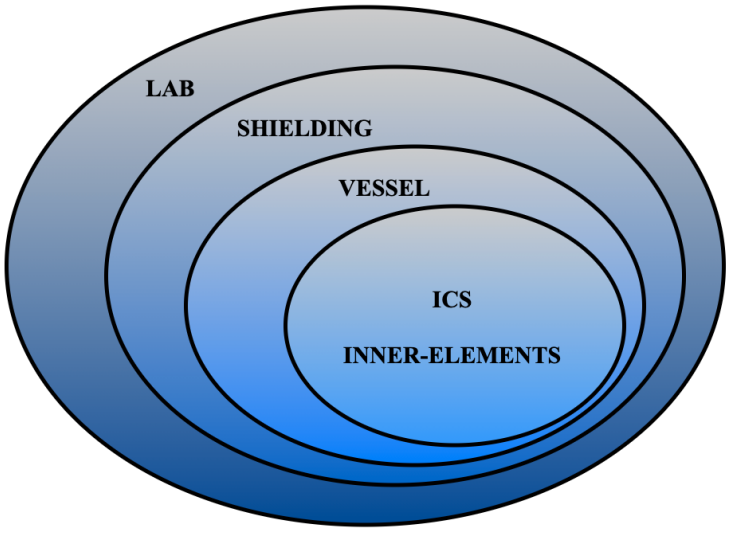


Figure 4.13: Volume organization of the NEXT-100 geometry.

4.4. NEXT-100 implementation in NEXUS

In this section we describe the geometrical implementation of NEXT-100 geometry in NEXUS. Simulation parts related to the event generation, physics lists and user actions (see Figure 4.1) are general for all other NEXT detectors and will not be detailed here (physical processes are described in §4.3.4).

The geometrical implementation of NEXT-100 detector is based on the engineering design drawings. Each detector sub-elements in the drawings are extremely detailed, since they must exactly fit during assembly. It is not the purpose of the simulation to implement each screw and nut of the detector, but to contain all the relevant volumes with the proper dimensions and relative placements. The implementation in NEXUS is a simplified but accurate geometry that reproduces the real NEXT-100 detector.

The geometrical implementation of NEXT-100 detector inside NEXUS follows the specifications provided by GEANT4 [123], which is written in the *C++* programming language. In this framework, each detector volume must be placed inside another, with the highest level volume known as WORLD. The NEXT-100 volumes are grouped in the following larger logical volumes LAB, SHIELDING, VESSEL, ICS and INNER-ELEMENTS each one contained within another as schematically shown in Figure 4.13. INNER-ELEMENTS volume contains the most relevant parts of the detector, being composed by the FIELD-CAGE, ENERGY-PLANE and TRACKING-PLANE. The surrounding volumes are needed in order to simulate the propagation of the external backgrounds from the different materials and from outside the shielding castle in the LSC laboratory hall. The whole detector is inside the LAB volume, which defines the laboratory walls from which external backgrounds can be simulated, such as natural radiactivity, neutrons and muons. Muon simulation, of particular interest in this thesis, is implemented using the angular distribution of the muon arrival direction inside the laboratory.

A relevant simulation feature in the event or primary generation are vertices from which an event is simulated. NEXUS has the ability to choose from which detector volume a certain event must be simulated. For example, ^{83m}Kr events are simulated from the ACTIVE volume inside the FIELD-CAGE, calibration ^{137}Cs source are simulated from the dedicated PORT-TUBES inside the VESSEL, or ^{208}Tl and ^{214}Bi events might be

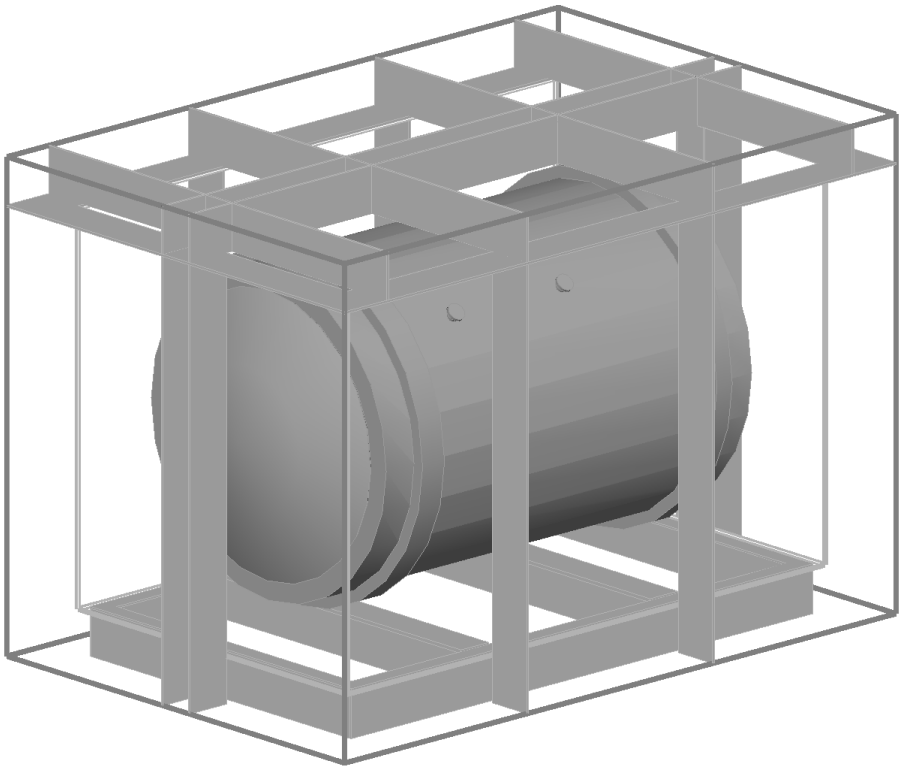


Figure 4.14: NEXUS implementation of the external shielding. The figure shows the LEAD-BOX (dark-grey) and the internal STEEL-BOX (light-grey). The VESSEL is also shown inside the shielding box.

simulated from any radioactive volume such as the SiPM DICE-BOARDs at the TRACKING-PLANE. Table 4.3 list most of the volumes and vertices implemented in the geometry of NEXT-100 detector. Vertices are mostly used for background simulation, like ^{214}Bi decays. Its decay products are propagated and they may reach the ACTIVE volume producing a measurable signal. In general only those volumes with a significant radioactive budget are implemented. The ACTIVE volume contains a vertex used for physics simulations, namely events that take place at the xenon bulk like ^{83m}Kr or $\beta\beta$ events. High energy calibration events like ^{137}Cs are simulated at the four dedicated PORT-TUBE volumes. Also, EL-GAP vertex is used for the creation of SiPM light table or PSF (§4.3.3).

The NEXT-100 external SHIELDING castle (see Figure 4.14), is composed by a LEAD-BOX supported by steel BEAMs and an internal STEEL-BOX. The VESSEL is contained within this doubly layered box and supported by a steel beam PEDESTAL filled with lead, such that the detector is fully surrounded by an external lead shielding.

The NEXT-100 VESSEL hosts another shielding layer, the ICS (inner copper shielding). The ICS protects against external gamma radiations, and contains four holes for the calibration PORT-TUBEs and four more for the not implemented high voltage feedthroughs. The energy and tracking planes are also supported by its corresponding copper plates, fully shielding the interior of the active volume (Figure 4.15).

The energy plane (Figure 4.16) is composed by the holed EP-COPPER-PLATE with 60 PMTs. The holes are separated from the xenon gas by the sapphire window, and contain both the PMT and its electronics PMT-BASE, included due to its large radioactivity. The

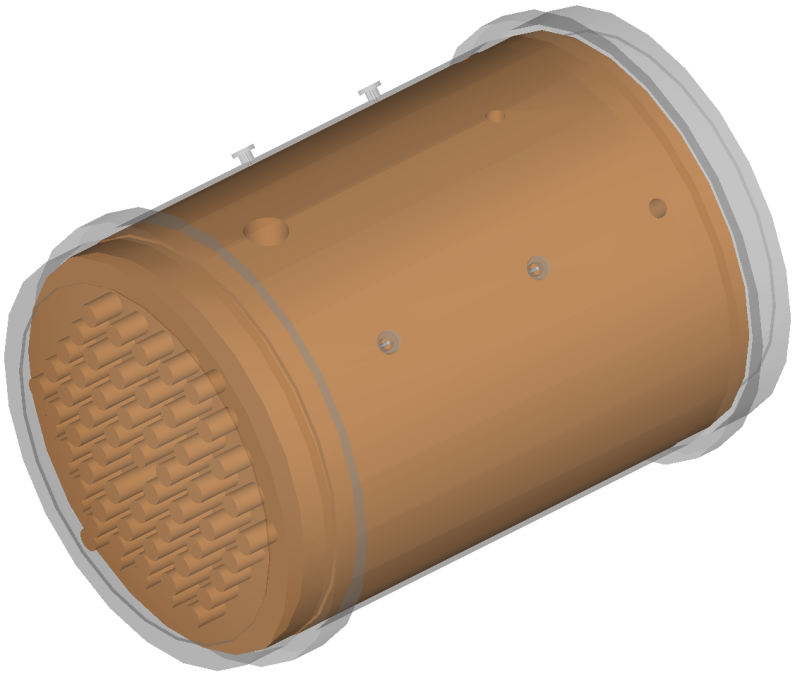
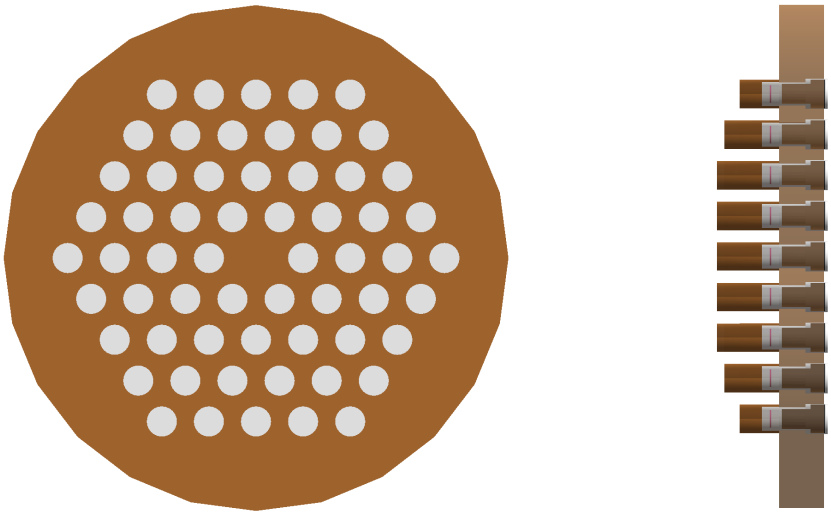


Figure 4.15: Copper shielding inside the VESSEL. The copper shielding is composed by a central copper cylinder, the ICS, and the energy and tracking copper plates. The four port holes are also shown at the detector laterals, as well HVFT holes (one in the lateral and two in the upper part). VESSEL has ∼200 cm length and ∼68 cm radius.

PMT itself is also composed by the body, the photo-cathode, where the arriving photons are counted, and the window which simulate the optical properties provided by the manufacturer. Also, the sapphire window is covered by a thin volume of TPB simulating the wavelength shifting.

The tracking plane (Figure 4.17) is composed the TP-COPPER-PLATE which holds the SiPM boards. The boards are composed by 56 kapton SIPM-BOARDs with an array of 8x8 SIPMs each, and covered by 6 mm teflon SIPM-BOARD-MASK, holed at the SiPM's positions. Both the mask and the SiPM's windows are covered by a thin TPB volume. The SIPMs are built following the manufacturer specifications, composed by a window and sensitive area were photons are ultimately measured. The back part of the TP-COPPER-PLATE also contains the DB-PLUGS, which are the connectors between the front kapton SIPM-BOARDs and the external electronics. The DB-PLUGS are implemented due to their relatively large radioactivity, which must be accounted in the total background budget. Simulation of sensor electronics (both for PMTs and SiPMs) is not implemented in NEXUS, but within the IC framework §5.2.

Inside the copper shielding we find the most important part of the detector, the FIELD-CAGE (Figure 4.18). The detector medium, the xenon, is divided in three regions: ACTIVE (from cathode to gate), BUFFER (from sapphire windows to cathode) and EL-GAP (from gate to anode). The electrodes are implemented with two different volumes, the grid and the ring. The electrode grids are simulated as a transparent dielectric material which implements the measured transparency of the real meshes, instead of implementing the full wire pattern. The xenon is surrounded by the teflon LIGHT-TUBE, coated with wavelength-shifting TPB. The external part of the tube implements the copper FIELD-RINGs holded by the PE500 RING-HOLDERs. Both materials are only implemented in order to provide the correct amount of material as seen by external



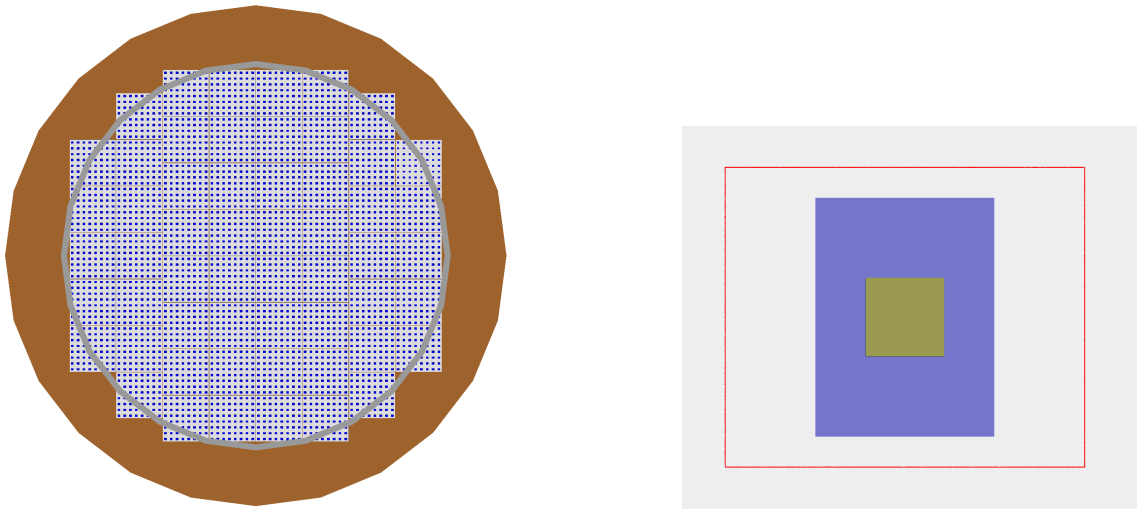
(a) front **(b)** lateral

Figure 4.16: NEXT-100 energy plane views. The front view shows the sapphire windows protecting the PMTs inside the copper plate. The lateral view shows the PMTs and the PMT-BASES (red). EP-COPPER-PLATE has 67 cm radius and 12 cm thickness.

background events, but do not play any role in the drift electrostatic field inside the gas which is assumed uniform in the simulation. The HDPE-TUBE is also included.

Particles arriving or decaying in the ACTIVE volume interact with xenon producing ionization electrons which are drifted toward the EL-GAP, after traversing the GATE-GRID. Inside the EL-GAP, the electrons produce the EL light which is measured at the sensors. Figure 4.19 shows an example of a simulated event in NEXUS.

USC UNIVERSIDADE DE SANTIAGO DE COMPOSTELA



(a) front **(b)** SiPM inside mask hole

Figure 4.17: NEXT-100 tracking plane views. The front view shows the teflon SIPM-BOARD-MASKs (white) in the copper plate with the SiPM holes (blue). The ANODE-RING is also show (grey). The right image shows a SIPM inside its mask hole. The 6×5 cm^2 hole walls (red) and the SiPM window (blue) are coated with TPB. The photo-sensitive area behind the SiPM window is also shown (yellow).

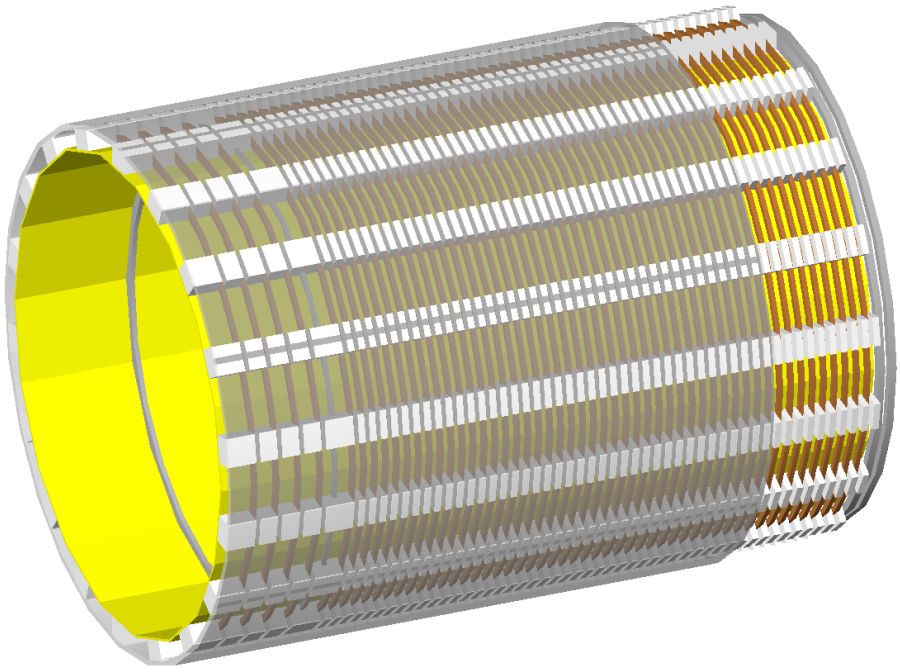


Figure 4.18: Elements of NEXT-100 field cage. The teflon panels that makeup the LIGHT-TUBE are shown in yellow. In the front side it is show part of the CATHODE-RING, and the GATE-RING and ANODE-RING are shown in the back (grey). The tube is surrounded by the copper FIELD-RINGs and the RING-HOLDERs (white). The HDPE-TUBE is shown partly transparent in order to visualize the inner elements. Field cage has ~ 120 cm length and ~ 42 cm radius.

Table 4.3: Main volumes and vertices implemented in the NEXT-100 detector at NEXUS. Sensor (PMT and SIPM) materials are not specified since they are composed by several sub-volumes with different materials each.

Group	Volume	Material	Vertex	Use
SHIELDING	LEAD-BOX	Lead	No	-
	STEEL-BOX	Steel	Yes	Background
	PEDESTAL	Steel	Yes	Background
	BEAMS	Steel	Yes	Background
	INNER-AIR	Air	Yes	Background
VESSEL	VESSEL	Steel	Yes	Background
	PORT-TUBE	Air	Yes	Calibration
ICS	ICS	Copper	Yes	Background
INNER-ELEMENTS				
ENERGY-PLANE	EP-COPPER-PLATE	Copper	Yes	Background
	SAPPHIRE-WINDOW	Sapphire	Yes	Background
	OPTICAL-PAD	Silicone	Yes	Background
	PMT	-	Yes	Background
	PMT-BASE	Kapton	Yes	Background
TRACKING-PLANE	TP-COPPER-PLATE	Copper	Yes	Background
	SIPM-BOARD	Kapton	Yes	Background
	SIPM	-	No	-
	SIPM-BOARD-MASK	Teflon	No	-
	BOARD-PLUGS	Peek	Yes	Background
FIELD-CAGE	ACTIVE	Xenon	Yes	Physics
	BUFFER	Xenon	Yes	Background
	EL-GAP	Xenon	Yes	PSF
	LIGHT-TUBE	Teflon	Yes	Background
	FIELD-RING	Copper	Yes	Background
	RING-HOLDER	PE500	No	-
	CATHODE-RING	Steel	Yes	Background
	ANODE-RING	Steel	Yes	Background
	GATE-RING	Steel	Yes	Background
	HDPE-TUBE	HDPE	No	-

USC UNIVERSIDADE DE SANTIAGO DE COMPOSTELA

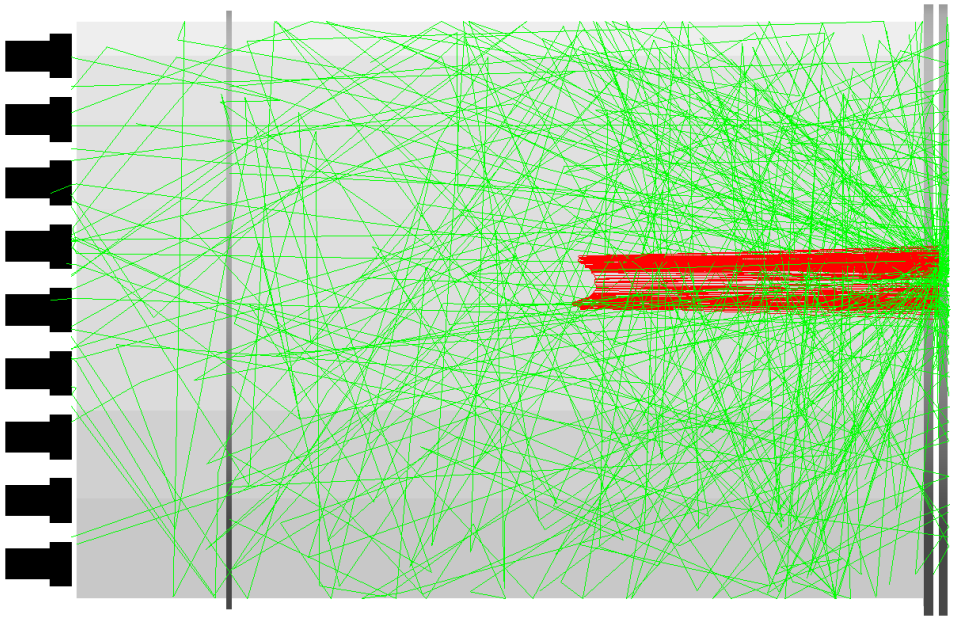


Figure 4.19: Simulation of a 2 MeV electron track at the center of the chamber in NEXT-100. From the main track the ionization electrons are drifted towards the EL gap (red). The photons generated at the EL (green) are collected at the sensors. The S1 signal is not visible due to the larger amount of EL photons. Both the ionization and EL yields are modified in this simulation for visualization purpose.

USC UNIVERSIDADE DE SANTIAGO DE COMPOSTELA

USC
UNIVERSIDADE
DE SANTIAGO
DE COMPOSTELA

CHAPTER 5
Data processing in NEXT

5.1. Introduction

The DAQ system in NEXT detectors is continuously reading the signals at the light sensors. When a valid trigger is found, the event is saved for further processing. The first step consists in decoding the sensor signals into a human readable format [115] in the form of *raw-waveforms*.

In this Chapter we will introduce the data processing stages from the raw-waveforms to the higher level data structures used in the NEXT analysis. We start introducing the processing pipeline in Section 5.2. In Section 5.3 we describe the set of algorithms employed within the pipeline. Finally Section 5.4 highlights some implementation details of the software framework.

5.2. Processing pipeline

The data processing in NEXT is divided into several logical units called *cities*. A city reads some type of event data as input, applies some operations or algorithms over it and outputs the result. The parameters of these transformations are controlled via configuration files. The processing city pipeline in NEXT is schematically shown in Figure 5.1, where city names are mostly taken from the cities in Italo Calvino's book *Invisible Cities* [126].

The processing pipeline is slightly different for MC and detector data. The MC full-simulation zero-suppressed waveforms (Figure 4.2) are processed in BUFFY to produce binned non-zero-suppressed MC raw-waveforms. The same output data structure is produced after DETSIM over the fast-simulation MC hits. The next cities are DIOMIRA and IRENE or HYPATHIA. DIOMIRA is a city that simulates sensor electronics and IRENE finds the signals in the waveform buffer. The output of DIOMIRA is therefore indistinguishable from the data raw-waveforms. In some cases you might want to skip the simulation of the electronics, for example if you do not know the sensor calibration constants. Then you can simply use HYPATHIA to find the signals in the MC buffers.

After IRENE, the processing is the same for MC and real detector data. At this point, it is divided for *trigger-1* and *trigger-2* data. Trigger-1, essentially low energy ^{83m}Kr and x-rays, provides two relevant data objects to perform corrections over the high energy trigger-2 data: the *map* and the *PSF*. Processing of trigger-2 data finishes with ISAURA that outputs the high level per-track and event information used in NEXT analysis.

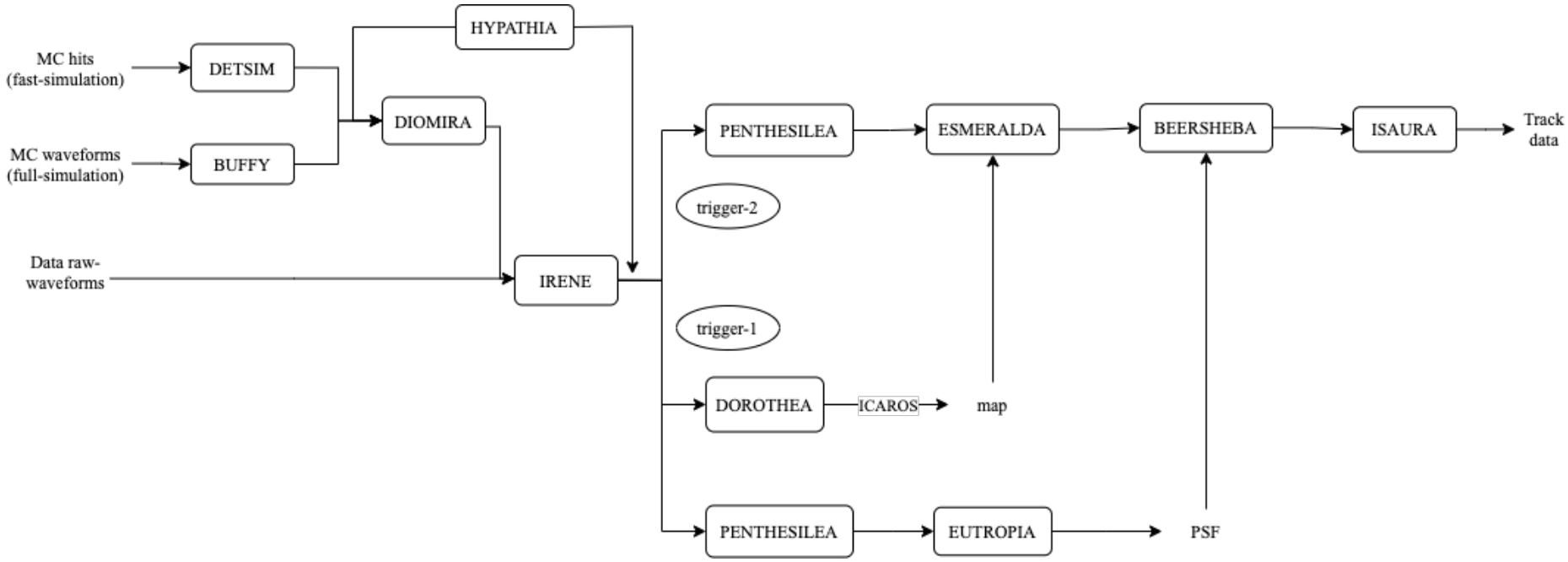


Figure 5.1: NEXT processing pipeline. Logical units (cities) are shown in boxes and data-like inputs and outputs as unboxed text. The separation of trigger-1 and trigger-2 processing is also shown. See text for details.

USC UNIVERSIDADE DE SANTIAGO DE COMPOSTELA

Table 5.1: Summary of the input and output data structures of the IC cities. More detailed description about the algorithms are given in the text.

	Input	Output	Description
DETSIM	MC track	Sensor wf	Simulates sensor response from fast simulated events
BUFFY	MC zero-sup. wf	Sensor wf	Pads zero-suppresed wf
DIOMIRA	Sensor wf	Raw sensor wf	Simulates sensor electronics
IRENE	Raw sensor wf	PMAP	Deconvolutes raw wf and finds signal candidates
HYPATHIA	Sensor wf	PMAP	Finds signal candidates
DOROTHEA	PMAPS	DST	Produces data summary
PENTHESILEA	PMAPS	HDST	Produces raw hits
ESMERALDA	HDST	CHITS	Corrects raw hits using the krypton maps
BEERSHEBA	CHITS	DECO	Applies LR deconvolution
ISAURA	DECO	TRACKS	Finds tracks, applies BFS and finds *blobs*

Notice that PENTHESILEA is used in both trigger-1 and trigger-2 processing paths, since it is used with different configuration parameters.

Each city in the processing pipeline applies an algorithm to the input data in order to subtract relevant higher level information. A brief description of the transformations is shown in Table 5.1. A more detailed description of each city and its different data structures from a more technical point of view is given in [127].

5.3. Algorithms

In what follows we give a description of the several algorithms and transformations used in the data processing pipeline.

5.3.1. Simulation of sensor electronics

The result of DETSIM and BUFFY consist of sensor waveforms (not zero-suppressed MC raw waveforms), as shown in Figure 4.8. The signal units are photo-electrons (pes) since none of these cities simulates the electronic effects. In order for the MC simulations to resemble as much as possible to detector data we must introduce the electronic distortions into the MC raw-waveforms, performed at DIOMIRA.

Detector data is digitized in the DAQ, providing a waveform whose units and baseline are different from those simulated in MC. The units are ADC counts instead of photo-electron counts, and therefore we must know the experimentally measured

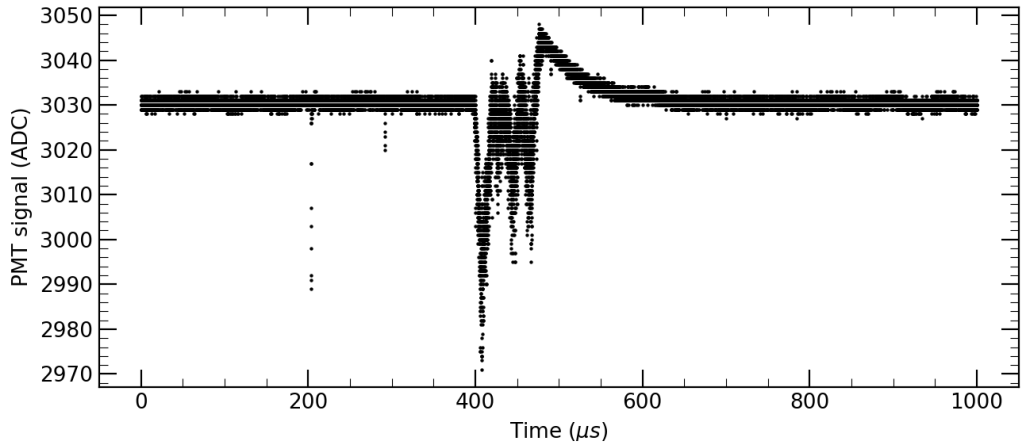


Figure 5.2: PMT trigger-2 raw-waveform from NEXT-DEMO. The simulation of electronic effects on MC would produce similar raw-waveform looks. We can clearly identify the RC baseline restoration of the electronics.

conversion constant [128], the sensor gain (g). This value is obtained from the single photo-electron distribution, which for PMTs will be gaussianly distributed with mean $\mu = g$ and variance $\sigma = \sigma_{1pe}$. Therefore the pes to ADC conversion consists on sampling each time bin entry with signal n_{pes} with a gaussian distribution with mean $\mu = g \cdot n_{pes}$ and variance $\sigma = \sqrt{g \cdot n_{pes}} \cdot \sigma_{1pe}$. For SiPMs the proccess is similar but the sampling is not gaussian but computed using its dark-noise PDF. Moreover, sensor waveforms must be ADC-translated to account for the characteristic baseline of the sensor depending on its bias voltage.

Due to the negative voltage configuration of the PMTs requiring and AC coupling scheme, its first order behaviour is that of a high pass filter (HPF) [113]. Therefore this functions must also be applied to the PMT waveforms which also depends on the experimentally measured parameters of the electronics. A PMT raw-waveform after the full electronic simulation would look as shown in Figure 5.2 which includes the ACD conversion, baseline translation and application of the HPF function. At this point the MC waveforms are indistinguishable from real detector data.

The raw-waveforms are not the objects that we can use to compute the number of photo-electrons measured at the sensors, which provide a directly proportional measurement of event energies. Therefore we need to transform the ADC counts to photo-electrons. Note that it might seem confusing since we have already described the inverse process, which only applies to MC. At this point we have data-like objects and we must process them equally for data and MC. The process of calibrating he raw-waveforms is performed in the first part of IRENE city, the process being the inverse of obtaining raw-waveforms from MC: apply the inverse function of the HPF (*Baseline Restoration algorithm*, BLR), translate the baseline to zero and ADC to pes conversion. The final result is shown in Figure 5.3, which resembles that of Figure 4.8 after DETSIM where electronics were not simulated.

USC UNIVERSIDADE DE SANTIAGO DE COMPOSTELA

5.3.2. Peak finding algorithm

After the raw-waveform is calibrated (Figure 5.3) we can easily find the signal peaks. This search is done in the second part of IRENE city. We should recall that the DAQ

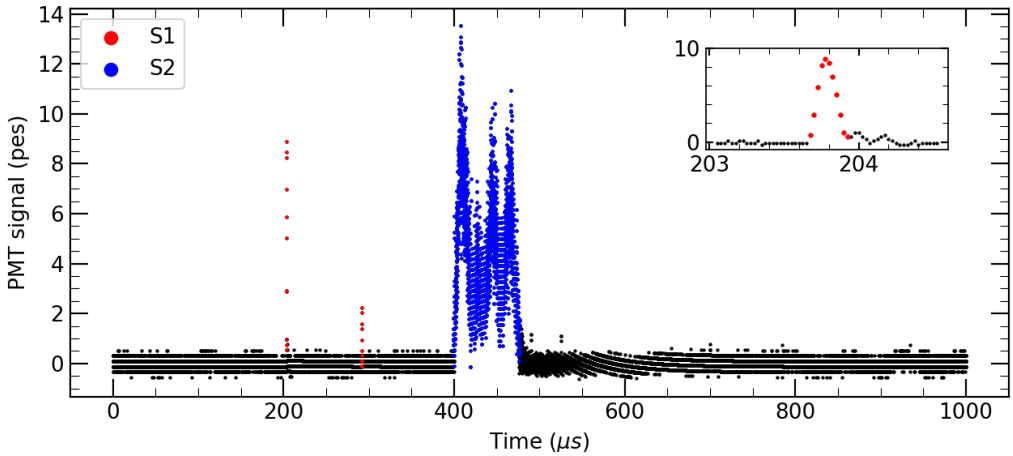


Figure 5.3: PMT calibrated waveform from Figure 5.2 showing the signals founded by the peak finding algorithm. Two S1 signals are found, the first shown in the upper right corner.

places the triggers (found S2s) at some fixed position in the waveform time buffer. For example the waveform in Figure 5.3 is placed at 400 μs. Then the peak finding algorithm will label all the signals above this point as S2s, and signals below as S1s. To find a signal we can simply request the selection of entries above some energy *threshold* (in pes). Since a signal might sometimes reach values below the threshold, we also include a *stride* parameter that allows for a maximum consecutive number of bins to be below the threshold before considering the signal to end. The selection of the signals is done using the summed calibrated signal of the PMTs. The signal in the SiPMs is selected using the start and end times found in the PMTs. Both in NEXT-DEMO, NEXT-White and NEXT-100 in the future, the sampling time is 25 ns for PMTs and 1 μs for SiPMs, which require to rebin the PMT signal to 1 μs to know the energy associated to the tracking hits.

If the experimental calibration parameters are unknown, we can skip the electronic simulation in the processing pipeline (Figure 5.1) by using HYPATHIA city, which only implements the peak finding functions used in the second part of IRENE. For the analysis of this thesis, no electronic simulation was performed due to the lack of knoledge of the electronic parameters for NEXT-100, as the sensor calibration campaign has not started yet.

5.3.3. Energy corrections

Once PMTs and SiPMs waveforms are sampled with the same time binning, we can define the *hits*. Each hit is defined as a position (x, y, z), SiPM signal Q and PMT signal $\overline{E}$. The event longitudinal position (z) is computed using the time difference between the S1 and S2 signals. If more that one S1 signals exists, the convention is to choose the first S1 as the start of the event[1]. The transverse position (x, y) is the position of the fired SiPM. The energy assignment to the hits is done as follows: for each time slice, we compute the total signal at the SiPMs in the slice and assign the energy to

[1]Notice that events with multiple S1s will be only used at dedicated analysis, but they will be commonly filtered-out.

each hit as a weighted by its SiPM signal, namely

$$\overline{E}(x,y,z) = \frac{Q(x,y,z)}{\sum_{x,y} Q(x,y,z)} \cdot \overline{E}(z), \tag{5.1}$$

where $\overline{E}(z)$ is the measured PMT signal at time z and $Q(x,y,z)$ is the charge measured by the SiPM at position (x, y) at time z. The creation of hits if done in PENTHESILEA city.

The hit energy $\overline{E}(x,y,z)$, in pes, is a measurement of the number of photons arriving at the PMTs for an energy deposition $E(x,y,z)$, in units of energy, at the (x,y,z) position inside the active volume. The energy deposition E is the energy deposited by the initial charged particle in the gaseous xenon in the form of ionization electrons. If the same value of E is deposited at different points in the detector active volume, the measured $\overline{E}(x,y,z)$ would differ because of the solid angle and reflection pattern for different x, y emission points at the EL, and the different number of arriving ionization electrons due to attachment, which decays exponentially as a function of z.

In order to obtain the correct energy of a given event, we must perform both the solid angle an lifetime corrections,

$$E(x,y,z) = m(x,y) \cdot e^{z/\tau(x,y)} \cdot \overline{E}(x,y,z) \tag{5.2}$$

where $m(x,y)$ is the transverse position dependent correction factor and $\tau(x,y)$ the attachment lifetime in units of distance. Notice that we included a point dependent attachment, as it is the common situation in NEXT detectors [122]. The energy corrections are performed in ESMERALDA city using the *correction maps*.

5.3.3.1. Low energy calibration in NEXT

To compute the correction factors $m(x,y)$ and $\tau(x,y)$ we must be able to produce the same energy depositions spanning all the active volume. It can be achieved using low energy events, which provide point-like depositions. Knowing the fixed value of energy E, which is the same for this class of events we are able to map the detector's active volume and subtract the correction factors $m(x,y)$ and $\tau(x,y)$. From (5.2)

$$\overline{E}(x,y,z) = \frac{1}{m(x,y)} \cdot e^{-z/\tau(x,y)} \cdot E = \overline{E}_0(x,y) \cdot e^{-z/\tau(x,y)}, \tag{5.3}$$

where we have defined $E_0(x,y) \equiv E/m(x,y)$, as the energy measured by the PMTs for events at $z = 0$.

Having a clean and large sample of events with known deposition energy E, can provide the values of $\overline{E}_0(x,y)$ and $\tau(x,y)$, and therefore the correction map. We can select events occurring at a fixed transverse region x, y using the SiPM reconstructed signal, and perform a fit in z to get E_0 and τ as shown in Figure 5.4. Performing this fit to all the possible x, y transverse regions in the chamber, we can compute the correction maps for $\overline{E}_0(x,y)$ and $\tau(x,y)$. Since E is assumed to be known, we can recover the correction factor $m(x,y)$ used in (5.2).

USC DE SANTIAGO DE COMPOSTELA

Events used to map the detector response in NEXT are ^{83m}Kr decays. As shown in Figure 5.5, ^{83}Rb decays to the metaestable ^{83m}Kr via electron capture. This ^{83m}Kr, with a half-life of 1.83 hours is introduced in the gas system and spreads throughout the

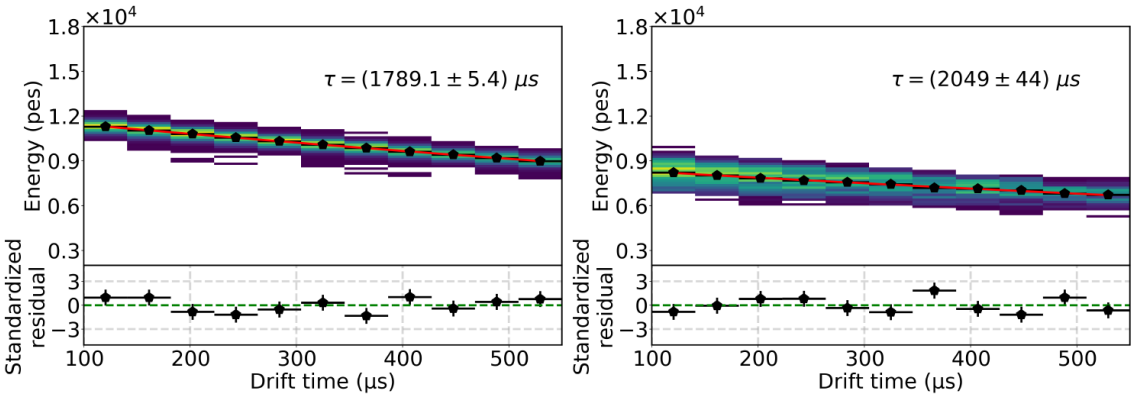


Figure 5.4: Exponential (5.3) fits to the measured energy distribution of ^{83m}Kr events in two different regions of the NEXT-White chamber. Color indicates the number of events (the brighter the more events), and red line shows the fit result. The left plot shows the fit for region x = [0, 50] mm, y = [0, 50] mm and the right plot the region x = [120, 150] mm, y = [120, 150] mm. From [122].

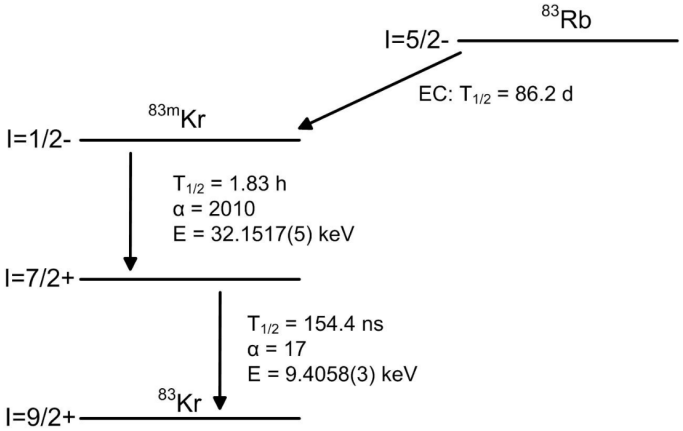


Figure 5.5: ^{83}Rb decays to a metaestable ^{83m}Kr state via electron capture and its subsequent decay. ^{83m}Kr decays are used in NEXT to map the chamber's signal response as a function of the decay position. From [129].

whole detector chamber. It provides point-like depositions of $E = 41.5$ keV, which are registered by the DAQ as trigger-1 events.

The generation of correction maps requires a new data structure provided by DOROTHEA city (Figure 5.1). In DOROTHEA, ^{83m}Kr events are collapsed to a single global hit which characterized the event position and total energy and charge. The global ^{83m}Kr position is computed by the mean value of its hits, weighted by its charge. This summarized data is then processed in an external dedicated software, ICAROS, which computes the correction factors in a readable structure to be used in ESMERALDA.

5.3.4. Lucy-Richardson deconvolution

At this point the events are composed by a collection of hits with positions x, y, z and energy E. The tracks are affected by two extra physical effects still not corrected, the diffusion of the ionization electrons during drift and the EL light emission. The diffusion spread is proportional to $\sqrt{z}$, becoming on the order of cm for tracks with larger drift times. Besides, ionization electrons emit light uniformly in the EL, therefore

it is not only measured by the closest SiPM to the transverse emission point but also in nearby sensors. The EL light emission resembles that of an optical system that transversely spreads light from the emission source. This optical blurring is described by a *point spread function* (PSF) which characterizes the response of the system to a point-like emission.

Both diffusion and EL light emission can be characterized in NEXT using the point-like depositions of ^{83m}Kr events [130]. These events provide a PSF with the combined effects of diffusion and EL light. For decays near the gate, the PSF will only characterize the effect of light emission, but as we move away the diffusion will appear and the PSF will be a convolution of both the light emission and diffusion. In NEXT we obtain a z dependent PSF using EUTROPIA and use it to correct both effects using the BEERSHEBA city.

The algorithm used to correct for the diffusion and EL light emission is the so-called Lucy-Richardson (LR) [131] [132]. It is an iterative method deduced by applying the Bayes theorem to the reconstruction of an image. An image W is modified after passing trough an optical system, such that the reconstructed image H would be a convolution of the former with the point spread function (PSF) of the system

$$H(x,y) = (PSF * W)(x,y) = \sum_{x',y'} PSF(x,y;x',y') \cdot W(x',y'). \tag{5.4}$$

By knowing the PSF and the measured image H, the LR provides the original image W through the iteration

$$W^{i+1}(x,y) = W^{i}(x,y) \cdot \left(PSF^{T} * \frac{H}{PSF * W^{i}} \right)(x,y) \quad i = 0,1,... \tag{5.5}$$

where $PSF^{T}(x,y;x',y') = PSF(x',y';x,y)$ and the first iteration image assumes a Bayesian uniform prior, such that $W^{0}(x,y) = \sum_{x,y} H(x,y)/N$ being N the number of x,y pixels of the original image.

Since the combined effect of transverse diffusion and EL spread is much larger than the longitudinal diffusion, and due to the technical and performance drawbacks of a 3D PSF, we only apply the LR algorithm in the transverse dimensions. LR deconvolution has probed to greatly improve the NEXT tracking capabilities [97]. The track definition improves and with it the topological performance in the blob identification.

The transverse distance between hits in NEXT is nothing more that the distance between neighbour SiPMs. In order to use LR algorithm we must artificially span the number of hits since the PSF changes significantly at this distance scale. The artificial hits are generated through an interpolation method.

Figures 5.6 show the same event track before and after the LR deconvolution, respectively. At bare eye, it is noticeable the greater spread reduction after the deconvolution. The track is much better confined spatially and its end points are easier to identify.

The PSF computed from ^{83m}Kr and used in the data processing is a different object than the PSF used in DETSIM. The latter is computed thought the MC simulation of a known number of emitted photons inside the EL gap, and therefore it is not affected by diffusion. The PSF used in the deconvolution is computed through the mean value of charge deposited by a ^{83m}Kr event at a given transverse (x,y) distance, and, due to diffusion, it would also depend on the longitudinal position z. As shown in Figure

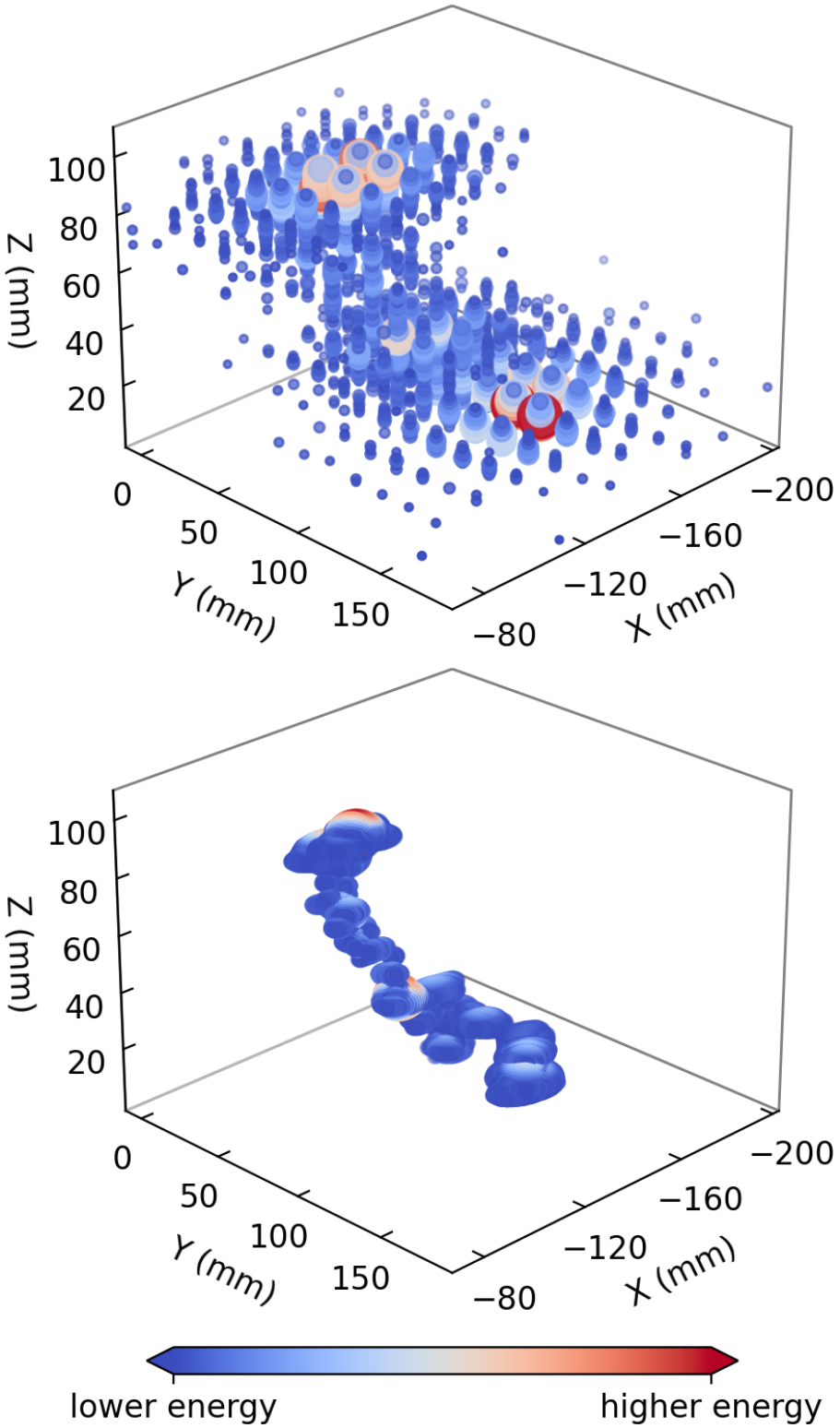


Figure 5.6: Simulated $0\nu\beta\beta$ event in NEXT-100 before (top) and after (bottom) LR deconvolution. The hit size and color scales with the energy. The effect of the PSF produces a large spread in the signal measured at the TP which is greatly reduced after the deconvolution.

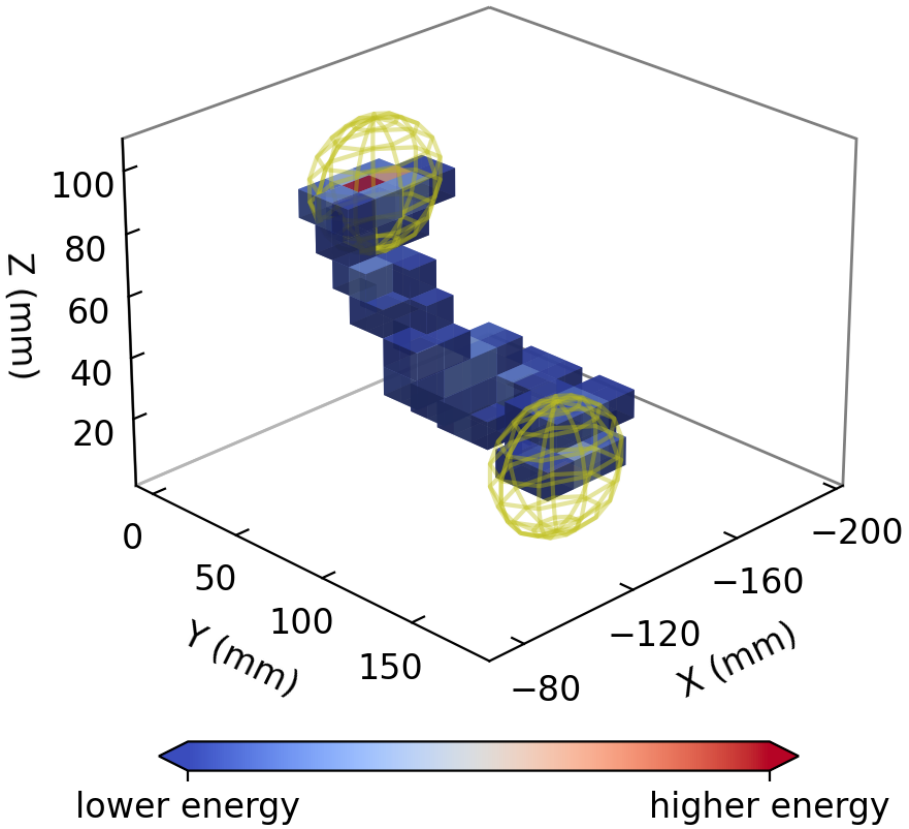


Figure 5.7: Voxelization and extremes of the track in Figure 5.6. The voxel size is $10 \times 10 \times 10$ mm and the blob-sphere radius 21 mm (yellow).

5.1, it is computed by a custom configuration of PENTHESILEA city which provides ^{83m}Kr collapsed at its mean longitudinal z position, and then by EUTROPIA city which computes the PSF.

5.3.5. Longest path algorithm

The last city in the processing chain ISAURA, divides the events in tracks and searches their end point blobs. This is done after grouping the hits in square *voxels*, as shown in Figure 5.7. We assign to each voxel an energy equal to the hits inside it, which is used to set a threshold to remove low energy voxels in order to improve the identification of tracks and extremes. Using voxels greatly reduces the number of elements (ie hits) in the event and we can proceed to split it in *tracks*. Voxels with shared edges are considered to be in the same track, thus by neighbour searching we can find all the voxels of a given track. Once one track is found, we can continue searching for more tracks if voxels in the event remain ungrouped.

The end points of the voxelized tracks are found using a longest path algorithm. First, for each pair of voxels in a track we compute the shortest distance between them using the Dijkstra's algorithm [133]. The pair of voxels with the longest distance are considered the end-points. The exact position of the extremes is assigned to the center of mass, where positions are weighted by energy, of the hits inside an sphere with *blob* radius. These hits might belong to different voxels. The extreme defines the position of the *blob* and the energy is assigned to the energy of the hits within the sphere of *blob* radius.

5.4. Software framework

The actual software of NEXT cities (Figure 5.1) is implemented in the *Invisible Cities* (IC) framework [134], written in *Python* programming language. *Python* is a dynamically typed, interpreted programming language, designed with special emphasis on readability. With a wide community of users, mostly outside Particle Physics, allows the existence of large number of active maintained libraries. In NEXT we particularly benefit from scientific libraries such as *numpy* [135], *pandas* [136], *scipy* [137], *matplotlib* [138], etc. This approach is particularly interesting because it breaks with the common standard in particle physics community of using *C++* language and the ROOT framework [139] with a much reduced number of maintainers and users. Also, the file format *hdf5* [125] used by IC (and also by NEXUS) is also actively maintained.

Other fundamental advantage of using *Python* is that it allows *C/C++* performance, since libraries can work as wrappers. Besides, if some lower level performance is needed such as faster looping for a particular function, we can use *Cython* [124] language which works as a *Python* to *C* compiler to easily create extensions. *Cython* is used in specific functions for DETSIM and IRENE.

Each city in the processing pipeline (Figure 5.1) is written in a single *Python* module inside IC. The city module imports functions from other modules in the framework, but the core logical structure is implemented in its dedicated module. The folder organization of the repository is as follows:

- *cities*: contains the city modules.
- *config*: contains the configuration files for the cities.
- *core*: contains generic functions, not specific to the cities but useful for example in statistical analysis, fitting or testing.
- *database*: contains functions allowing the synchronization and interaction with sensor databases, saved in dedicated servers. Also saves the test data files.
- *dataflow*: contains functions that define the conceptual and logical structure of the cities, as we will see below.
- *detsim*: contains classes and functions used in DETSIM and BUFFY cities.
- *evm*: contains classes and functions that define the event model of the cities, such as the definition of an event data structure, the hits, etc.
- *filters*: contains classes and functions that implements the filtering of S1 and S2 signals, used in PENTHESILEA and DOROTHEA.
- *io*: contains input-output functions that read/write data from/to files.
- *reco*: contains the functions implementing the algorithms explained above §5.3.
- *sierpe*: contains functions used in electronic reconstruction and simulation.
- *types*: contains classes and variables defining data types and stuctures.

The IC framework is constantly evolving by the collaboration members. It follows a collaborative development strategy, any new code added to the framework, either new code or modifications, has to be reviewed by collaboration peers. The review process is useful to ensure the new code is understandable and adapts to the framework's standards. Besides, the framework itself includes tests for all the functions. Any new code included in IC must come with corresponding tests, and it must pass the full test suite in order to be approved. This unit testing implementation is helpful both for code writer and reviewer, the writer probes that the code performs the desired functionality. There are two type of tests in the IC framework:

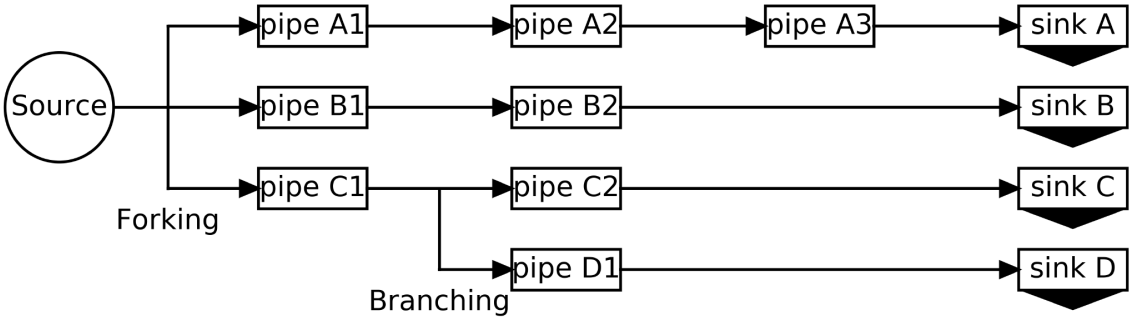


Figure 5.8: Diagrammatic representation of the standard code structure of IC cities. The source reads the input data that is processed in pipes until the result is finally saved at the sinks. From [122].

- *Exact result tests*: they perform the desired operations and compare the output with a previously saved result. They are deterministic, the resulting computations must always be exactly the same. If some operation in the testing function is accidentally modified, the test will fail, ensuring that broken dependencies are not included in the official software. All the cities in IC have at least one test of this type.
- *Variable input tests*: they recursively call the testing function with different input values previously configured and check that the operation finishes and the result type is the expected. For example, we can test a sum function with two integer values as input and check that the result is also an integer. These tests are useful when only specific properties of the output are relevant without the burden of creating an exact test for them, which made the code harder to modify.

A worth mentioning feature of IC is the standard code structure of the cities. A city is a program that reads an input file that contains event data. It processes the events in the file one by one and writes the results in an output file. The resulting file data is also provided in a per event basis in order to be further processed by the following city in the pipeline (Figure 5.1). This approach suggest the structure of a city to be divided in three parts:

- *Source*: it is the function that reads the input file and returns data for each event. During the running of the city, the source function is called for all the events in the input file. In *Python* jargon it is an *iterator function* [2].
- *Pipelines*: after event data is read by the source, this data is processed by the city transformation pipeline. It is composed by *pipes* each of them made of one or several consecutive functions that operate on the event data. Since the input event might contain different type of data (for example for waveforms you have SiPM and PMT waveforms which are arrays with different size), the pipeline also allows branching, such that the main data pipeline is splitted into multiple sub-pipelines.
- *Sinks*: once all the transformations are performed, the computed event data is saved to the output file. Each pipeline finishes at a sink function that writes the data in the desired structure.

This structure is the so-called *dataflow*, schematically shown in Figure 5.8.

[2] Iterator functions are functions that return data in batches.

Part III

Results and conclusions

USC
UNIVERSIDADE
DE SANTIAGO
DE COMPOSTELA

USC
UNIVERSIDADE
DE SANTIAGO
DE COMPOSTELA

CHAPTER 6

Sensitivity of NEXT-100 detector to $0\nu\beta\beta$

6.1. Introduction

In Chapters 4 and 5 we have introduced the simulation and data reconstruction methods in NEXT. Using these tools, in this Chapter we will be able to estimate the sensitivity of NEXT-100 detector to neutrinoless double beta decay, which ultimately relies on several variables (Chapter 2): the background rate, the energy resolution, the exposure (source mass times running time) and the signal selection efficiency over background. To simulate the background components of the detector, we will first introduce a tentative background model for NEXT-100, based on previous knowledge about its main components [118] and the radiogenic measurement campaign carried out during the years 2021-2022. Previous studies about the sensitivity of NEXT-100 can be found in [63], [140] and [115]. The main difference with respect to the analysis presented here is that the detector final design or reconstruction procedure were not completely known, so they were based on pure Monte-Carlo reconstructions or extrapolations based on NEXT-White detector. Also, simulations of the cosmogenic induced backgrounds were not included in the past. The analysis in this Chapter includes the simulation of the terrestial and cosmogenic backgrounds, the full NEXT data-like reconstruction procedure and the simulation of the detector based on the final design.

This Chapter is organized as follows. Section 6.2 introduces the background model and radiogenic measurements for NEXT-100. The details of the simulation and reconstruction are described in Section 6.3. In Section 6.4, constituting the main results of this thesis, analyzes the output of the simulation to report the sensitivity of NEXT-100 in the energy region of interest ($Q_{\beta\beta} \sim 2.5$ MeV).

6.2. Background model

We are interested background sources that can generate signals in the energy region of interest of ^{136}Xe ($Q_{\beta\beta} = 2.458$ MeV). As discussed in Chapter 2, one of the desired features of a double beta isotope is to have a relatively large $Q_{\beta\beta}$ value to avoid most part of the **terrestrial natural background** spectrum. Natural decays from the ^{232}Th and ^{238}U chains are the main components of background since they are always present at some level in the construction materials and mountain rocks (recall that the detector is placed in an underground laboratory). The contribution of the natural decay series

can be divided in three different sources: the impurities in the detector materials, the airborne radon present in the laboratory filtered through the walls, and the gamma radiation from the natural decays in the rocks. In the region of the two neutrino mode $2\nu\beta\beta$, where the energy distribution is continuous and covers a wide range of energies (E $\sim$ 0.8-2.2 MeV), the ^{40}K and ^{60}Co gamma emitting isotopes must be also included in the model [118].

Besides the terrestrial natural background, another contributors are the so-called **cosmogenic backgrounds**, composed by muons that arrive to the detector or backgrounds generated as a byproduct of the muon interaction with the mountain rocks and detector materials. In what follows we discuss the contribution of the different backgrounds to the NEXT-100 background model in the $0\nu\beta\beta$ region of interest.

6.2.1. Terrestrial backgrounds

There are three components of terrestrial backgrounds coming from the natural decay series of ^{232}Th and ^{238}U: impurities in the detector materials (radiogenic background), airborne radon in the laboratory and external gamma radiation from the rocks. From the three types of radiation α, β and γ we will only be interested in the last two: α particles can be easily identified in NEXT since they produce point-like energy depositions. Besides, only α from the light tube will produce signals at the edges of the chamber (α from external volumes will be stopped before reaching the active volume), which will be vetoed anyway after fiducialization.

The decay chain of ^{232}Th and ^{238}U is shown in Figure 6.1. We can easily identify the relevant contributors to the ^{136}Xe ($Q_{\beta\beta} = 2.458$ MeV), which are gammas with energies larger or around the $Q_{\beta\beta}$ as no β particles are emitted in this region. Figure 6.2 shows the spectra at the ROI from these natural backgrounds.

• From the ^{232}Th chain, the $Q_{\beta\beta}$ lies betweeen the photopeak and the Compton edge of the 2615 keV of ^{208}Tl. Even though the Compton edge lies at 2382 keV, the Compton scattered gamma can produce another electron close enough to the interaction vertex to generate an total deposition in the $Q_{\beta\beta}$ region. The ^{208}Tl decay is a well known emission in NEXT since it was used in the high energy calibration of NEXT-White (§3.4.2.1) and will be also used in NEXT-100.

• From the ^{238}U chain, the ^{214}Bi 2448 keV photopeak lies only 10 keV above the $Q_{\beta\beta}$, overlapping with the signal peak for energy resolutions as good as 0.4% FWHM. More gammas in the interest region are emitted by the ^{214}Bi, but with much lower intensities than the 2448 keV photopeak. All these lower intensity gammas will be also taken into account in the background simulation (§6.3).

From its origin, NEXT Collaboration has been committed to the characterization of the background activities of the different detector materials ([142–145]). Activity measurements are performed mostly via gamma ray spectroscopy using high-resolution, high-purity germanium detectors (HPGe) belonging to the Radiopurity Service of the LSC. However, when higher sensitivity is required and the measured material can be destroyed (for example copper samples from machining shavings), another techniques like Glow Discharge Mass Spectrometry (GDMS) or Inductively Coupled Plasma Mass Spectrometry (ICPMS) are used at external companies or laboratories as PNNL (*Pacific Northwest National Laboratory*).

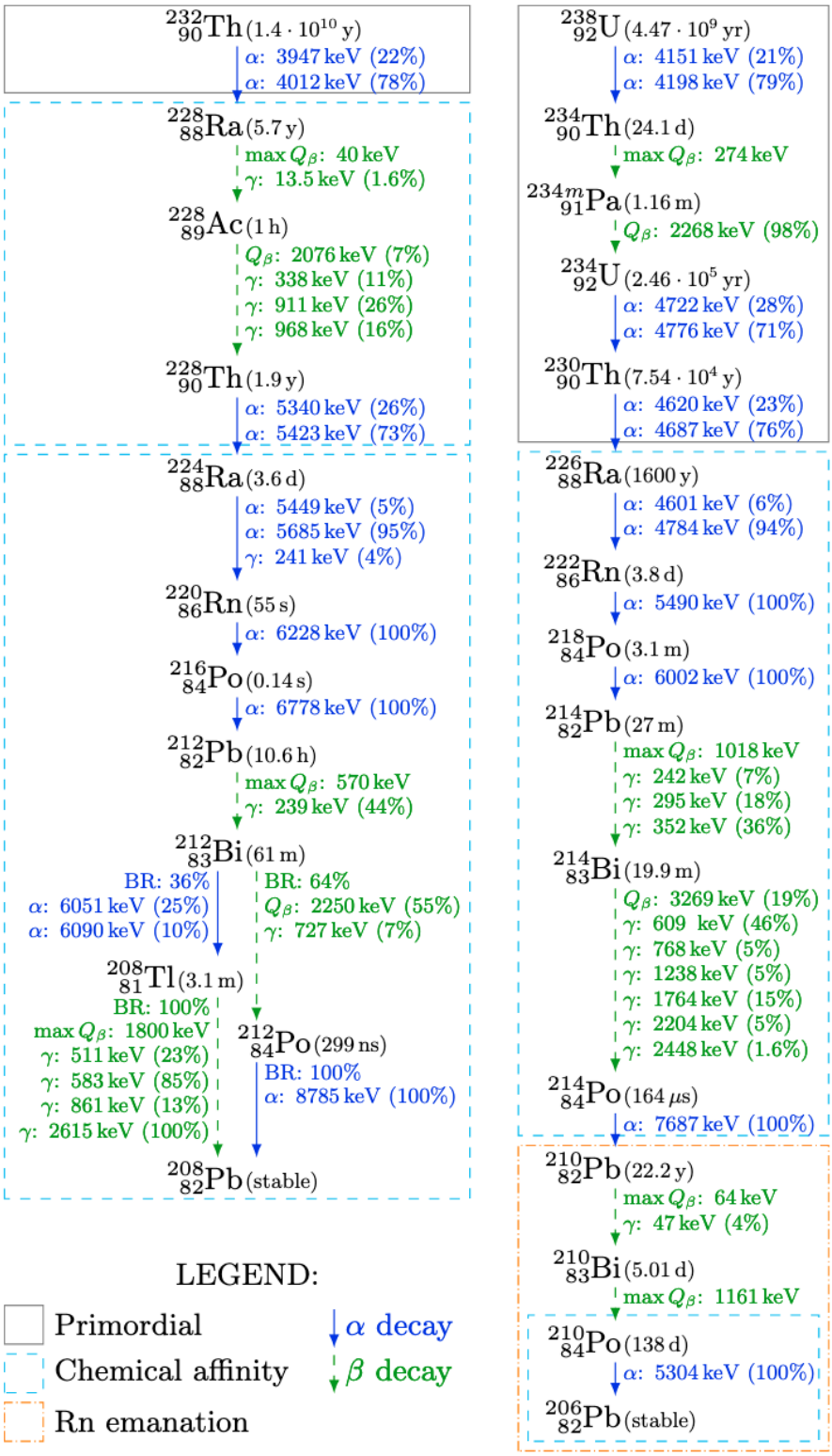


Figure 6.1: ^{232}Th and ^{238}U decay chains. For each isotope, the α decays with intensity I>1% and γ decays with I>5% or energy close to any $\beta\beta$ isotope are shown. All β decays with Q-value above 2 MeV are also shown. Boxes highlight the chain parts commonly found in equilibrium. From [141].

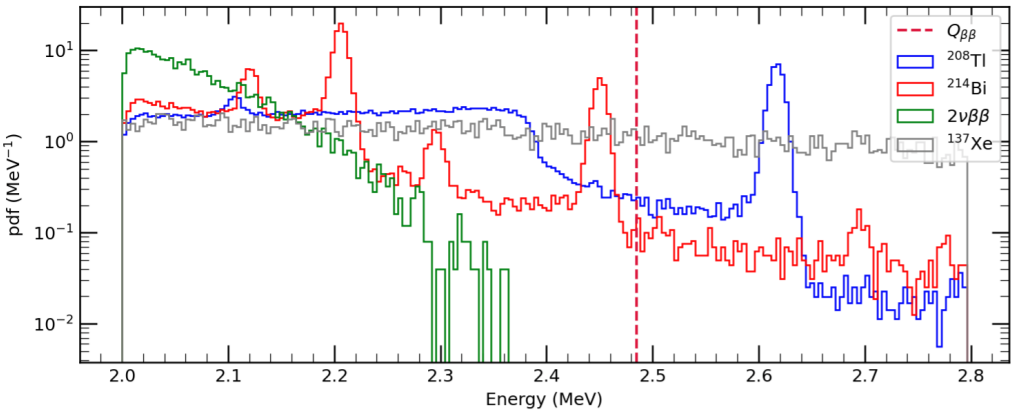


Figure 6.2: Background spectra for terrestrial backgrounds in the [2.0-2.8] MeV energy window. ^{208}Tl and ^{214}Bi peaks are clearly identified, and also the end part of the $2\nu\beta\beta$ spectrum which becomes negligible in the $Q_{\beta\beta}$ region. The spectra is not representing the relative contributions of each background in NEXT-100, but the normalized pdfs in the ROI. The spectra is obtained from the simulation and post-reconstruction described in §6.3.

The total activities for the different detector components are shown in Table 6.1. Since the measurement campaign is a dynamic process, some of the measurements are still unknown or only upper limits could be reported. We will assume in this work secular equilibrium, thus the activities are asumed to remain constant during the running period. Notice also that even though total activities are shown, the relative contribution of each component to the background index of the experiment would ultimately depend on the probability of a photon to reach the active volume and generate a signal in the energy region of interest. For example, LEAD-BOX shielding has a high activity, but its contribution will be highly screened by itself and by the inner copper shielding. On the other hand, LIGHT-TUBE has a low activity, but being in direct contact with the active volume makes its contribution more likely. Figure 6.3 shows the efficiency for backgrounds from the different volumes to generate an energy deposition in the active volume with [2.40, 2.50] MeV. The values in this plot are the composed efficiency of: the efficiency of the gamma to be 2.40 MeV or higer in a ^{214}Bi or ^{208}Tl decay, the efficiency of volume screening (ie to arrive to the active volume), and the efficiency that the deposited energy in the xenon lies in the [2.40, 2.50] MeV energy window. On the other hand, the efficiency of μ events will also involve the type of deposition (§6.2.2). For ^{137}Xe events the volume screening is not included as they are present in the active volume itself.

Figure 6.4 shows the contribution in the energy region of interest in counts·year^{-1} of the different components using the total activities in Table 6.1 and the efficiencies in Figure 6.3. Notice that this plot is previous to any analysis selection, being the rates only the expectation for events depositing energies between [2.40, 2.50] MeV. As we will see (§6.4), analysis selections will provide a significant reduction of the rates, with efficiencies depending on the background type.

The radon activity in the LSC Hall A is very high for the standards of a $0\nu\beta\beta$ experiment (~70 Bq·m^{-3}). Nevertheless, the installation of the Radon Abatement System (RAS) provides a reduction of 4-5 orders of magnitude, with a radon concentration of ~1 mBq·m^{-3} [146]. This radon depleted air is being fluxed inside the NEXT castle

Table 6.1: ^{208}Tl and ^{214}Bi total activities in mBq for the different detector components from NEXT-100. Total activities are obtained through the product of the component specific activity times its total mass. Each volume component corresponds to a volume in the simulation, which may be composed by several physical volumes, for example SIPM-BOARD activity is the summed activity of the SiPMs, the teflon masks and the dice boards. Upper limits are shown when no central value has still been measured. Also, asterisk (*) represents extrapolated values using the specific activity for NEXT-White detector if the component is still to be measured.

Volume	Material	Technique	A(^{208}Tl)	A(^{214}Bi)
LEAD-BOX	Lead	GDMS	$2.17 \cdot 10^{2}$	$< 5.32 \cdot 10^{3}$
STEEL-BOX	Steel	HPGe	8.74	$2.03 \cdot 10^{1}$
PEDESTAL	Steel	HPGe	$5.04 \cdot 10^{2}$	$3.58 \cdot 10^{2}$
BEAMS	Steel	HPGe	$7.08 \cdot 10^{2}$	$5.03 \cdot 10^{2}$
VESSEL	Steel	GDMS, HPGe	$< 8.82 \cdot 10^{2}$	$< 3.42 \cdot 10^{3}$
ICS	Copper	GDMS	< 7.87	$< 1.67 \cdot 10^{1}$
EP-COPPER-PLATE	Copper	GDMS	$< 4.73 \cdot 10^{1}$	$< 8.20 \cdot 10^{1}$
SAPPHIRE-WINDOW	Sapphire	HPGe	$< 2.16 \cdot 10^{1}$	$< 6.60 \cdot 10^{1}$
OPTICAL-PAD	Silicone	HPGe	< 3.19*	< 7.92*
PMT	Kovar	HPGe	$1.14 \cdot 10^{1}$	$2.10 \cdot 10^{1}$
PMT-BASE	Kapton	HPGe	$1.54 \cdot 10^{1}$	$4.09 \cdot 10^{1}$
TP-COPPER-PLATE	Copper	ICPMS	< 0.21	< 2.28
SIPM-BOARD	-	-	< 9.22	$< 3.56 \cdot 10^{1}$
BOARD-PLUGS	Peek	HPGe	$1.18 \cdot 10^{2}$	$1.55 \cdot 10^{2}$
LIGHT-TUBE	Teflon	ICPMS, HPGe	< 7.97	< 3.55
FIELD-RING	Copper	ICPMS	< 2.69	$< 2.69 \cdot 10^{1}$
CATHODE-RING	Steel	ICPMS	$< 5.03 \cdot 10^{-2}$	1.14
ANODE-RING	Steel	ICPMS	$< 5.19 \cdot 10^{-2}$	1.18
GATE-RING	Steel	ICPMS	$< 5.19 \cdot 10^{-2}$	1.18
HDPE-TUBE	HDPE	ICPMS, HPGe	$< 3.74 \cdot 10^{-1}$	< 3.07

USC UNIVERSIDADE DE SANTIAGO DE COMPOSTELA

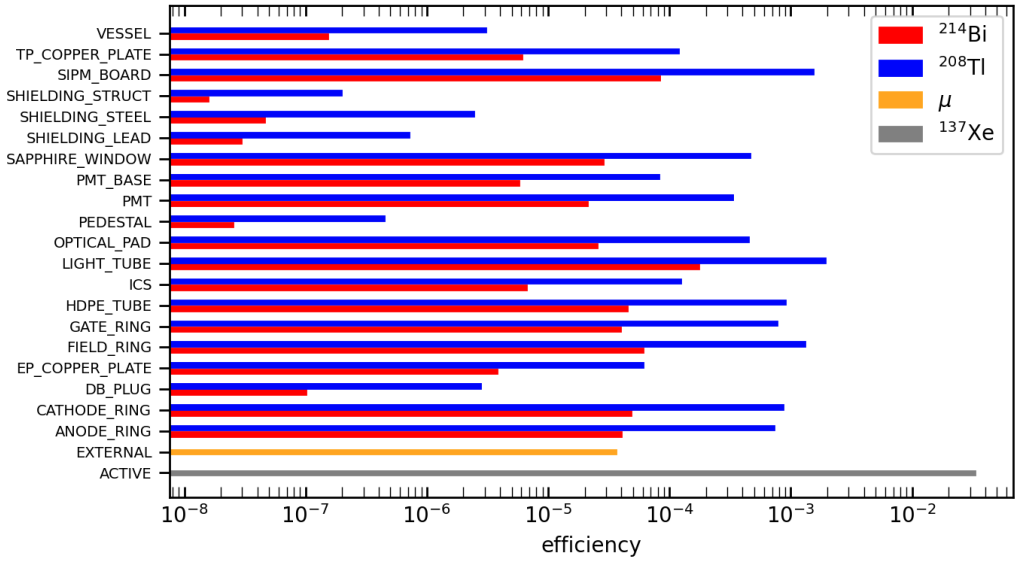


Figure 6.3: Efficiencies for the different background components to produce an energy deposition within [2.40, 2.50] MeV. Expected efficiencies from cosmogenics (muons and ^{137}Xe) are also included.

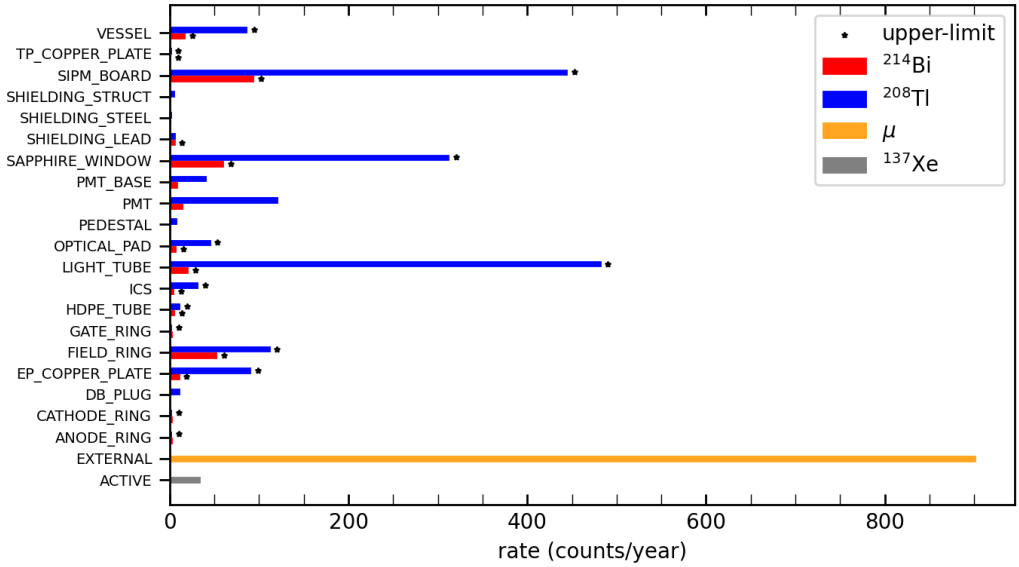


Figure 6.4: Expected background rate from different detector components in the energy region of interest [2.40, 2.50] MeV assuming the total activities in Table 6.1 and efficiencies in Figure 6.3. Expected contributions from cosmogenics (muons and ^{137}Xe) are also included.

shielding, making the radon contribution negligible for NEXT-White [118]. Since the air volume inside the shielding castle is greatly reduced for NEXT-100 due to its double size, and the radiogenic contribution is similar, we can safely assume the airborne radon contribution to be negligible in NEXT-100 too. Besides, notice that radon events can be vetoed: radon (either ^{220}Rn or ^{230}Rn) progeny is positively charged, thus they will be concentrated in the cathode. In the $0\nu\beta\beta$ ROI the only relevant contributors are the gammas from ^{214}Bi and ^{208}Tl decays which can be identified using the subsequent α of the Po. On the other hand, we will assume in this work the optimistic scenario in which the internal radon contamination is negligible, but this will have to be studied

once the detector starts operation.

The total gamma flux from the laboratory rocks has been measured at the LSC (Hall A) [147], with values of (0.68 ± 0.17 cm^{-2}s^{-1}) for ^{238}U chain and (0.38 ± 0.02 cm^{-2}s^{-1}) for ^{232}Th chain. This background is reduced four orders of magnitude in NEXT-White and NEXT-100 due to the 20 cm lead castle shielding, making it negligible compared to the radiogenic contributions. Moreover, for NEXT-100 the tickness of the inner copper shielding was doubled, providing even larger shielding to gamma radiation.

An extra terrestial background are the neutrons coming from the laboratory rocks. Neutrons are produced in (α, n) reactions on light elements (Li, F, Na, etc) and spontaneous fission, mainly from ^{238}U [148]. Neutron captures can activate some nuclei whose decay emits gamma radiation which can contribute to the background rate.

Total neutron flux at the LSC Hall A in the LSC has been measured to be (3.44 ± 0.35)$\times 10^{-2}$ m^{-2}s^{-1} [149], being about four orders of magnitude smaller than the neutron flux at sea level. This quantity corresponds to both, neutrons from terrestial backgounds and neutrons induced by cosmogenic muons on the rocks. In principle, this contribution is negligible with respect to the radiogenic backgrounds and will not be considered in the analysis as it was not needed for the background model of NEXT-White [118], even though a dedicated simulation should be performed in the future. In any case, a further reduction in the neutron flux can be achieved with an extra neutron absorber shielding surrounding the detector if needed [150], such that the relevant neutron induced backgrounds will come from those neutrons produced by cosmogenic radiation in detector materials.

6.2.2. Cosmogenic backgrounds

Muons are the most abundant particles at sea level [61]. In order to shield against muons, low background experiments place their detectors in underground facilities. Muons will loose energy by ionization, radiative processes (bremsstrahlung and pair production) and photonuclear interactions in the rocks. Due to the energy loss, a significant amount of muons will decay before reaching the laboratory. The muon flux in the underground laboratory will ultimately depend on the depth and rock composition. NEXT-100 detector will be placed at Laboratorio Subterráneo de Canfranc (LSC) with a total muon flux of (5.26 ± 0.21) $\times 10^{-3}$ m^{-2}s^{-1} [151], a reduction of more than one order of magnitude with respect to sea level.

Muons can contribute to the background budget in the $Q_{\beta\beta}$ region through several mechanisms: the muon itself crossing the detector; high energy electrons from muon ionizations of elements close to the active volume; and nuclear activation decays from neutron captures or photonuclear reactions from previous processes induced by the muon, such as neutron scattering or electromagnetic showers. Most of the neutron activated nuclei decay promptly (within the next ~ 2 μs) via gamma emission, thus they can be easily removed with a muon veto surrounding the lead shielding. On the other hand, the activation of ^{136}Xe to ^{137}Xe constitutes an irreducible component to the background budget due to its large half-life of ~ 3.8 mins as compared to prompt-gamma emissions. As shown in Figure 6.2, part of the ^{137}Xe spectra lies in the $Q_{\beta\beta}$ region.

As we will see in §6.4, crossing muons, ionizations and prompt-gamma contribu-

tions to the background budget will be negligible compared to terrestial backgrounds. Nevertheless, the irreducible ^{137}Xe decays should be taken into account.

6.3. Simulation and data production

Simulation of background and signal events is carried out using the NEXT simulation toolkit NEXUS (§4.2). NEXUS uses GEANT4 to simulate the particle interactions in the detector active volume and materials. We are interested in simulations in which a primary background (e.g. a ^{208}Tl decay) is generated from a certain detector volume until some energy is deposited at the active volume of xenon. Such a deposition will generate a background signal in the detector that will be further processed. We also simulate signal $0\nu\beta\beta$ events in order to study the signal efficiency, required to compute the sensitivity (2.13). Signal events are simulated using the DECAY0 event generator [152], which allows the simulation of 12 different decay modes (including the zero and two $\beta\beta$ modes with light Majorana neutrino exchange) for 21 candidate isotopes.

Even though $\sim$ 3 years is a realistic exposure time for NEXT-100, the number of events expected at the ROI for this exposure will be very low, thus a large statistics sample is simulated. This is achieved using the DETSIM algorithm, as described in §4.3.

For $0\nu\beta\beta$ signals, a total of $1.5\cdot10^4$ events have been uniformly simulated throughout the active volume, with $\sim$30% of them depositing an energy below the $Q_{\beta\beta}$ (see §6.4.1). Even though these events are outside the $Q_{\beta\beta}$ peak, they must be taken into account in the computation of the total signal efficiency. Besides background and signal events, 4 million ^{83m}Kr events were simulated in the active volume in order to compute the geometrical corrections and psf used in the data reconstruction procedure (Chapter 5). Figure 6.5 shows the S2 Light Table used in the simulation and the geometrical krypton map after the fitting procedure. For R<45 cm, the krypton map reproduces very well the geometrical correction of the LT. The mismatch at larger radius is identified as a bias in the reconstructed radial position of the krypton events, which tends to be displaced towards smaller radius. As we will see, a fiducial selection of R<45 cm will be required in the sensitivity analysis which will avoid this reconstruction bias anyway. The 10 ms lifetime assumed in the simulations is also recovered with the electron lifetime estimation using krypton events.

We have simulated exposures between ten and thousands of years for radiogenic backgrounds (^{208}Tl and ^{214}Bi) based on the detector component activities (Table 6.1), accounting for a total of $\sim 2\cdot10^{10}$ simulated events. Even though this seems an extremely large number of events, only $\sim 3\cdot10^4$ events generate an energy deposition within the [2.40, 2.50] MeV energy window, which are further processed for analysis.

From the cosmogenics part, we have simulated a total muon exposure of $\sim$ 55 years, with a total of $\sim 1.4\cdot10^9$ events simulated, of which $\sim 5\cdot10^4$ leave an energy deposit in the [2.40, 2.50] MeV energy window. Another high statistics dedicated muon simulation is performed to compute the rate of ^{137}Xe production, obtaining a value of $\sim 3.7\cdot10^{-5}$ activations per primary muon. Based on this rate we have simulated a $\sim$ 200 year exposure for ^{137}Xe, with a total of $\sim 2\cdot10^5$ events with $\sim 6\cdot10^3$ of them generating a deposition within [2.40, 2.50] MeV. Muon flux is simulated based on the

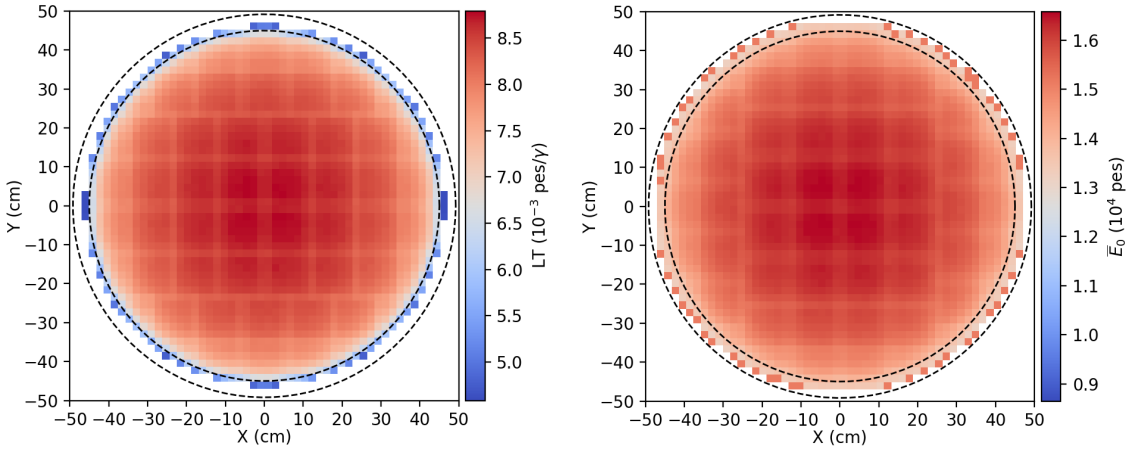


Figure 6.5: Total PMT S2 Light Table (left) and geometrical ($\overline{E}_0$) krypton map from the simulation (right). Dashed black lines shows 49.2 cm (detector's radius) and 45 cm (fiducial) circunferences. For R<45 cm, the map recovers the geometrical factor of the LT. Recall the factor between both objects is the number of photons produced by a krypton events (4.5). Notice also the shadowing effect induced by the sipm board mask is also recovered in the map.

total flux and angular spectrum at the LSC [151], and muons energies are assumed to be uniformly distributed up to 2000 GeV. This energy distribution does not correspond to the energy spectra in the LSC Hall A, which is work in progress in the collaboration. In principle, the energy distribution will peak at around 1000 GeV and be reduced at higher energies, thus the considered distribution is in any case conservative. Also, simulations show that the probability of a muon to generate a deposition of $\sim Q_{\beta\beta}$ does not strongly depend on energy. Moreover, the production rate of ^{137}Xe increases with energy [153], thus this background will be conservatively overestimated.

The simulations were performed in the **fast simulation** mode of NEXUS (Chapter 4), which provides the collection of hits deposited by an event. In order to mimic the detector's response (ie photons arriving at sensors), we use the DETSIM algorithm. Afterwards, the simulated data is processed following the algorithms and structures used in real detector data (Chapter 5), including the energy corrections and Lucy-Richardson deconvolution. Both the krypton map and psf are computed from the simulated ^{83m}Kr events in the usual way through ICAROS and EUTROPIA.

All the simulations and subsequent data processing were run at the Finis-Terrae III supercomputer at the *Centro de Supercomputación de Galicia* (CESGA) [154]. The assumed values of the detector operation conditions are shown in Table 6.2: 293 K of gas temperature based on the mean temperature of the LSC HallA, and the tentative running conditions of 13.5 bar pressure, electroluminiscence region field of 17.5 kV/cm and drift field of 400 V/cm. From the EL-field and gas pressure, we assume a rounded EL-gain of 1000 photons per ionization electron (3.6). A 10 ms lifetime is assumed based on the mean value for NEXT-White. The diffusion and drift velocities are obtained through a Garfield++ simulation [155] for the running parameters above. Under such conditions, we obtain a simulated energy resolution of $\sim$ 0.62% FWHM at $Q_{\beta\beta}$ after energy corrections.

Table 6.2: Detector conditions and derived parameters assumed for NEXT-100 simulations.

Parameter	Value	Comment
Temperature	293 K	Based on LSC Hall A mean
Pressure	13.5 bar	Tentative running condition
Drift field	400 V/cm	Tentative running condition
EL field	17.5 kV/cm	Tentative running condition
Lifetime	10 ms	Based on NEXT-White mean
EL gain	1000 phot./ie^-	Estimated from 3.6
Difusion (long.)	0.38 mm/$\sqrt{\text{cm}}$	From Garfield++ simulation
Difusion (trans.)	1.10 mm/$\sqrt{\text{cm}}$	From Garfield++ simulation
Drift velocity	0.84 mm/μs	From Garfield++ simulation
EL velocity	2.75 mm/μs	From Garfield++ simulation

6.4. Sensitivity of NEXT-100 detector

In §2.2 we discussed how to estimate the sensitivity of a $0\nu\beta\beta$ experiment with background. This conservative definition assumes that no true signal exists, therefore the result of a counting experiment will be only composed by background events. The half-life sensitivity is given by

$$S(T^{0\nu}_{1/2}) = \log 2 \cdot t \cdot N_0 \cdot \frac{\epsilon}{\overline{N}_{CL}(b)}, \tag{6.1}$$

where $\overline{N}_{CL}(b)$ is defined in (2.7) as the mean upper limit of the number of events for the expected background b; ϵ is the signal efficiency; t is the running time of the experiment; and $N_0 = N_A \cdot M/W$ is the initial number of nuclei of interest (^{137}Xe in case of study). In §6.4.1 we compute the values of ϵ and b to estimate the counting experiment sensitivity (6.1).

On the other hand, if we no longer assume that no true signal exist, we can compute the expected limits to the $T^{0\nu}_{1/2}$ that we will report as a function of the observed number of signal candidates. This second approach based on confidence intervals to report the expected sensitivity will be presented in §6.4.2.

6.4.1. Counting experiment

The objective is to optimize the signal selection in order to maximize the experimental sensitivity. We will distinguish between two types of selections: first the *analysis selections* prepare the data samples to be used for signal and background discrimination in the *discrimination selections*. This distinction is clear if we recall that the main feature of NEXT experiment is the ability to separate between signal and background events using the Bragg peaks. This is done using the track of the events, but it may well be that the same event is composed by multiple tracks (from multi-compton or

bremstrahlung), thus an *analysis selection* of single track events is required before the Bragg peak *discrimination selection*. Fortunately, some of the *analysis selections* further improve the discrimination between signal and background events, as we will see below.

Signal efficiency ϵ and background counts b in (6.1) will depend on the actual selections performed over the initial signal and background datasets. In order to maximize the sensitivity, the quotient $\epsilon/\overline{N}_{CL}(b)$ must be maximized by the selections performed. As described in §2.2, this is equivalent to maximize the figure of merit $\eta = \epsilon/\sqrt{\epsilon_b}$ where ϵ_b is the signal efficiency over the background sample. Notice that the signal selection figure of merit, η, must be $\eta > 1$ in order to improve the sensitivity (6.1). Any selection will be well justified if it fullfills this condition.

The initial data sample for both signal and background events consist of events with a total energy deposition in the xenon active volume within [2.40, 2.50] MeV. We distinguish four types of events: signals ($0\nu\beta\beta$); radiogenic background from detector materials (^{208}Tl and ^{214}Bi); prompt-gammas from muon induced nuclear activations, electromagnetic cascades, electrons from muon ionizations in the detector materials and muons crossing the active volume (μ); and long lived nuclear activations (^{137}Xe). Over this sample we will apply the following set of *analysis selections*:

• **reconstruction (reco)**: this selections keeps only the events passing all the inner selections in the IC reconstruction chain. The most important and restrictive selection is the request of a single S1 and a single S2 for each event. It is particularly relevant for muon events, which can activate a large number of nuclei throughout the detector materials. Since the decay is almost instantaneously, the decaying photons will produce signals in different parts of the detector which are reconstructed as multi S2 events. Other selections applied can be consulted through the configuration files in Appendix B, which were chosen to minimally affect the data samples.

• **energy (ene)**: part of the IC reconstruction procedure apply the energy corrections using the krypton map (§5.3.3). The maps are ill-defined at the very edges of the detector due to the misreconstruction of krypton events. A deposition at high radius will leave an asymetrical light pattern which bias the reconstructed position with respect the true. This bad reconstruction will be translated in a misestimation of the krypton map at the edges. As such, the reconstructed energy of events with hits at high radius can be outside the [2.40, 2.50] MeV window. Even though this effect can be implicitly removed by the posterior **fiducial** selection, we require the events to have a reconstructed energy within [2.40, 2.50] MeV.

• **fiducial (fid)**: Figure 6.6 shows the true MC energy deposited by $0\nu\beta\beta$ events as a function of its mean radial position [1]. The sum of the initial energies of the electrons in the simulation is exactly $Q_{\beta\beta}$, nevertheless a no negligible $\sim 30\%$ of events leave less energy in the active volume, with most of them at large radius (R>45 cm). The reason of the missing energy can be easily explained:

- in $\sim 11\%$ of $0\nu\beta\beta$ events a $\beta\beta$ electron at high radius penetrate in the light-tube walls from the active volume. Some electrons even enter and come back again.
- in $\sim 4\%$ of $0\nu\beta\beta$ events a $\beta\beta$ electron penetrate the buffer and EL regions.
- $\sim 15\%$ of $0\nu\beta\beta$ events emit a bremsstrahlung that leaves the active volume.

[1] High energy events like $0\nu\beta\beta$ leave extended trajectories on the detector, thus we choose to define its radial position as its center of mass, the mean transverse position weighted by energy.

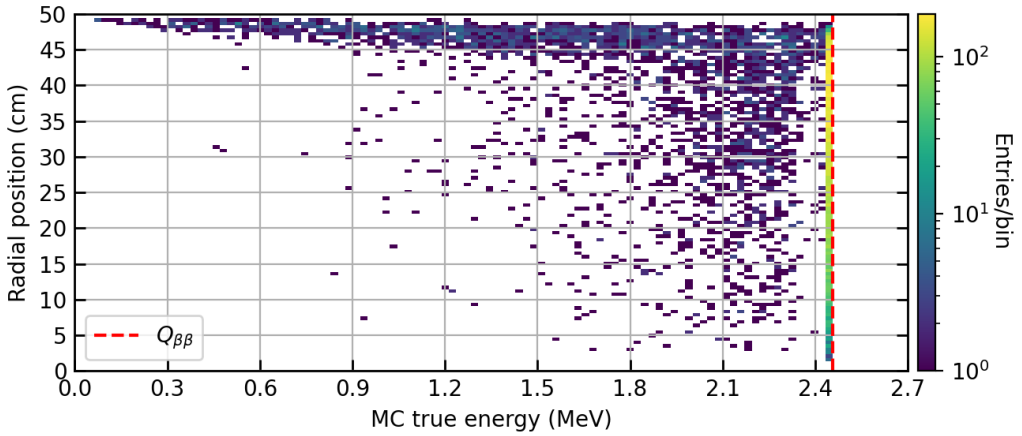


Figure 6.6: Energy deposited by simulated $0\nu\beta\beta$ events as a function of their radial position. The *MC true energy* corresponds to the total energy of the simulated tracks before reconstruction. Degraded $Q_{\beta\beta}$ events ($\sim$30%) is due to $\beta\beta$ electrons penetrating into the light tube or above the electrodes and bremsstrahlung losses.

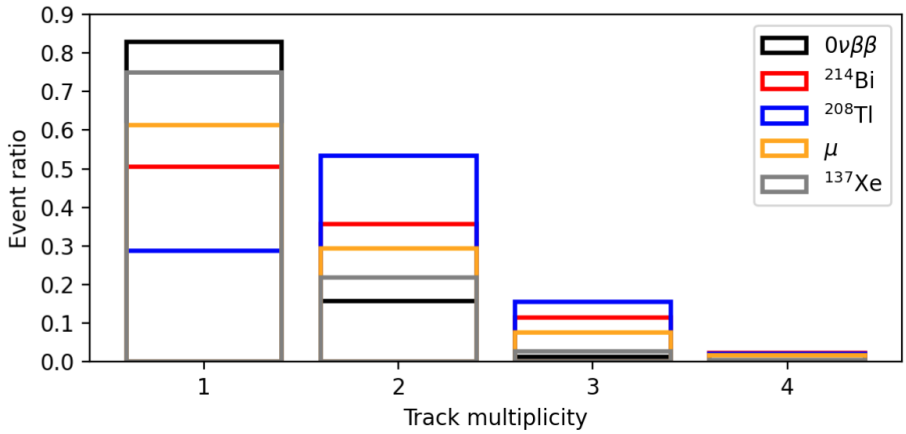


Figure 6.7: Track multiplicity for signal and background events.

Based on this, we assume a fiducial volume inside 4 cm from the chamber edges (R<45 cm) and 2 cm from the electrodes. Moreover, this selection eliminates events coming from ionizations or beta decays near the active volume, such as the light-tube or field-rings. Assuming these limits, the total xenon mass of 71.5 kg is reduced to 58.3 kg for the simulated running conditions. As noted before, this selection is correlated with **energy**, since after the [2.40, 2.50] MeV selection most part of $0\nu\beta\beta$ events at high radius are removed.

• **track**: this selects the events with a single reconstructed track. This selection is needed in order to apply the **topological** cut in the upcoming *discrimination selections*. It provides an improvement in the signal and background discrimination ($\eta > 1$) since the track multiplicity (number of tracks per event) is larger for background events than for signal events. Recall that track multiplicity is the discrimination variable of liquid xenon experiments (EXO-200 [72]). Figure 6.7 shows the track multiplicity for the different event types considered in the analysis. Notice the significantly higher number of $0\nu\beta\beta$ events with one track ($\sim$ 83%) with respect to the ^{208}Tl ($\sim$ 27%), since ^{208}Tl events in the [2.40, 2.50] MeV window come from secondary compton depositions. Nevertheless, when depositions are close enough, the event will be reconstructed as single track.

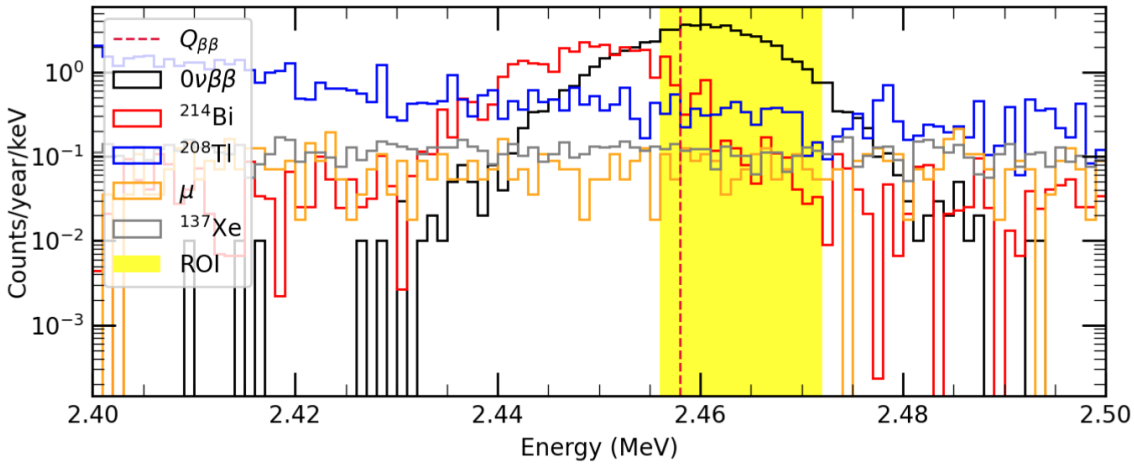


Figure 6.8: Energy distribution of signal and background events after the *analysis selection*. A large half-life of $T^{0\nu}_{1/2} = 1.3 \cdot 10^{24}$ years is assumed for visualization purpuses. The rates for background events are obtained through the radioactivity values and muon flux. The ROI selection window [2.456, 2.472] MeV that maximizes η is shown in yellow.

• **overlap (ovl)**: as described in 5.3.5 the *blobs* are defined as the energy of the hits inside a sphere of a chosen radius (Figure 5.7). It might be that the track extremes are so close that hits in one blob are also present in the other. This selection removes these events to avoid blob energy double counting.

After the application of the *analysis selections* above we can further study the discrimination power of the technology through the *discrimination selections*. There are two variables that we can use to distinguish between background and signal events: the total energy and the energy of the least energetic blob (E_{b_2}):

• **region of interest (ROI)**: this selection is applied over the total energy of the event by selecting an energy window in which the figure of merit η is maximized. Figure 6.8 shows the optimized energy window together with signal and background distributions.

• **topological (topo)**: this constitutes the most important discrimination selection of the experiment. Since signal-like events contain two high energetic blobs, the energy of the least energetic blob will be higher in signal events. Figure 6.9 shows the distribution of the energy of the least energetic blob for the simulated signal and background events after the *analysis selection*. Again, the optimal selection is chosen to maximize η, obtaining the value $E_{b_2} > 0.57$ MeV.

Based on the radiogenic activities (Table 6.1) and muon flux at LSC Hall A, we can compute the expected background rates after applying the selections above, shown in Figure 6.10. The contribution from detector component is shown in Figure 6.11. The background rate from muons will be assumed negligible in what follows: $> 99\%$ muon induced deposits lie within a 2 ms time window after the muon crosses the detector, thus a DAQ dead time will virtually be able to veto these backgrounds. A plastic muon veto detector with $> 90\%$ efficiency will surround the external castle with this purpose. The final background rate is expected to be around 1 counts/year after selections.

The signal and background efficiencies after both the *analysis* and *discrimination* selections are shown in Figure 6.12. Notice that this selection efficiency must be

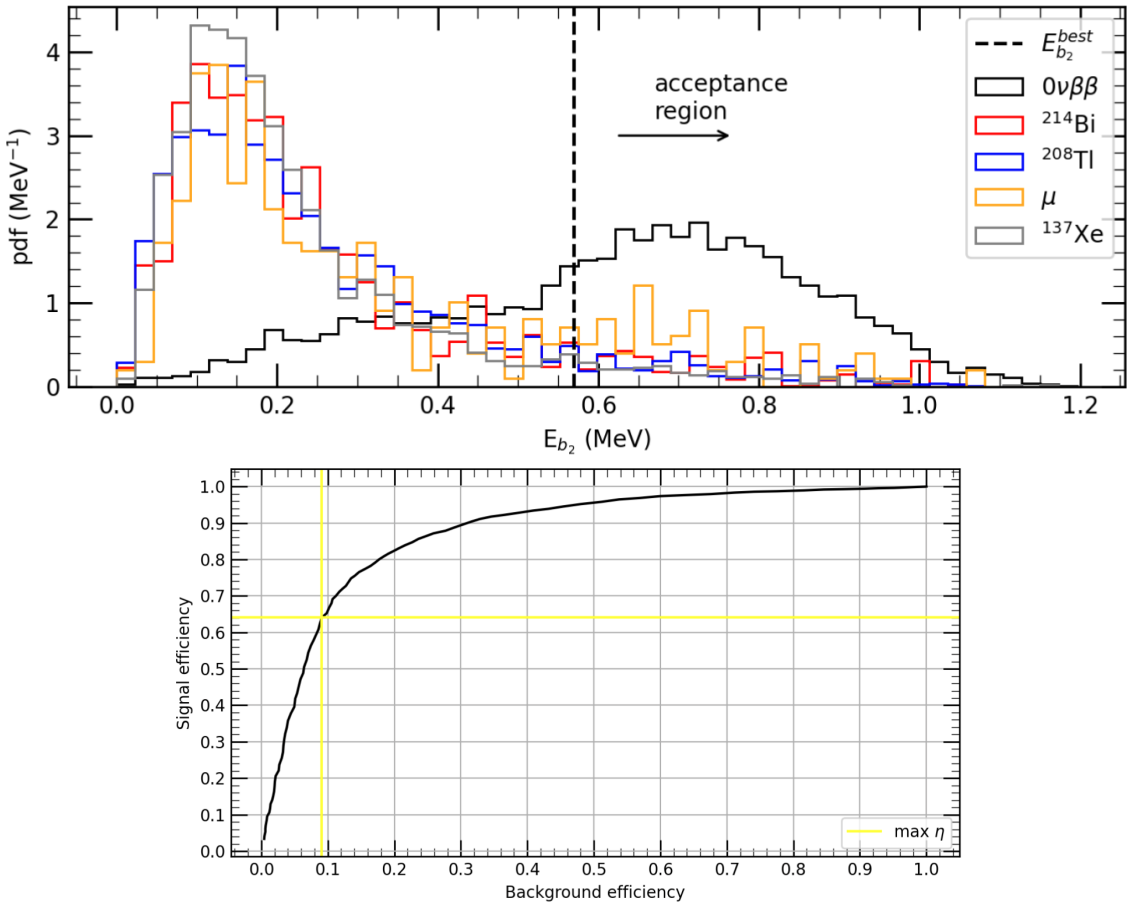


Figure 6.9: Top plot shows the distribution of the energy of the least energetic blob for signal and background events. The arrow shows the region of blob selection based on the blob energy that maximizes the figure of merit η. Lower plot shows the signal vs background efficiencies with a varying E_{b_2} selection (ROC curve). Yellow lines show the efficiencies at which η is maximized, corresponding to a $E_{b_2} > 0.57$ MeV selection.

computed using all the signal events instead of the events in the energy region [2.40, 2.50] MeV, since a significant amount $\sim$ 30% of them are degraded, as described before. Background event efficiencies are shown for comparative purposes, since the parameter of interest in the counting experiment sensitivity (6.1) is the absolute background rate (Figure 6.10). We obtain a signal efficiency of $\epsilon = 18\%$ after applying all the selections. Figur e 6.13 shows an example of a signal and a background event passing all the selections.

Finally, we can plug in the obtained values for the background rate of ~ 1 counts/year, and signal efficiency ($\epsilon = 18\%$) into (6.1). From the assumed running conditions in the simulation, we get a total xenon mass of $M_T = 71.5$ kg, which translates to $M = 64.3$ kg of ^{136}Xe source mass with the measured enrichment factor of 90%. The sensitivity curves at 90% CL for different exposures and background rates are shown in Figure 6.14. For the tentative running time of 3 years, we conclude the half-life sensitivity of $S(T^{0\nu}_{1/2}) \gtrsim 2.4 \cdot 10^{25}$ years at 90% CL, with the $\gtrsim$ symbol explicitly showing that the estimated background rate is still an upper limit.

USC DE SANTIAGO DE COMPOSTELA

(counts/year)	**nexus**	**reco**	**ene**	**fid**	**track**	**ovl**	**ROI**	**topo**
^{214}Bi	296	94	76	71	35	35	4.9	0.45
^{208}Tl	1800	312	277	240	56	56	5.2	0.47
muons (μ)	900	50	15	13	7	7	1.32	0.12
^{137}Xe	33	25	19	15	11	11	1.73	0.16

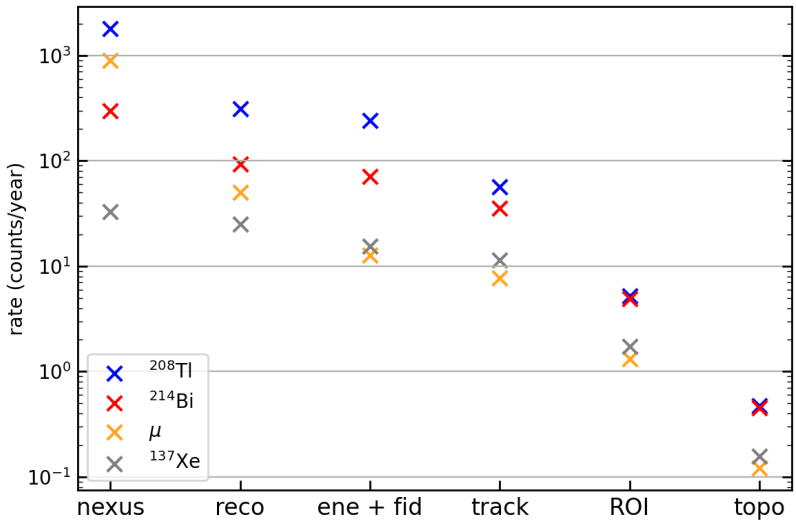


Figure 6.10: Background rates (counts/year) after each selection. Top table shows the numerical values. The **nexus** selection shows the rate of events with an energy deposition within [2.40, 2.50] MeV previous to reconstruction.

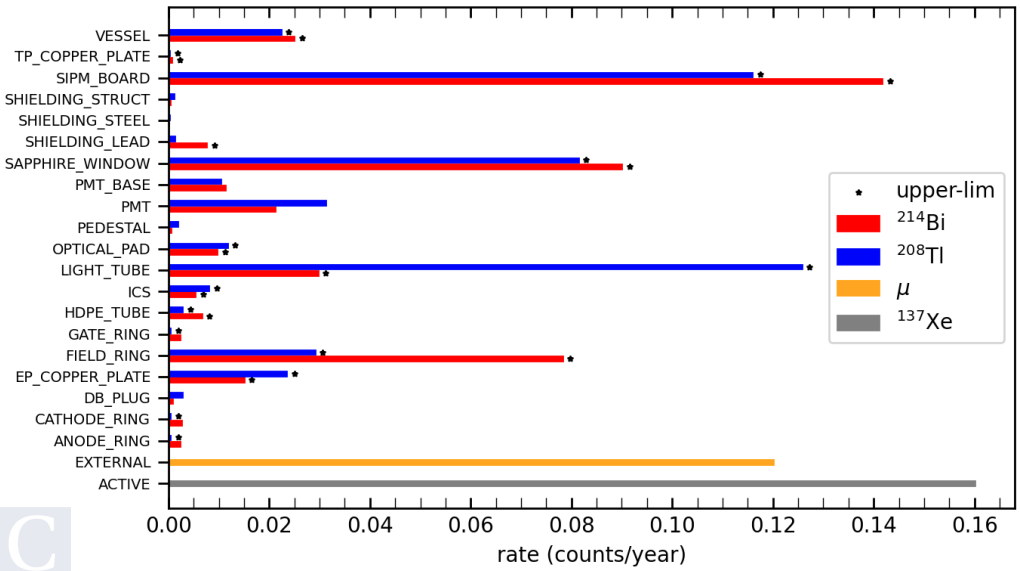


Figure 6.11: Final contribution from each detector volume to the background rate after the signal selection cuts. Bars marked with an asterisk (*) represent upper limits.

efficiencies (%)	**reco**	**ene**	**fid**	**track**	**ovl**	**ROI**	**topo**
$0\nu\beta\beta$	83	54	50	42	42	28	18
^{214}Bi	32	26	24	12	12	1.67	0.15
^{208}Tl	17	15	13	3	3	0.29	0.026
muons (μ)	5.6	1.66	1.40	0.86	0.86	0.15	0.013
^{137}Xe	76	55	47	35	35	5	0.48

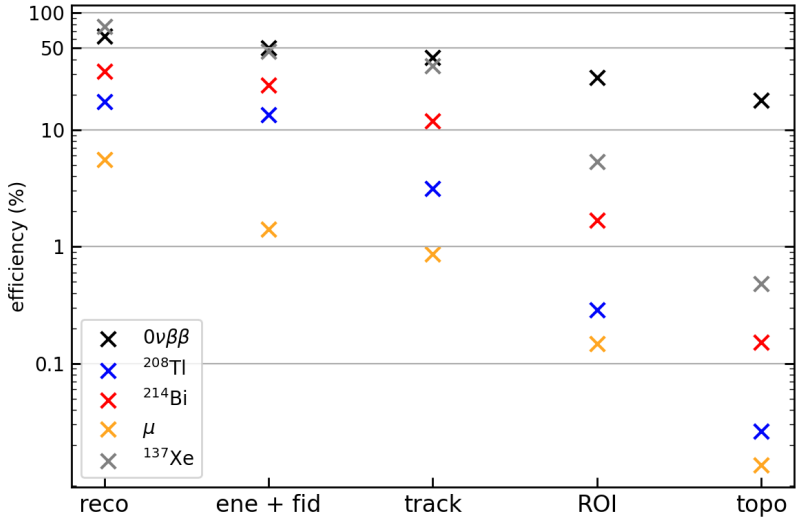


Figure 6.12: Signal and background efficiencies for each selection. Signal efficiencies are reported with respect to the total number of simulated $0\nu\beta\beta$. On the other hand, background efficiencies are reported with respect to the events with a total energy deposition within [2.40, 2.50] MeV.

USC UNIVERSIDADE DE SANTIAGO DE COMPOSTELA

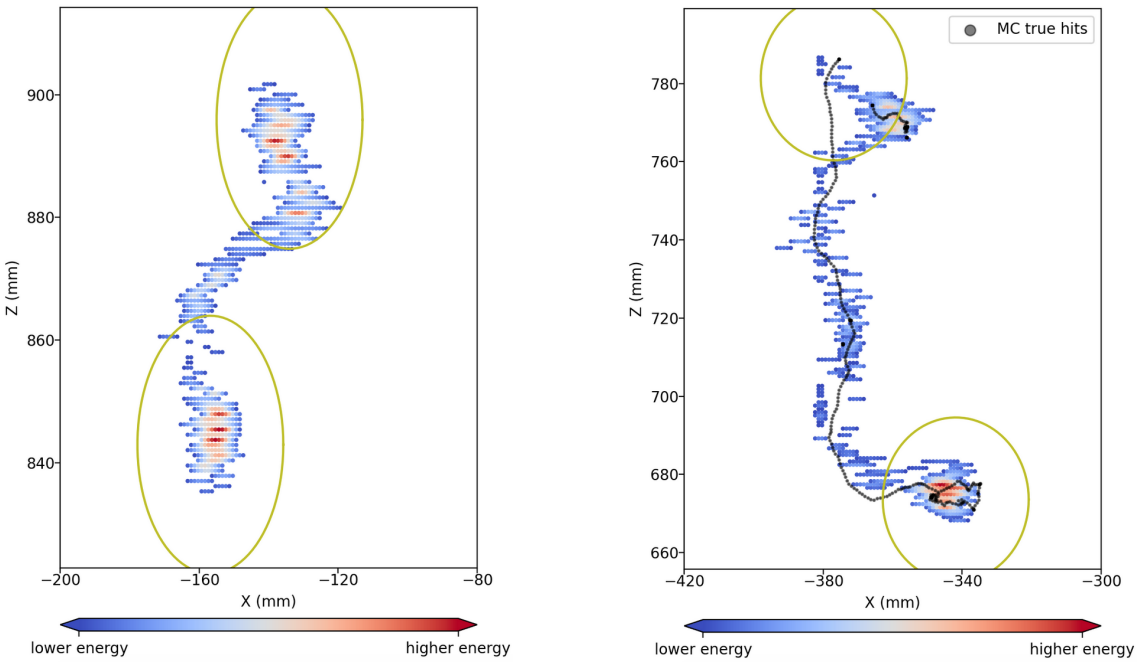


Figure 6.13: Bidimensional projections of signal (right) and background (left) events passing the *discrimination selections*. The background events corresponds to a ^{214}Bi coming from the EP-COPPER-PLATE, being misidentified as signal due to the bad reconstruction of a bremsstrahlung close to the start of the electron track as shown by the MC hits. The hits inside the yellow circles constitute the *blob*.

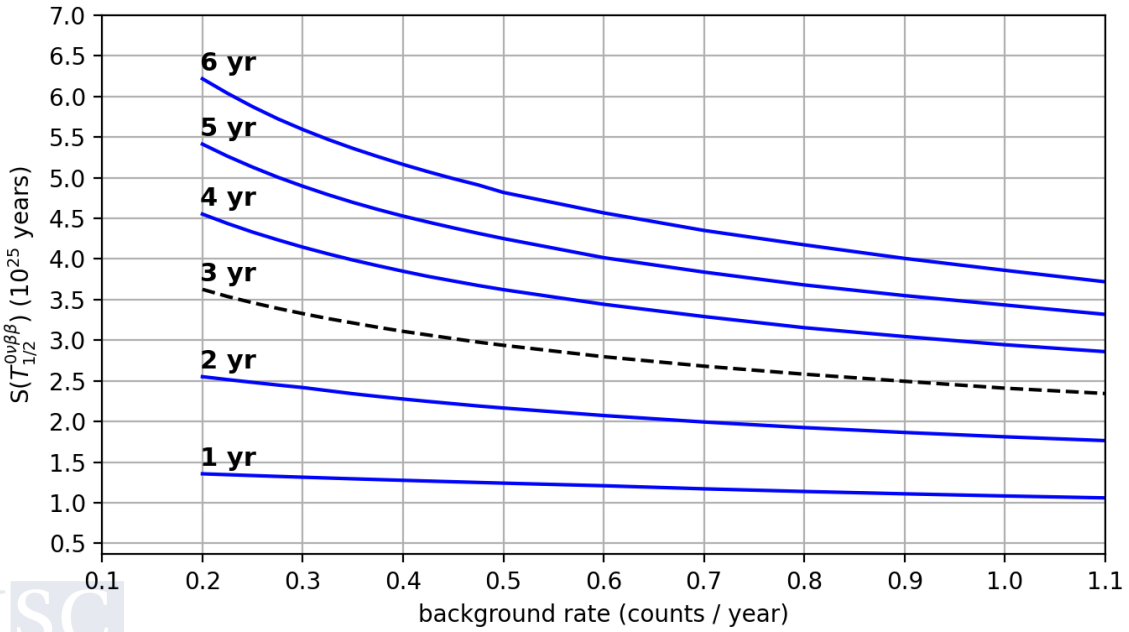


Figure 6.14: Sensitivity curves at 90% CL for NEXT-100 for different exposures. Dashed black line shows the curve for the tentative running time of 3 years.

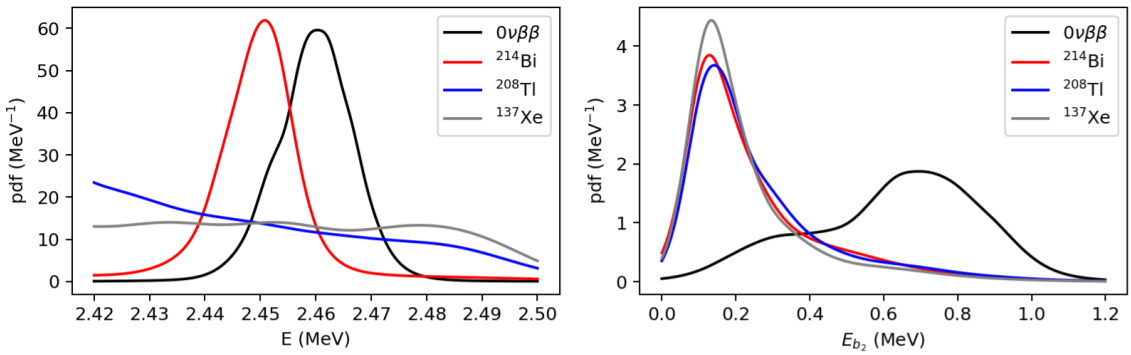


Figure 6.15: Total event energy (E) and least energetic *blob* energy (E_{b_2}) probability density functions for each type of event. The distributions are obtained using the whole simulation dataset after *analysis selection* and smoothed out through a KDE algorithm.

6.4.2. Confidence intervals

The counting experiment analysis in §6.4.1 defines the sensitivity as if no true signal exists, thus all the events passing the signal selections are assumed to be background events. The motivation for this definition is the comparison between different double beta experimental proposals. Nevertheless, when performing the experiment we will use our background model to estimate both the number of signal and background events. Once we estimate the number of observed signal events, we can report the final result as a confidence interval. In what follows we obtain the confidence intervals for the $0\nu\beta\beta$ decay half-life in NEXT-100.

To compute the confidence intervals (§2.2.1) we generate toy experiments for a range of double beta half-lifes $T^{0\nu}_{\beta\beta}$. For each $T^{0\nu}_{\beta\beta}$, we perform a large number ($\sim 10^4$) of toy experiments and fit them to estimate the number of 'observed' $0\nu\beta\beta$ events ($n_{\beta\beta}$), thus obtaining the probability distribution of the number of events for the simulated half-life

$$p(n_{\beta\beta}|T^{0\nu}_{\beta\beta}) \tag{6.2}$$

We assume the tentative running time of 3 years for NEXT-100. The number of background events in each toy experiment will be sampled from a poisson distribution with mean values given by those in Figure 6.10 after the *analysis selections* (ie the values at the **overlap** column). We will assume the presence of a muon veto, such that muon induced backgrounds except ^{137}Xe are negligible.

The toy experiments are generated by sampling the E and E_{b_2} probability density functions (pdfs) for signal and background events, shown in Figure 6.15. The pdfs are computed using the complete statistics of the simulation for each type of event after the *analysis selection* by smoothing out the histogram through a *kernel density estimation* (KDE) algorithm. Notice that the energy region [2.40, 2.50] MeV is slightly contracted in the lower bound to 2.42 MeV in order to avoid the edge effect of the KDE, requiring to add an extra efficiency over the *analysis selections*.

Based on the two discrimination variables (the total event energy E and the energy of the least energetic *blob* E_{b_2}) we define two different fit strategies:

- **Type I**: over our dataset we apply a signal selection, based on the *topological* selection in §6.4.1 keeping only the events with $E_{b_2} > 0.57$ MeV. We perform a fit

only to the total energy variable to estimate the number of events of each type.

- **Type II**: we do not perform any extra selection over our dataset. We perform a combined fit to the energy and E_{b_2} spectra to estimate the number of events of each type.

The number of signal and background events of each toy experiment are obtained by an extended maximum likelihood fit, consisting in maximizing the following expression

$$\mathcal{L}(\{E_i, E_{b_{2i}}\}|T^{0\nu}_{1/2}) = \text{Pois}(N|n_T) \times \prod_i^N p_E(E_i) \times p_{E_{b_2}}(E_{b_{2i}}), \tag{6.3}$$

where N represents the total number of events in the toy experiment; $n_T = n_{\beta\beta} + n_{Bi} + n_{Tl} + n_{Xe}$ where $n_{\beta\beta}, n_{Bi}, n_{Tl}, n_{Xe}$ are the number of events of each type to be estimated; and $p_E, p_{E_{b_2}}$ are the total energy and *blob* energy weighted pdfs

$$p_{E,E_{b_2}} = \frac{1}{n_T}\left(n_{\beta\beta}\ p^{\beta\beta}_{E,E_{b_2}} + n_{Bi}\ p^{Bi}_{E,E_{b_2}} + n_{Tl}\ p^{Tl}_{E,E_{b_2}} + n_{Xe}\ p^{Xe}_{E,E_{b_2}}\right) \tag{6.4}$$

The likelihood (6.3) is used with the **Type II** strategy in which both energy and *blob* energy information is used in the fit. For the **Type I** fit, the likelihood is the same but dropping out the $p_{E_{b_2}}$. We have verified that the total energy E and the *blob* energy E_{b_2} are not correlated in the small energy window of interest [2.40, 2.50] MeV: the energy pdf is not modified after the $E_{b_2} > 0.57$ MeV selection in the **Type I** strategy and the likelihood is the product of both pdfs in the **Type II** fits.

Examples of the distributions for the number of events for both types of strategies are shown in Figure 6.16 and Figure 6.17. Notice that the number of events is lower in the **Type I** distributions due to the topological selection. Also, the number of events of each type in the fit are constrained to be positive.

By computing $p(n_{\beta\beta}|T^{0\nu}_{1/2})$ for a sensible range of half-lifes to cover the 2D $(n_{\beta\beta}, T^{0\nu}_{1/2})$ space, we can obtain the confidence intervals (§2.2.1). The Feldman-Cousins intervals at 90% confidence level for both **Type I** and **Type II** strategies are shown in Figure 6.18.

We can define the sensitivity as the half-life limit we would report if the result of our experiment are zero signal event candidates. From the confidence intervals (Figure 6.18), we find that for $n_{\beta\beta} = 0$, we would report a lower limit of the half-life $T^{0\nu}_{1/2} > 3.6 \cdot 10^{25}$ years using the **Type I** fit stragtegy and $T^{0\nu}_{1/2} > 4.15 \cdot 10^{25}$ years using the **Type II**. These values corresponds to our experimental sensitivity at 90% CL after the tentative running time of 3 years.

USC UNIVERSIDADE DE SANTIAGO DE COMPOSTELA

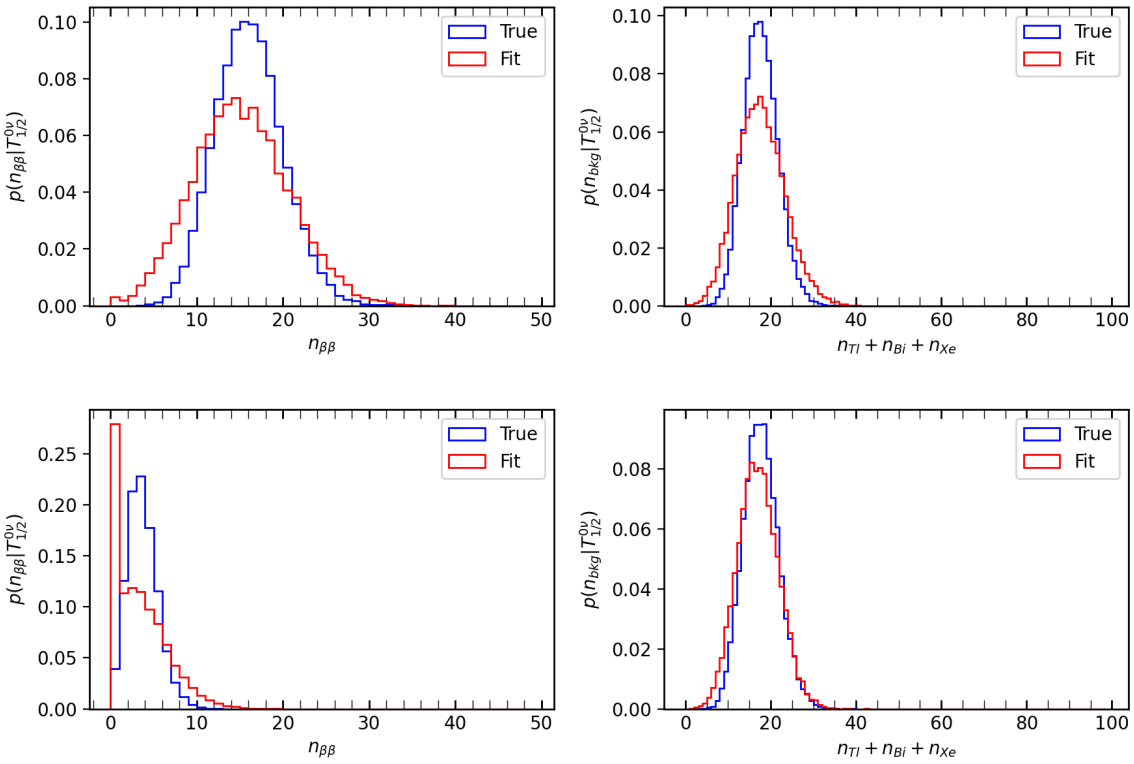


Figure 6.16: Type I distributions of the number of events in the toy experiment (True) and the number of events estimated by the fit (Fit). Top plots assume a relatively small half-life of $T^{0\nu}_{1/2} = 1 \cdot 10^{25}$ years and bottom plots $T^{0\nu}_{1/2} = 5 \cdot 10^{25}$ years. Left plots show the distribution for the number of signals ($n_{\beta\beta}$) and right plots show the total number of backgrounds (n_{bkg}).

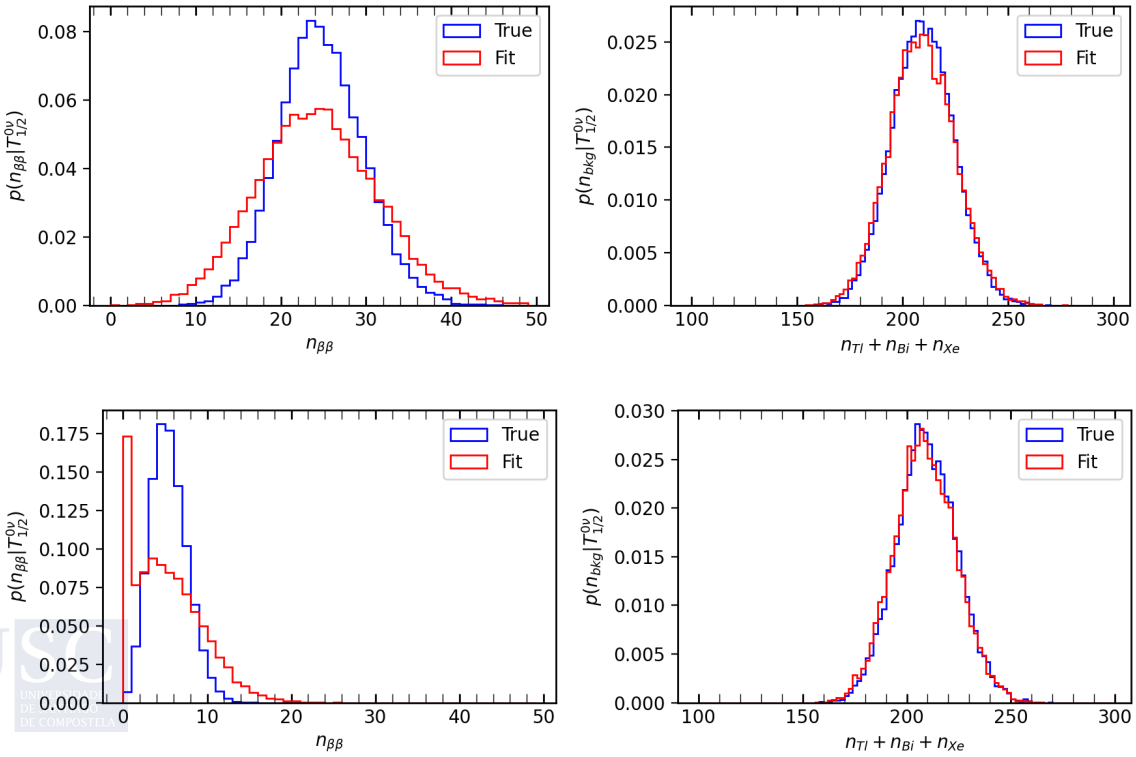


Figure 6.17: Same description as Figure 6.16 for the **TypeII** strategy.

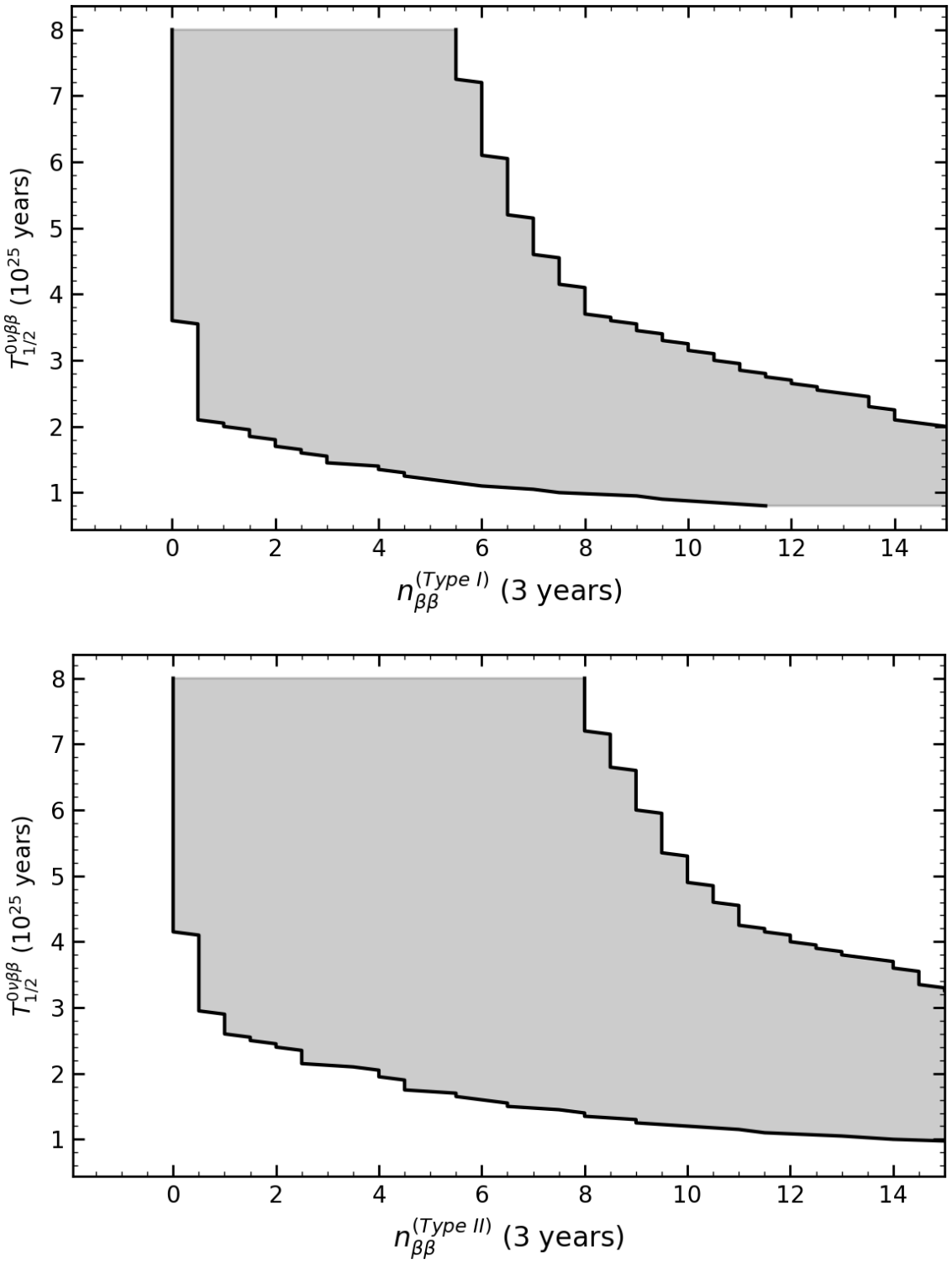


Figure 6.18: Confidence intervals at 90% CL for NEXT-100 after 3 years of running time, assuming the background contribution from radiogenic origin in Table 6.1 and ^{137}Xe activations from muons. Top plot shown the intervals for **TypeI** strategy and bottom plot for **TypeII**.

USC UNIVERSIDADE DE SANTIAGO DE COMPOSTELA

USC
UNIVERSIDADE
DE SANTIAGO
DE COMPOSTELA

CHAPTER 7
Summary and conclusions

The Standard Model of particle physics was built under the assumption that neutrinos were massless particles, as it was not contradicted by any experimental evidence at the time. However, the picture dramatically changed with the discovery of neutrino oscillations, requiring neutrinos to be massive. Neutrino oscillation experiments measure the neutrino flux from a source after traveling a significant distance, resulting in neutrinos changing their flavour composition between source to detection. The explanation requires to assume that flavour neutrinos are no longer the fundamental states of nature, but the existence of massive neutrinos. This raises two important questions: how many massive neutrinos exist? what is the mass generation mechanism and the absolute mass of massive neutrinos?. Neutrino oscillation experiments can only provide answers to the first, but another type of search must be devised to the second.

Neutrino masses can be accommodated in the SM in two different settings, Dirac or Majorana. From the theoretical point of view, the Majorana nature is favored as it could explain the small neutrino mass compared to the other fermions. The most important observable difference is that neutrinos being Majorana imply the violation of lepton number conservation. The most sensitive process in this search is neutrinoless double beta decay.

Neutrinoless double beta decay ($0\nu\beta\beta$) is a process in which a nucleus decays emitting two electrons, thus lepton number is violated in two units ($\Delta L = +2$). An appropiate experimental technique must be able to precisely measure the total energy of the electrons and reduce the background contributions as much as possible. Another essential feature of a double beta experiment is scaling, as half-lifes are expected to be higher than 10^{26} years. In this thesis, we focussed in the NEXT (*Neutrino Experiment with a Xenon TPC*) proposal. NEXT searches for $0\nu\beta\beta$ in ^{136}Xe using an electroluminiscence xenon TPC. The main features NEXT technique are the very good energy resolution of less than 1% at FWHM in the region of interest ($Q_{\beta\beta}$) and the 3D reconstruction of the electron trajectories, which allows to distinguish between signal and background events by using their different topological signatures. After an R&D phase, NEXT succesfully operated a relatively large scale detector with ~ 4 kg of xenon, NEXT-White, which allowed to probe the calibration methods, asses the background model and measure the half-life of the two neutrino mode of the double beta. Nowadays, NEXT collaboration is building the NEXT-100, a larger detector with ~ 70 kg of xenon with the aim of searching for the zero neutrino mode. In order to minimize the background contribution, both NEXT-White and NEXT-100 are built using radiopure

materials and placed in *Canfranc Underground Laboratory*, an underground facility in the Spanish Pyrenees.

The objective of this thesis was to study the sensitivity of NEXT-100 to neutrinoless double beta decay. Since NEXT-100 is under construction, the analysis was entirely driven by MC simulations and the background model built based on previous experience with NEXT-White, the radiogenic measurement campaign carried out by the collaboration and the knowledge of the muon flux inside the laboratory. Simulations were performed usign two set of software tools: the GEANT4 implementation of the detector which allows the simulation of the energy loss of the different types of events; and DETSIM which implements the simulation of the detector's response. This allows the simulation of large exposure samples of both signal and background events, which are analyzed to estimate the sensitivity.

The sensitivity is studied using two different methods: the counting experiment limit which assumes that no true signal exists, and by the use of the confidence intervals. In the counting experiment we perform a set of *analysis selections* which provide single track data samples which are used to discriminate between signal and background events in the *discrimination selections* based on the total energy and the Bragg peak. We optimize the signal selection over background, resulting in a signal efficiency of $\sim 18\%$ and a background rate less than 1 count per year which translates into the conservative half-life sensitivity of $T^{0\nu}_{1/2} \gtrsim 2.4 \cdot 10^{25}$ years after a tentative running time of 3 years. A more realistic method to study the sensitivity is introduced, consisting in the generation of toy MC experiments and computing the confidence intervals. Using a combined fit to the two variables of discrimination, the total energy of the event and the energy of the least energetic *blob*, we obtain the half-life sensitivity of $T^{0\nu}_{1/2} > 4.15 \cdot 10^{25}$ years after 3 years of running time. Figure 7.1 shows the sensitivity to $m_{\beta\beta}$ in order to compare with the limits already set by past and ongoing experiments. The study carried out in this thesis concludes that NEXT-100 prospects in the search of neutrinoless double beta decay are similar to its main competitors in the hundred-kilogram escale detector masses.

USC UNIVERSIDADE DE SANTIAGO DE COMPOSTELA

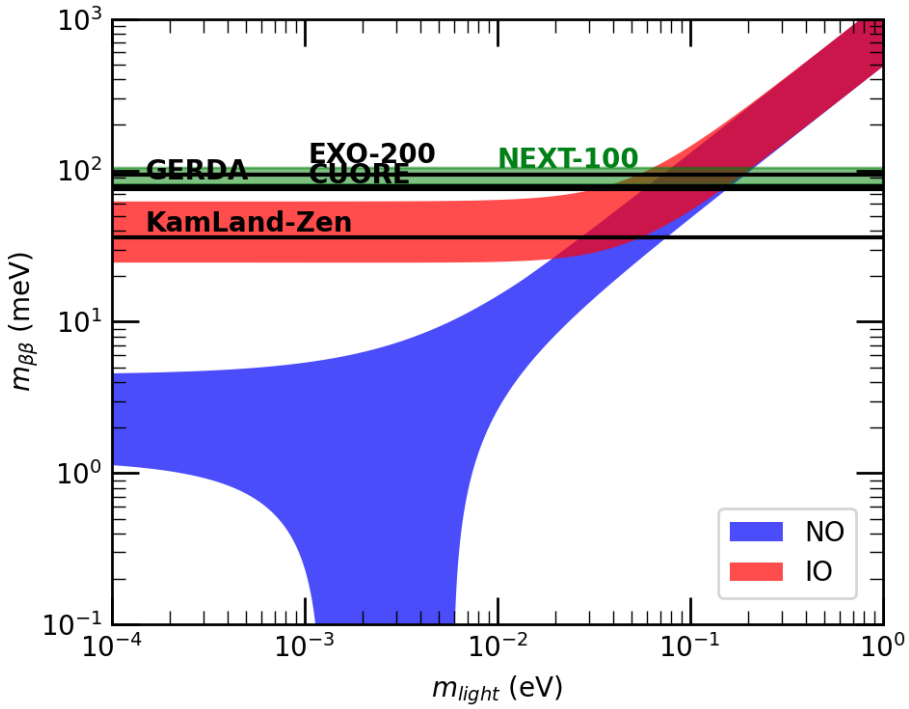


Figure 7.1: Effective majorana mass $m_{\beta\beta}$ as a function of of the mass of the lightest neutrino in the three neutrino mixing scenario, using the mixing parameters from Table 1.4. Black horizontal lines show the lowest value of the $m_{\beta\beta}$ reported by each experiment (Table 2.2). Shaded green area shows the $m_{\beta\beta}$ region for NEXT-100 after 3 years of running time for the sensitivities reported in this thesis. The $m_{\beta\beta}$ is computed using the QRPA nuclear matrix element for xenon [156], which provides the lowest limit amongst the computation methods, and the phase space factor from [157].

USC
UNIVERSIDADE DE SANTIAGO DE COMPOSTELA

USC
UNIVERSIDADE
DE SANTIAGO
DE COMPOSTELA

Bibliography

[1] Samoil Bilenky. *Introduction to the Physics of Massive and Mixed Neutrinos*. Vol. 947. Springer, 2018, pp.1–273. DOI: 10.1007/978-3-319-74802-3.

[2] C. D. Ellis and W. A. Wooster. "The Continuous Spectrum of β-Rays". In: *Nature* 119.2998 (Apr. 1927), pp. 563–564. ISSN: 1476-4687. DOI: 10.1038/119563c0.

[3] F Reines and C L Cowan Jr. *On the detection of the free neutrino*. Aug. 1953. DOI: 10.2172/4425708.

[4] C. Giunti and C. W. Kim. *Fundamentals of Neutrino Physics and Astrophysics*. Oxford, UK: Oxford University Press, 2007, pp. 1–728.

[5] C. S. Wu et al. "Experimental Test of Parity Conservation in Beta Decay". In: *Phys. Rev.* 105 (4 Feb. 1957), pp. 1413–1415. DOI: 10.1103/PhysRev.105.1413.

[6] Ettore Majorana. "Teoria simmetrica dell'elettrone e del positrone". In: *Nuovo Cim.* 14 (1937), pp. 171–184. DOI: 10.1007/BF02961314.

[7] Hermann Weyl. "Gravitation and the Electron". In: *Proceedings of the National Academy of Sciences of the United States of America* 15.4 (1929), pp. 323–334. ISSN: 00278424.

[8] T. D. Lee and C. N. Yang. "Parity Nonconservation and a Two-Component Theory of the Neutrino". In: *Phys. Rev.* 105 (5 Mar. 1957), pp. 1671–1675. DOI: 10.1103/PhysRev.105.1671.

[9] M. Goldhaber, L. Grodzins, and A. W. Sunyar. "Helicity of Neutrinos". In: *Phys. Rev.* 109 (3 Feb. 1958), pp. 1015–1017. DOI: 10.1103/PhysRev.109.1015.

[10] Wikipedia. *Standard Model — Wikipedia, The Free Encyclopedia*. 2021.

[11] Rabindra N. Mohapatra and Goran Senjanovi ć. "Neutrino Mass and Spontaneous Parity Nonconservation". In: *Phys. Rev. Lett.* 44 (14 Apr. 1980), pp. 912–915. DOI: 10.1103/PhysRevLett.44.912.

[12] Particle Data Group et al. "Review of Particle Physics". In: *Progress of Theoretical and Experimental Physics* 2020.8 (Aug. 2020). ISSN: 2050-3911. DOI: 10.1093/ptep/ptaa104.

[13] Andrei D Sakharov. "Violation of CP invariance, C asymmetry, and baryon asymmetry of the universe". In: *Soviet Physics Uspekhi* 34.5 (May 1991), pp. 392–393. DOI: 10.1070/pu1991v034n05abeh002497.

[14] R. Davis. "A review of the Homestake solar neutrino experiment". In: *Prog. Part. Nucl. Phys.* 32 (1994), pp. 13–32.

[15] B. Aharmim et al. "Electron energy spectra, fluxes, and day-night asymmetries of B-8 solar neutrinos from measurements with NaCl dissolved in the heavy-water detector at the Sudbury Neutrino Observatory". In: *Phys. Rev. C* 72 (2005), p. 055502. DOI: 10.1103/PhysRevC.72.055502. arXiv: nucl-ex/0502021.

USC UNIVERSIDADE DE SANTIAGO DE COMPOSTELA

[16] J. Hosaka et al. “Solar neutrino measurements in super-Kamiokande-I”. In: *Phys. Rev. D* 73 (2006), p. 112001. DOI: 10.1103/PhysRevD.73.112001. arXiv: hep-ex/0508053.

[17] A. Y. Smirnov. “The Mikheyev-Smirnov-Wolfenstein (MSW) Effect”. In: *International Conference on History of the Neutrino: 1930-2018*. Jan. 2019. arXiv: 1901.11473 [hep-ph].

[18] A. Renshaw et al. “First Indication of Terrestrial Matter Effects on Solar Neutrino Oscillation”. In: *Phys. Rev. Lett.* 112.9 (2014), p. 091805. DOI: 10.1103/PhysRevLett.112.091805. arXiv: 1312.5176 [hep-ex].

[19] K. S. Hirata et al. “Observation of a small atmospheric ν_μ/ν_e ratio in Kamiokande”. In: *Phys. Lett.* B280 (1992), pp. 146–152.

[20] Y. Ashie et al. “A Measurement of Atmospheric Neutrino Oscillation Parameters by Super-Kamiokande I”. In: *Phys. Rev.* D71 (2005), p. 112005. arXiv: hep-ex/0501064.

[21] P.F. de Salas et al. “2020 Global reassessment of the neutrino oscillation picture”. In: (June 2020). arXiv: 2006.11237 [hep-ph].

[22] A. Aguilar et al. “Evidence for neutrino oscillations from the observation of $\bar{\nu}_e$ appearance in a $\bar{\nu}_\mu$ beam”. In: *Phys. Rev.* D64 (2001), p. 112007. arXiv: hep-ex/0104049.

[23] Teppei Katori and Janet Conrad. “Beyond Standard Model Searches in the MiniBooNE Experiment”. In: *Adv.High Energy Phys.* 2015 (2015), p. 362971. arXiv: 1404.7759 [hep-ex].

[24] P. Abratenko et al. “High-performance Generic Neutrino Detection in a LArTPC near the Earth’s Surface with the MicroBooNE Detector”. In: (Dec. 2020). arXiv: 2012.07928 [hep-ex].

[25] Francesca Di Lodovico and on behalf of the Hyper-Kamiokande Collaboration. “The Hyper-Kamiokande Experiment”. In: *Journal of Physics: Conference Series* 888.1 (Sept. 2017), p. 012020. DOI: 10.1088/1742-6596/888/1/012020.

[26] *Deep Underground Neutrino Experiment*. URL: https://www.dunescience.org/.

[27] “JUNO physics and detector”. In: *Progress in Particle and Nuclear Physics* 123 (Mar. 2022), p. 103927. DOI: 10.1016/j.ppnp.2021.103927.

[28] S Adrián-Martínez et al. “Letter of intent for KM3NeT 2.0”. In: *Journal of Physics G: Nuclear and Particle Physics* 43.8 (June 2016), p. 084001. DOI: 10.1088/0954-3899/43/8/084001.

[29] M. Aker et al. “Direct neutrino-mass measurement with sub-electronvolt sensitivity”. In: *Nature Physics* 18.2 (Feb. 2022), pp. 160–166. ISSN: 1745-2481. DOI: 10.1038/s41567-021-01463-1.

[30] M. Aker et al. “Improved Upper Limit on the Neutrino Mass from a Direct Kinematic Method by KATRIN”. In: *Physical Review Letters* 123.22 (Nov. 2019). DOI: 10.1103/physrevlett.123.221802. arXiv: 1909.06048 [hep-ex].

[31] Ali Ashtari Esfahani et al. “Determining the neutrino mass with cyclotron radiation emission spectroscopy—Project 8”. In: *J. Phys. G* 44.5 (2017), p. 054004. DOI: 10.1088/1361-6471/aa5b4f. arXiv: 1703.02037 [physics.ins-det].

[32] C. Hassel et al. “Recent Results for the ECHo Experiment”. In: *Journal of Low Temperature Physics* 184.3 (Aug. 2016), pp. 910–921. ISSN: 1573-7357. DOI: 10.1007/s10909-016-1541-9.

USC UNIVERSIDADE DE SANTIAGO DE COMPOSTELA

[33] A. Puiu et al. “HOLMES, an experiment for a direct measurement of neutrino mass”. In: *Nuovo Cimento* 42.4 (2019). ISSN: 2037-4909. DOI: {10.1393/ncc/i2019-19178-6}.

[34] Bruce H. J. McKellar. “The influence of mixing of finite mass neutrinos on beta decay spectra”. In: *Phys. Lett.* B97 (1980), p. 93.

[35] M. Goeppert-Mayer. “Double beta-disintegration”. In: *Phys. Rev.* 48 (1935), pp. 512–516.

[36] S. R. Elliott, A. A. Hahn, and M. K. Moe. “Direct evidence for two-neutrino double-beta decay in ^{82}Se”. In: *Phys. Rev. Lett.* 59 (18 Nov. 1987), pp. 2020–2023. DOI: 10.1103/PhysRevLett.59.2020.

[37] W.H. Furry. “On transition probabilities in double beta-disintegration”. In: *Phys. Rev.* 56 (1939), pp. 1184–1193. DOI: 10.1103/PhysRev.56.1184.

[38] Stefano Dell’Oro et al. “Neutrinoless Double Beta Decay: 2015 Review”. In: *Advances in High Energy Physics* 2016 (Apr. 2016), p. 2162659. ISSN: 1687-7357. DOI: 10.1155/2016/2162659.

[39] W.C. Haxton and G.J. Stephenson. “Double beta decay”. In: *Progress in Particle and Nuclear Physics* 12 (1984), pp. 409–479. ISSN: 0146-6410. DOI: https://doi.org/10.1016/0146-6410(84)90006-1.

[40] M. Hirsch. “Neutrinoless double beta decay, neutrino mass and bilinear R parity breaking supersymmetry”. In: *Nucl. Phys. B Proc. Suppl.* 81 (2000). Ed. by V. Berezinsky, G. Raffelt, and J. W. F. Valle, pp. 249–253. DOI: 10.1016/S0920-5632(99)00883-X. arXiv: hep-ph/9909443.

[41] J. Schechter and J. W. F. Valle. “Neutrinoless double-β decay in SU(2)×U(1) theories”. In: *Phys. Rev. D* 25 (11 June 1982), pp. 2951–2954. DOI: 10.1103/PhysRevD.25.2951.

[42] Eiichi Takasugi. “Can the neutrinoless double beta decay take place in the case of Dirac neutrinos?” In: *Physics Letters B* 149.4 (1984), pp. 372–376. ISSN: 0370-2693. DOI: https://doi.org/10.1016/0370-2693(84)90426-X.

[43] Michael Duerr, Manfred Lindner, and Alexander Merle. “On the Quantitative Impact of the Schechter-Valle Theorem”. In: *JHEP* 06 (2011), p. 091. DOI: 10.1007/JHEP06(2011)091. arXiv: 1105.0901 [hep-ph].

[44] Masaru Doi, Tsuneyuki Kotani, and Eiichi Takasugi. “Double Beta Decay and Majorana Neutrino”. In: *Progress of Theoretical Physics Supplement* 83 (Mar. 1985), pp. 1–175. ISSN: 0375-9687. DOI: 10.1143/PTPS.83.1.

[45] J. Kotila and F. Iachello. “Phase space factors for double-β decay”. In: *Phys. Rev. C* 85 (2012), p. 034316. DOI: 10.1103/PhysRevC.85.034316. arXiv: 1209.5722 [nucl-th].

[46] Jonathan Engel and Javier Menéndez. “Status and Future of Nuclear Matrix Elements for Neutrinoless Double-Beta Decay: A Review”. In: *Rept. Prog. Phys.* 80.4 (2017), p. 046301. DOI: 10.1088/1361-6633/aa5bc5. arXiv: 1610.06548 [nucl-th].

[47] Juris Meija et al. “Isotopic compositions of the elements 2013 (IUPAC Technical Report)”. In: *Pure and Applied Chemistry* 88.3 (1Mar. 2016), pp. 293–306. DOI: https://doi.org/10.1515/pac-2015-0503.

[48] B. Pritychenko. “Systematics of Evaluated Half-lives of Double-beta Decay”. In: *Nuclear Data Sheets* 120 (2014), pp. 102–105. ISSN: 0090-3752. DOI: https://doi.org/10.1016/j.nds.2014.07.018.

USC UNIVERSIDADE DE SANTIAGO DE COMPOSTELA

[49] S. Umehara et al. "Neutrino-less double-β decay of ^{48}Ca studied by CaF_2(Eu) scintillators". In: *Phys. Rev. C* 78 (5 Nov. 2008), p. 058501. DOI: 10.1103/PhysRevC.78.058501.

[50] M. Agostini et al. "Final Results of GERDA on the Search for Neutrinoless Double-β Decay". In: *Phys. Rev. Lett.* 125 (25 Dec. 2020), p. 252502. DOI: 10.1103/PhysRevLett.125.252502. arXiv: 2009.06079 [nucl-ex].

[51] R. Arnold et al. "Final results on ^{82}Se double beta decay to the ground state of ^{82}Kr from the NEMO-3 experiment". In: *The European Physical Journal C* 78.10 (Oct. 2018), p. 821. ISSN: 1434-6052. DOI: 10.1140/epjc/s10052-018-6295-x.

[52] J. Argyriades et al. "Measurement of the two neutrino double beta decay half-life of Zr-96 with the NEMO-3 detector". In: *Nuclear Physics A* 847.3 (2010), pp. 168–179. ISSN: 0375-9474. DOI: https://doi.org/10.1016/j.nuclphysa.2010.07.009.

[53] R. Arnold et al. "Results of the search for neutrinoless double-β decay in ^{100}Mo with the NEMO-3 experiment". In: *Phys. Rev. D* 92 (7 Oct. 2015), p. 072011. DOI: 10.1103/PhysRevD.92.072011.

[54] R. Arnold et al. "Measurement of the $2\nu\beta\beta$ decay half-life and search for the $0\nu\beta\beta$ decay of ^{116}Cd with the NEMO-3 detector". In: *Phys. Rev. D* 95 (1 Jan. 2017), p. 012007. DOI: 10.1103/PhysRevD.95.012007.

[55] D. Q. Adams et al. "Improved Limit on Neutrinoless Double-Beta Decay in ^{130}Te with CUORE". In: *Phys. Rev. Lett.* 124 (12 Mar. 2020), p. 122501. DOI: 10.1103/PhysRevLett.124.122501.

[56] CUORE Collaboration et al. *Measurement of the $2\nu\beta\beta$ Decay Half-life of ^{130}Te with CUORE*. 2020. arXiv: 2012.11749 [nucl-ex].

[57] KamLandZen Collaboration. *First Search for the Majorana Nature of Neutrinos in the Inverted Mass Ordering Region with KamLAND-Zen*. 2022. DOI: 10.48550/arxiv.2203.02139. arXiv: 2203.02139 [hep-ex].

[58] R. Arnold et al. "Measurement of the $2\nu\beta\beta$ decay half-life of ^{150}Nd and a search for $0\nu\beta\beta$ decay processes with the full exposure from the NEMO-3 detector". In: *Phys. Rev. D* 94 (7 Oct. 2016), p. 072003. DOI: 10.1103/PhysRevD.94.072003.

[59] J. Neyman and Harold Jeffreys. "Outline of a Theory of Statistical Estimation Based on the Classical Theory of Probability". In: *Philosophical Transactions of the Royal Society of London. Series A, Mathematical and Physical Sciences* 236.767 (1937), pp. 333–380. DOI: 10.1098/rsta.1937.0005.

[60] Gary J. Feldman and Robert D. Cousins. "Unified approach to the classical statistical analysis of small signals". In: *Physical Review D* 57.7 (Apr. 1998), pp. 3873–3889. DOI: 10.1103/physrevd.57.3873.

[61] R. L. Workman et al. "Review of Particle Physics". In: *PTEP* 2022 (2022), p. 083C01. DOI: 10.1093/ptep/ptac097.

[62] J.J Gómez-Cadenas et al. "Sense and sensitivity of double beta decay experiments". In: *Journal of Cosmology and Astroparticle Physics* 2011.06 (June 2011), pp. 007–007. DOI: 10.1088/1475-7516/2011/06/007.

[63] Justo Martín Albo. "The NEXT experiment for neutrinoless double beta decay searches". PhD thesis. IFIC, 2015.

[64] Michelle J. Dolinski, Alan W.P. Poon, and Werner Rodejohann. "Neutrinoless Double-Beta Decay: Status and Prospects". In: *Annual Review of Nuclear and Particle Science* 69.1 (2019), pp. 219–251. DOI: 10.1146/annurev-nucl-101918-023407.

[65] The CUPID Interest Group. *CUPID pre-CDR*. 2019. arXiv: 1907.09376.

USC UNIVERSIDADE DE SANTIAGO DE COMPOSTELA

[66] Ruben Saakyan. "Two-Neutrino Double-Beta Decay". In: *Annual Review of Nuclear and Particle Science* 63.1 (2013), pp. 503–529. DOI: 10.1146/annurev-nucl-102711-094904.

[67] E. L. Fireman. "A Measurement of the Half-Life of Double Beta-Decay from $_{50}Sn^{124}$". In: *Phys. Rev.* 75 (2 Jan. 1949), pp. 323–324. DOI: 10.1103/PhysRev.75.323.

[68] M. Gunther et al. "Heidelberg - Moscow beta-beta experiment with Ge-76: Full setup with five detectors". In: *Phys. Rev. D* 55 (1997), pp. 54–67. DOI: 10.1103/PhysRevD.55.54.

[69] C. E. Aalseth et al. "The IGEX Ge-76 neutrinoless double beta decay experiment: Prospects for next generation experiments". In: *Phys. Rev. D* 65 (2002), p. 092007. DOI: 10.1103/PhysRevD.65.092007. arXiv: hep-ex/0202026.

[70] H. V. Klapdor-kleingrothaus and I. Krivosheina. "The evidence for the observation of 0ν beta beta decay: The identification of 0ν beta beta events from the full spectra." In: *Modern Physics Letters A* 21 (2006), pp. 1547–1566.

[71] A. Gando et al. "Limit on Neutrinoless $\beta\beta$ Decay of ^{136}Xe from the First Phase of KamLAND-Zen and Comparison with the Positive Claim in ^{76}Ge". In: *Phys. Rev. Lett.* 110.6 (2013), p. 062502. DOI: 10.1103/PhysRevLett.110.062502. arXiv: 1211.3863 [hep-ex].

[72] G. Anton et al. "Search for Neutrinoless Double-β Decay with the Complete EXO-200 Dataset". In: *Phys. Rev. Lett.* 123 (16 Oct. 2019), p. 161802. DOI: 10.1103/PhysRevLett.123.161802. arXiv: 1906.02723 [hep-ex].

[73] S. I. Alvis et al. "A Search for Neutrinoless Double-Beta Decay in ^{76}Ge with 26 kg-yr of Exposure from the MAJORANA DEMONSTRATOR". In: *Phys. Rev. C* 100.2 (2019), p. 025501. DOI: 10.1103/PhysRevC.100.025501. arXiv: 1902.02299 [nucl-ex].

[74] K.-H. Ackermann et al. "The Gerda experiment for the search of $0\nu\beta\beta$ decay in ^{76}Ge". In: *The European Physical Journal C* 73.3 (Mar. 2013). DOI: 10.1140/epjc/s10052-013-2330-0. arXiv: 1212.4067 [nucl-ex].

[75] N. Abgrall et al. "The large enriched germanium experiment for neutrinoless double beta decay (LEGEND)". In: *AIP Conference Proceedings* 1894.1 (2017), p. 020027. DOI: 10.1063/1.5007652.

[76] Denys Poda and Andrea Giuliani. "Low background techniques in bolometers for double-beta decay search". In: *International Journal of Modern Physics A* 32.30 (2017), p. 1743012. DOI: 10.1142/S0217751X17430126.

[77] M.H. Lee. "AMoRE: a search for neutrinoless double-beta decay of 100Mo using low-temperature molybdenum-containing crystal detectors". In: *Journal of Instrumentation* 15.08 (Aug. 2020), pp. C08010–C08010. ISSN: 1748-0221. DOI: 10.1088/1748-0221/15/08/c08010.

[78] M Auger et al. "The EXO-200 detector, part I: detector design and construction". In: *Journal of Instrumentation* 7.05 (May 2012), P05010–P05010. ISSN: 1748-0221. DOI: 10.1088/1748-0221/7/05/p05010. arXiv: 1202.2192 [physics.ins-det].

[79] nEXO Collaboration et al. *nEXO Pre-Conceptual Design Report*. 2018. arXiv: 1805.11142 [physics.ins-det].

[80] S. Wang. "The TPC detector of PandaX-III Neutrinoless Double Beta Decay experiment". In: *Journal of Instrumentation* 15.03 (Mar. 2020), pp. C03052–C03052. ISSN: 1748-0221. DOI: 10.1088/1748-0221/15/03/c03052.

USC UNIVERSIDADE DE SANTIAGO DE COMPOSTELA

[81] F. Agostini et al. *Sensitivity of the DARWIN observatory to the neutrinoless double beta decay of ^{136}Xe*. 2020. arXiv: 2003.13407 [physics.ins-det].

[82] SNO+ Collaboration et al. *Development, characterisation, and deployment of the SNO+ liquid scintillator*. 2020. arXiv: 2011.12924 [physics.ins-det].

[83] Yoshiyuki Fukuda et al. "ZICOS - Neutrinoless Double Beta Decay experiment using Zr-96 with an organic liquid scintillator -". In: *Journal of Physics: Conference Series* 1468 (Feb. 2020), p. 012139. DOI: 10.1088/1742-6596/1468/1/012139.

[84] J. Gruszko et al. "Detecting Cherenkov light from 1–2 MeV electrons in linear alkylbenzene". In: *Journal of Instrumentation* 14.02 (Feb. 2019), P02005–P02005. ISSN: 1748-0221. DOI: 10.1088/1748-0221/14/02/p02005.

[85] J. R. Alonso et al. *Advanced Scintillator Detector Concept (ASDC): A Concept Paper on the Physics Potential of Water-Based Liquid Scintillator*. 2014. arXiv: 1409.5864 [physics.ins-det].

[86] S. Ajimura et al. *Low background measurement in CANDLES-III for studying the neutrino-less double beta decay of ^{48}Ca*. 2020. arXiv: 2008.09288 [hep-ex].

[87] Matsuda Sayuri. "Search for Neutrinoless Double-Beta Decay in ^{136}Xe after Intensive Background Reduction with KamLAND-Zen". PhD thesis. Tohoku University, 2016. URL: https://ci.nii.ac.jp/naid/500001051902.

[88] A.S. Barabash et al. "Calorimeter development for the SuperNEMO double beta decay experiment". In: *Nuclear Instruments and Methods in Physics Research Section A: Accelerators, Spectrometers, Detectors and Associated Equipment* 868 (2017), pp. 98–108. ISSN: 0168-9002. DOI: https://doi.org/10.1016/j.nima.2017.06.044.

[89] https://next.ific.uv.es/next/.

[90] Norman Davidson and A. E. Larsh. "Conductivity Pulses in Liquid Argon". In: *Phys. Rev.* 74 (2 July 1948), pp. 220–220. DOI: 10.1103/PhysRev.74.220.

[91] Ernest Solomon. "Molecular theory of gases and liquids. Joseph O. Hirschfelder, Charles F. Curtiss, and R. Byron Bird. John Wiley & Sons, Inc., New York (1954). 1219 pages. $20". In: *AIChE Journal* 1.2 (1955), pp. 272–272. DOI: https://doi.org/10.1002/aic.690010225.

[92] G. J. Mahler et al. "A portable gamma-ray spectrometer using compressed xenon". In: *IEEE Transactions on Nuclear Science* 45.3 (June 1998), pp. 1029–1033. DOI: 10.1109/23.682701.

[93] Ikuko Murayama and Shogo Nakamura. "Time profile of the scintillation from liquid and gaseous xenon". In: *Nuclear Instruments and Methods in Physics Research Section A: Accelerators, Spectrometers, Detectors and Associated Equipment* 763 (2014), pp. 533–537. ISSN: 0168-9002. DOI: https://doi.org/10.1016/j.nima.2014.07.003.

[94] *Noble Gas Detectors*. John Wiley & Sons, Ltd, 2006. ISBN: 9783527610020. DOI: https://doi.org/10.1002/9783527610020.ch9.

[95] C.D.R. Azevedo et al. "Microscopic simulation of xenon-based optical TPCs in the presence of molecular additives". In: *Nuclear Instruments and Methods in Physics Research Section A: Accelerators, Spectrometers, Detectors and Associated Equipment* 877 (2018), pp. 157–172. ISSN: 0168-9002. DOI: https://doi.org/10.1016/j.nima.2017.08.049.

USC UNIVERSIDADE DE SANTIAGO DE COMPOSTELA

[96] V Álvarez et al. "Ionization and scintillation response of high-pressure xenon gas to alpha particles". In: *Journal of Instrumentation* 8.05 (May 2013), P05025–P05025. ISSN: 1748-0221. DOI: 10.1088/1748-0221/8/05/p05025.

[97] A. Simón et al. "Boosting background suppression in the NEXT experiment through Richardson-Lucy deconvolution". In: *Journal of High Energy Physics* 2021.7 (July 2021), p. 146. ISSN: 1029-8479. DOI: 10.1007/JHEP07(2021)146.

[98] E.D.C. Freitas et al. "Secondary scintillation yield in high-pressure xenon gas for neutrinoless double beta decay ($0\nu\beta\beta$) search". In: *Physics Letters B* 684.4 (2010), pp. 205–210. ISSN: 0370-2693. DOI: https://doi.org/10.1016/j.physletb.2010.01.013.

[99] C A B Oliveira et al. "Energy resolution studies for NEXT". In: *Journal of Instrumentation* 6.05 (May 2011), P05007–P05007. ISSN: 1748-0221. DOI: 10.1088/1748-0221/6/05/p05007.

[100] Aleksey Bolotnikov and Brian Ramsey. "The spectroscopic properties of high-pressure xenon". In: *Nuclear Instruments and Methods in Physics Research Section A: Accelerators, Spectrometers, Detectors and Associated Equipment* 396.3 (1997), pp. 360–370. ISSN: 0168-9002. DOI: https://doi.org/10.1016/S0168-9002(97)00784-5.

[101] David Nygren. "High-pressure xenon gas electroluminescent TPC for 0-$\nu\beta\beta$-decay search". In: *Nuclear Instruments and Methods in Physics Research Section A: Accelerators, Spectrometers, Detectors and Associated Equipment* 603.3 (2009), pp. 337–348. ISSN: 0168-9002. DOI: https://doi.org/10.1016/j.nima.2009.01.222.

[102] L. Strüder et al. "X-Ray Detectors". In: *X-Ray Spectrometry: Recent Technological Advances*. John Wiley & Sons, Ltd, 2004. Chap. 4, pp. 133–275. ISBN: 9780470020432. DOI: https://doi.org/10.1002/0470020431.ch4.

[103] Joshua Edward Renner. "High Pressure Xenon Detectors for Rare Physics Searches". PhD thesis. UC Berkeley, 2014.

[104] J. Miyamoto and G.F. Knoll. "The statistics of avalanche electrons in micro-strip and micro-gap gas chambers". In: *Nuclear Instruments and Methods in Physics Research Section A: Accelerators, Spectrometers, Detectors and Associated Equipment* 399.1 (1997), pp. 85–93. ISSN: 0168-9002. DOI: https://doi.org/10.1016/S0168-9002(97)00919-4.

[105] J.N. Marx and D.R.Nygren. *The Time Projection Chamber*. URL: https://physicstoday.scitation.org/doi/10.1063/1.2994775.

[106] H J Hilke. "Time projection chambers". In: *Reports on Progress in Physics* 73.11 (Oct. 2010), p. 116201. DOI: 10.1088/0034-4885/73/11/116201.

[107] NEXT Collaboration et al. *The NEXT-100 experiment for neutrinoless double beta decay searches (Conceptual Design Report)*. 2011. arXiv: 1106.3630 [physics.ins-det].

[108] V Álvarez et al. "NEXT-100 Technical Design Report (TDR). Executive summary". In: *Journal of Instrumentation* 7.06 (June 2012), T06001–T06001. DOI: 10.1088/1748-0221/7/06/t06001.

[109] NEXT Collaboration et al. *Near-Intrinsic Energy Resolution for 30 to 662 keV Gamma Rays in a High Pressure Xenon Electroluminescent TPC*. 2012. arXiv: 1211.4474 [physics.ins-det].

USC UNIVERSIDADE DE SANTIAGO DE COMPOSTELA

[110] V Álvarez et al. “Initial results of NEXT-DEMO, a large-scale prototype of the NEXT-100 experiment”. In: *Journal of Instrumentation* 8.04 (Apr. 2013), P04002–P04002. DOI: 10.1088/1748-0221/8/04/p04002.

[111] V Álvarez et al. “Operation and first results of the NEXT-DEMO prototype using a silicon photomultiplier tracking array”. In: *Journal of Instrumentation* 8.09 (Sept. 2013), P09011–P09011. DOI: 10.1088/1748-0221/8/09/p09011.

[112] F. Monrabal et al. “The NEXT White (NEW) detector”. In: *Journal of Instrumentation* 13.12 (Dec. 2018), P12010–P12010. DOI: 10.1088/1748-0221/13/12/p12010.

[113] V. Álvarez et al. “The electronics of the energy plane of the NEXT-White detector”. In: *Nuclear Instruments and Methods in Physics Research Section A: Accelerators, Spectrometers, Detectors and Associated Equipment* 917 (Feb. 2019), pp. 68–76. ISSN: 0168-9002. DOI: 10.1016/j.nima.2018.11.126.

[114] J. Rodríguez et al. “The front-end electronics for the 1.8-kchannel SiPM tracking plane in the NEW detector”. In: *Journal of Instrumentation* 10.01 (Jan. 2015), pp. C01025–C01025. DOI: 10.1088/1748-0221/10/01/c01025.

[115] José María Benlloch Rodríguez. “The NEXT experiment: DAQ, backgrounds and medical applications”. PhD thesis. IFIC, 2020.

[116] J. Renner et al. “Energy calibration of the NEXT-White detector with 1% resolution near $Q_{\beta\beta}$ of 136Xe”. In: *Journal of High Energy Physics* 2019.10 (Oct. 2019), p. 230. ISSN: 1029-8479. DOI: 10.1007/JHEP10(2019)230.

[117] P. Ferrario et al. “Demonstration of the event identification capabilities of the NEXT-White detector”. In: *Journal of High Energy Physics* 2019.10 (Oct. 2019), p. 52. ISSN: 1029-8479. DOI: 10.1007/JHEP10(2019)052.

[118] NEXT Collaboration et al. “Radiogenic backgrounds in the NEXT double beta decay experiment”. In: *Journal of High Energy Physics* 2019.10, 51 (Oct. 2019), p. 51. DOI: 10.1007/JHEP10(2019)051. arXiv: 1905.13625 [physics.ins-det].

[119] P. Novella et al. “Measurement of the ^{136}Xe two-neutrino double-β-decay half-life via direct background subtraction in NEXT”. In: *Phys. Rev. C* 105 (5 May 2022), p. 055501. DOI: 10.1103/PhysRevC.105.055501. arXiv: 2111.11091 [nucl-ex].

[120] Iván Rivilla et al. “Fluorescent bicolour sensor for low-background neutrinoless double β decay experiments”. In: *Nature* 583.7814 (July 2020), pp. 48–54. ISSN: 1476-4687. DOI: 10.1038/s41586-020-2431-5.

[121] David R Nygren. “Detecting the barium daughter in ^{136}Xe 0-$\nu\beta\beta$ decay using single-molecule fluorescence imaging techniques”. In: *Journal of Physics: Conference Series* 650 (Nov. 2015), p. 012002. DOI: 10.1088/1742-6596/650/1/012002.

[122] Gonzalo Martínez Lema. “Low energy calibration, reconstruction software and light-collection efficiency parametrization of the NEXT-White detector”. PhD thesis. USC, 2018.

[123] S. Agostinelli et al. “Geant4—a simulation toolkit”. In: *Nuclear Instruments and Methods in Physics Research Section A: Accelerators, Spectrometers, Detectors and Associated Equipment* 506.3 (2003), pp. 250–303. ISSN: 0168-9002. DOI: https://doi.org/10.1016/S0168-9002(03)01368-8.

[124] *C-Extensions for Python*. May 2021. URL: https://cython.org/.

[125] *The HDF5 Library and File Format*. May 2021. URL: https://www.hdfgroup.org/solutions/hdf5.

[126] Wikipedia. *Invisible Cities — Wikipedia, The Free Encyclopedia*. 2021.
[127] NEXT Collaboration. *NEXT Software Documentation*. URL: https://next-exp-sw.readthedocs.io/en/latest/.
[128] Miquel Nebot Guinot. "Calibration and background model of the NEW detector at the LSC". PhD thesis. IFIC, 2017.
[129] S. Rosendahl et al. "A novel83mKr tracer method for characterizing xenon gas and cryogenic distillation systems". In: *Journal of Instrumentation* 9.10 (Oct. 2014), P10010–P10010. ISSN: 1748-0221. DOI: 10.1088/1748-0221/9/10/p10010.
[130] A. Simón et al. "Electron drift properties in high pressure gaseous xenon". In: *Journal of Instrumentation* 13.07 (July 2018), P07013–P07013. ISSN: 1748-0221. DOI: 10.1088/1748-0221/13/07/p07013.
[131] L. B. Lucy. "An iterative technique for the rectification of observed distributions". In: *Astronomical Journal* 79 (June 1974), p. 745. DOI: 10.1086/111605.
[132] William Hadley Richardson. "Bayesian-Based Iterative Method of Image Restoration". In: *J. Opt. Soc. Am.* 62.1 (Jan. 1972), pp. 55–59. DOI: 10.1364/JOSA.62.000055.
[133] E. W. Dijkstra. "A note on two problems in connexion with graphs". In: *Numerische Mathematik* 1.1 (Dec. 1959), pp. 269–271. ISSN: 0945-3245. DOI: 10.1007/BF01386390.
[134] NEXT Collaboration. *Invisible Cities*. URL: https://github.com/next-exp/IC.
[135] Charles R. Harris et al. "Array programming with NumPy". In: *Nature* 585.7825 (Sept. 2020), pp. 357–362. DOI: 10.1038/s41586-020-2649-2.
[136] Wes McKinney. "Data Structures for Statistical Computing in Python". In: *Proceedings of the 9th Python in Science Conference*. Ed. by Stéfan van der Walt and Jarrod Millman. 2010, pp. 56–61. DOI: 10.25080/Majora-92bf1922-00a.
[137] Pauli Virtanen et al. "SciPy 1.0: Fundamental Algorithms for Scientific Computing in Python". In: *Nature Methods* 17 (2020), pp. 261–272. DOI: 10.1038/s41592-019-0686-2.
[138] J. D. Hunter. "Matplotlib: A 2D graphics environment". In: *Computing in Science & Engineering* 9.3 (2007), pp. 90–95. DOI: 10.1109/MCSE.2007.55.
[139] Rene Brun and Fons Rademakers. "ROOT — An object oriented data analysis framework". In: *Nuclear Instruments and Methods in Physics Research Section A: Accelerators, Spectrometers, Detectors and Associated Equipment* 389.1 (1997), pp. 81–86. ISSN: 0168-9002. DOI: https://doi.org/10.1016/S0168-9002(97)00048-X.
[140] Javier Muñoz Vidal. "The NEXT path to neutrino inverse hierarchy". PhD thesis. IFIC, 2018.
[141] Matteo Agostini et al. *Toward the discovery of matter creation with neutrinoless double-beta decay*. 2022. DOI: 10.48550/arxiv.2202.01787.
[142] V. Álvarez et al. "Radiopurity control in the NEXT-100 double beta decay experiment: procedures and initial measurements". In: *Journal of Instrumentation* 8.01 (Jan. 2013), T01002–T01002. DOI: 10.1088/1748-0221/8/01/t01002.
[143] T. Dafni et al. *Results of the material screening program of the NEXT experiment*. 2014. DOI: 10.48550/arxiv.1411.1222.
[144] S. Cebrián et al. "Radiopurity assessment of the tracking readout for the NEXT double beta decay experiment". In: *Journal of Instrumentation* 10.05 (May 2015), P05006–P05006. DOI: 10.1088/1748-0221/10/05/p05006.

[145] S. Cebrián et al. “Radon and material radiopurity assessment for the NEXT double beta decay experiment”. In: *AIP Conference Proceedings*. AIP, 2015. DOI: 10.1063/1.4927990.

[146] J. Perez-Perez et al. *Radon Mitigation Applications at the Laboratorio Subterraneo de Canfranc (LSC)*. 2021. DOI: 10.48550/arxiv.2112.15371.

[147] A. Bettini. “The Canfranc Underground Laboratory (LSC)”. In: *The European Physical Journal Plus* 127.9 (Sept. 2012), p. 112. ISSN: 2190-5444. DOI: 10.1140/epjp/i2012-12112-1.

[148] H. Wulandari et al. “Neutron flux at the Gran Sasso underground laboratory revisited”. In: *Astroparticle Physics* 22.3-4 (Nov. 2004), pp. 313–322. DOI: 10.1016/j.astropartphys.2004.07.005.

[149] D. Jordan et al. “Measurement of the neutron background at the Canfranc Underground Laboratory LSC”. In: *Astroparticle Physics* 42 (2013), pp. 1–6. ISSN: 0927-6505. DOI: https://doi.org/10.1016/j.astropartphys.2012.11.007.

[150] Abdul J. Khan et al. “Investigation of neutron shielding materials for low-background gamma spectrometry”. In: *Journal of Radioanalytical and Nuclear Chemistry* 328.3 (June 2021), pp. 941–950. ISSN: 1588-2780. DOI: 10.1007/s10967-021-07715-x.

[151] Wladyslaw Henryk Trzaska et al. *Cosmic-ray muon flux at Canfranc Underground Laboratory*. 2019. DOI: 10.48550/arxiv.1902.00868.

[152] O. A. Ponkratenko, V. I. Tretyak, and Yu. G. Zdesenko. “Event generator DECAY4 for simulating double-beta processes and decays of radioactive nuclei”. In: *Physics of Atomic Nuclei* 63.7 (July 2000), pp. 1282–1287. DOI: 10.1134/1.855784.

[153] NEXT Collaboration et al. *Sensitivity of a tonne-scale NEXT detector for neutrinoless double beta decay searches*. 2020. DOI: 10.48550/arxiv.2005.06467.

[154] *Inicio - CESGA - Centro de Supercomputación de Galicia*. Sept. 2022. URL: https://www.cesga.es/.

[155] URL: https://garfieldpp.web.cern.ch/garfieldpp/.

[156] J. Terasaki. “Strength of the isoscalar pairing interaction determined by a relation between double-charge change and double-pair transfer for double-β decay”. In: *Phys. Rev. C* 102 (4 Oct. 2020), p. 044303. DOI: 10.1103/PhysRevC.102.044303.

[157] M. Mirea, T. Pahomi, and S. Stoica. *Phase Space Factors for Double Beta Decay: an up-date*. 2014. DOI: 10.48550/arxiv.1411.5506.

USC UNIVERSIDADE DE SANTIAGO DE COMPOSTELA

APPENDIX A
NEXUS configuration files

Listing A.1: NEXUS initialization macro file. Indented lines below comments (#) indicate which type of event must include them. Variables starting with $ denote paths to configuration or delayed macros.

```
/PhysicsList/RegisterPhysics G4EmStandardPhysics_option4
/PhysicsList/RegisterPhysics G4DecayPhysics
/PhysicsList/RegisterPhysics G4RadioactiveDecayPhysics
/PhysicsList/RegisterPhysics G4StepLimiterPhysics
# use for muon simulations
    /PhysicsList/RegisterPhysics G4EmExtraPhysics
    /PhysicsList/RegisterPhysics G4HadronElasticPhysicsHP
    /PhysicsList/RegisterPhysics G4HadronPhysicsQGSP_BERT_HP
    /PhysicsList/RegisterPhysics G4StoppingPhysics
    /PhysicsList/RegisterPhysics G4IonPhysics
    /PhysicsList/RegisterPhysics G4StepLimiterPhysics
    /physics_lists/em/MuonNuclear true

/nexus/RegisterGeometry  Next100

# use for signal events
    /nexus/RegisterGenerator Decay0Interface
# use for ion events (Tl-208, Bi-214, Xe-137)
    /nexus/RegisterGenerator IonGenerator
# use for Kr events
    /nexus/RegisterGenerator Kr83mGenerator
# use for muon events
    /nexus/RegisterGenerator MuonAngleGenerator

/nexus/RegisterRunAction      DefaultRunAction
/nexus/RegisterEventAction    DefaultEventAction
/nexus/RegisterTrackingAction DefaultTrackingAction

/nexus/RegisterPersistencyManager PersistencyManager
/nexus/RegisterMacro        $CFG_MACRO
```

Listing A.2: NEXUS configuration macro file. Indented lines below comments (#) indicate which type of event must include them. Variables starting with $ must be set before running the simulation.

```
/control/verbose  1
/run/verbose      1
/event/verbose    0
/tracking/verbose 0

/Geometry/Next100/max_step_size  1.  mm
/Geometry/Next100/pressure      13.5 bar
/Geometry/Next100/elfield       false

/nexus/random_seed            $RNDSEED
/nexus/persistency/start_id   $STARTID
/nexus/persistency/outputFile $OUTFILE
```

USC UNIVERSIDADE DE SANTIAGO DE COMPOSTELA

```
/Actions/DefaultEventAction/min_energy 2.4 MeV
/Actions/DefaultEventAction/max_energy 2.5 MeV

# use for signal events
    /Generator/Decay0Interface/inputFile       none
    /Generator/Decay0Interface/Xe136DecayMode  1
    /Generator/Decay0Interface/Ba136FinalState 0
    /Generator/Decay0Interface/region          ACTIVE
# use for Xe-137 events
    /Generator/IonGenerator/atomic_number 54
    /Generator/IonGenerator/mass_number   137
    /Generator/IonGenerator/region        ACTIVE
    /Generator/IonGenerator/decay_at_time_zero true
# use for Tl-208 events
    /Generator/IonGenerator/atomic_number  81
    /Generator/IonGenerator/mass_number   208
    /Generator/IonGenerator/region        $VOLUME
# use for Bi-214 events
    /Generator/IonGenerator/atomic_number  83
    /Generator/IonGenerator/mass_number   214
    /Generator/IonGenerator/region        $VOLUME
# use for Kr events
    /Generator/Kr83mGenerator/region ACTIVE
# use for muon events
    /Generator/MuonAngleGenerator/region     HALLA_INNER
    /Generator/MuonAngleGenerator/angles_on  true
    /Generator/MuonAngleGenerator/azimuth_rotation 150 deg
    /Generator/MuonAngleGenerator/angle_file MuonAnaAllRuns.csv
    /Generator/MuonAngleGenerator/angle_dist za
    /Generator/MuonAngleGenerator/max_energy 2000 GeV
```

USC UNIVERSIDADE DE SANTIAGO DE COMPOSTELA

APPENDIX B
IC configuration files

Listing B.1: Common parameters for all cities

```
files_in    = "{files_in}"
file_out    = "{file_out}"
compression = "ZLIB4"
run_number  = 0
detector_db = "next100"
print_mod   = 10000
event_range = all
```

Listing B.2: DETSIM configuration file

```
s1_lighttable = "$LT_PATH/NEXT100_S1_LT.h5"
s2_lighttable = "$LT_PATH/NEXT100_S2_LT.h5"
sipm_psf      = "$LT_PATH/NEXT100_PSF.h5"

physics_params = dict(ws = 39.2 * eV,
                      wi = 22.0 * eV,
                      fano_factor = 0.15,
                      conde_policarpo_factor = 0.4,
                      drift_velocity         = 0.84 * mm / mus,
                      el_drift_velocity      = 2.75 * mm / mus,
                      transverse_diffusion   = 1.10 * mm / cm**0.5,
                      longitudinal_diffusion = 0.38 * mm / cm**0.5,
                      el_gain                = 1000,
                      lifetime               =   10 * ms)

buffer_params = dict(pmt_width   =  25  * ns,
                     sipm_width  =   1  * mus,
                     max_time    = 3000 * mus,
                     length      = 1500 * mus,
                     pre_trigger =  10  * mus,
                     trigger_thr =   0)

rate = 0.5 * hertz
```

Listing B.3: HYPATHIA configuration file

```
pmt_wfs_rebin  = 1
pmt_pe_rms     = 0
sipm_noise_cut = 1.0 * pes
filter_padding = 50

thr_csum_s1 = 0.1 * pes
thr_csum_s2 = 0.1 * pes
thr_sipm      = 1.0 * pes
thr_sipm_type = "common"

s1_tmin       =   9 * mus
s1_tmax       =  12 * mus
s1_stride     =   4
s1_lmin       =   4
s1_lmax       =  40
```

USC UNIVERSIDADE DE SANTIAGO DE COMPOSTELA

```
s1_rebin_stride = 1

s2_tmin      =     12 * mus
s2_tmax      =   1500 * mus
s2_stride    =     40
s2_lmin      =     20
s2_lmax      = 100000
s2_rebin_stride = 40
thr_sipm_s2      = 5.0 * pes
```

Listing B.4: DOROTHEA configuration file

```
drift_v      = 0.84 * mm / mus

s1_nmin      =    1
s1_nmax      =    5
s1_emin      =    5 * pes
s1_emax      =  100 * pes
s1_wmin      =   75 * ns
s1_wmax      =  500 * ns
s1_hmin      =    2 * pes
s1_hmax      =  100 * pes
s1_ethr      =    0 * pes

s2_nmin      =    1
s2_nmax      =    5
s2_emin      =  100 * pes
s2_emax      =  1e9 * pes
s2_wmin      =  0.5 * mus
s2_wmax      = 1000 * mus
s2_hmin      =  100 * pes
s2_hmax      =  1e9 * pes
s2_ethr      =    0 * pes
s2_nsipmmin =    1
s2_nsipmmax = 3000

barycenter_params = dict(
  Qthr             = 15 * pes,
  lm_radius        = -1 * mm ,
)

global_reco_params = barycenter_params
del barycenter_params
```

Listing B.5: PENTHESILEA configuration file

```
drift_v      = 0.84 * mm / mus

s1_nmin      =    1
s1_nmax      =    1
s1_emin      =    5 * pes
s1_emax      =  1e4 * pes
s1_wmin      =   75 * ns
s1_wmax      =    2 * mus
s1_hmin      =    2 * pes
s1_hmax      =  1e4 * pes
s1_ethr      =    0 * pes

s2_nmin      =    1
s2_nmax      =    1
s2_emin      =  100 * pes
s2_emax      =  1e9 * pes
s2_wmin      =  0.5 * mus
s2_wmax      = 1000 * mus
s2_hmin      =  100 * pes
s2_hmax      =  1e9 * pes
s2_ethr      =    0 * pes
s2_nsipmmin =    1
s2_nsipmmax = 3000

rebin = 1
```

USC UNIVERSIDAD DE SANTIAGO DE COMPOSTELA

```
slice_reco_params = dict(Qthr            =  5    * pes,
                         Qlm             =  1    * pes,
                         lm_radius       =  0.01 * mm ,
                         new_lm_radius   =  0.01 * mm ,
                         msipm           =  1         )

global_reco_params = dict(Qthr             = 20 * pes,
                          lm_radius        = -1 * mm)
```

Listing B.6: ESMERALDA configuration file

```
cor_hits_params = dict(map_fname             = ↩
    ↪ '$LT_PATH/map_NEXT100_MC.h5',
                       threshold_charge_low  =  5 * pes,
                       threshold_charge_high = 30 * pes,
                       same_peak             = True,
                       norm_strat            = 'kr',
                       apply_temp            = False)


paolina_params  = dict(vox_size         = [15 * mm, 15 * mm, 15 ↩
    ↪ * mm],
                       strict_vox_size  = False,
                       energy_threshold = 20 * keV,
                       min_voxels       = 3,
                       blob_radius      = 21 * mm,
                       max_num_hits     = 30000)
```

Listing B.7: BEERSHEBA configuration file

```
deconv_params = dict(
                  drop_dist       = [16., 16.],
                  psf_fname       = ↩
                      ↪ "$LT_PATH/NEXT100_PSF_kr83m.h5",
                  q_cut           = 10,
                  e_cut           = 12e-3,
                  n_iterations    = 100,
                  iteration_tol   = 1e-10,
                  sample_width    = [15.55, 15.55],
                  bin_size        = [ 1.,  1.],
                  energy_type     = "Ec",
                  diffusion       = (1., 0.2),
                  deconv_mode     = "joint",
                  n_dim           = 2,
                  cut_type        = "abs",
                  inter_method    = "cubic")
```

Listing B.8: ISAURA configuration file

```
paolina_params      = dict(
   vox_size         = [10 * mm, 10 * mm, 5 * mm],
   strict_vox_size  = False,
   energy_threshold = 10 * keV,
   min_voxels       = 3,
   blob_radius      = 20 * mm,
   max_num_hits     = 100000)
```

USC UNIVERSIDADE DE SANTIAGO DE COMPOSTELA

USC
UNIVERSIDADE
DE SANTIAGO
DE COMPOSTELA

APPENDIX C

Permissions for the reproduction of figures

USC
UNIVERSIDADE
DE SANTIAGO
DE COMPOSTELA

Gmail **Gonzalo Díaz López <gonzalodiazlopez10@gmail.com>**

Permission for the reproduction of figures

2 mensajes

Gonzalo Díaz López <gonzalodiazlopez10@gmail.com> 5 de enero de 2023, 13:52
Para: Justo Martín-Albo <justo.martin-albo@ific.uv.es>

Dear J.Martín-Albo:
I am a PhD student at the University of Santiago de Compostela (Spain) working in the NEXT experiment. I request your permission to reproduce the following figure(s) from your work PhD thesis: The NEXT experiment for neutrinoless double beta decay searches in my PhD thesis with title *Sensitivity of NEXT-100 detector to neutrinoless double beta decay*.

1. Figure 2.7. (nuclear matrix elements)
2. Figure 3.3. (average upper limits)
3. Figure 6.1. (structure of NEXUS)

Sorry for the inconvenience, my institution is particularly sensitive about the reproduction of figures from other works in the PhD dissertations.
Kind regards,
Gonzalo Díaz López

Justo Martín-Albo <justo.martin-albo@ific.uv.es> 11 de enero de 2023, 18:04
Para: Gonzalo Díaz López <gonzalodiazlopez10@gmail.com>

Dear Gonzalo,
Thank you for your email. You have my permission to use the figures for your thesis, as long as they are properly attributed and there is no commercial purpose.

All the best finalising your thesis!

| **Justo Martín-Albo**
| *Ramón y Cajal Researcher*
| Instituto de Física Corpuscular (IFIC)
| CSIC & Universitat de València
[El texto citado está oculto]

USC UNIVERSIDADE DE SANTIAGO DE COMPOSTELA

SPRINGER NATURE LICENSE TERMS AND CONDITIONS

Jan 04, 2023

This Agreement between Gonzalo Diaz ("You") and Springer Nature ("Springer Nature") consists of your license details and the terms and conditions provided by Springer Nature and Copyright Clearance Center.

License Number	5461950267770
License date	Jan 04, 2023
Licensed Content Publisher	Springer Nature
Licensed Content Publication	Journal of High Energy Physics
Licensed Content Title	On the quantitative impact of the Schechter-Valle theorem
Licensed Content Author	Michael Duerr et al
Licensed Content Date	Jun 21, 2011
Type of Use	Thesis/Dissertation
Requestor type	non-commercial (non-profit)
Format	print and electronic
Portion	figures/tables/illustrations
Number of figures/tables /illustrations	1
Will you be translating?	no
Circulation/distribution	1 - 29
Author of this Springer Nature content	no
Title	Sensitivity of NEXT-100 detector to neutrinoless double beta decay
Institution name	Universidade de Santiago de Compostela
Expected presentation date	Jan 2023
Portions	Figure 1
Requestor Location	Gonzalo Diaz Rúa de Xoaquín Díaz de Rábago, s/n Santiago de Compostela, 15705 Spain Attn: Gonzalo Diaz
Total	**0.00 EUR**

Terms and Conditions

Springer Nature Customer Service Centre GmbH Terms and Conditions

The following terms and conditions ("Terms and Conditions") together with the terms specified in your [RightsLink] constitute the License ("License") between you as Licensee and Springer Nature Customer Service Centre GmbH as Licensor. By clicking 'accept' and completing the transaction for your use of the material ("Licensed Material"), you confirm your acceptance of and obligation to be bound by these Terms and Conditions.

USC UNIVERSIDADE DE SANTIAGO DE COMPOSTELA

1. Grant and Scope of License

1. 1. The Licensor grants you a personal, non-exclusive, non-transferable, non-sublicensable, revocable, world-wide License to reproduce, distribute, communicate to the public, make available, broadcast, electronically transmit or create derivative works using the Licensed Material for the purpose(s) specified in your RightsLink Licence Details only. Licenses are granted for the specific use requested in the order and for no other use, subject to these Terms and Conditions. You acknowledge and agree that the rights granted to you under this License do

not include the right to modify, edit, translate, include in collective works, or create derivative works of the Licensed Material in whole or in part unless expressly stated in your RightsLink Licence Details. You may use the Licensed Material only as permitted under this Agreement and will not reproduce, distribute, display, perform, or otherwise use or exploit any Licensed Material in any way, in whole or in part, except as expressly permitted by this License.

1. 2. You may only use the Licensed Content in the manner and to the extent permitted by these Terms and Conditions, by your RightsLink Licence Details and by any applicable laws.

1. 3. A separate license may be required for any additional use of the Licensed Material, e.g. where a license has been purchased for print use only, separate permission must be obtained for electronic re-use. Similarly, a License is only valid in the language selected and does not apply for editions in other languages unless additional translation rights have been granted separately in the License.

1. 4. Any content within the Licensed Material that is owned by third parties is expressly excluded from the License.

1. 5. Rights for additional reuses such as custom editions, computer/mobile applications, film or TV reuses and/or any other derivative rights requests require additional permission and may be subject to an additional fee. Please apply to journalpermissions@springernature.com or bookpermissions@springernature.com for these rights.

2. Reservation of Rights

Licensor reserves all rights not expressly granted to you under this License. You acknowledge and agree that nothing in this License limits or restricts Licensor's rights in or use of the Licensed Material in any way. Neither this License, nor any act, omission, or statement by Licensor or you, conveys any ownership right to you in any Licensed Material, or to any element or portion thereof. As between Licensor and you, Licensor owns and retains all right, title, and interest in and to the Licensed Material subject to the license granted in Section 1.1. Your permission to use the Licensed Material is expressly conditioned on you not impairing Licensor's or the applicable copyright owner's rights in the Licensed Material in any way.

3. Restrictions on use

3. 1. Minor editing privileges are allowed for adaptations for stylistic purposes or formatting purposes provided such alterations do not alter the original meaning or intention of the Licensed Material and the new figure(s) are still accurate and representative of the Licensed Material. Any other changes including but not limited to, cropping, adapting, and/or omitting material that affect the meaning, intention or moral rights of the author(s) are strictly prohibited.

3. 2. You must not use any Licensed Material as part of any design or trademark.

3. 3. Licensed Material may be used in Open Access Publications (OAP), but any such reuse must include a clear acknowledgment of this permission visible at the same time as the figures/tables/illustration or abstract and which must indicate that the Licensed Material is not part of the governing OA license but has been reproduced with permission. This may be indicated according to any standard referencing system but must include at a minimum 'Book/Journal title, Author, Journal Name (if applicable), Volume (if applicable), Publisher, Year, reproduced with permission from SNCSC'.

4. STM Permission Guidelines

4. 1. An alternative scope of license may apply to signatories of the STM Permissions Guidelines ("STM PG") as amended from time to time and made available at https://www.stm-assoc.org/intellectual-property/permissions/permissions-guidelines/.

4. 2. For content reuse requests that qualify for permission under the STM PG, and which may be updated from time to time, the STM PG supersede the terms and conditions contained in this License.

4. 3. If a License has been granted under the STM PG, but the STM PG no longer apply at the time of publication, further permission must be sought from the Rightsholder. Contact journalpermissions@springernature.com or bookpermissions@springernature.com for these rights.

5. Duration of License

5. 1. Unless otherwise indicated on your License, a License is valid from the date of purchase ("License Date")

until the end of the relevant period in the below table:

Reuse in a medical communications project	Reuse up to distribution or time period indicated in License
Reuse in a dissertation/thesis	Lifetime of thesis
Reuse in a journal/magazine	Lifetime of journal/magazine
Reuse in a book/textbook	Lifetime of edition
Reuse on a website	1 year unless otherwise specified in the License
Reuse in a presentation/slide kit/poster	Lifetime of presentation/slide kit/poster. Note: publication whether electronic or in print of presentation/slide kit/poster may require further permission.
Reuse in conference proceedings	Lifetime of conference proceedings
Reuse in an annual report	Lifetime of annual report
Reuse in training/CME materials	Reuse up to distribution or time period indicated in License
Reuse in newsmedia	Lifetime of newsmedia
Reuse in coursepack/classroom materials	Reuse up to distribution and/or time period indicated in license

6. Acknowledgement

6. 1. The Licensor's permission must be acknowledged next to the Licensed Material in print. In electronic form, this acknowledgement must be visible at the same time as the figures/tables/illustrations or abstract and must be hyperlinked to the journal/book's homepage.

6. 2. Acknowledgement may be provided according to any standard referencing system and at a minimum should include "Author, Article/Book Title, Journal name/Book imprint, volume, page number, year, Springer Nature".

7. Reuse in a dissertation or thesis

7. 1. Where 'reuse in a dissertation/thesis' has been selected, the following terms apply: Print rights of the Version of Record are provided for; electronic rights for use only on institutional repository as defined by the Sherpa guideline (www.sherpa.ac.uk/romeo/) and only up to what is required by the awarding institution.

7. 2. For theses published under an ISBN or ISSN, separate permission is required. Please contact journalpermissions@springernature.com or bookpermissions@springernature.com for these rights.

7. 3. Authors must properly cite the published manuscript in their thesis according to current citation standards and include the following acknowledgement: '*Reproduced with permission from Springer Nature*'.

8. License Fee

You must pay the fee set forth in the License Agreement (the "License Fees"). All amounts payable by you under this License are exclusive of any sales, use, withholding, value added or similar taxes, government fees or levies or other assessments. Collection and/or remittance of such taxes to the relevant tax authority shall be the responsibility of the party who has the legal obligation to do so.

9. Warranty

9. 1. The Licensor warrants that it has, to the best of its knowledge, the rights to license reuse of the Licensed Material. **You are solely responsible for ensuring that the material you wish to license is original to the Licensor and does not carry the copyright of another entity or third party (as credited in the published version).** If the credit line on any part of the Licensed Material indicates that it was reprinted or adapted with permission from another source, then you should seek additional permission from that source to reuse the material.

9. 2. EXCEPT FOR THE EXPRESS WARRANTY STATED HEREIN AND TO THE EXTENT PERMITTED BY APPLICABLE LAW, LICENSOR PROVIDES THE LICENSED MATERIAL "AS IS" AND MAKES NO OTHER REPRESENTATION OR WARRANTY. LICENSOR EXPRESSLY DISCLAIMS ANY LIABILITY FOR ANY CLAIM

ARISING FROM OR OUT OF THE CONTENT, INCLUDING BUT NOT LIMITED TO ANY ERRORS, INACCURACIES, OMISSIONS, OR DEFECTS CONTAINED THEREIN, AND ANY IMPLIED OR EXPRESS WARRANTY AS TO MERCHANTABILITY OR FITNESS FOR A PARTICULAR PURPOSE. IN NO EVENT SHALL LICENSOR BE LIABLE TO YOU OR ANY OTHER PARTY OR ANY OTHER PERSON OR FOR ANY SPECIAL, CONSEQUENTIAL, INCIDENTAL, INDIRECT, PUNITIVE, OR EXEMPLARY DAMAGES, HOWEVER CAUSED, ARISING OUT OF OR IN CONNECTION WITH THE DOWNLOADING, VIEWING OR USE OF THE LICENSED MATERIAL REGARDLESS OF THE FORM OF ACTION, WHETHER FOR BREACH OF CONTRACT, BREACH OF WARRANTY, TORT, NEGLIGENCE, INFRINGEMENT OR OTHERWISE (INCLUDING, WITHOUT LIMITATION, DAMAGES BASED ON LOSS OF PROFITS, DATA, FILES, USE, BUSINESS OPPORTUNITY OR CLAIMS OF THIRD PARTIES), AND WHETHER OR NOT THE PARTY HAS BEEN ADVISED OF THE POSSIBILITY OF SUCH DAMAGES. THIS LIMITATION APPLIES NOTWITHSTANDING ANY FAILURE OF ESSENTIAL PURPOSE OF ANY LIMITED REMEDY PROVIDED HEREIN.

10. Termination and Cancellation

10. 1. The License and all rights granted hereunder will continue until the end of the applicable period shown in Clause 5.1 above. Thereafter, this license will be terminated and all rights granted hereunder will cease.

10. 2. Licensor reserves the right to terminate the License in the event that payment is not received in full or if you breach the terms of this License.

11. General

11. 1. The License and the rights and obligations of the parties hereto shall be construed, interpreted and determined in accordance with the laws of the Federal Republic of Germany without reference to the stipulations of the CISG (United Nations Convention on Contracts for the International Sale of Goods) or to Germany´s choice-of-law principle.

11. 2. The parties acknowledge and agree that any controversies and disputes arising out of this License shall be decided exclusively by the courts of or having jurisdiction for Heidelberg, Germany, as far as legally permissible.

11. 3. This License is solely for Licensor's and Licensee's benefit. It is not for the benefit of any other person or entity.

Questions? For questions on Copyright Clearance Center accounts or website issues please contact springernaturesupport@copyright.com or +1-855-239-3415 (toll free in the US) or +1-978-646-2777. For questions on Springer Nature licensing please visit https://www.springernature.com/gp/partners/rights-permissions-third-party-distribution

Other Conditions:

Version 1.4 - Dec 2022

Questions? customercare@copyright.com or +1-855-239-3415 (toll free in the US) or +1-978-646-2777.

USC UNIVERSIDADE DE SANTIAGO DE COMPOSTELA

American Physical Society
Reuse and Permissions License

04-Jan-2023

This license agreement between the American Physical Society ("APS") and Gonzalo Diaz ("You") consists of your license details and the terms and conditions provided by the American Physical Society and SciPris.

Licensed Content Information

License Number:	**RNP/23/JAN/061679**
License date:	04-Jan-2023
DOI:	10.1103/PhysRevC.72.055502
Title:	Electron energy spectra, fluxes, and day-night asymmetries of $\{\}^{8}$B solar neutrinos from measurements with NaCl dissolved in the heavy-water detector at the Sudbury Neutrino Observatory
Author:	B. Aharmim et al. (SNO Collaboration)
Publication:	Physical Review C
Publisher:	American Physical Society
Cost:	USD $ 0.00

Request Details

Does your reuse require significant modifications: No

Specify intended distribution locations:	Spain
Reuse Category:	Reuse in a thesis/dissertation
Requestor Type:	Student
Items for Reuse:	Figures/Tables
Number of Figure/Tables:	1
Figure/Tables Details:	Figure 29
Format for Reuse:	Print and Electronic
Total number of print copies:	Up to 1000

Information about New Publication:

University/Publisher:	Universidade of Santiago de Compostela
Title of dissertation/thesis:	Sensitivity of NEXT-100 detector to neutrinoless double beta decay
Author(s):	Gonzalo Díaz López
Expected completion date:	Jan. 2023

License Requestor Information

Name:	Gonzalo Diaz
Affiliation:	Individual
Email Id:	gonzalodiazlopez10@gmail.com
Country:	Spain

USC UNIVERSIDADE DE SANTIAGO DE COMPOSTELA

American Physical Society
Reuse and Permissions License

TERMS AND CONDITIONS

The American Physical Society (APS) is pleased to grant the Requestor of this license a non-exclusive, non-transferable permission, limited to Print and Electronic format, provided all criteria outlined below are followed.

1. You must also obtain permission from at least one of the lead authors for each separate work, if you haven't done so already. The author's name and affiliation can be found on the first page of the published Article.
2. For electronic format permissions, Requestor agrees to provide a hyperlink from the reprinted APS material using the source material's DOI on the web page where the work appears. The hyperlink should use the standard DOI resolution URL, http://dx.doi.org/{DOI}. The hyperlink may be embedded in the copyright credit line.
3. For print format permissions, Requestor agrees to print the required copyright credit line on the first page where the material appears: "Reprinted (abstract/excerpt/figure) with permission from [(FULL REFERENCE CITATION) as follows: Author's Names, APS Journal Title, Volume Number, Page Number and Year of Publication.] Copyright (YEAR) by the American Physical Society."
4. Permission granted in this license is for a one-time use and does not include permission for any future editions, updates, databases, formats or other matters. Permission must be sought for any additional use.
5. Use of the material does not and must not imply any endorsement by APS.
6. APS does not imply, purport or intend to grant permission to reuse materials to which it does not hold copyright. It is the requestor's sole responsibility to ensure the licensed material is original to APS and does not contain the copyright of another entity, and that the copyright notice of the figure, photograph, cover or table does not indicate it was reprinted by APS with permission from another source.
7. The permission granted herein is personal to the Requestor for the use specified and is not transferable or assignable without express written permission of APS. This license may not be amended except in writing by APS.
8. You may not alter, edit or modify the material in any manner.
9. You may translate the materials only when translation rights have been granted.
10. APS is not responsible for any errors or omissions due to translation.
11. You may not use the material for promotional, sales, advertising or marketing purposes.
12. The foregoing license shall not take effect unless and until APS or its agent, Aptara, receives payment in full in accordance with Aptara Billing and Payment Terms and Conditions, which are incorporated herein by reference.
13. Should the terms of this license be violated at any time, APS or Aptara may revoke the license with no refund to you and seek relief to the fullest extent of the laws of the USA. Official written notice will be made using the contact information provided with the permission request. Failure to receive such notice will not nullify revocation of the permission.
14. APS reserves all rights not specifically granted herein.
15. This document, including the Aptara Billing and Payment Terms and Conditions, shall be the entire agreement between the parties relating to the subject matter hereof.

USC
UNIVERSIDADE DE SANTIAGO DE COMPOSTELA

Gmail **Gonzalo Díaz López <gonzalodiazlopez10@gmail.com>**

Permission for reproduction of figures

3 mensajes

Gonzalo Díaz López <gonzalodiazlopez10@gmail.com> 5 de enero de 2023, 13:35
Para: stefano.pirro@lngs.infn.it

Dear S.Pirro:
I am a PhD student at the University of Santiago de Compostela (Spain) working in the NEXT experiment. I request your permission to reproduce the following figure(s) from your work CUPID pre-CDR (https://arxiv.org/abs/1907.09376) in my PhD thesis with title *Sensitivity of NEXT-100 detector to neutrinoless double beta decay*.

1. Figure 3. (position of signals and background end-points)
2. Figure 6 (left). (CUORE cryostat)

Sorry for the inconvenience, my institution is particularly sensitive about the reproduction of figures from other works in the PhD dissertations.
Kind regards,
Gonzalo Díaz López

Stefano Pirro <stefano.pirro@lngs.infn.it> 7 de enero de 2023, 18:21
Para: Gonzalo Díaz López <gonzalodiazlopez10@gmail.com>
Cc: Fabio Bellini <fabio.bellini@roma1.infn.it>

Dear Gonzalo,

I do not think there will be any kind of problem once you refer the figures to the original paper. In any case I put Fabio in CC that is more (than me) in charge for these issues.

Good luck for you PhD work !

Best,

SP

[El texto citado está oculto]

Fabio Bellini <Fabio.Bellini@roma1.infn.it> 9 de enero de 2023, 9:44
Para: gonzalodiazlopez10@gmail.com
Cc: Stefano Pirro <stefano.pirro@lngs.infn.it>

Dear Gonzalo

It's fine for us if figures are properly credited (something like "plot/picture courtesy of CUPID Collaboration [citation]")

Best

Fabio (on behalf of the EB)
[El texto citado está oculto]

USC UNIVERSIDADE DE SANTIAGO DE COMPOSTELA

CCC Marketplace

Order Number: 1307275
Order Date: 04 Jan 2023

Payment Information

Gonzalo Diaz
gonzalodiazlopez10@gmail.com
Payment method: Invoice

Billing Address:
Gonzalo Diaz
Rúa de Xoaquín Díaz de Rábago, s/n
Santiago De Compostela, 15705
Spain

+34 608228522
gonzalodiazlopez10@gmail.com

Customer Location:
Gonzalo Diaz
Rúa de Xoaquín Díaz de Rábago, s/n
Santiago De Compostela, 15705
Spain

Order Details

1. Journal of Instrumentation

Billing Status: Open

Article: The EXO-200 detector, part I: detector design and construction

Order License ID	1307275-1	**Type of use**	Republish in a thesis/dissertation
Order detail status	Completed		
ISSN	1748-0221	**Publisher**	IOP Publishing
		Portion	Chart/graph/table/figure

0,00 EUR
Republication Permission

LICENSED CONTENT

Publication Title	Journal of Instrumentation	**Publication Type**	e-Journal
Article Title	The EXO-200 detector, part I: detector design and construction	**Start Page**	P05010
		End Page	P05010
		Issue	05
Author/Editor	Institute of Physics (Great Britain), Institute of Physics Publishing., International School for Advanced Studies (Trieste, Italy)	**Volume**	7
		URL	http://www.iop.org/EJ/jinst/
Date	01/01/2006		
Language	English		
Country	United Kingdom of Great Britain and Northern Ireland		
Rightsholder	IOP Publishing, Ltd		

REQUEST DETAILS

Portion Type	Chart/graph/table /figure	**Distribution**	Other territories and/or countries
Number of Charts / Graphs / Tables / Figures Requested	1	**Enter Territories/Countries**	Spain
Format (select all that apply)	Print, Electronic	**Translation**	Original language of publication
Who Will Republish the Content?	Academic institution	**Copies for the Disabled?**	No
Duration of Use	Life of current and all future editions	**Minor Editing Privileges?**	No
Lifetime Unit Quantity	Up to 499	**Incidental Promotional Use?**	No
Rights Requested	Main product	**Currency**	EUR

NEW WORK DETAILS

Title	Sensitivity of NEXT-100 detector to neutrinoless double beta decay	**Institution Name**	Universidade de Santiago de Compostela
Instructor Name	José Ángel Hernando Morata	**Expected Presentation Date**	2023-01-31

ADDITIONAL DETAILS

The Requesting Person/Organization to Appear on the License	Gonzalo Díaz López

REUSE CONTENT DETAILS

Title, Description or Numeric Reference of the Portion(s)	Figure 2	**Title of the Article/Chapter the Portion Is From**	The EXO-200 detector, part I: detector design and construction
Editor of Portion(s)	N/A	**Author of Portion(s)**	N/A
Volume of Serial or Monograph	7	**Issue, if Republishing an Article From a Serial**	05
Page or Page Range of Portion	P05010-P05010	**Publication Date of Portion**	2012-05-23

IOP Publishing, Ltd Terms and Conditions

These special terms and conditions are in addition to the standard terms and conditions for CCC's Republication Service and, together with those standard terms and conditions, govern the use of the Works. As the User you will make all reasonable efforts to contact the author(s) of the article which the Work is to be reused from, to seek consent for your intended use. Contacting one author who is acting expressly as authorised agent for their co-author(s) is acceptable. User will reproduce the following wording prominently alongside the Work: the source of the Work, including author, article title, title of journal, volume number, issue number (if relevant), page range (or first page if this is the only information available) and date of first publication; and a link back to the article (via DOI); and if practicable, and IN ALL CASES for new works published under any of the Creative Commons licences, the words "© IOP Publishing. Reproduced with permission. All rights reserved" Without the express permission of the author(s) and the Rightsholder of the article from which the Work is to be reused, User shall not use it in any way which, in the opinion of the Rightsholder, could: (i) distort or alter the author(s)' original intention(s) and meaning; (ii) be prejudicial to the honour or reputation of the author(s); and/or (iii) imply endorsement by the author(s) and/or the Rightsholder. This licence does not apply to any article which is credited to another source and which does not have the copyright line '© IOP Publishing Ltd'. User must check the copyright line of the article from which the Work is to be reused to check that IOP Publishing Ltd has all the necessary rights to be able to grant permission. User is solely responsible for identifying and obtaining separate licences and permissions from the copyright owner for reuse of any such third party material/figures which the Rightsholder is not the copyright owner of. The Rightsholder shall not reimburse any fees which User pays for a republication license for such third party content. This licence does not apply to any material/figure which is credited to another source in the Rightsholder's publication or has been obtained from a third party. User must check the Version of Record of the article from which the Work is to be reused, to check whether any of the material in the Work is third party material. Third party citations and/or copyright notices and/or permissions statements may not be included in any other version of the article from which the Work is to be reused and so cannot be relied upon by the User. User is solely responsible for identifying and obtaining separate licences and permissions from the copyright owner for reuse of any such third party material/figures where the Rightsholder is not the copyright owner. The Rightsholder shall not reimburse any fees which User pays for a republication license for such third party content. User and CCC acknowledge that the Rightsholder may, from time to time, make changes or additions to these special terms and conditions without express notification, provided that these shall not apply to permissions already secured and paid for by User prior to such change or addition. User acknowledges that the Rightsholder (which includes companies within its group and third parties for whom it publishes its titles) may make use of personal data collected through the service in the course of their business. If User is the author of the Work, User may automatically have the right to reuse it under the rights granted back when User transferred the copyright in the article to the Rightsholder. User should check the copyright form and the relevant author rights policy to check whether permission is required. If User is the author of the Work and does require permission for proposed reuse of the Work, User should select 'Author of requested content' as the Requestor Type. The Rightsholder shall not reimburse any fees which User pays for a republication license. If User is the author of the article which User wishes to reuse in User's thesis or dissertation, the republication licence covers the right to include the Version of Record of the article, provided it is not then shared or deposited online. User must include citation details. Where User wishes to share their thesis or dissertation online, they should remove the Version of Record before uploading it. User may include a Preprint or the Accepted Manuscript (after the embargo period) in the online version of the thesis or dissertation, provided they do so in accordance with the Rightsholder's policies on sharing Preprints or Accepted Manuscripts. User may need to obtain separate permission for any third party content included within the article. User must check this with the copyright owner of such third party content. Any online or commercial use of User's thesis or dissertation containing the article, including publication via ProQuest, would need to be expressly notified in writing to the Rightsholder at the time of request and would require separate written permission from the Rightsholder. As well as CCC, the Rightsholder shall have the right to bring any legal action that it deems necessary to enforce its rights should it consider that the Work infringes those rights in any way. For content reuse requests that qualify for permission under the STM Permissions Guidelines, which may be updated from time to time, the STM Permissions Guidelines supplement the terms and conditions contained in this license.

USC UNIVERSIDADE DE SANTIAGO DE COMPOSTELA

Total Items: 1

Subtotal: 0,00 EUR

Order Total: 0,00 EUR

Marketplace Order General Terms and Conditions

The following terms and conditions ("General Terms"), together with any applicable Publisher Terms and Conditions, govern User's use of Works pursuant to the Licenses granted by Copyright Clearance Center, Inc. ("CCC") on behalf of the applicable Rightsholders of such Works through CCC's applicable Marketplace transactional licensing services (each, a "Service").

1) **Definitions.** For purposes of these General Terms, the following definitions apply:

"License" is the licensed use the User obtains via the Marketplace platform in a particular licensing transaction, as set forth in the Order Confirmation.

"Order Confirmation" is the confirmation CCC provides to the User at the conclusion of each Marketplace transaction. "Order Confirmation Terms" are additional terms set forth on specific Order Confirmations not set forth in the General Terms that can include terms applicable to a particular CCC transactional licensing service and/or any Rightsholder-specific terms.

"Rightsholder(s)" are the holders of copyright rights in the Works for which a User obtains licenses via the Marketplace platform, which are displayed on specific Order Confirmations.

"Terms" means the terms and conditions set forth in these General Terms and any additional Order Confirmation Terms collectively.

"User" or "you" is the person or entity making the use granted under the relevant License. Where the person accepting the Terms on behalf of a User is a freelancer or other third party who the User authorized to accept the General Terms on the User's behalf, such person shall be deemed jointly a User for purposes of such Terms.

"Work(s)" are the copyright protected works described in relevant Order Confirmations.

2) **Description of Service.** CCC's Marketplace enables Users to obtain Licenses to use one or more Works in accordance with all relevant Terms. CCC grants Licenses as an agent on behalf of the copyright rightsholder identified in the relevant Order Confirmation.

3) **Applicability of Terms.** The Terms govern User's use of Works in connection with the relevant License. In the event of any conflict between General Terms and Order Confirmation Terms, the latter shall govern. User acknowledges that Rightsholders have complete discretion whether to grant any permission, and whether to place any limitations on any grant, and that CCC has no right to supersede or to modify any such discretionary act by a Rightsholder.

4) **Representations; Acceptance.** By using the Service, User represents and warrants that User has been duly authorized by the User to accept, and hereby does accept, all Terms.

5) **Scope of License; Limitations and Obligations.** All Works and all rights therein, including copyright rights, remain the sole and exclusive property of the Rightsholder. The License provides only those rights expressly set forth in the terms and conveys no other rights in any Works

6) **General Payment Terms.** User may pay at time of checkout by credit card or choose to be invoiced. If the User chooses to be invoiced, the User shall: (i) remit payments in the manner identified on specific invoices, (ii) unless otherwise specifically stated in an Order Confirmation or separate written agreement, Users shall remit payments upon receipt of the relevant invoice from CCC, either by delivery or notification of availability of the invoice via the Marketplace platform, and (iii) if the User does not pay the invoice within 30 days of receipt, the User may incur a service charge of 1.5% per month or the maximum rate allowed by applicable law, whichever is less. While User may exercise the rights in the License immediately upon receiving the Order Confirmation, the License is automatically revoked and is null and void, as if it had never been issued, if CCC does not receive complete payment on a timely basis.

7) **General Limits on Use.** Unless otherwise provided in the Order Confirmation, any grant of rights to User (i) involves only the rights set forth in the Terms and does not include subsequent or additional uses, (ii) is non-exclusive and non-transferable, and (iii) is subject to any and all limitations and restrictions (such as, but not limited to, limitations on duration of use or circulation) included in the Terms. Upon completion of the licensed use as set forth in the Order Confirmation, User shall either secure a new permission for further use of the Work(s) or immediately cease any new use of the Work(s) and shall render inaccessible (such as by deleting or by removing or severing links or other locators) any further copies of the Work. User may only make alterations to the Work if and as expressly set forth in the Order Confirmation. No Work may be used in any way that is defamatory, violates the rights of third parties (including such third parties' rights of copyright, privacy, publicity,

or other tangible or intangible property), or is otherwise illegal, sexually explicit, or obscene. In addition, User may not conjoin a Work with any other material that may result in damage to the reputation of the Rightsholder. User agrees to inform CCC if it becomes aware of any infringement of any rights in a Work and to cooperate with any reasonable request of CCC or the Rightsholder in connection therewith.

8) **Third Party Materials.** In the event that the material for which a License is sought includes third party materials (such as photographs, illustrations, graphs, inserts and similar materials) that are identified in such material as having been used by permission (or a similar indicator), User is responsible for identifying, and seeking separate licenses (under this Service, if available, or otherwise) for any of such third party materials; without a separate license, User may not use such third party materials via the License.

9) **Copyright Notice.** Use of proper copyright notice for a Work is required as a condition of any License granted under the Service. Unless otherwise provided in the Order Confirmation, a proper copyright notice will read substantially as follows: "Used with permission of [Rightsholder's name], from [Work's title, author, volume, edition number and year of copyright]; permission conveyed through Copyright Clearance Center, Inc." Such notice must be provided in a reasonably legible font size and must be placed either on a cover page or in another location that any person, upon gaining access to the material which is the subject of a permission, shall see, or in the case of republication Licenses, immediately adjacent to the Work as used (for example, as part of a by-line or footnote) or in the place where substantially all other credits or notices for the new work containing the republished Work are located. Failure to include the required notice results in loss to the Rightsholder and CCC, and the User shall be liable to pay liquidated damages for each such failure equal to twice the use fee specified in the Order Confirmation, in addition to the use fee itself and any other fees and charges specified.

10) **Indemnity.** User hereby indemnifies and agrees to defend the Rightsholder and CCC, and their respective employees and directors, against all claims, liability, damages, costs, and expenses, including legal fees and expenses, arising out of any use of a Work beyond the scope of the rights granted herein and in the Order Confirmation, or any use of a Work which has been altered in any unauthorized way by User, including claims of defamation or infringement of rights of copyright, publicity, privacy, or other tangible or intangible property.

11) **Limitation of Liability.** UNDER NO CIRCUMSTANCES WILL CCC OR THE RIGHTSHOLDER BE LIABLE FOR ANY DIRECT, INDIRECT, CONSEQUENTIAL, OR INCIDENTAL DAMAGES (INCLUDING WITHOUT LIMITATION DAMAGES FOR LOSS OF BUSINESS PROFITS OR INFORMATION, OR FOR BUSINESS INTERRUPTION) ARISING OUT OF THE USE OR INABILITY TO USE A WORK, EVEN IF ONE OR BOTH OF THEM HAS BEEN ADVISED OF THE POSSIBILITY OF SUCH DAMAGES. In any event, the total liability of the Rightsholder and CCC (including their respective employees and directors) shall not exceed the total amount actually paid by User for the relevant License. User assumes full liability for the actions and omissions of its principals, employees, agents, affiliates, successors, and assigns.

12) **Limited Warranties.** THE WORK(S) AND RIGHT(S) ARE PROVIDED "AS IS." CCC HAS THE RIGHT TO GRANT TO USER THE RIGHTS GRANTED IN THE ORDER CONFIRMATION DOCUMENT. CCC AND THE RIGHTSHOLDER DISCLAIM ALL OTHER WARRANTIES RELATING TO THE WORK(S) AND RIGHT(S), EITHER EXPRESS OR IMPLIED, INCLUDING WITHOUT LIMITATION IMPLIED WARRANTIES OF MERCHANTABILITY OR FITNESS FOR A PARTICULAR PURPOSE. ADDITIONAL RIGHTS MAY BE REQUIRED TO USE ILLUSTRATIONS, GRAPHS, PHOTOGRAPHS, ABSTRACTS, INSERTS, OR OTHER PORTIONS OF THE WORK (AS OPPOSED TO THE ENTIRE WORK) IN A MANNER CONTEMPLATED BY USER; USER UNDERSTANDS AND AGREES THAT NEITHER CCC NOR THE RIGHTSHOLDER MAY HAVE SUCH ADDITIONAL RIGHTS TO GRANT.

13) **Effect of Breach.** Any failure by User to pay any amount when due, or any use by User of a Work beyond the scope of the License set forth in the Order Confirmation and/or the Terms, shall be a material breach of such License. Any breach not cured within 10 days of written notice thereof shall result in immediate termination of such License without further notice. Any unauthorized (but licensable) use of a Work that is terminated immediately upon notice thereof may be liquidated by payment of the Rightsholder's ordinary license price therefor; any unauthorized (and unlicensable) use that is not terminated immediately for any reason (including, for example, because materials containing the Work cannot reasonably be recalled) will be subject to all remedies available at law or in equity, but in no event to a payment of less than three times the Rightsholder's ordinary license price for the most closely analogous licensable use plus Rightsholder's and/or CCC's costs and expenses incurred in collecting such payment.

14) **Additional Terms for Specific Products and Services.** If a User is making one of the uses described in this Section 14, the additional terms and conditions apply:

a) ***Print Uses of Academic Course Content and Materials (photocopies for academic coursepacks or classroom handouts).*** For photocopies for academic coursepacks or classroom handouts the following

additional terms apply:

i) The copies and anthologies created under this License may be made and assembled by faculty members individually or at their request by on-campus bookstores or copy centers, or by off-campus copy shops and other similar entities.

ii) No License granted shall in any way: (i) include any right by User to create a substantively non-identical copy of the Work or to edit or in any other way modify the Work (except by means of deleting material immediately preceding or following the entire portion of the Work copied) (ii) permit "publishing ventures" where any particular anthology would be systematically marketed at multiple institutions.

iii) Subject to any Publisher Terms (and notwithstanding any apparent contradiction in the Order Confirmation arising from data provided by User), any use authorized under the academic pay-per-use service is limited as follows:

A) any License granted shall apply to only one class (bearing a unique identifier as assigned by the institution, and thereby including all sections or other subparts of the class) at one institution;

B) use is limited to not more than 25% of the text of a book or of the items in a published collection of essays, poems or articles;

C) use is limited to no more than the greater of (a) 25% of the text of an issue of a journal or other periodical or (b) two articles from such an issue;

D) no User may sell or distribute any particular anthology, whether photocopied or electronic, at more than one institution of learning;

E) in the case of a photocopy permission, no materials may be entered into electronic memory by User except in order to produce an identical copy of a Work before or during the academic term (or analogous period) as to which any particular permission is granted. In the event that User shall choose to retain materials that are the subject of a photocopy permission in electronic memory for purposes of producing identical copies more than one day after such retention (but still within the scope of any permission granted), User must notify CCC of such fact in the applicable permission request and such retention shall constitute one copy actually sold for purposes of calculating permission fees due; and

F) any permission granted shall expire at the end of the class. No permission granted shall in any way include any right by User to create a substantively non-identical copy of the Work or to edit or in any other way modify the Work (except by means of deleting material immediately preceding or following the entire portion of the Work copied).

iv) Books and Records; Right to Audit. As to each permission granted under the academic pay-per-use Service, User shall maintain for at least four full calendar years books and records sufficient for CCC to determine the numbers of copies made by User under such permission. CCC and any representatives it may designate shall have the right to audit such books and records at any time during User's ordinary business hours, upon two days' prior notice. If any such audit shall determine that User shall have underpaid for, or underreported, any photocopies sold or by three percent (3%) or more, then User shall bear all the costs of any such audit; otherwise, CCC shall bear the costs of any such audit. Any amount determined by such audit to have been underpaid by User shall immediately be paid to CCC by User, together with interest thereon at the rate of 10% per annum from the date such amount was originally due. The provisions of this paragraph shall survive the termination of this License for any reason.

b) ***Digital Pay-Per-Uses of Academic Course Content and Materials (e-coursepacks, electronic reserves, learning management systems, academic institution intranets).*** For uses in e-coursepacks, posts in electronic reserves, posts in learning management systems, or posts on academic institution intranets, the following additional terms apply:

i) The pay-per-uses subject to this Section 14(b) include:

A) **Posting e-reserves, course management systems, e-coursepacks for text-based content,** which grants authorizations to import requested material in electronic format, and allows electronic access to this material to members of a designated college or university class, under the direction of an instructor designated by the college or university, accessible only under appropriate electronic controls (e.g., password);

B) **Posting e-reserves, course management systems, e-coursepacks for material consisting of photographs or other still images not embedded in text,** which grants not only the authorizations described in Section 14(b)(i)(A) above, but also the following authorization: to include the requested material in course materials for use consistent with Section 14(b)(i)(A) above, including any necessary resizing, reformatting or modification of the resolution of such requested material (provided that such modification does not alter the underlying editorial content or meaning of the requested material, and provided that the resulting modified content is used solely within the scope of, and in a manner consistent with, the particular authorization described in the Order Confirmation and the Terms), but not including any other form of manipulation, alteration or editing of the requested material;

C) **Posting e-reserves, course management systems, e-coursepacks or other academic distribution for audiovisual content,** which grants not only the authorizations described in Section 14(b)(i)(A) above, but also the following authorizations: (i) to include the requested material in course materials for use consistent with Section 14(b)(i)(A) above; (ii) to display and perform the requested material to such members of such class in the physical classroom or remotely by means of streaming media or other video formats; and (iii) to "clip" or reformat the requested material for purposes of time or content management or ease of delivery, provided that such “clipping” or reformatting does not alter the underlying editorial content or meaning of the requested material and that the resulting material is used solely within the scope of, and in a manner consistent with, the particular authorization described in the Order Confirmation and the Terms. Unless expressly set forth in the relevant Order Conformation, the License does not authorize any other form of manipulation, alteration or editing of the requested material.

ii) Unless expressly set forth in the relevant Order Confirmation, no License granted shall in any way: (i) include any right by User to create a substantively non-identical copy of the Work or to edit or in any other way modify the Work (except by means of deleting material immediately preceding or following the entire portion of the Work copied or, in the case of Works subject to Sections 14(b)(1)(B) or (C) above, as described in such Sections) (ii) permit "publishing ventures" where any particular course materials would be systematically marketed at multiple institutions.

iii) Subject to any further limitations determined in the Rightsholder Terms (and notwithstanding any apparent contradiction in the Order Confirmation arising from data provided by User), any use authorized under the electronic course content pay-per-use service is limited as follows:

A) any License granted shall apply to only one class (bearing a unique identifier as assigned by the institution, and thereby including all sections or other subparts of the class) at one institution;

B) use is limited to not more than 25% of the text of a book or of the items in a published collection of essays, poems or articles;

C) use is limited to not more than the greater of (a) 25% of the text of an issue of a journal or other periodical or (b) two articles from such an issue;

D) no User may sell or distribute any particular materials, whether photocopied or electronic, at more than one institution of learning;

E) electronic access to material which is the subject of an electronic-use permission must be limited by means of electronic password, student identification or other control permitting access solely to students and instructors in the class;

F) User must ensure (through use of an electronic cover page or other appropriate means) that any person, upon gaining electronic access to the material, which is the subject of a permission, shall see:

- a proper copyright notice, identifying the Rightsholder in whose name CCC has granted permission,
- a statement to the effect that such copy was made pursuant to permission,
- a statement identifying the class to which the material applies and notifying the reader that the material has been made available electronically solely for use in the class, and
- a statement to the effect that the material may not be further distributed to any person outside the class, whether by copying or by transmission and whether electronically or in paper form, and

USC UNIVERSIDADE DE SANTIAGO DE COMPOSTELA

User must also ensure that such cover page or other means will print out in the event that the person accessing the material chooses to print out the material or any part thereof.

G) any permission granted shall expire at the end of the class and, absent some other form of authorization, User is thereupon required to delete the applicable material from any electronic storage or to block electronic access to the applicable material.

iv) Uses of separate portions of a Work, even if they are to be included in the same course material or the same university or college class, require separate permissions under the electronic course content pay-per-use Service. Unless otherwise provided in the Order Confirmation, any grant of rights to User is limited to use completed no later than the end of the academic term (or analogous period) as to which any particular permission is granted.

v) Books and Records; Right to Audit. As to each permission granted under the electronic course content Service, User shall maintain for at least four full calendar years books and records sufficient for CCC to determine the numbers of copies made by User under such permission. CCC and any representatives it may designate shall have the right to audit such books and records at any time during User's ordinary business hours, upon two days' prior notice. If any such audit shall determine that User shall have underpaid for, or underreported, any electronic copies used by three percent (3%) or more, then User shall bear all the costs of any such audit; otherwise, CCC shall bear the costs of any such audit. Any amount determined by such audit to have been underpaid by User shall immediately be paid to CCC by User, together with interest thereon at the rate of 10% per annum from the date such amount was originally due. The provisions of this paragraph shall survive the termination of this license for any reason.

c) ***Pay-Per-Use Permissions for Certain Reproductions (Academic photocopies for library reserves and interlibrary loan reporting) (Non-academic internal/external business uses and commercial document delivery).*** The License expressly excludes the uses listed in Section (c)(i)-(v) below (which must be subject to separate license from the applicable Rightsholder) for: academic photocopies for library reserves and interlibrary loan reporting; and non-academic internal/external business uses and commercial document delivery.

i) electronic storage of any reproduction (whether in plain-text, PDF, or any other format) other than on a transitory basis;

ii) the input of Works or reproductions thereof into any computerized database;

iii) reproduction of an entire Work (cover-to-cover copying) except where the Work is a single article;

iv) reproduction for resale to anyone other than a specific customer of User;

v) republication in any different form. Please obtain authorizations for these uses through other CCC services or directly from the rightsholder.

Any license granted is further limited as set forth in any restrictions included in the Order Confirmation and/or in these Terms.

d) ***Electronic Reproductions in Online Environments (Non-Academic-email, intranet, internet and extranet).*** For "electronic reproductions", which generally includes e-mail use (including instant messaging or other electronic transmission to a defined group of recipients) or posting on an intranet, extranet or Intranet site (including any display or performance incidental thereto), the following additional terms apply:

i) Unless otherwise set forth in the Order Confirmation, the License is limited to use completed within 30 days for any use on the Internet, 60 days for any use on an intranet or extranet and one year for any other use, all as measured from the "republication date" as identified in the Order Confirmation, if any, and otherwise from the date of the Order Confirmation.

ii) User may not make or permit any alterations to the Work, unless expressly set forth in the Order Confirmation (after request by User and approval by Rightsholder); provided, however, that a Work consisting of photographs or other still images not embedded in text may, if necessary, be resized, reformatted or have its resolution modified without additional express permission, and a Work consisting of audiovisual content may, if necessary, be "clipped" or reformatted for purposes of time or content management or ease of delivery (provided that any such resizing, reformatting, resolution modification or “clipping” does not alter the underlying editorial content or meaning of the Work used, and that the

resulting material is used solely within the scope of, and in a manner consistent with, the particular License described in the Order Confirmation and the Terms.

15) **Miscellaneous.**

a) User acknowledges that CCC may, from time to time, make changes or additions to the Service or to the Terms, and that Rightsholder may make changes or additions to the Rightsholder Terms. Such updated Terms will replace the prior terms and conditions in the order workflow and shall be effective as to any subsequent Licenses but shall not apply to Licenses already granted and paid for under a prior set of terms.

b) Use of User-related information collected through the Service is governed by CCC's privacy policy, available online at www.copyright.com/about/privacy-policy/.

c) The License is personal to User. Therefore, User may not assign or transfer to any other person (whether a natural person or an organization of any kind) the License or any rights granted thereunder; provided, however, that, where applicable, User may assign such License in its entirety on written notice to CCC in the event of a transfer of all or substantially all of User's rights in any new material which includes the Work(s) licensed under this Service.

d) No amendment or waiver of any Terms is binding unless set forth in writing and signed by the appropriate parties, including, where applicable, the Rightsholder. The Rightsholder and CCC hereby object to any terms contained in any writing prepared by or on behalf of the User or its principals, employees, agents or affiliates and purporting to govern or otherwise relate to the License described in the Order Confirmation, which terms are in any way inconsistent with any Terms set forth in the Order Confirmation, and/or in CCC's standard operating procedures, whether such writing is prepared prior to, simultaneously with or subsequent to the Order Confirmation, and whether such writing appears on a copy of the Order Confirmation or in a separate instrument.

e) The License described in the Order Confirmation shall be governed by and construed under the law of the State of New York, USA, without regard to the principles thereof of conflicts of law. Any case, controversy, suit, action, or proceeding arising out of, in connection with, or related to such License shall be brought, at CCC's sole discretion, in any federal or state court located in the County of New York, State of New York, USA, or in any federal or state court whose geographical jurisdiction covers the location of the Rightsholder set forth in the Order Confirmation. The parties expressly submit to the personal jurisdiction and venue of each such federal or state court.

USC UNIVERSIDADE DE SANTIAGO DE COMPOSTELA

ELSEVIER LICENSE TERMS AND CONDITIONS

Jan 04, 2023

This Agreement between Gonzalo Diaz ("You") and Elsevier ("Elsevier") consists of your license details and the terms and conditions provided by Elsevier and Copyright Clearance Center.

License Number	5462100025167
License date	Jan 04, 2023
Licensed Content Publisher	Elsevier
Licensed Content Publication	Nuclear Physics A
Licensed Content Title	Search for double-beta decay of 136Xe to excited states of 136Ba with the KamLAND-Zen experiment
Licensed Content Author	K. Asakura,A. Gando,Y. Gando,T. Hachiya,S. Hayashida,H. Ikeda,K. Inoue,K. Ishidoshiro,T. Ishikawa,S. Ishio,M. Koga,S. Matsuda,T. Mitsui,D. Motoki,K. Nakamura,S. Obara,M. Otani,T. Oura,I. Shimizu,Y. Shirahata,J. Shirai,A. Suzuki,H. Tachibana et al.
Licensed Content Date	Feb 1, 2016
Licensed Content Volume	946
Licensed Content Issue	n/a
Licensed Content Pages	11
Start Page	171
End Page	181
Type of Use	reuse in a thesis/dissertation
Portion	figures/tables/illustrations
Number of figures/tables /illustrations	1
Format	both print and electronic
Are you the author of this Elsevier article?	No
Will you be translating?	No
Title	Sensitivity of NEXT-100 detector to neutrinoless double beta decay
Institution name	Universidade de Santiago de Compostela
Expected presentation date	Jan 2023
Portions	Figure 2
Requestor Location	Gonzalo Diaz Rúa de Xoaquín Díaz de Rábago, s/n Santiago de Compostela, 15705 Spain Attn: Gonzalo Diaz
Publisher Tax ID	GB 494 6272 12
Total	**0.00 EUR**
Terms and Conditions	

INTRODUCTION

1. The publisher for this copyrighted material is Elsevier. By clicking "accept" in connection with completing this licensing transaction, you agree that the following terms and conditions apply to this transaction (along with the Billing and Payment terms and conditions established by Copyright Clearance Center, Inc. ("CCC"), at the time that you opened your Rightslink account and that are available at any time at http://myaccount.copyright.com).

GENERAL TERMS

2. Elsevier hereby grants you permission to reproduce the aforementioned material subject to the terms and conditions indicated.

3. Acknowledgement: If any part of the material to be used (for example, figures) has appeared in our publication with credit or acknowledgement to another source, permission must also be sought from that source. If such permission is not obtained then that material may not be included in your publication/copies. Suitable acknowledgement to the source must be made, either as a footnote or in a reference list at the end of your publication, as follows:
"Reprinted from Publication title, Vol /edition number, Author(s), Title of article / title of chapter, Pages No., Copyright (Year), with permission from Elsevier [OR APPLICABLE SOCIETY COPYRIGHT OWNER]." Also Lancet special credit - "Reprinted from The Lancet, Vol. number, Author(s), Title of article, Pages No., Copyright (Year), with permission from Elsevier."

4. Reproduction of this material is confined to the purpose and/or media for which permission is hereby given.

5. Altering/Modifying Material: Not Permitted. However figures and illustrations may be altered/adapted minimally to serve your work. Any other abbreviations, additions, deletions and/or any other alterations shall be made only with prior written authorization of Elsevier Ltd. (Please contact Elsevier's permissions helpdesk here). No modifications can be made to any Lancet figures/tables and they must be reproduced in full.

6. If the permission fee for the requested use of our material is waived in this instance, please be advised that your future requests for Elsevier materials may attract a fee.

7. Reservation of Rights: Publisher reserves all rights not specifically granted in the combination of (i) the license details provided by you and accepted in the course of this licensing transaction, (ii) these terms and conditions and (iii) CCC's Billing and Payment terms and conditions.

8. License Contingent Upon Payment: While you may exercise the rights licensed immediately upon issuance of the license at the end of the licensing process for the transaction, provided that you have disclosed complete and accurate details of your proposed use, no license is finally effective unless and until full payment is received from you (either by publisher or by CCC) as provided in CCC's Billing and Payment terms and conditions. If full payment is not received on a timely basis, then any license preliminarily granted shall be deemed automatically revoked and shall be void as if never granted. Further, in the event that you breach any of these terms and conditions or any of CCC's Billing and Payment terms and conditions, the license is automatically revoked and shall be void as if never granted. Use of materials as described in a revoked license, as well as any use of the materials beyond the scope of an unrevoked license, may constitute copyright infringement and publisher reserves the right to take any and all action to protect its copyright in the materials.

9. Warranties: Publisher makes no representations or warranties with respect to the licensed material.

10. Indemnity: You hereby indemnify and agree to hold harmless publisher and CCC, and their respective officers, directors, employees and agents, from and against any and all claims arising out of your use of the licensed material other than as specifically authorized pursuant to this license.

11. No Transfer of License: This license is personal to you and may not be sublicensed, assigned, or transferred by you to any other person without publisher's written permission.

12. No Amendment Except in Writing: This license may not be amended except in a writing signed by both parties (or, in the case of publisher, by CCC on publisher's behalf).

13. Objection to Contrary Terms: Publisher hereby objects to any terms contained in any purchase order, acknowledgment, check endorsement or other writing prepared by you, which terms are inconsistent with these terms and conditions or CCC's Billing and Payment terms and conditions. These terms and conditions, together with CCC's Billing and Payment terms and conditions (which are incorporated herein), comprise the entire agreement between you and publisher (and CCC) concerning this licensing transaction. In the event of any conflict between your obligations established by these terms and conditions and those established by CCC's Billing and Payment terms and conditions, these terms and conditions shall control.

14. Revocation: Elsevier or Copyright Clearance Center may deny the permissions described in this License at their sole discretion, for any reason or no reason, with a full refund payable to you. Notice of such denial will be made using the contact information provided by you. Failure to receive such notice will not alter or invalidate the denial. In no event will Elsevier or Copyright Clearance Center be responsible or liable for any costs, expenses or damage incurred by you as a result of a denial of your permission request, other than a refund of the amount(s) paid by you to Elsevier and/or Copyright Clearance Center for denied permissions.

LIMITED LICENSE

The following terms and conditions apply only to specific license types:

15. **Translation**: This permission is granted for non-exclusive world **English** rights only unless your license was granted for translation rights. If you licensed translation rights you may only translate this content into the languages you requested. A professional translator must perform all translations and reproduce the content word for word preserving the integrity of the article.

16. **Posting licensed content on any Website**: The following terms and conditions apply as follows: Licensing material from an Elsevier journal: All content posted to the web site must maintain the copyright information line on the bottom of each image; A hyper-text must be included to the Homepage of the journal from which you are licensing at http://www.sciencedirect.com/science/journal/xxxxx or the Elsevier homepage for books at http://www.elsevier.com; Central Storage: This license does not include permission for a scanned version of the material to be stored in a central repository such as that provided by Heron/XanEdu.

Licensing material from an Elsevier book: A hyper-text link must be included to the Elsevier homepage at http://www.elsevier.com . All content posted to the web site must maintain the copyright information line on the bottom of each image.

Posting licensed content on Electronic reserve: In addition to the above the following clauses are applicable: The web site must be password-protected and made available only to bona fide students registered on a relevant course. This permission is granted for 1 year only. You may obtain a new license for future website posting.
17. **For journal authors:** the following clauses are applicable in addition to the above:
Preprints:
A preprint is an author's own write-up of research results and analysis, it has not been peer-reviewed, nor has it had any other value added to it by a publisher (such as formatting, copyright, technical enhancement etc.).
Authors can share their preprints anywhere at any time. Preprints should not be added to or enhanced in any way in order to appear more like, or to substitute for, the final versions of articles however authors can update their preprints on arXiv or RePEc with their Accepted Author Manuscript (see below).
If accepted for publication, we encourage authors to link from the preprint to their formal publication via its DOI. Millions of researchers have access to the formal publications on ScienceDirect, and so links will help users to find, access, cite and use the best available version. Please note that Cell Press, The Lancet and some society-owned have different preprint policies. Information on these policies is available on the journal homepage.
Accepted Author Manuscripts: An accepted author manuscript is the manuscript of an article that has been accepted for publication and which typically includes author-incorporated changes suggested during submission, peer review and editor-author communications.
Authors can share their accepted author manuscript:

- immediately
    - via their non-commercial person homepage or blog
    - by updating a preprint in arXiv or RePEc with the accepted manuscript
    - via their research institute or institutional repository for internal institutional uses or as part of an invitation-only research collaboration work-group
    - directly by providing copies to their students or to research collaborators for their personal use
    - for private scholarly sharing as part of an invitation-only work group on commercial sites with which Elsevier has an agreement
- After the embargo period
    - via non-commercial hosting platforms such as their institutional repository
    - via commercial sites with which Elsevier has an agreement

In all cases accepted manuscripts should:

- link to the formal publication via its DOI
- bear a CC-BY-NC-ND license - this is easy to do
- if aggregated with other manuscripts, for example in a repository or other site, be shared in alignment with our hosting policy not be added to or enhanced in any way to appear more like, or to substitute for, the published journal article.

Published journal article (JPA): A published journal article (PJA) is the definitive final record of published research that appears or will appear in the journal and embodies all value-adding publishing activities including peer review co-ordination, copy-editing, formatting, (if relevant) pagination and online enrichment.
Policies for sharing publishing journal articles differ for subscription and gold open access articles:
Subscription Articles: If you are an author, please share a link to your article rather than the full-text. Millions of researchers have access to the formal publications on ScienceDirect, and so links will help your users to find, access, cite, and use the best available version.
Theses and dissertations which contain embedded PJAs as part of the formal submission can be posted publicly by the awarding institution with DOI links back to the formal publications on ScienceDirect.
If you are affiliated with a library that subscribes to ScienceDirect you have additional private sharing rights for others' research accessed under that agreement. This includes use for classroom teaching and internal training at the institution (including use in course packs and courseware programs), and inclusion of the article for grant funding purposes.
Gold Open Access Articles: May be shared according to the author-selected end-user license and should contain a CrossMark logo, the end user license, and a DOI link to the formal publication on ScienceDirect.
Please refer to Elsevier's posting policy for further information.
18. **For book authors** the following clauses are applicable in addition to the above: Authors are permitted to place a brief summary of their work online only. You are not allowed to download and post the published electronic version of your chapter, nor may you scan the printed edition to create an electronic version. **Posting to a repository:** Authors are permitted to post a summary of their chapter only in their institution's repository.
19. **Thesis/Dissertation**: If your license is for use in a thesis/dissertation your thesis may be submitted to your institution in either print or electronic form. Should your thesis be published commercially, please reapply for permission. These requirements include permission for the Library and Archives of Canada to supply single copies, on demand, of the complete thesis and include permission for Proquest/UMI to supply single copies, on demand, of the complete thesis. Should your thesis be published commercially, please reapply for permission. Theses and dissertations which contain embedded PJAs as part of the formal submission can be posted publicly by the awarding institution with DOI links back to the formal publications

on ScienceDirect.

Elsevier Open Access Terms and Conditions

You can publish open access with Elsevier in hundreds of open access journals or in nearly 2000 established subscription journals that support open access publishing. Permitted third party re-use of these open access articles is defined by the author's choice of Creative Commons user license. See our open access license policy for more information.

Terms & Conditions applicable to all Open Access articles published with Elsevier:

Any reuse of the article must not represent the author as endorsing the adaptation of the article nor should the article be modified in such a way as to damage the author's honour or reputation. If any changes have been made, such changes must be clearly indicated.

The author(s) must be appropriately credited and we ask that you include the end user license and a DOI link to the formal publication on ScienceDirect.

If any part of the material to be used (for example, figures) has appeared in our publication with credit or acknowledgement to another source it is the responsibility of the user to ensure their reuse complies with the terms and conditions determined by the rights holder.

Additional Terms & Conditions applicable to each Creative Commons user license:

CC BY: The CC-BY license allows users to copy, to create extracts, abstracts and new works from the Article, to alter and revise the Article and to make commercial use of the Article (including reuse and/or resale of the Article by commercial entities), provided the user gives appropriate credit (with a link to the formal publication through the relevant DOI), provides a link to the license, indicates if changes were made and the licensor is not represented as endorsing the use made of the work. The full details of the license are available at http://creativecommons.org/licenses/by/4.0.

CC BY NC SA: The CC BY-NC-SA license allows users to copy, to create extracts, abstracts and new works from the Article, to alter and revise the Article, provided this is not done for commercial purposes, and that the user gives appropriate credit (with a link to the formal publication through the relevant DOI), provides a link to the license, indicates if changes were made and the licensor is not represented as endorsing the use made of the work. Further, any new works must be made available on the same conditions. The full details of the license are available at http://creativecommons.org/licenses/by-nc-sa/4.0.

CC BY NC ND: The CC BY-NC-ND license allows users to copy and distribute the Article, provided this is not done for commercial purposes and further does not permit distribution of the Article if it is changed or edited in any way, and provided the user gives appropriate credit (with a link to the formal publication through the relevant DOI), provides a link to the license, and that the licensor is not represented as endorsing the use made of the work. The full details of the license are available at http://creativecommons.org/licenses/by-nc-nd/4.0. Any commercial reuse of Open Access articles published with a CC BY NC SA or CC BY NC ND license requires permission from Elsevier and will be subject to a fee.

Commercial reuse includes:

- Associating advertising with the full text of the Article
- Charging fees for document delivery or access
- Article aggregation
- Systematic distribution via e-mail lists or share buttons

Posting or linking by commercial companies for use by customers of those companies.

20. **Other Conditions**:

v1.10

Questions? customercare@copyright.com or +1-855-239-3415 (toll free in the US) or +1-978-646-2777.

USC UNIVERSIDADE DE SANTIAGO DE COMPOSTELA

CCC Marketplace

This is a License Agreement between Gonzalo Díaz López ("User") and Copyright Clearance Center, Inc. ("CCC") on behalf of the Rightsholder identified in the order details below. The license consists of the order details, the Marketplace Order General Terms and Conditions below, and any Rightsholder Terms and Conditions which are included below.

All payments must be made in full to CCC in accordance with the Marketplace Order General Terms and Conditions below.

Order Date	06-Jan-2023	**Type of Use**	Republish in a thesis/dissertation
Order License ID	1308353-1		
ISSN	1748-0221	**Publisher**	IOP Publishing
		Portion	Chart/graph/table/figure

LICENSED CONTENT

Publication Title	Journal of Instrumentation	**Publication Type**	e-Journal
Article Title	NEXT-100 Technical Design Report (TDR). Executive summary	**Start Page**	T06001
		End Page	T06001
Author/Editor	Institute of Physics (Great Britain), Institute of Physics Publishing., International School for Advanced Studies (Trieste, Italy)	**Issue**	06
		Volume	7
		URL	http://www.iop.org/EJ/jinst/
Date	01/01/2006		
Language	English		
Country	United Kingdom of Great Britain and Northern Ireland		
Rightsholder	IOP Publishing, Ltd		

REQUEST DETAILS

Portion Type	Chart/graph/table/figure	**Distribution**	Other territories and/or countries
Number of Charts / Graphs / Tables / Figures Requested	1	**Enter Territories/Countries**	Spain
Format (select all that apply)	Print, Electronic	**Translation**	Original language of publication
Who Will Republish the Content?	Academic institution	**Copies for the Disabled?**	No
		Minor Editing Privileges?	No
Duration of Use	Life of current and all future editions	**Incidental Promotional Use?**	No
Lifetime Unit Quantity	Up to 499	**Currency**	EUR
Rights Requested	Main product		

NEW WORK DETAILS

Title	Sensitivity of NEXT-100 detector to neutrinoless double beta decay	**Institution Name**	Universidade de Santiago de Compostela
Instructor Name	José Ángel Hernando Morata	**Expected Presentation Date**	2023-01-31

ADDITIONAL DETAILS

Order Reference Number	N/A	**The Requesting Person/Organization to Appear on the License**	Gonzalo Díaz López

REUSE CONTENT DETAILS

Title, Description or Numeric Reference of the Portion(s)	Figure 2	**Title of the Article/Chapter the Portion Is From**	NEXT-100 Technical Design Report (TDR). Executive summary
Editor of Portion(s)	N/A	**Author of Portion(s)**	N/A
Volume of Serial or Monograph	7	**Issue, if Republishing an Article From a Serial**	06
Page or Page Range of Portion	T06001-T06001	**Publication Date of Portion**	2012-06-06

RIGHTSHOLDER TERMS AND CONDITIONS

These special terms and conditions are in addition to the standard terms and conditions for CCC's Republication Service and, together with those standard terms and conditions, govern the use of the Works. As the User you will make all reasonable efforts to contact the author(s) of the article which the Work is to be reused from, to seek consent for your intended use. Contacting one author who is acting expressly as authorised agent for their co-author(s) is acceptable. User will reproduce the following wording prominently alongside the Work: the source of the Work, including author, article title, title of journal, volume number, issue number (if relevant), page range (or first page if this is the only information available) and date of first publication; and a link back to the article (via DOI); and if practicable, and IN ALL CASES for new works published under any of the Creative Commons licences, the words "© IOP Publishing. Reproduced with permission. All rights reserved" Without the express permission of the author(s) and the Rightsholder of the article from which the Work is to be reused, User shall not use it in any way which, in the opinion of the Rightsholder, could: (i) distort or alter the author(s)' original intention(s) and meaning; (ii) be prejudicial to the honour or reputation of the author(s); and/or (iii) imply endorsement by the author(s) and/or the Rightsholder. This licence does not apply to any article which is credited to another source and which does not have the copyright line '© IOP Publishing Ltd'. User must check the copyright line of the article from which the Work is to be reused to check that IOP Publishing Ltd has all the necessary rights to be able to grant permission. User is solely responsible for identifying and obtaining separate licences and permissions from the copyright owner for reuse of any such third party material/figures which the Rightsholder is not the copyright owner of. The Rightsholder shall not reimburse any fees which User pays for a republication license for such third party content. This licence does not apply to any material/figure which is credited to another source in the Rightsholder's publication or has been obtained from a third party. User must check the Version of Record of the article from which the Work is to be reused, to check whether any of the material in the Work is third party material. Third party citations and/or copyright notices and/or permissions statements may not be included in any other version of the article from which the Work is to be reused and so cannot be relied upon by the User. User is solely responsible for identifying and obtaining separate licences and permissions from the copyright owner for reuse of any such third party material/figures where the Rightsholder is not the copyright owner. The Rightsholder shall not reimburse any fees which User pays for a republication license for such third party content. User and CCC acknowledge that the Rightsholder may, from time to time, make changes or additions to these special terms and conditions without express notification, provided that these shall not apply to permissions already secured and paid for by User prior to such change or addition. User acknowledges that the Rightsholder (which includes companies within its group and third parties for whom it publishes its titles) may make use of personal data collected through the service in the course of their business. If User is the author of the Work, User may automatically have the right to reuse it under the rights granted back when User transferred the copyright in the article to the Rightsholder. User should check the copyright form and the relevant author rights policy to check whether permission is required. If User is the author of the Work and does require permission for proposed reuse of the Work, User should select 'Author of requested content' as the Requestor Type. The Rightsholder shall not reimburse any fees which User pays for a republication license. If User is the author of the article which User wishes to reuse in User's thesis or dissertation, the republication licence covers the right to include the Version of Record of the article, provided it is not then shared or deposited online. User must include citation details. Where User wishes to share their thesis or dissertation online, they should remove the Version of Record before uploading it. User may include a Preprint or the Accepted Manuscript (after the embargo period) in the online version of the thesis or dissertation, provided they do so in accordance with the Rightsholder's policies on sharing Preprints or Accepted Manuscripts. User may need to obtain separate permission for any third party content included within the article. User must check this with the copyright owner of such third party content. Any online or commercial use of User's thesis or dissertation containing the article, including publication via ProQuest, would need to be expressly notified in writing to the Rightsholder at the time of request and would require separate written permission from the Rightsholder. As well as CCC, the Rightsholder shall have the right to bring any legal action that it deems necessary to enforce its rights should it consider that the Work infringes those rights in any way. For content reuse requests that qualify for permission under the STM Permissions Guidelines, which may be updated from

time to time, the STM Permissions Guidelines supplement the terms and conditions contained in this license.

Marketplace Order General Terms and Conditions

The following terms and conditions ("General Terms"), together with any applicable Publisher Terms and Conditions, govern User's use of Works pursuant to the Licenses granted by Copyright Clearance Center, Inc. ("CCC") on behalf of the applicable Rightsholders of such Works through CCC's applicable Marketplace transactional licensing services (each, a "Service").

1) **Definitions.** For purposes of these General Terms, the following definitions apply:

"License" is the licensed use the User obtains via the Marketplace platform in a particular licensing transaction, as set forth in the Order Confirmation.

"Order Confirmation" is the confirmation CCC provides to the User at the conclusion of each Marketplace transaction. "Order Confirmation Terms" are additional terms set forth on specific Order Confirmations not set forth in the General Terms that can include terms applicable to a particular CCC transactional licensing service and/or any Rightsholder-specific terms.

"Rightsholder(s)" are the holders of copyright rights in the Works for which a User obtains licenses via the Marketplace platform, which are displayed on specific Order Confirmations.

"Terms" means the terms and conditions set forth in these General Terms and any additional Order Confirmation Terms collectively.

"User" or "you" is the person or entity making the use granted under the relevant License. Where the person accepting the Terms on behalf of a User is a freelancer or other third party who the User authorized to accept the General Terms on the User's behalf, such person shall be deemed jointly a User for purposes of such Terms.

"Work(s)" are the copyright protected works described in relevant Order Confirmations.

2) **Description of Service.** CCC's Marketplace enables Users to obtain Licenses to use one or more Works in accordance with all relevant Terms. CCC grants Licenses as an agent on behalf of the copyright rightsholder identified in the relevant Order Confirmation.

3) **Applicability of Terms.** The Terms govern User's use of Works in connection with the relevant License. In the event of any conflict between General Terms and Order Confirmation Terms, the latter shall govern. User acknowledges that Rightsholders have complete discretion whether to grant any permission, and whether to place any limitations on any grant, and that CCC has no right to supersede or to modify any such discretionary act by a Rightsholder.

4) **Representations; Acceptance.** By using the Service, User represents and warrants that User has been duly authorized by the User to accept, and hereby does accept, all Terms.

5) **Scope of License; Limitations and Obligations.** All Works and all rights therein, including copyright rights, remain the sole and exclusive property of the Rightsholder. The License provides only those rights expressly set forth in the terms and conveys no other rights in any Works

6) **General Payment Terms.** User may pay at time of checkout by credit card or choose to be invoiced. If the User chooses to be invoiced, the User shall: (i) remit payments in the manner identified on specific invoices, (ii) unless otherwise specifically stated in an Order Confirmation or separate written agreement, Users shall remit payments upon receipt of the relevant invoice from CCC, either by delivery or notification of availability of the invoice via the Marketplace platform, and (iii) if the User does not pay the invoice within 30 days of receipt, the User may incur a service charge of 1.5% per month or the maximum rate allowed by applicable law, whichever is less. While User may exercise the rights in the License immediately upon receiving the Order Confirmation, the License is automatically revoked and is null and void, as if it had never been issued, if CCC does not receive complete payment on a timely basis.

7) **General Limits on Use.** Unless otherwise provided in the Order Confirmation, any grant of rights to User (i) involves only the rights set forth in the Terms and does not include subsequent or additional uses, (ii) is non-exclusive and non-transferable, and (iii) is subject to any and all limitations and restrictions (such as, but not limited to, limitations on duration of use or circulation) included in the Terms. Upon completion of the licensed use as set forth in the Order Confirmation, User shall either secure a new permission for further use of the Work(s) or immediately cease any new use of the Work(s) and shall render inaccessible (such as by deleting or by removing or severing links or other locators) any further copies of the Work. User may only make alterations to the Work if and as expressly set forth in the Order Confirmation. No Work may be used in any way that is defamatory, violates the rights of third parties (including such third parties' rights of copyright, privacy, publicity, or other tangible or intangible property), or is otherwise illegal, sexually explicit, or obscene. In addition, User may not conjoin a Work with any other material that may result in damage to the reputation of the Rightsholder. User agrees to inform CCC if it becomes aware of any infringement of any rights in a Work and to cooperate with any reasonable request of CCC or the Rightsholder in connection therewith.

8) **Third Party Materials.** In the event that the material for which a License is sought includes third party materials (such as photographs, illustrations, graphs, inserts and similar materials) that are identified in such material as having been used by permission (or a similar indicator), User is responsible for identifying, and seeking separate licenses (under this Service, if available, or otherwise) for any of such third party materials; without a separate license, User may not use such third party materials via the License.

9) **Copyright Notice.** Use of proper copyright notice for a Work is required as a condition of any License granted under the Service. Unless otherwise provided in the Order Confirmation, a proper copyright notice will read substantially as follows: "Used with permission of [Rightsholder's name], from [Work's title, author, volume, edition number and year of copyright]; permission conveyed through Copyright Clearance Center, Inc." Such notice must be provided in a reasonably legible font size and must be placed either on a cover page or in another location that any person, upon gaining access to the material which is the subject of a permission, shall see, or in the case of republication Licenses, immediately adjacent to the Work as used (for example, as part of a by-line or footnote) or in the place where substantially all other credits or notices for the new work containing the republished Work are located. Failure to include the required notice results in loss to the Rightsholder and CCC, and the User shall be liable to pay liquidated damages for each such failure equal to twice the use fee specified in the Order Confirmation, in addition to the use fee itself and any other fees and charges specified.

10) **Indemnity.** User hereby indemnifies and agrees to defend the Rightsholder and CCC, and their respective employees and directors, against all claims, liability, damages, costs, and expenses, including legal fees and expenses, arising out of any use of a Work beyond the scope of the rights granted herein and in the Order Confirmation, or any use of a Work which has been altered in any unauthorized way by User, including claims of defamation or infringement of rights of copyright, publicity, privacy, or other tangible or intangible property.

11) **Limitation of Liability.** UNDER NO CIRCUMSTANCES WILL CCC OR THE RIGHTSHOLDER BE LIABLE FOR ANY DIRECT, INDIRECT, CONSEQUENTIAL, OR INCIDENTAL DAMAGES (INCLUDING WITHOUT LIMITATION DAMAGES FOR LOSS OF BUSINESS PROFITS OR INFORMATION, OR FOR BUSINESS INTERRUPTION) ARISING OUT OF THE USE OR INABILITY TO USE A WORK, EVEN IF ONE OR BOTH OF THEM HAS BEEN ADVISED OF THE POSSIBILITY OF SUCH DAMAGES. In any event, the total liability of the Rightsholder and CCC (including their respective employees and directors) shall not exceed the total amount actually paid by User for the relevant License. User assumes full liability for the actions and omissions of its principals, employees, agents, affiliates, successors, and assigns.

12) **Limited Warranties.** THE WORK(S) AND RIGHT(S) ARE PROVIDED "AS IS." CCC HAS THE RIGHT TO GRANT TO USER THE RIGHTS GRANTED IN THE ORDER CONFIRMATION DOCUMENT. CCC AND THE RIGHTSHOLDER DISCLAIM ALL OTHER WARRANTIES RELATING TO THE WORK(S) AND RIGHT(S), EITHER EXPRESS OR IMPLIED, INCLUDING WITHOUT LIMITATION IMPLIED WARRANTIES OF MERCHANTABILITY OR FITNESS FOR A PARTICULAR PURPOSE. ADDITIONAL RIGHTS MAY BE REQUIRED TO USE ILLUSTRATIONS, GRAPHS, PHOTOGRAPHS, ABSTRACTS, INSERTS, OR OTHER PORTIONS OF THE WORK (AS OPPOSED TO THE ENTIRE WORK) IN A MANNER CONTEMPLATED BY USER; USER UNDERSTANDS AND AGREES THAT NEITHER CCC NOR THE RIGHTSHOLDER MAY HAVE SUCH ADDITIONAL RIGHTS TO GRANT.

13) **Effect of Breach.** Any failure by User to pay any amount when due, or any use by User of a Work beyond the scope of the License set forth in the Order Confirmation and/or the Terms, shall be a material breach of such License. Any breach not cured within 10 days of written notice thereof shall result in immediate termination of such License without further notice. Any unauthorized (but licensable) use of a Work that is terminated immediately upon notice thereof may be liquidated by payment of the Rightsholder's ordinary license price therefor; any unauthorized (and unlicensable) use that is not terminated immediately for any reason (including, for example, because materials containing the Work cannot reasonably be recalled) will be subject to all remedies available at law or in equity, but in no event to a payment of less than three times the Rightsholder's ordinary license price for the most closely analogous licensable use plus Rightsholder's and/or CCC's costs and expenses incurred in collecting such payment.

14) **Additional Terms for Specific Products and Services.** If a User is making one of the uses described in this Section 14, the additional terms and conditions apply:

a) ***Print Uses of Academic Course Content and Materials (photocopies for academic coursepacks or classroom handouts).*** For photocopies for academic coursepacks or classroom handouts the following additional terms apply:

i) The copies and anthologies created under this License may be made and assembled by faculty members individually or at their request by on-campus bookstores or copy centers, or by off-campus copy shops and other similar entities.

ii) No License granted shall in any way: (i) include any right by User to create a substantively non-identical copy of the Work or to edit or in any other way modify the Work (except by means of deleting material immediately preceding or following the entire portion of the Work copied) (ii) permit "publishing ventures" where any particular anthology would be systematically marketed at multiple institutions.

iii) Subject to any Publisher Terms (and notwithstanding any apparent contradiction in the Order Confirmation arising from data provided by User), any use authorized under the academic pay-per-use service is limited as follows:

A) any License granted shall apply to only one class (bearing a unique identifier as assigned by the institution, and thereby including all sections or other subparts of the class) at one institution;

B) use is limited to not more than 25% of the text of a book or of the items in a published collection of essays, poems or articles;

C) use is limited to no more than the greater of (a) 25% of the text of an issue of a journal or other periodical or (b) two articles from such an issue;

D) no User may sell or distribute any particular anthology, whether photocopied or electronic, at more than one institution of learning;

E) in the case of a photocopy permission, no materials may be entered into electronic memory by User except in order to produce an identical copy of a Work before or during the academic term (or analogous period) as to which any particular permission is granted. In the event that User shall choose to retain materials that are the subject of a photocopy permission in electronic memory for purposes of producing identical copies more than one day after such retention (but still within the scope of any permission granted), User must notify CCC of such fact in the applicable permission request and such retention shall constitute one copy actually sold for purposes of calculating permission fees due; and

F) any permission granted shall expire at the end of the class. No permission granted shall in any way include any right by User to create a substantively non-identical copy of the Work or to edit or in any other way modify the Work (except by means of deleting material immediately preceding or following the entire portion of the Work copied).

iv) Books and Records; Right to Audit. As to each permission granted under the academic pay-per-use Service, User shall maintain for at least four full calendar years books and records sufficient for CCC to determine the numbers of copies made by User under such permission. CCC and any representatives it may designate shall have the right to audit such books and records at any time during User's ordinary business hours, upon two days' prior notice. If any such audit shall determine that User shall have underpaid for, or underreported, any photocopies sold or by three percent (3%) or more, then User shall bear all the costs of any such audit; otherwise, CCC shall bear the costs of any such audit. Any amount determined by such audit to have been underpaid by User shall immediately be paid to CCC by User, together with interest thereon at the rate of 10% per annum from the date such amount was originally due. The provisions of this paragraph shall survive the termination of this License for any reason.

b) ***Digital Pay-Per-Uses of Academic Course Content and Materials (e-coursepacks, electronic reserves, learning management systems, academic institution intranets).*** For uses in e-coursepacks, posts in electronic reserves, posts in learning management systems, or posts on academic institution intranets, the following additional terms apply:

i) The pay-per-uses subject to this Section 14(b) include:

A) **Posting e-reserves, course management systems, e-coursepacks for text-based content,** which grants authorizations to import requested material in electronic format, and allows electronic access to this material to members of a designated college or university class, under the direction of an instructor designated by the college or university, accessible only under appropriate electronic controls (e.g., password);

B) **Posting e-reserves, course management systems, e-coursepacks for material consisting of photographs or other still images not embedded in text,** which grants not only the authorizations described in Section 14(b)(i)(A) above, but also the following authorization: to include the requested material in course materials for use consistent with Section 14(b)(i)(A) above, including any necessary resizing, reformatting or modification of the resolution of such requested material (provided that such modification does not alter the underlying editorial content or meaning of the requested material, and provided that the resulting modified content is used solely within the scope of, and in a manner consistent with, the particular authorization described in the Order Confirmation and the Terms), but not including any other form of manipulation, alteration or editing of the requested material;

C) **Posting e-reserves, course management systems, e-coursepacks or other academic distribution for audiovisual content,** which grants not only the authorizations described in Section 14(b)(i)(A) above, but also the following authorizations: (i) to include the requested material in course materials for use consistent with Section 14(b)(i)(A) above; (ii) to display and perform the requested material to such members of such class in the physical classroom or remotely by means of streaming media or other video formats; and (iii) to "clip" or reformat the requested material for purposes of time or content management or ease of delivery, provided that such “clipping” or reformatting does not alter the underlying editorial content or meaning of the requested material and that the resulting material is used solely within the scope of, and in a manner consistent with, the particular authorization described in the Order Confirmation and the Terms. Unless expressly set forth in the relevant Order Conformation, the License does not authorize any other form of manipulation, alteration or editing of the requested material.

ii) Unless expressly set forth in the relevant Order Confirmation, no License granted shall in any way: (i) include any right by User to create a substantively non-identical copy of the Work or to edit or in any other way modify the Work (except by means of deleting material immediately preceding or following the entire portion of the Work copied or, in the case of Works subject to Sections 14(b)(1)(B) or (C) above, as described in such Sections) (ii) permit "publishing ventures" where any particular course materials would be systematically marketed at multiple institutions.

iii) Subject to any further limitations determined in the Rightsholder Terms (and notwithstanding any apparent contradiction in the Order Confirmation arising from data provided by User), any use authorized under the electronic course content pay-per-use service is limited as follows:

A) any License granted shall apply to only one class (bearing a unique identifier as assigned by the institution, and thereby including all sections or other subparts of the class) at one institution;

B) use is limited to not more than 25% of the text of a book or of the items in a published collection of essays, poems or articles;

C) use is limited to not more than the greater of (a) 25% of the text of an issue of a journal or other periodical or (b) two articles from such an issue;

D) no User may sell or distribute any particular materials, whether photocopied or electronic, at more than one institution of learning;

E) electronic access to material which is the subject of an electronic-use permission must be limited by means of electronic password, student identification or other control permitting access solely to students and instructors in the class;

F) User must ensure (through use of an electronic cover page or other appropriate means) that any person, upon gaining electronic access to the material, which is the subject of a permission, shall see:

- a proper copyright notice, identifying the Rightsholder in whose name CCC has granted permission,
- a statement to the effect that such copy was made pursuant to permission,
- a statement identifying the class to which the material applies and notifying the reader that the material has been made available electronically solely for use in the class, and
- a statement to the effect that the material may not be further distributed to any person outside the class, whether by copying or by transmission and whether electronically or in paper form, and User must also ensure that such cover page or other means will print out in the event that the person accessing the material chooses to print out the material or any part thereof.

G) any permission granted shall expire at the end of the class and, absent some other form of authorization, User is thereupon required to delete the applicable material from any electronic storage or to block electronic access to the applicable material.

iv) Uses of separate portions of a Work, even if they are to be included in the same course material or the same university or college class, require separate permissions under the electronic course content pay-per-use Service. Unless otherwise provided in the Order Confirmation, any grant of rights to User is limited to use completed no later than the end of the academic term (or analogous period) as to which any particular permission is granted.

v) Books and Records; Right to Audit. As to each permission granted under the electronic course content Service, User shall maintain for at least four full calendar years books and records sufficient for CCC to determine the numbers of copies made by User under such permission. CCC and any representatives it may designate shall have the right to audit such books and records at any time during User's ordinary business hours, upon two days' prior notice. If any such audit shall determine that User shall have underpaid for, or underreported, any electronic copies used by three percent (3%) or more, then User shall bear all the costs of any such audit; otherwise, CCC shall bear the costs of any such audit. Any amount determined by such audit to have been underpaid by User shall immediately be paid to CCC by User, together with interest thereon at the rate of 10% per annum from the date such amount was originally due. The provisions of this paragraph shall survive the termination of this license for any reason.

UMinho UNIVERSIDADE DO MINHO

c) ***Pay-Per-Use Permissions for Certain Reproductions (Academic photocopies for library reserves and interlibrary loan reporting) (Non-academic internal/external business uses and commercial document delivery).*** The License expressly excludes the uses listed in Section (c)(i)-(v) below (which must be subject to separate license from the applicable Rightsholder) for: academic photocopies for library reserves and interlibrary loan reporting; and non-academic internal/external business uses and commercial document delivery.

i) electronic storage of any reproduction (whether in plain-text, PDF, or any other format) other than on a

transitory basis;

ii) the input of Works or reproductions thereof into any computerized database;

iii) reproduction of an entire Work (cover-to-cover copying) except where the Work is a single article;

iv) reproduction for resale to anyone other than a specific customer of User;

v) republication in any different form. Please obtain authorizations for these uses through other CCC services or directly from the rightsholder.

Any license granted is further limited as set forth in any restrictions included in the Order Confirmation and/or in these Terms.

d) ***Electronic Reproductions in Online Environments (Non-Academic-email, intranet, internet and extranet).*** For "electronic reproductions", which generally includes e-mail use (including instant messaging or other electronic transmission to a defined group of recipients) or posting on an intranet, extranet or Intranet site (including any display or performance incidental thereto), the following additional terms apply:

i) Unless otherwise set forth in the Order Confirmation, the License is limited to use completed within 30 days for any use on the Internet, 60 days for any use on an intranet or extranet and one year for any other use, all as measured from the "republication date" as identified in the Order Confirmation, if any, and otherwise from the date of the Order Confirmation.

ii) User may not make or permit any alterations to the Work, unless expressly set forth in the Order Confirmation (after request by User and approval by Rightsholder); provided, however, that a Work consisting of photographs or other still images not embedded in text may, if necessary, be resized, reformatted or have its resolution modified without additional express permission, and a Work consisting of audiovisual content may, if necessary, be "clipped" or reformatted for purposes of time or content management or ease of delivery (provided that any such resizing, reformatting, resolution modification or “clipping” does not alter the underlying editorial content or meaning of the Work used, and that the resulting material is used solely within the scope of, and in a manner consistent with, the particular License described in the Order Confirmation and the Terms.

15) **Miscellaneous.**

a) User acknowledges that CCC may, from time to time, make changes or additions to the Service or to the Terms, and that Rightsholder may make changes or additions to the Rightsholder Terms. Such updated Terms will replace the prior terms and conditions in the order workflow and shall be effective as to any subsequent Licenses but shall not apply to Licenses already granted and paid for under a prior set of terms.

b) Use of User-related information collected through the Service is governed by CCC's privacy policy, available online at www.copyright.com/about/privacy-policy/.

c) The License is personal to User. Therefore, User may not assign or transfer to any other person (whether a natural person or an organization of any kind) the License or any rights granted thereunder; provided, however, that, where applicable, User may assign such License in its entirety on written notice to CCC in the event of a transfer of all or substantially all of User's rights in any new material which includes the Work(s) licensed under this Service.

d) No amendment or waiver of any Terms is binding unless set forth in writing and signed by the appropriate parties, including, where applicable, the Rightsholder. The Rightsholder and CCC hereby object to any terms contained in any writing prepared by or on behalf of the User or its principals, employees, agents or affiliates and purporting to govern or otherwise relate to the License described in the Order Confirmation, which terms are in any way inconsistent with any Terms set forth in the Order Confirmation, and/or in CCC's standard operating procedures, whether such writing is prepared prior to, simultaneously with or subsequent to the Order Confirmation, and whether such writing appears on a copy of the Order Confirmation or in a separate instrument.

e) The License described in the Order Confirmation shall be governed by and construed under the law of the State of New York, USA, without regard to the principles thereof of conflicts of law. Any case, controversy, suit, action, or proceeding arising out of, in connection with, or related to such License shall be brought, at CCC's sole discretion, in any federal or state court located in the County of New York, State of New York, USA, or in any federal or state court whose geographical jurisdiction covers the location of the Rightsholder set forth in the Order Confirmation. The parties expressly submit to the personal jurisdiction and venue of each such federal or state court.

USC
DE SANTIAGO
DE COMPOSTELA

Gmail **Gonzalo Díaz López <gonzalodiazlopez10@gmail.com>**

Permission for the reproduction of figures

2 mensajes

Gonzalo Díaz López <gonzalodiazlopez10@gmail.com> 5 de enero de 2023, 14:07
Para: Josh Renner <josh.e.renner@gmail.com>

Dear J.E. Renner:
I am a PhD student at the University of Santiago de Compostela (Spain) working in the NEXT experiment. I request your permission to reproduce the following figure(s) from your work PhD thesis: High pressure xenon detectors for rare physics searches in my PhD thesis with title *Sensitivity of NEXT-100 detector to neutrinoless double beta decay*.

1. Figure 3.28. (energy resolution)

Sorry for the inconvenience, my institution is particularly sensitive about the reproduction of figures from other works in the PhD dissertations.
Kind regards,
Gonzalo Díaz López

Josh Renner <josh.e.renner@gmail.com> 5 de enero de 2023, 16:27
Para: Gonzalo Díaz López <gonzalodiazlopez10@gmail.com>

Dear Gonzalo,

You have my permission to use this figure from my PhD thesis.

Best,

Josh Renner
[El texto citado está oculto]

USC UNIVERSIDADE DE SANTIAGO DE COMPOSTELA

Gmail **Gonzalo Díaz López <gonzalodiazlopez10@gmail.com>**

Permiso

Javier Larrea <javier@jlarrea.com> 25 de noviembre de 2022, 10:17
Para: Gonzalo Díaz López <gonzalodiazlopez10@gmail.com>

Hola Gonzalo,
Sin problema, puedes utilizarlas.
Suerte con tu trabajo!!

Javier Larrea
https://www.jlarrea.com
680985527

> El 25 nov 2022, a las 9:51, Gonzalo Díaz López <gonzalodiazlopez10@gmail.com> escribió:
>
>
> Hola,
> soy un estudiante de doctorado en la Universidad de Santiago de Compostela, trabajando en el experimento NEXT.
> Escribo para solicitar tu permiso para poder utilizar en mi tesis dos fotos, que adjunto en este mail.
> Saludos,
> Gonzalo Díaz López
>
> <new_in_lsc.png>
>
> <new_platform.png>
>
>

American Physical Society
Reuse and Permissions License

05-Jan-2023

This license agreement between the American Physical Society ("APS") and Gonzalo Diaz ("You") consists of your license details and the terms and conditions provided by the American Physical Society and SciPris.

Licensed Content Information

License Number:	**RNP/23/JAN/061751**
License date:	05-Jan-2023
DOI:	10.1103/PhysRevC.105.055501
Title:	Measurement of the $^{136}\mathrm{Xe}$ two-neutrino double-b-decay half-life via direct background subtraction in NEXT
Author:	P. Novella et al. (NEXT Collaboration)
Publication:	Physical Review C
Publisher:	American Physical Society
Cost:	USD $ 0.00

Request Details

Does your reuse require significant modifications: No

Specify intended distribution locations:	Spain
Reuse Category:	Reuse in a thesis/dissertation
Requestor Type:	Student
Items for Reuse:	Figures/Tables
Number of Figure/Tables:	2
Figure/Tables Details:	Figure 5 and Figure 6 (top)
Format for Reuse:	Print and Electronic
Total number of print copies:	Up to 1000

Information about New Publication:

University/Publisher:	Universidade de Santiago de Compostela
Title of dissertation/thesis:	Sensitivity of NEXT-100 detector to neutrinoless double beta decay
Author(s):	Gonzalo Díaz López
Expected completion date:	Jan. 2023

License Requestor Information

Name:	Gonzalo Diaz
Affiliation:	Individual
Email Id:	gonzalodiazlopez10@gmail.com
Country:	Spain

USC UNIVERSIDADE DE SANTIAGO DE COMPOSTELA

American Physical Society
Reuse and Permissions License

TERMS AND CONDITIONS

The American Physical Society (APS) is pleased to grant the Requestor of this license a non-exclusive, non-transferable permission, limited to Print and Electronic format, provided all criteria outlined below are followed.

1. You must also obtain permission from at least one of the lead authors for each separate work, if you haven't done so already. The author's name and affiliation can be found on the first page of the published Article.
2. For electronic format permissions, Requestor agrees to provide a hyperlink from the reprinted APS material using the source material's DOI on the web page where the work appears. The hyperlink should use the standard DOI resolution URL, http://dx.doi.org/{DOI}. The hyperlink may be embedded in the copyright credit line.
3. For print format permissions, Requestor agrees to print the required copyright credit line on the first page where the material appears: "Reprinted (abstract/excerpt/figure) with permission from [(FULL REFERENCE CITATION) as follows: Author's Names, APS Journal Title, Volume Number, Page Number and Year of Publication.] Copyright (YEAR) by the American Physical Society."
4. Permission granted in this license is for a one-time use and does not include permission for any future editions, updates, databases, formats or other matters. Permission must be sought for any additional use.
5. Use of the material does not and must not imply any endorsement by APS.
6. APS does not imply, purport or intend to grant permission to reuse materials to which it does not hold copyright. It is the requestor's sole responsibility to ensure the licensed material is original to APS and does not contain the copyright of another entity, and that the copyright notice of the figure, photograph, cover or table does not indicate it was reprinted by APS with permission from another source.
7. The permission granted herein is personal to the Requestor for the use specified and is not transferable or assignable without express written permission of APS. This license may not be amended except in writing by APS.
8. You may not alter, edit or modify the material in any manner.
9. You may translate the materials only when translation rights have been granted.
10. APS is not responsible for any errors or omissions due to translation.
11. You may not use the material for promotional, sales, advertising or marketing purposes.
12. The foregoing license shall not take effect unless and until APS or its agent, Aptara, receives payment in full in accordance with Aptara Billing and Payment Terms and Conditions, which are incorporated herein by reference.
13. Should the terms of this license be violated at any time, APS or Aptara may revoke the license with no refund to you and seek relief to the fullest extent of the laws of the USA. Official written notice will be made using the contact information provided with the permission request. Failure to receive such notice will not nullify revocation of the permission.
14. APS reserves all rights not specifically granted herein.
15. This document, including the Aptara Billing and Payment Terms and Conditions, shall be the entire agreement between the parties relating to the subject matter hereof.

USC
UNIVERSIDADE DE SANTIAGO DE COMPOSTELA

ELSEVIER LICENSE TERMS AND CONDITIONS

Jan 04, 2023

This Agreement between Gonzalo Diaz ("You") and Elsevier ("Elsevier") consists of your license details and the terms and conditions provided by Elsevier and Copyright Clearance Center.

License Number	5461981194853
License date	Jan 04, 2023
Licensed Content Publisher	Elsevier
Licensed Content Publication	Nuclear Instruments and Methods in Physics Research Section A: Accelerators, Spectrometers, Detectors and Associated Equipment
Licensed Content Title	Time profile of the scintillation from liquid and gaseous xenon
Licensed Content Author	Ikuko Murayama,Shogo Nakamura
Licensed Content Date	Nov 1, 2014
Licensed Content Volume	763
Licensed Content Issue	n/a
Licensed Content Pages	5
Start Page	533
End Page	537
Type of Use	reuse in a thesis/dissertation
Portion	figures/tables/illustrations
Number of figures/tables /illustrations	1
Format	both print and electronic
Are you the author of this Elsevier article?	No
Will you be translating?	No
Title	Sensitivity of NEXT-100 detector to neutrinoless double beta decay
Institution name	Universidade de Santiago de Compostela
Expected presentation date	Jan 2023
Portions	Figure 5. Typical liquid and gaseos xenon emission spectrum
Requestor Location	Gonzalo Diaz Rúa de Xoaquín Díaz de Rábago, s/n Santiago de Compostela, 15705 Spain Attn: Gonzalo Diaz
Publisher Tax ID	GB 494 6272 12
Total	**0.00 EUR**
Terms and Conditions	

INTRODUCTION

1. The publisher for this copyrighted material is Elsevier. By clicking "accept" in connection with completing this licensing transaction, you agree that the following terms and conditions apply to this transaction (along with the Billing and Payment terms and conditions established by Copyright Clearance Center, Inc. ("CCC"), at the time that you opened your Rightslink account and that are available at any time at http://myaccount.copyright.com).

GENERAL TERMS

2. Elsevier hereby grants you permission to reproduce the aforementioned material subject to the terms and conditions indicated.

3. Acknowledgement: If any part of the material to be used (for example, figures) has appeared in our publication with credit or acknowledgement to another source, permission must also be sought from that source. If such permission is not obtained then that material may not be included in your publication/copies. Suitable acknowledgement to the source must be made, either as a footnote or in a reference list at the end of your publication, as follows:
"Reprinted from Publication title, Vol /edition number, Author(s), Title of article / title of chapter, Pages No., Copyright (Year), with permission from Elsevier [OR APPLICABLE SOCIETY COPYRIGHT OWNER]." Also Lancet special credit - "Reprinted from The Lancet, Vol. number, Author(s), Title of article, Pages No., Copyright (Year), with permission from Elsevier."
4. Reproduction of this material is confined to the purpose and/or media for which permission is hereby given.
5. Altering/Modifying Material: Not Permitted. However figures and illustrations may be altered/adapted minimally to serve your work. Any other abbreviations, additions, deletions and/or any other alterations shall be made only with prior written authorization of Elsevier Ltd. (Please contact Elsevier's permissions helpdesk here). No modifications can be made to any Lancet figures/tables and they must be reproduced in full.
6. If the permission fee for the requested use of our material is waived in this instance, please be advised that your future requests for Elsevier materials may attract a fee.
7. Reservation of Rights: Publisher reserves all rights not specifically granted in the combination of (i) the license details provided by you and accepted in the course of this licensing transaction, (ii) these terms and conditions and (iii) CCC's Billing and Payment terms and conditions.
8. License Contingent Upon Payment: While you may exercise the rights licensed immediately upon issuance of the license at the end of the licensing process for the transaction, provided that you have disclosed complete and accurate details of your proposed use, no license is finally effective unless and until full payment is received from you (either by publisher or by CCC) as provided in CCC's Billing and Payment terms and conditions. If full payment is not received on a timely basis, then any license preliminarily granted shall be deemed automatically revoked and shall be void as if never granted. Further, in the event that you breach any of these terms and conditions or any of CCC's Billing and Payment terms and conditions, the license is automatically revoked and shall be void as if never granted. Use of materials as described in a revoked license, as well as any use of the materials beyond the scope of an unrevoked license, may constitute copyright infringement and publisher reserves the right to take any and all action to protect its copyright in the materials.
9. Warranties: Publisher makes no representations or warranties with respect to the licensed material.
10. Indemnity: You hereby indemnify and agree to hold harmless publisher and CCC, and their respective officers, directors, employees and agents, from and against any and all claims arising out of your use of the licensed material other than as specifically authorized pursuant to this license.
11. No Transfer of License: This license is personal to you and may not be sublicensed, assigned, or transferred by you to any other person without publisher's written permission.
12. No Amendment Except in Writing: This license may not be amended except in a writing signed by both parties (or, in the case of publisher, by CCC on publisher's behalf).
13. Objection to Contrary Terms: Publisher hereby objects to any terms contained in any purchase order, acknowledgment, check endorsement or other writing prepared by you, which terms are inconsistent with these terms and conditions or CCC's Billing and Payment terms and conditions. These terms and conditions, together with CCC's Billing and Payment terms and conditions (which are incorporated herein), comprise the entire agreement between you and publisher (and CCC) concerning this licensing transaction. In the event of any conflict between your obligations established by these terms and conditions and those established by CCC's Billing and Payment terms and conditions, these terms and conditions shall control.
14. Revocation: Elsevier or Copyright Clearance Center may deny the permissions described in this License at their sole discretion, for any reason or no reason, with a full refund payable to you. Notice of such denial will be made using the contact information provided by you. Failure to receive such notice will not alter or invalidate the denial. In no event will Elsevier or Copyright Clearance Center be responsible or liable for any costs, expenses or damage incurred by you as a result of a denial of your permission request, other than a refund of the amount(s) paid by you to Elsevier and/or Copyright Clearance Center for denied permissions.

LIMITED LICENSE

The following terms and conditions apply only to specific license types:
15. **Translation**: This permission is granted for non-exclusive world **English** rights only unless your license was granted for translation rights. If you licensed translation rights you may only translate this content into the languages you requested. A professional translator must perform all translations and reproduce the content word for word preserving the integrity of the article.
16. **Posting licensed content on any Website**: The following terms and conditions apply as follows: Licensing material from an Elsevier journal: All content posted to the web site must maintain the copyright information line on the bottom of each image; A hyper-text must be included to the Homepage of the journal from which you are licensing at http://www.sciencedirect.com/science/journal/xxxxx or the Elsevier homepage for books at http://www.elsevier.com; Central Storage: This license does not include permission for a scanned version of the material to be stored in a central repository such as that provided by Heron/XanEdu.
Licensing material from an Elsevier book: A hyper-text link must be included to the Elsevier homepage at http://www.elsevier.com . All content posted to the web site must maintain the copyright information line on the bottom of each image.

Posting licensed content on Electronic reserve: In addition to the above the following clauses are applicable: The web site must be password-protected and made available only to bona fide students registered on a relevant course. This permission

is granted for 1 year only. You may obtain a new license for future website posting.
17. **For journal authors:** the following clauses are applicable in addition to the above:
Preprints:
A preprint is an author's own write-up of research results and analysis, it has not been peer-reviewed, nor has it had any other value added to it by a publisher (such as formatting, copyright, technical enhancement etc.).
Authors can share their preprints anywhere at any time. Preprints should not be added to or enhanced in any way in order to appear more like, or to substitute for, the final versions of articles however authors can update their preprints on arXiv or RePEc with their Accepted Author Manuscript (see below).
If accepted for publication, we encourage authors to link from the preprint to their formal publication via its DOI. Millions of researchers have access to the formal publications on ScienceDirect, and so links will help users to find, access, cite and use the best available version. Please note that Cell Press, The Lancet and some society-owned have different preprint policies. Information on these policies is available on the journal homepage.
Accepted Author Manuscripts: An accepted author manuscript is the manuscript of an article that has been accepted for publication and which typically includes author-incorporated changes suggested during submission, peer review and editor-author communications.
Authors can share their accepted author manuscript:

- immediately
    - via their non-commercial person homepage or blog
    - by updating a preprint in arXiv or RePEc with the accepted manuscript
    - via their research institute or institutional repository for internal institutional uses or as part of an invitation-only research collaboration work-group
    - directly by providing copies to their students or to research collaborators for their personal use
    - for private scholarly sharing as part of an invitation-only work group on commercial sites with which Elsevier has an agreement
- After the embargo period
    - via non-commercial hosting platforms such as their institutional repository
    - via commercial sites with which Elsevier has an agreement

In all cases accepted manuscripts should:

- link to the formal publication via its DOI
- bear a CC-BY-NC-ND license - this is easy to do
- if aggregated with other manuscripts, for example in a repository or other site, be shared in alignment with our hosting policy not be added to or enhanced in any way to appear more like, or to substitute for, the published journal article.

Published journal article (JPA): A published journal article (PJA) is the definitive final record of published research that appears or will appear in the journal and embodies all value-adding publishing activities including peer review co-ordination, copy-editing, formatting, (if relevant) pagination and online enrichment.
Policies for sharing publishing journal articles differ for subscription and gold open access articles:
Subscription Articles: If you are an author, please share a link to your article rather than the full-text. Millions of researchers have access to the formal publications on ScienceDirect, and so links will help your users to find, access, cite, and use the best available version.
Theses and dissertations which contain embedded PJAs as part of the formal submission can be posted publicly by the awarding institution with DOI links back to the formal publications on ScienceDirect.
If you are affiliated with a library that subscribes to ScienceDirect you have additional private sharing rights for others' research accessed under that agreement. This includes use for classroom teaching and internal training at the institution (including use in course packs and courseware programs), and inclusion of the article for grant funding purposes.
Gold Open Access Articles: May be shared according to the author-selected end-user license and should contain a CrossMark logo, the end user license, and a DOI link to the formal publication on ScienceDirect.
Please refer to Elsevier's posting policy for further information.
18. **For book authors** the following clauses are applicable in addition to the above: Authors are permitted to place a brief summary of their work online only. You are not allowed to download and post the published electronic version of your chapter, nor may you scan the printed edition to create an electronic version. **Posting to a repository:** Authors are permitted to post a summary of their chapter only in their institution's repository.
19. **Thesis/Dissertation**: If your license is for use in a thesis/dissertation your thesis may be submitted to your institution in either print or electronic form. Should your thesis be published commercially, please reapply for permission. These requirements include permission for the Library and Archives of Canada to supply single copies, on demand, of the complete thesis and include permission for Proquest/UMI to supply single copies, on demand, of the complete thesis. Should your thesis be published commercially, please reapply for permission. Theses and dissertations which contain embedded PJAs as part of the formal submission can be posted publicly by the awarding institution with DOI links back to the formal publications on ScienceDirect.

Elsevier Open Access Terms and Conditions

You can publish open access with Elsevier in hundreds of open access journals or in nearly 2000 established subscription journals that support open access publishing. Permitted third party re-use of these open access articles is defined by the author's choice of Creative Commons user license. See our open access license policy for more information.

Terms & Conditions applicable to all Open Access articles published with Elsevier:

Any reuse of the article must not represent the author as endorsing the adaptation of the article nor should the article be modified in such a way as to damage the author's honour or reputation. If any changes have been made, such changes must be clearly indicated.

The author(s) must be appropriately credited and we ask that you include the end user license and a DOI link to the formal publication on ScienceDirect.

If any part of the material to be used (for example, figures) has appeared in our publication with credit or acknowledgement to another source it is the responsibility of the user to ensure their reuse complies with the terms and conditions determined by the rights holder.

Additional Terms & Conditions applicable to each Creative Commons user license:

CC BY: The CC-BY license allows users to copy, to create extracts, abstracts and new works from the Article, to alter and revise the Article and to make commercial use of the Article (including reuse and/or resale of the Article by commercial entities), provided the user gives appropriate credit (with a link to the formal publication through the relevant DOI), provides a link to the license, indicates if changes were made and the licensor is not represented as endorsing the use made of the work. The full details of the license are available at http://creativecommons.org/licenses/by/4.0.

CC BY NC SA: The CC BY-NC-SA license allows users to copy, to create extracts, abstracts and new works from the Article, to alter and revise the Article, provided this is not done for commercial purposes, and that the user gives appropriate credit (with a link to the formal publication through the relevant DOI), provides a link to the license, indicates if changes were made and the licensor is not represented as endorsing the use made of the work. Further, any new works must be made available on the same conditions. The full details of the license are available at http://creativecommons.org/licenses/by-nc-sa/4.0.

CC BY NC ND: The CC BY-NC-ND license allows users to copy and distribute the Article, provided this is not done for commercial purposes and further does not permit distribution of the Article if it is changed or edited in any way, and provided the user gives appropriate credit (with a link to the formal publication through the relevant DOI), provides a link to the license, and that the licensor is not represented as endorsing the use made of the work. The full details of the license are available at http://creativecommons.org/licenses/by-nc-nd/4.0. Any commercial reuse of Open Access articles published with a CC BY NC SA or CC BY NC ND license requires permission from Elsevier and will be subject to a fee.

Commercial reuse includes:

- Associating advertising with the full text of the Article
- Charging fees for document delivery or access
- Article aggregation
- Systematic distribution via e-mail lists or share buttons

Posting or linking by commercial companies for use by customers of those companies.

20. **Other Conditions**:

v1.10

Questions? customercare@copyright.com or +1-855-239-3415 (toll free in the US) or +1-978-646-2777.

USC UNIVERSIDADE DE SANTIAGO DE COMPOSTELA

ELSEVIER LICENSE TERMS AND CONDITIONS

Jan 04, 2023

This Agreement between Gonzalo Diaz ("You") and Elsevier ("Elsevier") consists of your license details and the terms and conditions provided by Elsevier and Copyright Clearance Center.

License Number	5461990568685
License date	Jan 04, 2023
Licensed Content Publisher	Elsevier
Licensed Content Publication	Nuclear Instruments and Methods in Physics Research Section A: Accelerators, Spectrometers, Detectors and Associated Equipment
Licensed Content Title	The spectroscopic properties of high-pressure xenon
Licensed Content Author	Aleksey Bolotnikov,Brian Ramsey
Licensed Content Date	Sep 11, 1997
Licensed Content Volume	396
Licensed Content Issue	3
Licensed Content Pages	11
Start Page	360
End Page	370
Type of Use	reuse in a thesis/dissertation
Portion	figures/tables/illustrations
Number of figures/tables /illustrations	1
Format	both print and electronic
Are you the author of this Elsevier article?	No
Will you be translating?	No
Title	Sensitivity of NEXT-100 detector to neutrinoless double beta decay
Institution name	Universidade de Santiago de Compostela
Expected presentation date	Jan 2023
Portions	Figure 5. Density dependencies of the intrinsic energy resolution
Requestor Location	Gonzalo Diaz Rúa de Xoaquín Díaz de Rábago, s/n Santiago de Compostela, 15705 Spain Attn: Gonzalo Diaz
Publisher Tax ID	GB 494 6272 12
Total	**0.00 EUR**
Terms and Conditions	

INTRODUCTION

1. The publisher for this copyrighted material is Elsevier. By clicking "accept" in connection with completing this licensing transaction, you agree that the following terms and conditions apply to this transaction (along with the Billing and Payment terms and conditions established by Copyright Clearance Center, Inc. ("CCC"), at the time that you opened your Rightslink account and that are available at any time at http://myaccount.copyright.com).

GENERAL TERMS

2. Elsevier hereby grants you permission to reproduce the aforementioned material subject to the terms and conditions indicated.

3. Acknowledgement: If any part of the material to be used (for example, figures) has appeared in our publication with credit or acknowledgement to another source, permission must also be sought from that source. If such permission is not obtained then that material may not be included in your publication/copies. Suitable acknowledgement to the source must be made, either as a footnote or in a reference list at the end of your publication, as follows:
"Reprinted from Publication title, Vol /edition number, Author(s), Title of article / title of chapter, Pages No., Copyright (Year), with permission from Elsevier [OR APPLICABLE SOCIETY COPYRIGHT OWNER]." Also Lancet special credit - "Reprinted from The Lancet, Vol. number, Author(s), Title of article, Pages No., Copyright (Year), with permission from Elsevier."
4. Reproduction of this material is confined to the purpose and/or media for which permission is hereby given.
5. Altering/Modifying Material: Not Permitted. However figures and illustrations may be altered/adapted minimally to serve your work. Any other abbreviations, additions, deletions and/or any other alterations shall be made only with prior written authorization of Elsevier Ltd. (Please contact Elsevier's permissions helpdesk here). No modifications can be made to any Lancet figures/tables and they must be reproduced in full.
6. If the permission fee for the requested use of our material is waived in this instance, please be advised that your future requests for Elsevier materials may attract a fee.
7. Reservation of Rights: Publisher reserves all rights not specifically granted in the combination of (i) the license details provided by you and accepted in the course of this licensing transaction, (ii) these terms and conditions and (iii) CCC's Billing and Payment terms and conditions.
8. License Contingent Upon Payment: While you may exercise the rights licensed immediately upon issuance of the license at the end of the licensing process for the transaction, provided that you have disclosed complete and accurate details of your proposed use, no license is finally effective unless and until full payment is received from you (either by publisher or by CCC) as provided in CCC's Billing and Payment terms and conditions. If full payment is not received on a timely basis, then any license preliminarily granted shall be deemed automatically revoked and shall be void as if never granted. Further, in the event that you breach any of these terms and conditions or any of CCC's Billing and Payment terms and conditions, the license is automatically revoked and shall be void as if never granted. Use of materials as described in a revoked license, as well as any use of the materials beyond the scope of an unrevoked license, may constitute copyright infringement and publisher reserves the right to take any and all action to protect its copyright in the materials.
9. Warranties: Publisher makes no representations or warranties with respect to the licensed material.
10. Indemnity: You hereby indemnify and agree to hold harmless publisher and CCC, and their respective officers, directors, employees and agents, from and against any and all claims arising out of your use of the licensed material other than as specifically authorized pursuant to this license.
11. No Transfer of License: This license is personal to you and may not be sublicensed, assigned, or transferred by you to any other person without publisher's written permission.
12. No Amendment Except in Writing: This license may not be amended except in a writing signed by both parties (or, in the case of publisher, by CCC on publisher's behalf).
13. Objection to Contrary Terms: Publisher hereby objects to any terms contained in any purchase order, acknowledgment, check endorsement or other writing prepared by you, which terms are inconsistent with these terms and conditions or CCC's Billing and Payment terms and conditions. These terms and conditions, together with CCC's Billing and Payment terms and conditions (which are incorporated herein), comprise the entire agreement between you and publisher (and CCC) concerning this licensing transaction. In the event of any conflict between your obligations established by these terms and conditions and those established by CCC's Billing and Payment terms and conditions, these terms and conditions shall control.
14. Revocation: Elsevier or Copyright Clearance Center may deny the permissions described in this License at their sole discretion, for any reason or no reason, with a full refund payable to you. Notice of such denial will be made using the contact information provided by you. Failure to receive such notice will not alter or invalidate the denial. In no event will Elsevier or Copyright Clearance Center be responsible or liable for any costs, expenses or damage incurred by you as a result of a denial of your permission request, other than a refund of the amount(s) paid by you to Elsevier and/or Copyright Clearance Center for denied permissions.

LIMITED LICENSE

The following terms and conditions apply only to specific license types:
15. **Translation**: This permission is granted for non-exclusive world **English** rights only unless your license was granted for translation rights. If you licensed translation rights you may only translate this content into the languages you requested. A professional translator must perform all translations and reproduce the content word for word preserving the integrity of the article.
16. **Posting licensed content on any Website**: The following terms and conditions apply as follows: Licensing material from an Elsevier journal: All content posted to the web site must maintain the copyright information line on the bottom of each image; A hyper-text must be included to the Homepage of the journal from which you are licensing at http://www.sciencedirect.com/science/journal/xxxxx or the Elsevier homepage for books at http://www.elsevier.com; Central Storage: This license does not include permission for a scanned version of the material to be stored in a central repository such as that provided by Heron/XanEdu.
Licensing material from an Elsevier book: A hyper-text link must be included to the Elsevier homepage at http://www.elsevier.com . All content posted to the web site must maintain the copyright information line on the bottom of each image.

Posting licensed content on Electronic reserve: In addition to the above the following clauses are applicable: The web site must be password-protected and made available only to bona fide students registered on a relevant course. This permission

is granted for 1 year only. You may obtain a new license for future website posting.
17. **For journal authors:** the following clauses are applicable in addition to the above:
Preprints:
A preprint is an author's own write-up of research results and analysis, it has not been peer-reviewed, nor has it had any other value added to it by a publisher (such as formatting, copyright, technical enhancement etc.).
Authors can share their preprints anywhere at any time. Preprints should not be added to or enhanced in any way in order to appear more like, or to substitute for, the final versions of articles however authors can update their preprints on arXiv or RePEc with their Accepted Author Manuscript (see below).
If accepted for publication, we encourage authors to link from the preprint to their formal publication via its DOI. Millions of researchers have access to the formal publications on ScienceDirect, and so links will help users to find, access, cite and use the best available version. Please note that Cell Press, The Lancet and some society-owned have different preprint policies. Information on these policies is available on the journal homepage.
Accepted Author Manuscripts: An accepted author manuscript is the manuscript of an article that has been accepted for publication and which typically includes author-incorporated changes suggested during submission, peer review and editor-author communications.
Authors can share their accepted author manuscript:

- immediately
    - via their non-commercial person homepage or blog
    - by updating a preprint in arXiv or RePEc with the accepted manuscript
    - via their research institute or institutional repository for internal institutional uses or as part of an invitation-only research collaboration work-group
    - directly by providing copies to their students or to research collaborators for their personal use
    - for private scholarly sharing as part of an invitation-only work group on commercial sites with which Elsevier has an agreement
- After the embargo period
    - via non-commercial hosting platforms such as their institutional repository
    - via commercial sites with which Elsevier has an agreement

In all cases accepted manuscripts should:

- link to the formal publication via its DOI
- bear a CC-BY-NC-ND license - this is easy to do
- if aggregated with other manuscripts, for example in a repository or other site, be shared in alignment with our hosting policy not be added to or enhanced in any way to appear more like, or to substitute for, the published journal article.

Published journal article (JPA): A published journal article (PJA) is the definitive final record of published research that appears or will appear in the journal and embodies all value-adding publishing activities including peer review co-ordination, copy-editing, formatting, (if relevant) pagination and online enrichment.
Policies for sharing publishing journal articles differ for subscription and gold open access articles:
Subscription Articles: If you are an author, please share a link to your article rather than the full-text. Millions of researchers have access to the formal publications on ScienceDirect, and so links will help your users to find, access, cite, and use the best available version.
Theses and dissertations which contain embedded PJAs as part of the formal submission can be posted publicly by the awarding institution with DOI links back to the formal publications on ScienceDirect.
If you are affiliated with a library that subscribes to ScienceDirect you have additional private sharing rights for others' research accessed under that agreement. This includes use for classroom teaching and internal training at the institution (including use in course packs and courseware programs), and inclusion of the article for grant funding purposes.
Gold Open Access Articles: May be shared according to the author-selected end-user license and should contain a CrossMark logo, the end user license, and a DOI link to the formal publication on ScienceDirect.
Please refer to Elsevier's posting policy for further information.
18. **For book authors** the following clauses are applicable in addition to the above: Authors are permitted to place a brief summary of their work online only. You are not allowed to download and post the published electronic version of your chapter, nor may you scan the printed edition to create an electronic version. **Posting to a repository:** Authors are permitted to post a summary of their chapter only in their institution's repository.
19. **Thesis/Dissertation**: If your license is for use in a thesis/dissertation your thesis may be submitted to your institution in either print or electronic form. Should your thesis be published commercially, please reapply for permission. These requirements include permission for the Library and Archives of Canada to supply single copies, on demand, of the complete thesis and include permission for Proquest/UMI to supply single copies, on demand, of the complete thesis. Should your thesis be published commercially, please reapply for permission. Theses and dissertations which contain embedded PJAs as part of the formal submission can be posted publicly by the awarding institution with DOI links back to the formal publications on ScienceDirect.

Elsevier Open Access Terms and Conditions

You can publish open access with Elsevier in hundreds of open access journals or in nearly 2000 established subscription journals that support open access publishing. Permitted third party re-use of these open access articles is defined by the author's choice of Creative Commons user license. See our open access license policy for more information.

Terms & Conditions applicable to all Open Access articles published with Elsevier:

Any reuse of the article must not represent the author as endorsing the adaptation of the article nor should the article be modified in such a way as to damage the author's honour or reputation. If any changes have been made, such changes must be clearly indicated.

The author(s) must be appropriately credited and we ask that you include the end user license and a DOI link to the formal publication on ScienceDirect.

If any part of the material to be used (for example, figures) has appeared in our publication with credit or acknowledgement to another source it is the responsibility of the user to ensure their reuse complies with the terms and conditions determined by the rights holder.

Additional Terms & Conditions applicable to each Creative Commons user license:

CC BY: The CC-BY license allows users to copy, to create extracts, abstracts and new works from the Article, to alter and revise the Article and to make commercial use of the Article (including reuse and/or resale of the Article by commercial entities), provided the user gives appropriate credit (with a link to the formal publication through the relevant DOI), provides a link to the license, indicates if changes were made and the licensor is not represented as endorsing the use made of the work. The full details of the license are available at http://creativecommons.org/licenses/by/4.0.

CC BY NC SA: The CC BY-NC-SA license allows users to copy, to create extracts, abstracts and new works from the Article, to alter and revise the Article, provided this is not done for commercial purposes, and that the user gives appropriate credit (with a link to the formal publication through the relevant DOI), provides a link to the license, indicates if changes were made and the licensor is not represented as endorsing the use made of the work. Further, any new works must be made available on the same conditions. The full details of the license are available at http://creativecommons.org/licenses/by-nc-sa/4.0.

CC BY NC ND: The CC BY-NC-ND license allows users to copy and distribute the Article, provided this is not done for commercial purposes and further does not permit distribution of the Article if it is changed or edited in any way, and provided the user gives appropriate credit (with a link to the formal publication through the relevant DOI), provides a link to the license, and that the licensor is not represented as endorsing the use made of the work. The full details of the license are available at http://creativecommons.org/licenses/by-nc-nd/4.0. Any commercial reuse of Open Access articles published with a CC BY NC SA or CC BY NC ND license requires permission from Elsevier and will be subject to a fee.

Commercial reuse includes:

- Associating advertising with the full text of the Article
- Charging fees for document delivery or access
- Article aggregation
- Systematic distribution via e-mail lists or share buttons

Posting or linking by commercial companies for use by customers of those companies.

20. **Other Conditions**:

v1.10

Questions? customercare@copyright.com or +1-855-239-3415 (toll free in the US) or +1-978-646-2777.

USC UNIVERSIDADE DE SANTIAGO DE COMPOSTELA

JOHN WILEY AND SONS LICENSE TERMS AND CONDITIONS

Jan 04, 2023

This Agreement between Gonzalo Diaz ("You") and John Wiley and Sons ("John Wiley and Sons") consists of your license details and the terms and conditions provided by John Wiley and Sons and Copyright Clearance Center.

License Number	5461991410828
License date	Jan 04, 2023
Licensed Content Publisher	John Wiley and Sons
Licensed Content Publication	Wiley Books
Licensed Content Title	X-Ray Detectors
Licensed Content Author	P. Gryboś, W. Dąbrowski, E. Figueroa-Feliciano, et al
Licensed Content Date	Jun 9, 2004
Licensed Content Pages	139
Type of Use	Dissertation/Thesis
Requestor type	University/Academic
Format	Print and electronic
Portion	Figure/table
Number of figures/tables	1
Will you be translating?	No
Title	Sensitivity of NEXT-100 detector to neutrinoless double beta decay
Institution name	Universidade de Santiago de Compostela
Expected presentation date	Jan 2023
Portions	Figure 4.2.2
Requestor Location	Gonzalo Diaz Rúa de Xoaquín Díaz de Rábago, s/n Santiago de Compostela, 15705 Spain Attn: Gonzalo Diaz
Publisher Tax ID	EU826007151
Total	**0.00 EUR**
Terms and Conditions	

TERMS AND CONDITIONS

This copyrighted material is owned by or exclusively licensed to John Wiley & Sons, Inc. or one of its group companies (each a"Wiley Company") or handled on behalf of a society with which a Wiley Company has exclusive publishing rights in relation to a particular work (collectively "WILEY"). By clicking "accept" in connection with completing this licensing transaction, you agree that the following terms and conditions apply to this transaction (along with the billing and payment terms and conditions established by the Copyright Clearance Center Inc., ("CCC's Billing and Payment terms and conditions"), at the time that you opened your RightsLink account (these are available at any time at http://myaccount.copyright.com).

Terms and Conditions

- The materials you have requested permission to reproduce or reuse (the "Wiley Materials") are protected by copyright.
- You are hereby granted a personal, non-exclusive, non-sub licensable (on a stand-alone basis), non-transferable, worldwide, limited license to reproduce the Wiley Materials for the purpose specified in the licensing process. This license, **and any CONTENT (PDF or image file) purchased as part of your order,** is for a one-time use only and

limited to any maximum distribution number specified in the license. The first instance of republication or reuse granted by this license must be completed within two years of the date of the grant of this license (although copies prepared before the end date may be distributed thereafter). The Wiley Materials shall not be used in any other manner or for any other purpose, beyond what is granted in the license. Permission is granted subject to an appropriate acknowledgement given to the author, title of the material/book/journal and the publisher. You shall also duplicate the copyright notice that appears in the Wiley publication in your use of the Wiley Material. Permission is also granted on the understanding that nowhere in the text is a previously published source acknowledged for all or part of this Wiley Material. Any third party content is expressly excluded from this permission.

- With respect to the Wiley Materials, all rights are reserved. Except as expressly granted by the terms of the license, no part of the Wiley Materials may be copied, modified, adapted (except for minor reformatting required by the new Publication), translated, reproduced, transferred or distributed, in any form or by any means, and no derivative works may be made based on the Wiley Materials without the prior permission of the respective copyright owner.**For STM Signatory Publishers clearing permission under the terms of the STM Permissions Guidelines only, the terms of the license are extended to include subsequent editions and for editions in other languages, provided such editions are for the work as a whole in situ and does not involve the separate exploitation of the permitted figures or extracts,** You may not alter, remove or suppress in any manner any copyright, trademark or other notices displayed by the Wiley Materials. You may not license, rent, sell, loan, lease, pledge, offer as security, transfer or assign the Wiley Materials on a stand-alone basis, or any of the rights granted to you hereunder to any other person.

- The Wiley Materials and all of the intellectual property rights therein shall at all times remain the exclusive property of John Wiley & Sons Inc, the Wiley Companies, or their respective licensors, and your interest therein is only that of having possession of and the right to reproduce the Wiley Materials pursuant to Section 2 herein during the continuance of this Agreement. You agree that you own no right, title or interest in or to the Wiley Materials or any of the intellectual property rights therein. You shall have no rights hereunder other than the license as provided for above in Section 2. No right, license or interest to any trademark, trade name, service mark or other branding ("Marks") of WILEY or its licensors is granted hereunder, and you agree that you shall not assert any such right, license or interest with respect thereto

- NEITHER WILEY NOR ITS LICENSORS MAKES ANY WARRANTY OR REPRESENTATION OF ANY KIND TO YOU OR ANY THIRD PARTY, EXPRESS, IMPLIED OR STATUTORY, WITH RESPECT TO THE MATERIALS OR THE ACCURACY OF ANY INFORMATION CONTAINED IN THE MATERIALS, INCLUDING, WITHOUT LIMITATION, ANY IMPLIED WARRANTY OF MERCHANTABILITY, ACCURACY, SATISFACTORY QUALITY, FITNESS FOR A PARTICULAR PURPOSE, USABILITY, INTEGRATION OR NON-INFRINGEMENT AND ALL SUCH WARRANTIES ARE HEREBY EXCLUDED BY WILEY AND ITS LICENSORS AND WAIVED BY YOU.

- WILEY shall have the right to terminate this Agreement immediately upon breach of this Agreement by you.

- You shall indemnify, defend and hold harmless WILEY, its Licensors and their respective directors, officers, agents and employees, from and against any actual or threatened claims, demands, causes of action or proceedings arising from any breach of this Agreement by you.

- IN NO EVENT SHALL WILEY OR ITS LICENSORS BE LIABLE TO YOU OR ANY OTHER PARTY OR ANY OTHER PERSON OR ENTITY FOR ANY SPECIAL, CONSEQUENTIAL, INCIDENTAL, INDIRECT, EXEMPLARY OR PUNITIVE DAMAGES, HOWEVER CAUSED, ARISING OUT OF OR IN CONNECTION WITH THE DOWNLOADING, PROVISIONING, VIEWING OR USE OF THE MATERIALS REGARDLESS OF THE FORM OF ACTION, WHETHER FOR BREACH OF CONTRACT, BREACH OF WARRANTY, TORT, NEGLIGENCE, INFRINGEMENT OR OTHERWISE (INCLUDING, WITHOUT LIMITATION, DAMAGES BASED ON LOSS OF PROFITS, DATA, FILES, USE, BUSINESS OPPORTUNITY OR CLAIMS OF THIRD PARTIES), AND WHETHER OR NOT THE PARTY HAS BEEN ADVISED OF THE POSSIBILITY OF SUCH DAMAGES. THIS LIMITATION SHALL APPLY NOTWITHSTANDING ANY FAILURE OF ESSENTIAL PURPOSE OF ANY LIMITED REMEDY PROVIDED HEREIN.

- Should any provision of this Agreement be held by a court of competent jurisdiction to be illegal, invalid, or unenforceable, that provision shall be deemed amended to achieve as nearly as possible the same economic effect as the original provision, and the legality, validity and enforceability of the remaining provisions of this Agreement shall not be affected or impaired thereby.

- The failure of either party to enforce any term or condition of this Agreement shall not constitute a waiver of either party's right to enforce each and every term and condition of this Agreement. No breach under this agreement shall be deemed waived or excused by either party unless such waiver or consent is in writing signed by the party granting such waiver or consent. The waiver by or consent of a party to a breach of any provision of this Agreement shall not operate or be construed as a waiver of or consent to any other or subsequent breach by such other party.

- This Agreement may not be assigned (including by operation of law or otherwise) by you without WILEY's prior written consent.
- Any fee required for this permission shall be non-refundable after thirty (30) days from receipt by the CCC.
- These terms and conditions together with CCC's Billing and Payment terms and conditions (which are incorporated herein) form the entire agreement between you and WILEY concerning this licensing transaction and (in the absence of fraud) supersedes all prior agreements and representations of the parties, oral or written. This Agreement may not be amended except in writing signed by both parties. This Agreement shall be binding upon and inure to the benefit of the parties' successors, legal representatives, and authorized assigns.
- In the event of any conflict between your obligations established by these terms and conditions and those established by CCC's Billing and Payment terms and conditions, these terms and conditions shall prevail.
- WILEY expressly reserves all rights not specifically granted in the combination of (i) the license details provided by you and accepted in the course of this licensing transaction, (ii) these terms and conditions and (iii) CCC's Billing and Payment terms and conditions.
- This Agreement will be void if the Type of Use, Format, Circulation, or Requestor Type was misrepresented during the licensing process.
- This Agreement shall be governed by and construed in accordance with the laws of the State of New York, USA, without regards to such state's conflict of law rules. Any legal action, suit or proceeding arising out of or relating to these Terms and Conditions or the breach thereof shall be instituted in a court of competent jurisdiction in New York County in the State of New York in the United States of America and each party hereby consents and submits to the personal jurisdiction of such court, waives any objection to venue in such court and consents to service of process by registered or certified mail, return receipt requested, at the last known address of such party.

WILEY OPEN ACCESS TERMS AND CONDITIONS

Wiley Publishes Open Access Articles in fully Open Access Journals and in Subscription journals offering Online Open. Although most of the fully Open Access journals publish open access articles under the terms of the Creative Commons Attribution (CC BY) License only, the subscription journals and a few of the Open Access Journals offer a choice of Creative Commons Licenses. The license type is clearly identified on the article.

The Creative Commons Attribution License

The Creative Commons Attribution License (CC-BY) allows users to copy, distribute and transmit an article, adapt the article and make commercial use of the article. The CC-BY license permits commercial and non-

Creative Commons Attribution Non-Commercial License

The Creative Commons Attribution Non-Commercial (CC-BY-NC)License permits use, distribution and reproduction in any medium, provided the original work is properly cited and is not used for commercial purposes.(see below)

Creative Commons Attribution-Non-Commercial-NoDerivs License

The Creative Commons Attribution Non-Commercial-NoDerivs License (CC-BY-NC-ND) permits use, distribution and reproduction in any medium, provided the original work is properly cited, is not used for commercial purposes and no modifications or adaptations are made. (see below)

Use by commercial "for-profit" organizations

Use of Wiley Open Access articles for commercial, promotional, or marketing purposes requires further explicit permission from Wiley and will be subject to a fee.

Further details can be found on Wiley Online Library http://olabout.wiley.com/WileyCDA/Section/id-410895.html

Other Terms and Conditions:

v1.10 Last updated September 2015

Questions? customercare@copyright.com or +1-855-239-3415 (toll free in the US) or +1-978-646-2777.

Gmail **Gonzalo Díaz López <gonzalodiazlopez10@gmail.com>**

Permission for the reproduction of figures

2 mensajes

Gonzalo Díaz López <gonzalodiazlopez10@gmail.com> 5 de enero de 2023, 14:02
Para: Gonzalo Martínez Lema <gonzaponte@gmail.com>

Dear G.Martínez Lema:
I am a PhD student at the University of Santiago de Compostela (Spain) working in the NEXT experiment. I request your permission to reproduce the following figure(s) from your work PhD thesis: Low energy calibration, reconstruction software and light-collection efficiency parametrization of the NEXT-White detector in my PhD thesis with title *Sensitivity of NEXT-100 detector to neutrinoless double beta decay*.

1. Figure 5.10. (generic workflow)
2. Figure 6.6. (exponential fit)

Sorry for the inconvenience, my institution is particularly sensitive about the reproduction of figures from other works in the PhD dissertations.
Kind regards,
Gonzalo Díaz López

Gonzalo Martínez Lema <gonzaponte@gmail.com> 5 de enero de 2023, 14:14
Para: Gonzalo Díaz López <gonzalodiazlopez10@gmail.com>

Dear Gonzalo,

you have my permission.

Kind regards,
Gonzalo
[El texto citado está oculto]

USC UNIVERSIDADE DE SANTIAGO DE COMPOSTELA

Neutrinoless double beta decay is a lepton number violating process and its observation would imply the Majorana nature of neutrinos. This thesis was developed within the NEXT collaboration, that proposes the search for the decay in a high pressure xenon electroluminiscence TPC. The collaboration is actually building its hundred kilogram scale detector, NEXT-100. This thesis studies the sensitivity of NEXT-100 to neutrinoless double beta decay, requiring the implementation of the full detector simulation and its background components. Sensitivity is studied in the limit of a counting experiment and also through the confidence intervals, obtaining an expected reach similar to its main competitors.